ESTRUCTURA ELECTRONICA Y FENOMENOS DE CONFINAMIENTO EN SISTEMAS DE BAJA DIMENSIONALIDAD

Memoria presentada por
Lukasz Walczak
para optar al grado de
Doctor en Ciencias Físicas

Departamento de Física de la Materia Condensada
Universidad Autónoma de Madrid

Tesis dirigida por:
Enrique García Michel

Septiembre de 2014

ELECTRONIC STRUCTURE AND CONFINEMENT PHENOMENA IN LOW DIMENSIONAL SYSTEMS

A thesis presented by
Lukasz Walczak
for the degree of
Doctor of Philosophy
in the subject of Physics

Departamento de Física de la Materia Condensada
Universidad Autónoma de Madrid

Thesis directed by:
Enrique García Michel

September 2014

The capacity to be puzzled is the premise of all creation, be it in art or in science.

Erich Fromm

My family and friends

Contents

Resumen

Los sistemas de baja dimensionalidad basados en metales o semiconductores han sido objeto de un interés continuado desde hace ya algunos años. Por una parte, las propiedades cuánticas de estos sistemas ofrecen la posibilidad de analizar el comportamiento físico en la nanoescala; por otra, son numerosas las posibles aplicaciones tecnológicas basadas en estos sistemas. Entre otros usos, este tipo de materiales se pueden utilizar como una superficie activa en catálisis heterogénea, como un molde para el crecimiento de otros materiales de baja dimensionalidad o en el estudio de las propiedades termodinámicas de estos mismos materiales. En este trabajo hemos analizado las propiedades de varias superficies donde aparecen efectos como estos.

La mayor parte de la tesis doctoral consiste en el estudio de la estructura electrónica y cristalina de sistemas de baja dimensionalidad utilizando espectroscopia de fotoemisión resuelta en ángulo (ARPES) para la caracterización de estos sistemas. ARPES permite obtener información acerca de la estructura electrónica de una gran variedad de sistemas físicos y en particular de los estados electrónicos de superficie. Una de las principales ventajas de esta técnica es la posibilidad de cambiar tanto el ángulo de detección, como la energía del haz de fotones incidente, lo cual permite barrer tanto los vectores de onda paralelos y perpendiculares de la red recíproca a lo largo de las direcciones principales de alta simetría del cristal.

Para controlar la calidad de las superficies obtenidas se realizaron medidas utilizando técnicas de difracción de electrones de baja energía (LEED) o de microscopía de efecto túnel (STM), lo que permitió observar las reconstrucciones superficiales, así como espectroscopia de fotoemisión de rayos X (XPS), que es muy sensible a la contaminación superficial.

Algunos metales con orientación (110), como el platino, el iridio o el oro, presentan una reconstrucción natural (1x2) de su superficie. La reconstrucción se debe a la eliminación de una fila atómica de cada dos en la superficie, de modo que se forman cadenas de átomos en la dirección $[1\bar{1}0]$. La reconstrucción (1x2) dobla el punto de simetría $\bar{Y}$ de la superficie sobre el punto de simetría $\bar{\Gamma}$ y ambos se hacen equivalentes. Como consecuencia del doblado, desaparece la zona prohibida que existía en el punto simetría $\bar{Y}$, de modo que cabe esperar que no exista estado de superficie en ese punto después de la reconstrucción, tal y como se ha confirmado recientemente para Au(110)-(1x2). Sin embargo, se han observado en este trabajo estados de resonancia en los puntos $\bar{\Gamma}$ y $\bar{\Gamma}'$ de alta simetría, con un máximo de la energía

de ligadura de ~0.2 eV, que se atribuyen al estado de superficie tipo Shockley. En el punto $\overline{X}$ de alta simetría se observa una separación (splitting) de las bandas. Los cálculos teóricos llevados a cabo permiten asignar el origen de la separación a un doblado (1x2) de las bandas de volumen.

Los metales del grupo II, berilio y magnesio, se caracterizan por una alta densidad de estados superficiales, debido a la existencia de amplias zonas prohibidas en la proyección de los estados de volumen. Esto da lugar a intensas señales de superficie en los espectros de fotoemisión. Además, los estados de superficie de estos materiales (especialmente en la superficie (0001)) muestran un comportamiento de gas electrónico bidimensional prácticamente desacoplado del volumen. Igualmente, la superficie $(10\bar{1}0)$ presenta varios estados superficiales (de diferente naturaleza orbital) que aparecen en emisión normal y en el punto de simetría $\overline{A}$. Por otro lado, las superficies de Be resultan excepcionalmente interesantes por el intenso acoplamiento electrón-fonón que presentan, que incluso permitiría esperar la formación de una fase superconductora en la superficie a bajas temperaturas. El patrón rectangular de LEED está de acuerdo con la cristalografía esperada para la superficie vecinal de $Be(10\bar{1}0)$. En este trabajo se ha llevado a cabo la caracterización de la estructura electrónica de la superficie mediante ARPES. Las medidas en las dos direcciones, perpendicular y paralela a los escalones, para distintas energías de fotón, nos proporcionan una caracterización completa para los estados electrónicos de superficie. Se ha identificado un estado de resonancia de superficie en los puntos $\overline{M}$ y $\overline{A}$ de alta simetría, que también existe en $Be(10\bar{1}0)$ plano. Los mínimos de la energía de ligadura de estos estados son mayores que para la superficie plana, debido al confinamiento lateral provocada por los escalones. La posición del mínimo de uno de los estados de superficie (S1) en el momento paralelo medido respecto a la normal a la superficie óptica cambia linealmente con la energía de fotón, indicando que la función de onda electrónica está referida a las terrazas. En el punto $\overline{\Gamma}$ de alta simetría se observa la aparición de nuevos estados con respecto a la muestra plana. Estos estados no dispersan a lo largo de la dirección perpendicular a los escalones ($\overline{\Gamma A}$) en un rango de ± 0.2 Å^{-1} para todas energías de fotón. Sin embargo sí que lo hacen en la dirección paralela ($\overline{\Gamma M}$) de acuerdo a un modelo de electrones libres. La aparición y el comportamiento de estos estados en ambas direcciones de alta simetría está de acuerdo con la formación de estados de pozo cuántico unidimensionales.

Los semiconductores de la familia A_{III}-B_V con orientación (100) presentan un diagrama de fases de superficie con varias reconstrucciones que dependen

de la estequiometria superficial [11]. En los semiconductores como antimoniuro de indio (InSb), arseniuro de indio (InAs) y arseniuro de galio (GaAs), se observa una reconstrucción c(8x2), que se explica mediante un modelo que se denomina modelo ζ. El modelo se basa en la formación de una red sub-superficial de dímeros A_{III}. Este modelo puede describir la estructura atómica de superficie con la repetición de la celda básica (4x2), aunque no proporciona mucha información sobre la estructura electrónica y el origen de los estados de superficie. Por otra parte, en el caso de InAs se observa una transición de fase estructural a baja temperatura, que cabe esperar afecte a la estructura electrónica. Los resultados de ARPES muestran que los estados de superficie de los cristales de antimoniuro de indio (InSb) y de arseniuro de indio (InAs) presentan una estructura c(8x2) de carácter semiconductor, lo que puede explicarse mediante el modelo estructural tipo ζ. Las medidas de STM y STS están de acuerdo con el modelo de la reconstrucción. Igualmente, hemos establecido una relación entre la estructura electrónica de InSb(001)-c(8x2) y de InAs(001)4x2-c(8x2), su estructura cristalina y su distribución de enlaces insaturados (dangling bonds). Las periodicidades y energías de ligadura observadas con ARPES están de acuerdo con los resultados de STM y de espectroscopía de STS. Las bandas de volumen y las bandas de superficie de InSb presentan un desplazamiento de la energía de ligadura inducido por la temperatura, que indica la formación de un fotovoltaje de superficie. En el caso de InAs se observa además la formación de una capa de acumulación de carga, lo que se manifiesta en la aparición de estados de pozo cuántico. Estos estados se han caracterizado con gran resolución utilizando ARPES, lo que he permitido determinar la existencia de varios estados de pozo cuántico, así como de picos de pérdida de energía en la banda de valencia. Estos picos y sus energías de pérdida se han relacionado con la excitación de plasmones en la capa de acumulación de carga. Las energías de pérdida observadas son compatibles con la densidad electrónica determinada experimentalmente para esta capa.

Introduction

The world is nowadays fascinated by the new science and technology in the nanometer length scale. After being a dream for over 40 years, nanoscience and nanotechnology are now opening new ways to innovation in multiple activities. Among other, we may cite controlling, producing and manipulating materials at a smallest scale than ever thought. The father of the term nanotechnology N. Taniguchi [1] considers that the endpoint of the improving of the engineering precision will be the atomic roughness on a surface. Nanomaterials are already in our lives, like integrated circuits components of sizes below 100 nm [2] or the Intel line for a 22 nm processor based on 3D Tri-Gate transistors technology, which forecasts in the microelectronics road map a 10 nm transistor in 2015. Nanomaterials of various nature are here to stay [3].

Devices in the nanometer size scale exhibit new physical phenomena, among other reasons, because their characteristic size is comparable to the de Broglie wavelength of electrons. Therefore, the wave nature of carriers cannot be neglected in nowadays-electronic devices, whose properties are governed by quantum phenomena at the nanometer scale length. Research on low dimension systems provides crucial information relevant to understand the fundamental Physics behind them. Knowing the electronic structure of low dimensional system is an important issue, as it determines many other properties of a physical system, like the optical behaviour, transport, magnetic ordering, etc. The reduction of dimensionality affects such fundamental aspects as the nature of the electron wave function and their degree of confinement. To this end, Angle Resolved Photoemission is the most powerful technique for probing the electronic structure of low dimensional materials.

The goal of the research in this thesis work is to understand the electronic properties of physical systems affected by a dimensionality reduction and accordingly electronic confinement. We have considered first such a simple model system as a reconstructed, anisotropic metal surface of gold, which presents highly ordered metallic chains along one direction. The second model system is beryllium surfaces vicinal to a high symmetry orientation. As different miscut angles were used, a variety of terrace widths was probed, opening the analysis of different degrees of confinement. Finally, two III-V semiconductor surfaces reconstructed in a similar way, InSb(001) and InAs(001), have been analysed using ARPES and STM in an effort to understand the relationship between electronic structure, reconstruction geometry, and a rich phenomenological behaviour, which includes

a temperature induced phase transition and the existence of a surface accumulation layer in the case of InAs(100). Following these topics, the work presented in this thesis is organized in four main sections:

- **Experimental techniques.** This chapter collects the information on the experimental techniques used and the details on the sample preparation.

- **Surface electronic structure of Au(110)-(1x2).** The fascinating properties of Au(110)-(1x2) are presented in this chapter. They include the interaction of the Shockley surface state with the reconstruction and its sensitivity to the order-disorder phase transition of this surface at elevated temperatures.

- **Surface states on vicinal Beryllium surfaces: two-dimensional quantum well states.** In this chapter the properties several vicinal beryllium surfaces are presented. Each surface has a different terrace size, what affects the lateral confinement of the various surface states (of different orbital origins) present in the Be surfaces.

- **Surface electronic structure of A_{III}-B_V semiconductors and temperature dependence.** The c(8x2) surface reconstruction of InAs and InSb has interesting properties, like a rich A_{III} single atom rows along one high symmetry direction and a phase transition at low temperatures. The origin of the phase transition, the nature and role of the surface states and the properties of the surface accumulation layer seen for InAs are investigated.

1. Experimental techniques

The experimental methods used in this work are described in this chapter. In the first section, the main features of angle-resolved photoemission are summarized. In the second section, the methods for crystalline structure analysis are presented.

1.1 Analysis of the electronic structure

The photoemission spectroscopy method was the main experimental technique used for the analysis of the electronic structure. Here, general aspects of the technique and of its application to the study of surfaces are discussed.

1.1.1 Angle-Resolved Photoemission Spectroscopy

Angle-resolved photoemission spectroscopy (ARPES) is the most powerful technique for the analysis of the electronic structure of solids, adsorbates on solids or molecules. The phenomenon exploited by this technique is the photoelectric effect, i.e. the emission of electrons from their host material due to photon absorption. This effect was discovered by Hertz in 1887 [4], and later explained by Einstein in 1905 as a quantum phenomenon [5]. Nevertheless, the first studies on the electronic structure of a solid using ARPES were not performed until the 70's [6]. One of the problems at the birth of ARPES was the production of a sufficient flux of photons of tuneable energy. Synchrotron radiation facilities have overcome this problem supplying bright photon beams with a continuous energy spectrum.

ARPES probes the valence band electronic structure, with a good energy and angle resolution. Due to the electron binding energies involved, the photon energy in ARPES is in the range of 10 – 100 eV. This range of the photon energies corresponds to a short escape depth of photoelectrons, around 5 - 10 Å (Figure 1.1).

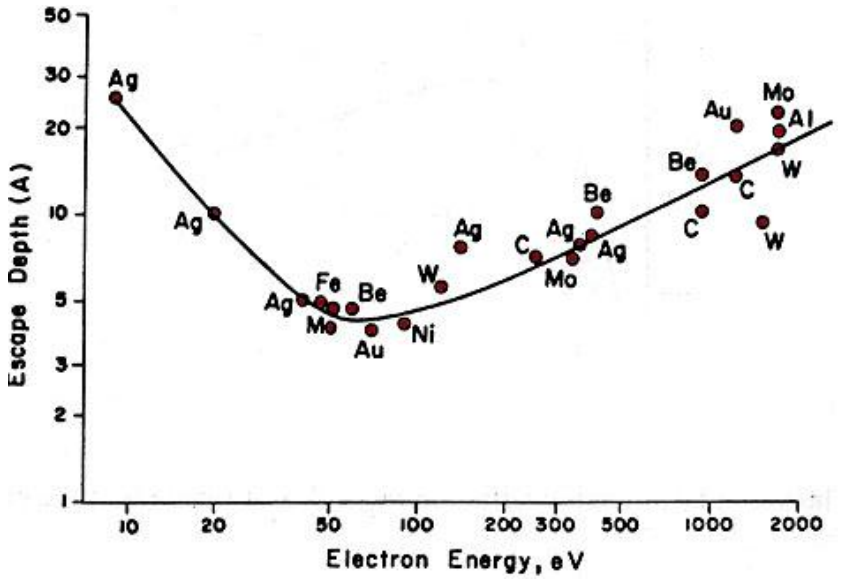

Figure 1.1 *Universal curve displaying the dependence of the electron escape depth with kinetic energy for a variety of different materials. The curve exhibits a minimum in the range of kinetic energies typical of ARPES [7].*

ARPES provides us with information about the electronic structure of the topmost atomic layers of a crystal, what makes this technique extremely useful to measure the electronic structure of many low dimensional systems. As any experimental method, ARPES has advantages and disadvantages, the most important of which are summarized in the following:

Advantages of ARPES:

- The technique is non-destructive.
- It supplies direct information about the electronic states.
- Photoelectron spectroscopy can determine precisely the energy levels.
- The speed of the photoemission process is in the fs range. Thus, it is fast enough to be insensitive to atomic rearrangements in the solid, like vibrations or diffusion.
- ARPES measures directly the electron momentum inside the solid. It has an unsurpassed resolution and a much better sensitivity than other techniques. It can also measure constant energy surfaces, including the Fermi surface, where it provides information complementary to data obtained from other techniques, like de Haas – van Alphen effect or Cyclotron Resonance experiments (these techniques measure extreme areas of orbits on the Fermi surface) [8].
- ARPES can determine all quantum numbers of electrons in a solid (energy, momentum, symmetry, spin).

- Under adequate circumstances, it can determine the geometrical arrangement of surface atoms and locate them with respect to the substrate lattice.
- It can be applied to small crystals.
- Nowadays, the ARPES technique is developing along two directions, namely the improvement of the analyser and the development of new types of sources. Analysers offer large aperture windows for detection and angular resolution (the acceptance angle is 30º degrees in one shot for VGScienta). Since recently spectrometers measuring of the time of flight of electrons are commercially available (ArtOf Scienta analyser). They provide a superior energy and angular resolution. Spin Resolved ARPES (to study magnetic material or their spin-related electronic structure) uses frequently detectors exploiting the Mott scattering process. Laser-based ARPES is a new way to perform electronic structure studies, where a nonlinear crystal is used to produce laser UV photons of energy higher than 6 eV, which are optimal to obtain a better momentum resolution of electrons.

Disadvantages or limitations of ARPES:

- All experiments need ultra-high vacuum. Impurities can be removed, but the measured surface is sensitive to contamination.
- Temperature effects: atoms vibrate at finite temperatures, and their position can change and affect the electronic states.
- Lifetime broadening: in order to probe the occupied electronic states, one has to remove one electron, i.e. one needs to create an excited state, and that state has a finite lifetime, what broadens the energy level.
- Excited-state effects: multi-electron excitation and one-electron excitation occur together. The process of electron excitation leaves behind a hole and disrupts the neutrality of the solid.
- It is not bulk sensitive, unless very high or very low kinetic energies (i.e. very high or very low excitation photon energies) are used.
- Requires clean, atomically flat surfaces in ultra-high vacuum
- As ARPES is sensitive to the electron momentum, it is most powerful when applied to long-range ordered structures or to periodic structures, but it provides much less information in the case of polycrystalline solids.
- The zone of detection (spot size) is limited by the source size.

1.1.1.1 Electronic states in solids

Surface states

The surface of a solid represents a breaking of the crystalline periodicity. Due to this loss of symmetry, the electronic states near the surface can be different from the electronic states in the bulk. In other words, the Schrödinger equation describing the electrons in the solid admits additional solutions near the surface regions, which would not be acceptable in the bulk. These solutions are called electronic surface states and represent electrons with wave functions strongly localized in the last atomic layers. Depending on the nature and localization of the electrons, the surface bands can have different origins [8]. Surface states were postulated for the first time by I. Tamm [9]. From his name, they are called Tamm states, and can be described as localized electronic states in the broken bonds of the last atomic layer, with small or none dispersion. Tamm states are frequent in semiconductor surfaces or in the d-levels of metals. Other kind of surface states is found in metals with strongly delocalized electrons. These states are named Shockley states, after W. Shockley, who described the nature of a free-electron like surface state, with a periodic two dimensional wave function, and a decaying amplitude towards the bulk [10]. Shockley states are seen in free electron metals (like noble metals). Surface states are always localized within a bulk band gap, as they are additional solutions to the Hamiltonian equation, not seen in the bulk. In some cases, the surface states can extend beyond the gap edges. In these cases, their wave functions may mix with bulk states, and are not strictly surface localized any more. However, these wave functions can still have a strong surface character, and are thus called "surface resonances". Semiconductor surface states tend to present localized surface states (of Tamm type), coming either from dangling bonds or from back bonds, whose energy levels are significantly shifted from the corresponding bulk values, owing both to the break of solid symmetry at the surface and surface reconstructions [11]. Semiconductor surface states are either of valence band or conduction band orbital origin, and thus are classified as having donor or acceptor character, respectively. The most important effect of semiconductor surface states is the pinning of the Fermi level at the surface. As the density is states of the surface states is significant, the Fermi level position at the surface is determined by the surface states (Fermi level pinning), and differs from the bulk Fermi level position. The pinning is in general accompanied by surface band bending.

1.1.1.2 Nearly free electron model. Three step photoemission process

The photoemission process is described in a simple way by the "three step photoemission model" [12] [13]. The first step of the process is the excitation to a state with sufficient energy to escape the solid, the second step is the transport of the electron to the surface, and the third step is the crossing of the surface barrier of the solid by the electron.

First step: excitation

The photoemission process is described considering the interaction of an electromagnetic wave characterized by the vector potential $\vec{A}(\vec{r},t)$ with an electron of charge e and mass m and moving in the potential $V(\vec{r})$. The corresponding Schrödinger equation is

$$i\hbar\frac{\partial\psi(\vec{r},t)}{\partial t}=\left[\frac{1}{2m}\left(\frac{\hbar}{i}\nabla-\frac{e}{c}\vec{A}(\vec{r},t)\right)^2+V(\vec{r})\right]\psi(\vec{r},t)=H\,\psi(\vec{r},t) \qquad \text{Eq.1}$$

Where $\psi(\vec{r},t)$ is the electron wave function. The electron is in the potential field of the crystal lattice corresponding to the main part of the Hamiltonian:

$$H_0=-\frac{\hbar^2}{2m}\Delta+V(\vec{r}) \qquad \text{Eq.2}$$

The influence of the electromagnetic field on the electron can be described as a perturbation of the Hamiltonian H_0, because the transition time during the photoemission process is short and the initial state cannot change significantly. Thus, the perturbation Hamiltonian (electromagnetic field) is

$$H_{int}=\frac{1}{2m}\left[-2\frac{e\hbar}{ic}\vec{A}\cdot\nabla-\frac{e\hbar}{ic}\left(div\vec{A}\right)+\frac{e^2}{c^2}\left|\vec{A}\right|^2\right] \qquad \text{Eq.3}$$

The last part of Eq. 3 can be neglected, because the intensity of the electromagnetic field is in general small compared to the potential field of the crystal. As in many other cases, the dipole approximation can be used. For the ultraviolet radiation, the potential vector is

constant on distances in the range of the atomic size. That means that $div\vec{A} = 0$ and the second to last part vanishes. This approximation is in principle only correct for direct transitions, and in fact, it fails for some ARPES experiments in low dimensional systems.

The transition probability between the initial state and a final state with energies E_i and E_f is calculated using the Fermi golden rule, so that the matrix element for the transition is:

$$M_{fi} = \frac{2\Pi}{\hbar}\left|\langle\psi_f|H_{int}|\psi_i\rangle\right|^2 \qquad \text{Eq.4}$$

This equation describes the optical excitation of an electron from the initial (bond) state to a final (eventually unbond) state. The expression of the internal current density is:

$$I(E_f) \propto \sum_{i,f,\vec{G}} M_{fi} \cdot \delta(E_f - E_i - \hbar\omega)\delta(\vec{k}_f - \vec{k}_i - \vec{G}) \qquad \text{Eq. 5}$$

where the first Dirac delta contains the energy conservation and the second Dirac delta is momentum conservation, being $\vec{k}_i$ and $\vec{k}_f$ the initial and final electron wave vectors and $\vec{G}$ a crystal lattice vector. The model is based on the sudden approximation, i.e., an electron is removed from the N electrons system so fast, that the remaining N-1 electrons are not affected by the photoemission process.

Second step: transport

In the second step, the electron propagates towards the surface of the crystal (transport). In the case of an inelastic interaction, the information on the initial state energy is lost and the electron contributes to the background (secondary electrons). The transport process of a photoelectron towards the surface is described by a mean free path λ (mfp). This magnitude is a measure of the probability of travelling without suffering inelastic scattering. The mfp depends on the electron kinetic energy, and for ARPES measurements amounts 5 to 20 Å, which makes ARPES a surface sensitive technique (see Figure 1.1).

Third step: transmission into the vacuum

The photon energy must be sufficient to permit that the photoelectron overcomes the work function of the crystal Φ_C and moves the electron above the vacuum energy E_v.

The photoelectron escapes from the crystal into the vacuum after crossing the surface barrier. Owing to the crossing, the electron loses kinetic energy, and only the parallel component of the momentum is conserved. Due to the lack of momentum conservation in the process, some hypothesis on the nature of the final state is required to describe the process. In many cases, a simple model considering that the final state is free-electron-like is sufficient. Then, the initial band structure is deduced in a relatively simple way from the ARPES energy distribution (see below). This is the most common approach, in particular when photoemission spectroscopy is used as a tool to map the electronic band structure of solids. If this simple model is not sufficient to explain the experimental data, a full calculation of the band structure is needed in order to know the final state more precisely.

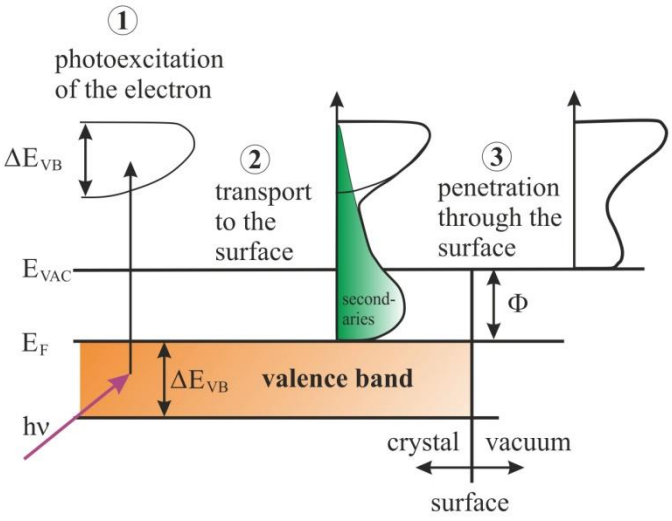

Figure 1.3 *Schematic representation of the three-step photoemission model. Note that the vertical energy scale is not accurate [14].*

1.1.1.3 The basic ARPES experiment

Kinetic energy of the electron

The excited electron has a kinetic energy E_{kin} outside the solid, which is measured by the electron energy analyser. The electron photoemitted by the incident photon beam of energy $h\nu$ is excited from the initial energy level E_i to the final energy level E_f (Figure 1.4). Considering energy conservation, the kinetic energy of the photoemitted electron outside the solid is:

$$E_{kin} = h\nu - \Phi_C - |E_B| \qquad \text{Eq. 6}$$

Where $|E_B|$ is the binding energy, whose absolute value is measured from the Fermi energy, so that $|E_B| = E_F - E_i$.

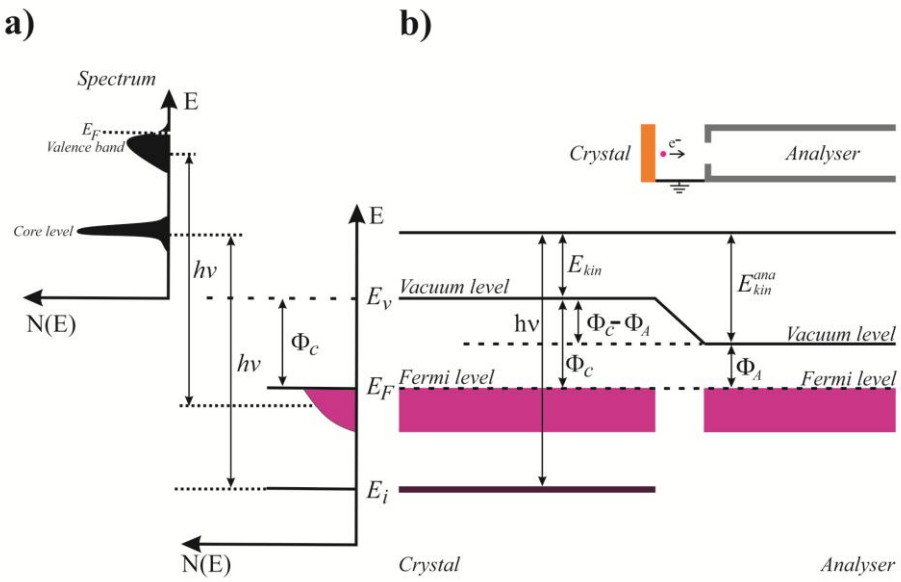

Figure 1.4 *Scheme of the energy levels in the solid and in the spectrometer (electron energy analyser).*

During the photoemission process the analyser and the sample are electrically connected, so that their Fermi levels coincide (Figure 1.4). In the analyser, the kinetic energy of the photoelectron is:

$$E_{kin}^{ana} = h\nu - \Phi_A - |E_B| \qquad \text{Eq. 7}$$

where Φ_A is the work function of the analyser. Due to this fact, the photoelectron kinetic energy is not affected by variations of the surface work function, and it would be only affected by changes of the analyser work function, which is almost constant.

In the case of metals, the photoelectrons with maximum kinetic energy are excited from the Fermi level, so that their binding energy is zero, and

$$E_{kin}^{max} = h\nu - \Phi_A \qquad \text{Eq. 8}$$

In all cases we assume that the work function of the crystal is higher than the work function of the analyser. This is usually the case for most crystalline samples. The minimum kinetic energy observed corresponds to secondary electrons and is equal to:

$$E_{kin}^{min} = \Phi_C - \Phi_A \qquad \text{Eq. 8}$$

Then, the width of the spectrum of the kinetic energy can be written as:

$$\Delta E = E_{kin}^{max} - E_{kin}^{min} = h\nu - \Phi_C \qquad \text{Eq. 9}$$

This equation can be used to determine the work function of the surface by measuring the width of the valence band spectrum. In general, the measurement involves determining the low energy cutoff of photoelectrons. The electrons of lowest kinetic energy determine the position of the cutoff. As these electrons are strongly affected by any residual magnetic or electric fields, it is a usual practice to polarize the sample a few volts, so that the whole valence band spectrum is shifted to higher kinetic energies.

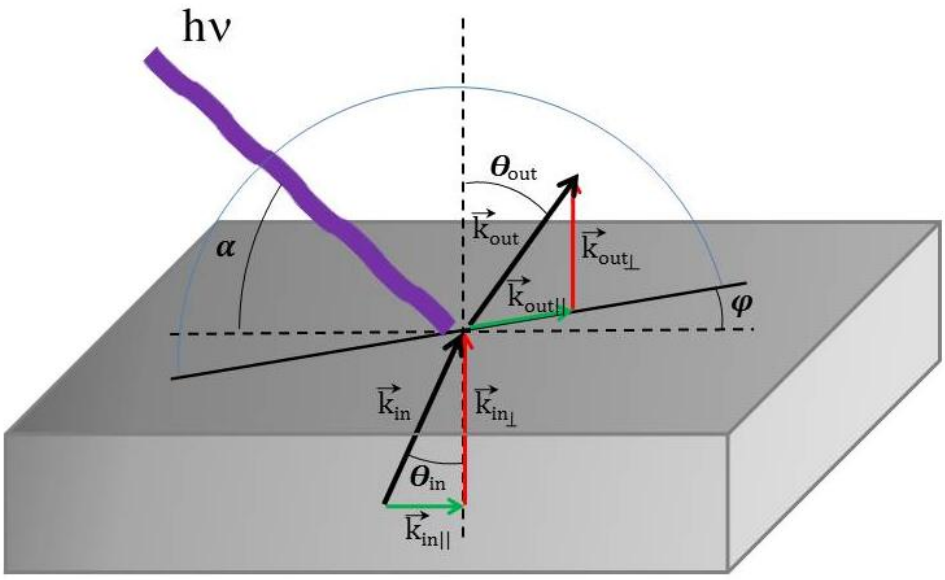

Figure 1.5 *Geometry of the ARPES experiment.*

The geometry of an ARPES experiment is shown in Figure 1.5. An incident beam of monochromatic radiation (energy hν) and incidence angle α, supplied by either a gas

discharge lamp or by a synchrotron radiation source, is directed onto a sample, which has to be a properly aligned single crystal (in order to perform angle or, equivalently, momentum-resolved measurements). As a result, electrons are photoemitted and escape into vacuum. Energy and momentum are conserved in this process.

In most cases, the photoelectrons are collected with an electron energy analyser (hemispherical analyser). In the analyser, the kinetic energy of excited electron is detected

$$|E_B| = h\nu - E_{kin} - \Phi_A \qquad \text{Eq. 10}$$

and the analyser is characterized by a finite acceptance angle, so that one measures the kinetic energy E_{kin} of electrons emitted along a given emission direction (θ_{out}, φ_{out}). This way, the wave vector or the momentum $\vec{k} = \vec{p}/\hbar$ of the photoelectron in vacuum is also completely determined: its modulus is given by $k = \sqrt{2mE_{kin}}/\hbar$ and its components parallel ($\overrightarrow{k_{||}}$) and perpendicular ($\overrightarrow{k_{\perp}}$) to the sample surface are obtained in terms of the polar (θ) and azimuthal (φ) angles. Either a multichannel detector or a channeltron detect the intensity of photoelectrons. Because of the translation symmetry in the x–y plane across the surface, the parallel component $\overrightarrow{k_{||}}$ of the electron momentum is actually conserved in the process:

$$k_{||} = \frac{1}{\hbar}\sqrt{2mE_{kin}} \cdot sin\theta_{out} \qquad \text{Eq. 11}$$

In turn, the perpendicular component $\overrightarrow{k_{\perp}}$ (corresponding to translation symmetry in the z plane) is not conserved. A model has to be assumed to estimate its value. A simple model frequently applied is to consider that the surface barrier is represented by a step potential of height V_0. This model reflects the potential difference between the inner of the solid and the vacuum. V_0 is the inner potential, and is in fact a parameter fit to the experiment. It can be estimated from the zero of the muffin tin potential or also from the distance between the bottom of the first band and the Fermi energy.

$$\overrightarrow{k_{\perp}} = \frac{1}{\hbar}\sqrt{2m(E_{kin}cos^2\phi_{out} + V_0) + \Phi_c} \qquad \text{Eq. 12}$$

These equations allow to determine the parallel and perpendicular components of the momentum of the electron inside the solid, starting from the experimental electron

binding energy (measured from the Fermi level), and the values of the emission angles (θ_{out} and φ_{out}).

Measurement of Energy Distribution Curves

The simplest ARPES spectrum is an Energy Distribution Curve (EDC) plot (Figure 1.6). The spectrum shows the photoelectron intensity, which is in first approximation the density of occupied states vs. the binding energy, for a specific emission direction.

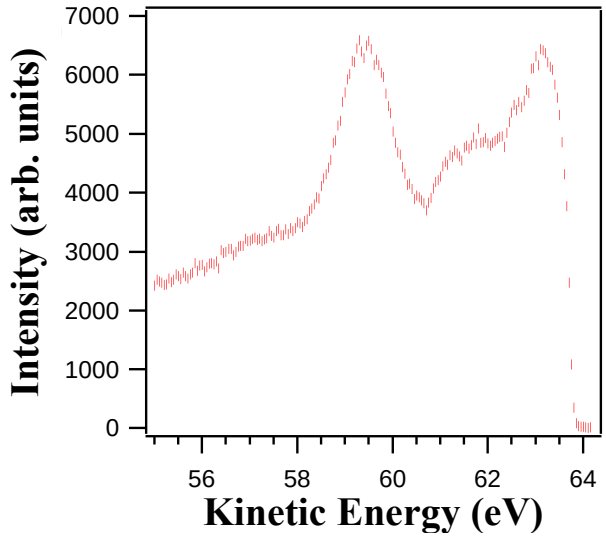

Figure 1.6 *Spectrum EDC for Pt(100) at $k_{||}$ = 0 Å^{-1} for the hν = 68 eV.*

Frequently, a series of EDCs taken for changing values of one of the emission angles is represented, mostly probing a high symmetry direction, as in Figure 1.7a, commonly called waterfall image. It highlights the changes in the spectrum for different emission angles, and thus the band dispersion along this direction. The same plot can be presented in a grayscale, where binding energy and emission angle are used in two axes, and the peak intensity is converted into a colour scale (Figure 1.7b). This kind of representation was made in this work using macros running in IGOR commercial software [15].

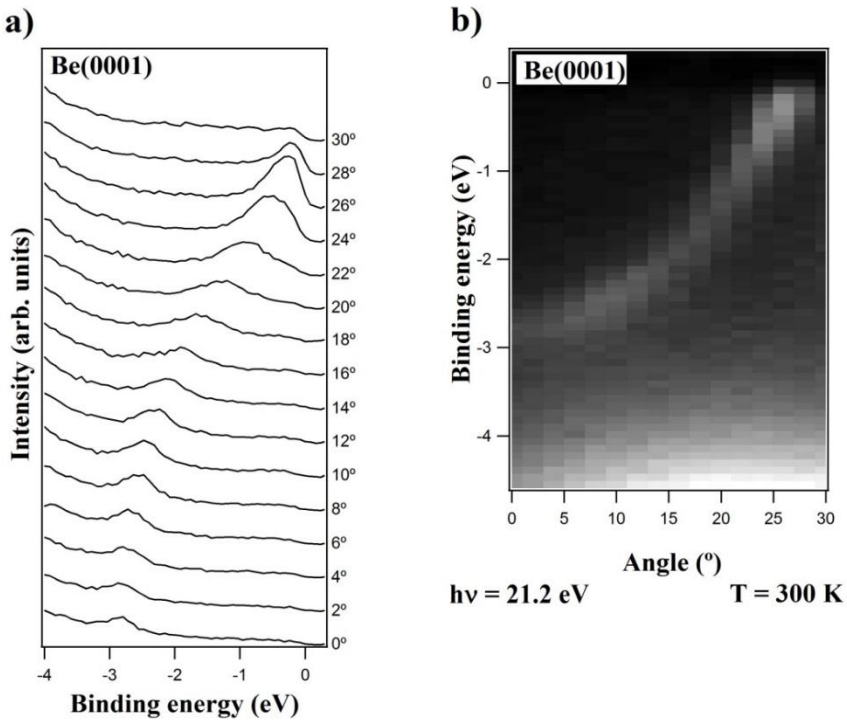

Figure 1.7 *ARPES measurements along one high symmetry direction for Be(0001); a) waterfall plot; b) grayscale plot.*

a high symmetry direction, as in Figure 1.7a, commonly called waterfall image. It highlights the changes in the spectrum for different emission angles, and thus the band dispersion along this direction. The same plot can be presented in a grayscale, where binding energy and emission angle are used in two axes, and the peak intensity is converted into a colour scale (Figure 1.7b). This kind of representation was made in this work using macros running in IGOR commercial software [15].

Fermi surface and constant energy surfaces measurement

ARPES permits a straightforward determination of an intensity distribution map in the complete parallel momentum space for selected binding energies. This map can visualize the distribution of a band or bands, coming either from the surface or from the bulk crystal. In general, the characterization of band/s close to the Fermi edge is relevant. If the photoemission intensity at the Fermi energy is measured for every emission angle, and the result is represented in a momentum scale, we obtain a 2D map called the Fermi Surface Map (FSM). On the other hand, maps of this kind can be made for any binding energy. The result is a Constant Energy Map (CEM).

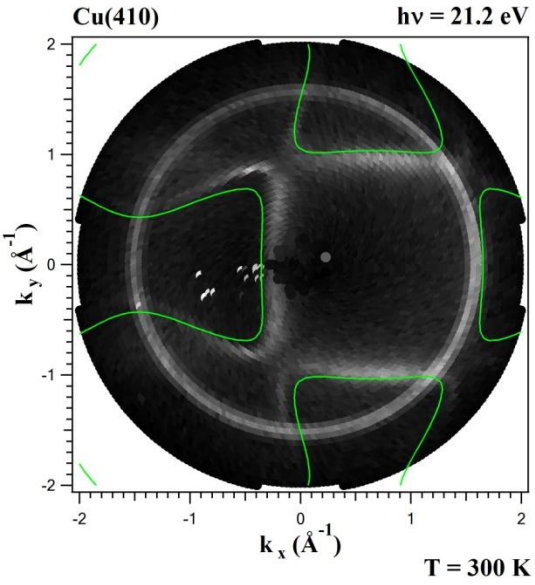

Figure 1.8 *FSM for Cu(410) with hν = 21.2 eV at room temperature in a grey scale (brighter means higher intensity), with calculated bands shown as green lines.*

The emission directions (θ, φ) are selected either moving the electron analyser in vacuum, or by making use of an analyser with a 2D detector and sufficient angular acceptance.

An example for Cu(410) is shown in Figure 1.8. One may easily recognize the "dog bone" shape present in Cu Fermi surface. Green lines correspond to the theoretical predictions simulated by code FLAN (Fermi Level Analyzer) developed by V. Joco [16].

Umklapp processes in photoemission

The majority of the transitions involved in the photo-excitation process are direct, i.e. they correspond to vertical transitions in a reduced zone representation of the reciprocal space, and there is no additional bulk lattice vector involved, $\left(\vec{G}_v\right)_{||} = 0$. An exception is found in some cases in bulk crystals and also in reconstructed surfaces [17]. In the case of a bulk crystal, the momentum of the electron is conserved inside the crystal, except by a reciprocal lattice vector, so that $\vec{k}_f = \vec{k}_i + \vec{G}_v$. Then, Eq.11 should takes the form [18] [19].

$$\overrightarrow{k_{\parallel}} = \frac{1}{\hbar}\sqrt{2mE_{kin}} \cdot sin\theta - \left(\vec{G}_v\right)_{||} \qquad \text{Eq. 13}$$

This process is called Umklapp process of the bulk. Direct transitions in metals are dominated by processes with $\left(\vec{G}_v\right)_{||} = 0$, although there are some exceptions. In presence of a reconstructed surface, the $\vec{k}_f$ can be also affected by a surface reciprocal lattice vector $\vec{G}_s$, so that the momentum outside the crystal is written as $\left(\vec{k}_{out}\right)_{||} = \left(\vec{k}_f\right)_{||} + \vec{G}_s$, and Eq. 13 takes the form:

$$\overrightarrow{k_{\parallel}} = \frac{1}{\hbar}\sqrt{2mE_{kin}} \cdot sin\theta - \left(\vec{G}_v\right)_{||} - \vec{G}_s \qquad \text{Eq. 14}$$

This effect is called surface Umklapp and is equivalent to the diffraction of photoelectrons when leaving the surface. For an electron observed outside the solid ($\left(\vec{k}_{out}\right)_{\perp} > 0$), energy conservation limits $\vec{G}_s$ so that

$$\left|\left(\vec{k}_f\right)_{||} + \vec{G}_s\right| \leq \sqrt{\frac{2mE_{kin}}{\hbar^2}} \qquad \text{Eq. 15}$$

Effect of the polarization of the light

When ARPES is performed under adequate conditions, polarization selection rules may enforce the detection of electrons with specific symmetries. We consider first the matrix element representing the photoemission process in Eq. 16,

$$M_{fi} = \langle \psi_f | \boldsymbol{A} \cdot \boldsymbol{p} | \psi_i \rangle \qquad \text{Eq. 16}$$

We consider now the emission plane in the photoemission process, which is defined by the incoming photon beam and the outgoing photoemitted electron. If the crystal has sufficient symmetry to have at least one mirror plane perpendicular to the surface plane, and the sample is positioned so that this mirror plane coincides with the emission plane, there will be selection rules in the photoemission process. To understand their origin, let us recall that if there is a mirror plane in the crystal bulk structure, then the operator representing the reflection with respect to this plane commutes with the Hamiltonian, and the Eigenstates of the Hamiltonian can be chosen with a defined symmetry with respect to the mirror plane. This means that the initial state wave functions ψ_i (electron bands) are either even (denoted as

'⊕') or odd (denoted as '⊖') functions with respect to the mirror plane. On the other hand, the final state wave function ψ_f must have even symmetry with respect to the emission plane. This must be like that because the electron analyser is in the emission plane, and if the wave function of the final state were of odd symmetry, it would have a node on the plane, and thus the intensity on the plane would be zero, and the state could not be detected. Finally, if we assume that the incoming light is linearly polarized, depending on the polarization of the light with respect to the emission plane (Figure 1.9), the operator in Eq. 16 will be even or odd. If the polarization vector is contained in the emission plane, it will be even with respect to reflection in the emission plane. If the polarization vector is perpendicular to the emission plane, it will be odd with respect to this reflection, as shown in Figure 1.9.

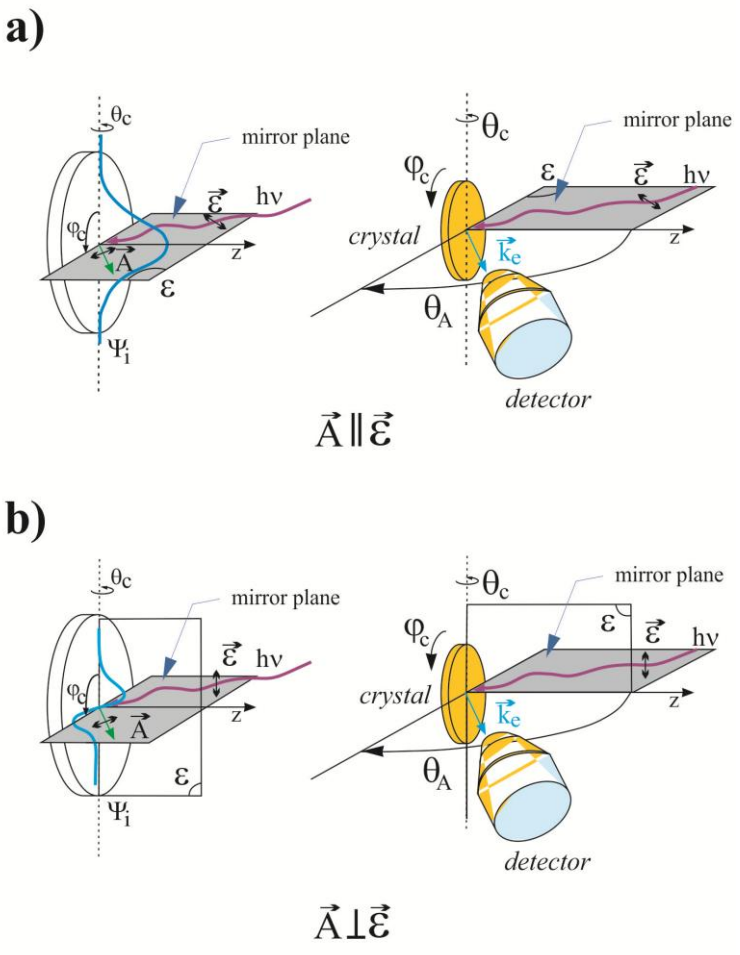

Figure 1.9 *Different polarization of the light source with respect to the mirror plane of the crystal with the analyser in fixed position: (a) polarization vector contained in the mirror plane, (b) polarization vector perpendicular to the mirror plane.*

In Figure 1.9a, the polarization of the light is contained in the emission plane and the operator $\boldsymbol{A} \cdot \boldsymbol{p}$ has even symmetry. Then, the matrix element will have the form $M_{fi} = \langle \oplus \mid \oplus \mid \psi_i \rangle$, and it will be non zero only if the initial state has also even symmetry. Thus, this geometry selects initial states of even symmetry.

Another possible situation is shown in the Figure 1.9b, where the polarization of the light is perpendicular to the mirror plane, so the operator $\boldsymbol{A} \cdot \boldsymbol{p}$ is odd. Then, the matrix element will be of the form $M_{fi} = \langle \oplus \mid \ominus \mid \psi_i \rangle$ and it will vanish unless ψ_i is also of odd symmetry. Thus, this geometry selects initial states of odd symmetry. There are no other possible combinations that give a non-zero matrix element.

In summary, exploiting the symmetry of the crystal and the geometry of the incident light, the symmetry of electron states can be determined in the experiment.

1.1.1.4 Description of the preparation of the crystals

Several different single crystalline samples were used in this work. The first sample is a Au crystal (Surface Preparation Laboratory) of orientation (110). The second set of samples are beryllium crystals vicinal to the $(10\bar{1}0)$ orientation. The samples were cut and polished in Lawrence Livermore National Laboratory, in Livermore (California, USA). The last crystals are wafers of InSb and InAs with (001) orientation (both from MaTeck GmbH). All used crystals require specific preparation procedures.

The Au(110) crystal was cleaned by several cycles of Ar^+ sputtering and annealing. For this crystal, the sputtering was done with a partial pressure of 10^{-6} mbar of Ar, and an energy of 1 keV. The ion incidence angle was 40º and the sample current was 3 μA. The crystal was annealed at 800 K.

The crystal was heated in front of the LEED (Low Energy Electron Diffraction) to reach the order-disorder phase transition. A (1x1) structure was observed above 700 K. Recovery to a stable structure (1x2) was fast, after a few seconds of switching off the heater. ARPES measurements were done during the heating of the crystal. Sample charging was avoided by using a gating electronics, although in some cases minor energy shifts were observed. A disordered (1x1) phase was also obtained by Au deposition using a homemade evaporator. After each deposition, the crystal was checked using LEED. Once the crystal presented a LEED (1x1) pattern, the surface was measured with ARPES. Finally, the Au(110) crystal

was sputtered for a long time (3 hours) to destroy the surface reconstruction. The LEED pattern showed a (1x2) reconstruction with high background.

The vicinal Be($10\bar{1}0$) samples were prepared using the methods described in reference [20]. In the initial step of preparation the crystal was cleaned by repetitive Ne^+ sputtering at 2 keV and with an ion current on the sample of 80 μA. The samples were annealed 10 minutes at T = 773 K (read from a pyrometer). These cycles were repeated until the initial oxide layer was removed. Once this was achieved, the vicinal Be($10\bar{1}0$) samples were sputtered at 1 keV and then it was sputtered and annealed (T = 823 K) for 10 minutes. After several cycles, in the final step the sample was annealed for 2 minutes (T = 823 K). The cleanliness of the sample was confirmed by observing sharp and intense spots in the LEED patterns, by monitoring a very intense Be 1s core level free of oxide, and later by detecting a spectrum of the valence band at hν = 31 eV and measuring the intensity of the surface state resonance.

The InSb wafers (epiready, nominally undoped) were treated in situ by Ar^+ annealing/sputtering cycles. After few cycles, a sharp single-domain c(8x2) reconstruction was observed. The sputtering was done $4.6x10^{-6}$ mbar, with an energy of 1 keV. The drain current was 4 μA. During the sputtering, the crystal was annealed at ~700 K during 1800 seconds. Then, the sample was annealed at ~700 K during the same time, without sputtering. The InAs crystal (nominally p doped) was initially annealed in UHV at 700 K, for several hours and then sputter-cleaned at 650 K using 700 eV Ar ionn beam and a current density of 0.5–1 μA/cm2. Cleaning cycles of 1 h duration were repeated until a clear LEED pattern was observed. A final thermal annealing to 700 K during 5 h was applied. The quality of the reconstruction was checked by LEED and scanning tunnelling microscopy (STM). Further details of the cleaning procedure are described in Ref. [21].

1.1.1.5 ARPES experimental setups

The ARPES experiments were performed using a setup available at our home laboratory (Figure 1.10) and also several setups receiving synchrotron light. Angle resolved photoemission spectroscopy experiment need intense and monochromatic light with tuneable energy. In a conventional laboratory, the ultraviolet light is obtained from two sources, a helium discharge lamp (UVL) and a helium plasma lamp, which in our case was produced by the high intensity ultraviolet source SCIENTA VUV 5000. This source is equipped

with a VUV 5050 source head and the VUV 5011 microwave generator. In the source head, the plasma of helium is created by the Electron Cyclotron Resonance (ECR) technique. A microwave flux generated from the external Klystron amplifier VUV 5011 (10.0 GHz, 250 W), is coupled to a small discharge cavity in a magnetic field tuned to the microwave frequency, in order to meet the ECR condition. The microwave generator is based on the Klystron design, which works by shooting an electron beam through a sequence of the resonator cavities. A leak valve doses the helium gas to the source head. The generated plasma emits high intensity ultraviolet radiation of narrow bandwidth for the lines of helium He Iα (21.218 eV), He Iβ (23.087 eV) and He IIα (40.814 eV). The flux is around $2x10^{13}$ photons/second. The He lines are observed above a background of Bremsstrahlung. In order to remove the background and select a single line, the next small chamber mounts a diffraction grating and a toroidal focusing mirror. In the last step, the light passes through a quartz capillary and reaches the sample. The size of the light spot on the sample is ~2 mm. The crystal is mounted on a transferable sample holder that can be heated (1500 K) and cooled (50 K), and is placed on sample manipulator built by Prevac [22]. It has 5 degrees of freedom, including three translations and two angular movements (azimuthal and polar).

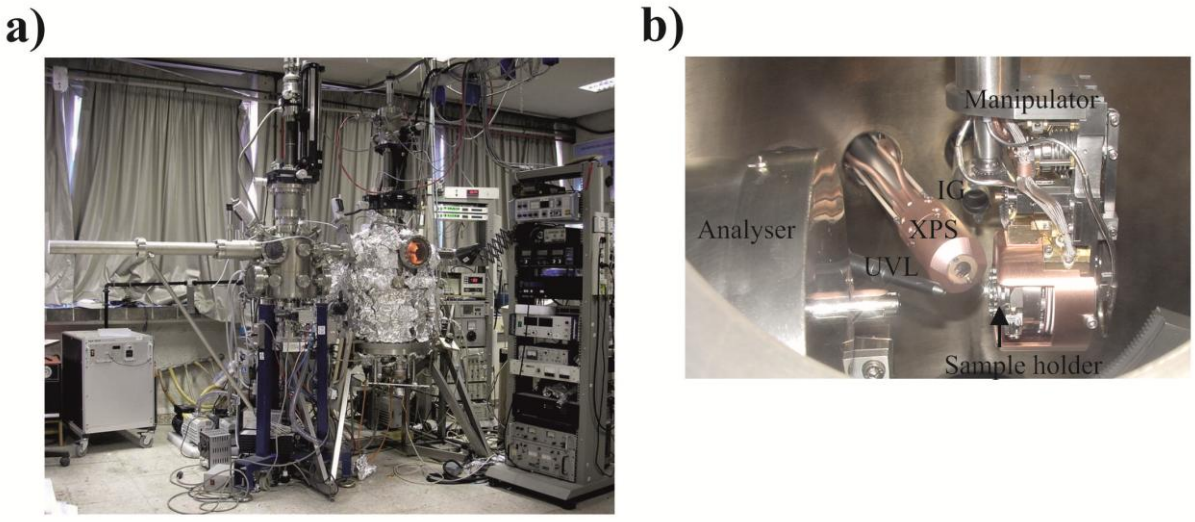

Figure 1.10 a) *ARPES setup in the home laboratory b) a view inside the UHV chamber.*

The temperature is controlled by the Sample Heating Power Supply HEAT2-PS [23] and it is measured by a K type thermocouple. The photoelectrons are detected by a hemispherical energy analyser (VG ARUPS10). This analyser is mounted on a two-axis goniometer inside an ultra-high vacuum chamber. The mean radius of the hemisphere is 75 mm. The "nose"

of the analyser has electric lenses and grids that permit several detection modes, with angular acceptances of 0.4º, 0.8º, 1.2º, and 2º, selected electronically. The analyser is operated in Fixed Analyser Transmission (FAT) mode, which provides a fixed energy resolution along the scan. The electron detector is a channeltron. The data acquisition system makes use of an operational amplifier and was designed and built by V. Joco. The ultra-high vacuum chamber where this setup is located operates at pressures better than $2x10^{-10}$ mbar and is pumped by a combination of turbomolecular and ion pumps. The energy resolution is 50 ± 7 meV measured on the tantalum plate at room temperature and it reaches 30 ± 7 meV at 77 K. The analyser was operated in the 0.4º angular resolution mode, with an actual value of the resolution of 1º, limited by the resolution of the goniometer. The energy resolution of a hemispherical analyser is better for a larger mean radius. However, then the size of the analyser is also larger and in general it is not possible to mount it on a UHV goniometer. It has to be mounted at a fixed position, and then the sample should be moved to access different emission angles. State-of-the-art analysers adopt different technical solutions, e.g. substituting the detector by a multi-channel plate, which permits simultaneous detection of spectra corresponding to a range of different emission angles. This kind of analysers have also a much better been angular resolution (in the range of 0.1º) and have an acceptance angular range in one shot in the range of 30º (VG Scienta R4000, [24]) or even more (38º, VG Scienta DA30 [25]). Analysers of this kind were used at several synchrotron radiation facilities, as collected in Table 1.1.

1.1.2 Synchrotron radiation

ARPES experiment requires a high flux of photons of well defined and tuneable energy. Synchrotron light sources are an excellent tool to obtain light having these features. In the ARPES technique a photon energy range of 10 - 200 eV is used.

Figure 1.15 *One of the modern synchrotron radiation facilities in Europe: ALBA synchrotron, in Cerdanyola del Vallès near Barcelona in Spain* [26].

Several synchrotron radiation facilities have been used in this work: the APE beamline at ELETTRA (Bassoviza, Italy) [27], the I4 beamline at MaxLab (Lund, Sweden) [28], and Cassiopée beamline at Soleil (Saint Aubin, France) [29]. Table 1.1 collects the main

Beamline	**Insertion devices**	**Monochromator**	**Energy range**	**Analyser**	**Energy resolution**	**Angular resolution**	**Manipulator Temperature (range for spectroscopy)**
I4 (MAXlab) BL33	undulator	Plane Grating Monochromator	15 – 120 eV	VG - ARUPS10	70 meV	1º	100 - 750 K
I4 (MAXlab)	undulator	Plane Grating Monochromator	14 - 200 eV	PHOIBOS 100 – SPECS	3 meV	0.2º (max. acceptance angle is 21º)	100 - 750 K
APE (Elettra)	variable-polarisation undulators	Plane Grating Monochromator	8 – 120 eV	Scienta SES-2002	0.6 meV	0.2 º (max. acceptance window is 21º)	16 – 588 K
Cassiopée (Soleil)	HU256 electromagnetic undulator	plane grating monochromator (SOLEIL Optics Group)	8 – 1500 eV	Scienta R4000	<1.8 meV	0.1º for 0.1 mm emission spot < 0.4º for 1 mm emission spot (acceptance angle 30º)	4 – 400 K

Table 1.1 *Technical features of the different synchrotron beamlines used in this work.*

technical parameters for each beamline. Due to the use of several different setups (home laboratory and the beamlines), the data presented in this work have different resolutions, and also the accessible temperature ranges are different, depending on the particular place where the experiments were made.

1.2 Analysis of the surface structure

A good characterization of the surface structure and long-range order is in general needed before undertaking a study on the electronic structure of any crystalline surface. Two techniques were used for the analysis of the surface structure. Low-energy electron diffraction is a fast technique that informs about the long range order on the crystal surface from an area of ~ 200 nm^2. Further details about the structure and the surface topography, can be obtained using scanning microscopy techniques.

1.2.1 Low Energy Electron Diffraction

The Low Energy Electron Diffraction (LEED) technique provides rich information on the surface structure and long-range order. First, it permits to check the quality of the surface crystal. As the electron kinetic energy is in the range 10 to 200 eV, the escape depth (λ_e) is in a range of 5-20 Å (~2-8 monolayers, Figure 1.1). This explains the high sensitivity of LEED to the topmost layers. LEED, as a diffraction technique, probes the long-range order at the sample surface and is well suited to visualize a reconstruction or a phase transition. Second, LEED facilitates in situ orientation of the crystal to reach a high symmetry direction in reciprocal space. Third, and most important, the LEED image can be used to determine the surface structure, as in the case of the superstructures of the stable surface of Au(110), the size of terraces for vicinal surfaces, or the onset of the phase transition at low temperature for A_{III}-B_V semiconductors.

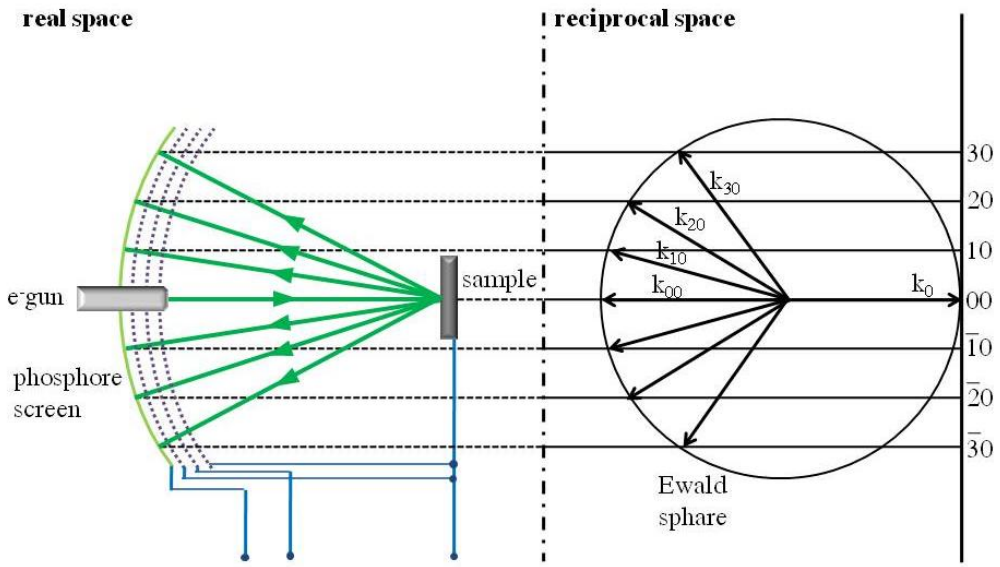

Figure 1.17 *Schematic layout of a LEED experiment. The gun accelerates the electrons (with a $\vec{k}_i$ vector) into a well-ordered surface structure. Following the interaction of accelerated electrons with the surface, the incoming electrons are elastically scattered (with a $\vec{k}_f$ vector with the same wavelength as $\vec{k}_i$ vector), and contribute to the diffraction pattern displayed on a fluorescent screen. Each intense spots on the screen correspond to a position in reciprocal space satisfying the Bragg condition (Ewald sphere).*

Electrons impinging on the surface are diffracted by the interaction with the surface structure. According to the scattering theory, constructive interference occurs if the so-called Bragg condition $\Delta\vec{k} = \vec{G}$ is fulfilled. Hereby, $\Delta\vec{k}$ denotes the scattering wavevector (difference of wave vector between incoming and scattered electron, $\vec{k}_i - \vec{k}_f$) and $\vec{G}$ is a reciprocal lattice vector, respectively. A LEED apparatus consists of an electron gun, a fluorescent screen, and 3 electron grids (Figure 1.17). The electrons impinge on the surface of the crystal. They are backscattered under the conservation of the momentum component parallel to the surface plane. It the Bragg condition is fulfilled, the electrons are scattered back and a spot on the fluorescent screen can be seen via a viewport. Altogether, the observer sees on the screen a projection of the Ewald sphere onto a plane (Figure 1.17). This projection presents the complete interference pattern in the reciprocal space. A projection from the screen (mostly named a LEED pattern) can be recorded by means of a CCD camera with the appropriate software. This has the advantage that images can subsequently be

analysed numerically. In the case of the analysis of the Au and A_{III}-B_V crystals, it was important to observe the reconstruction on those surfaces, as well the temperature induced phase transition on the surface. In the case of vicinal beryllium, it was important to determine the size of terraces determined. Also, high symmetry directions of the crystal were determined from the LEED patterns for orientation purposes in an ARPES experiment.

1.2.2 Scanning Tunnelling Microscope

The scanning tunnelling microscope (STM) technique belongs to the wider class of scanning probe microscopy techniques, where certain signal (for example in form of a tunnel current) is collected and represented versus surface position. The first STM data were presented in 1982 by G. Binnig et al. [30] (G. Binnig and H. Rohrer were awarded the Nobel Prize in 1986). STM technique can obtain a real space image of a surface by moving a sharp metal tip, made of tungsten wire, across the sample and recording the electron tunnel current between the tip and sample. Figure 1.18a shows the scheme of a STM apparatus.

The tunnelling current between sample and tip is due to the tunnel effect. If a voltage (U_{bias}) is applied across the distance d between tip and sample, a current of electrons (I_T) flows through the potential barrier in one direction (depending on voltage polarization). In first approximation, the value of the tunnelling current is:

$$I_T = \frac{U}{d} \exp(-Kd\sqrt{\phi}) \qquad \text{Eq. 28}$$

where K is a constant and ϕ is the average work function.

The crystal is mounted on a rough approach mechanism and on a piezoelectrically driven support. Once in the tunnelling region, the piezo electrically driven support displaces the tip parallel to the surface, while the tunnelling current of the piezo extension are recorded. This permits to obtain a two dimensional map (Figure 1.18b). The tip was made of W wire (1 mm diameter) with a radius of curvature less than 10 mm, by a chemical treatment. The tip was grounded. The Omicron microscope was in a UHV chamber (base pressure was $1x10^{-11}$ mbar). The whole UHV chamber was installed on special supports, eliminating the mechanical vibrations. Furthermore, the microscope was mounted into a cryotube, where

the tip and the sample were cooled down to liquid helium temperature. All STM results were analysed using the WSxM software [31].

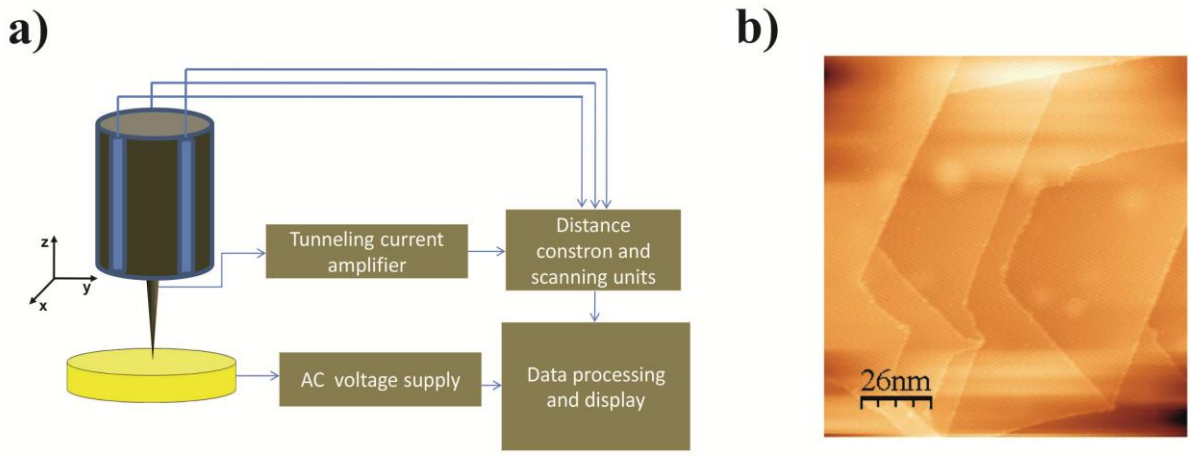

Figure 1.18 *a) Schematic of a Scanning Tunnelling Microscope. The tip is mounted on a piezoelectric tube, which can approach to the surface of the crystal (z axis) and move in the in plane directions (x-y directions). This is realized by a feedback loop controlling the distance (scanning control unit electronics). A tunnelling current amplifier is connected to the tip. It measures the tunnelling current between sample and tip. A computer processes the data and controls the STM microscope; b) STM image of Be(0001) (size 132 nm x 138 nm, bias voltage U = -0.2 V, and current I = 0.01 nA).*

Scanning Probe techniques provide ample information on the surface. Scanning tunnelling spectroscopy (STS) technique for instance, provides local information on the energy distribution of the density of states [32] [33]. STS is able to provide information on the electronic states at each pixel of a standard STM image.

2. Surface electronic structure of Au(110)-(1x2)

The (110) face of noble metals exhibits a simple electronic structure and a natural asymmetry, due to its rectangular unit cell. Due to this feature, (110) noble metal surfaces have been used as a substrate able to promote one-dimensional ordering of adsorbates. While the surfaces of Cu and Ag are not reconstructed, the surface of Au(110) exhibits a (1x2) reconstruction [34] [35], also observed in neighbour elements (Pt, Ir) [36] [37] [38], which has been the subject of theoretical and experimental attention during many years [39] [40] [41] [42] [43] [44] [45]. The (1x2) reconstruction is due to a missing atomic row, and its crystalline structure is well established both from diffraction techniques [46] [47] [48] and scanning tunnelling microscopy (STM) [49] [50]. The electronic structure has been studied both using angle-resolved photoemission [45] [51] and by theoretical calculations [52] [53], but it deserves further attention, as there are some incoherent results [45] [54] [55].

Recently published papers concerning Cu(110), Ag(110), and Au(110)-(1x1) have revealed a Shockley type state at $\overline{Y}$ point [45] [56] [57]. This surface state is related to the absolute hybridization gap at the bulk L point, which is projected at $\overline{Y}$ point along the (110) direction. Thus, is has the same origin as the well known surface state seen at the (111) surfaces of noble metals for normal emission [58] [59]. This state presents a free electron like behaviour, and it can affect the interaction properties of the surface. The Au(110) surface has a stable (1x2) reconstruction, but due to the (1x2) folding, the band gap is closed at $\overline{Y}$ point [45] [52] [60]. Theoretical calculations predict that the reconstruction shifts the Shockley surface state just above the Fermi level in Au(110)-(1x2) [45], so that it should become unoccupied. Earlier experimental studies on reconstructed Au(110) found that the surface state survives the reconstruction, probably as a surface resonance [53] [61] [62] [63]. However, more recent experimental investigations have observed the surface state for the metastable Au(110)-(1x1) (unreconstructed) surface with a binding energy (BE) of 0.59 eV, but not for the (1x2) reconstructed surface [45]. After adding charge donors like Na or Ag, the surface state became visible in the occupied part of the band structure [45].

The parabolic energy vs. parallel momentum dispersion of the Au(111) Shockley surface state, typical of a two-dimensional state, presents a splitting [64]. The origin of the splitting is the spin-orbit interaction (Rashba effect), which is fairly large for a heavy element like Au, combined with the asymmetry introduced by the surface termination, which affects the interaction Hamiltonian [65] [66] [67]. A Rashba splitting of the surface state

at $\overline{Y}$ point of Au(110) has been proposed as well [68] [69]. Furthermore, the relativistic first-principles electronic structure calculations (made in the k·p perturbation theory) find an anisotropic form of the Rashba splitting due to the mixing of the surface state with bulk states, which should be experimentally observable for unreconstructed and reconstructed Au(110) surfaces. However, no experimental study on Au(110) has found any sign of spin-orbit splitting [45] [61] [63] [70].

In this chapter, the surface crystalline structure and the electronic structure of Au(110)-(1x2) is presented. The first part (Subsection 2.1) includes the characterization of the crystalline structure of reconstructed and unreconstructed Au(110) surface. In the second part (Subsection 2.3), the band structure is described, including the bulk and surface bands characterization for both reconstructions of the surface. Conclusions for the reconstructed and the unreconstructed surface are presented at the last subsection (Subsection 2.4).

2.1 Crystalline structure of Au(110)-(1x2)

Pure gold crystallizes in a face-centred cubic lattice with a lattice constant of 4.08 Å. W. Moritz et al. [1] described for the first time the Au(110)-(1x2) reconstruction as being due to a missing row of atoms in the topmost layer, on the basis of LEED experiments. In addition, they reported that a (1x3) reconstruction can be obtained by using specific preparation conditions. Earlier STM measurements show that the majority of the surface structure forms (1x2) domains, but the results do not exclude formation of other domains like (1x3) and (1x4) [50]. The total surface energy has been calculated for several structural models [44] and also the atomic surface relaxation [52] [53] has been investigated to understand the origin of these reconstructions. The results support that (1x2) single domains are the preferred geometry of the surface, due to the low surface energy and the vibrational entropy contribution. Interestingly, the high order missing row reconstructions have values of the surface energy close to the (1x2) reconstruction. On the other hand, merely passing from the (1x2) reconstruction into a (1x1) reconstruction gives rise to a significant change of the surface energy. Previous work has shown that the (1x2) reconstruction is the stable structure up to 650 K, as observed by LEED [71] [72]. At the temperature of 750 K the structure becomes (1x1), due to an order-disorder phase transition. The (1x1) surface structure observed at high temperature is thus a disordered (1x2) structure. This disordered

(1x1) structure should be distinguished from the ordered (1x1) termination found in the two other noble metal (110) faces, Ag and Cu.

Theoretical calculations predict the existence of a critical temperature (T_c), where the surface should undergo a reversible order-disorder process by creation of antiphase defects [73]. Furthermore, 100 K above T_c a roughening transition is expected. Campuzano et al. observed the phase transition using LEED at T_c = 650 K [71] [72]. They identified it as belonging to the 2D Ising universality class. On the other hand, ion scattering experiments indicated a disordering of the Au(110) at temperatures in the range of 500 K, i.e. well below T_c [74] [75] [76]. Further experiments found that vacancy formation started at 530 K [77], in agreement with theoretical calculations [78]. Above T_c the disorder is not completely random, with more layers involved than simply the first one. This behaviour is concluded from step formation parallel to the missing row [77]. A synchrotron X–ray scattering study of the thermal disordering found a phase transition at T_c = 735 K, and characterized it as a first stage of the disorder process [79]. The second stage would be associated with the surface roughening. Finally, a LEED study indicated a preroughening transition starting at 350 K, on the basis of an analysis of the spot profiles [80].

The reported variability range for the phase transition temperature has been attributed to variations in domain size [81]. Scanning tunnelling microscopy measurements with variable temperature (up to 700 K) provide real space images of the surface up to 3D disordering [82] [83] [84] [85]. The missing row configuration was observed on small terraces up to the first

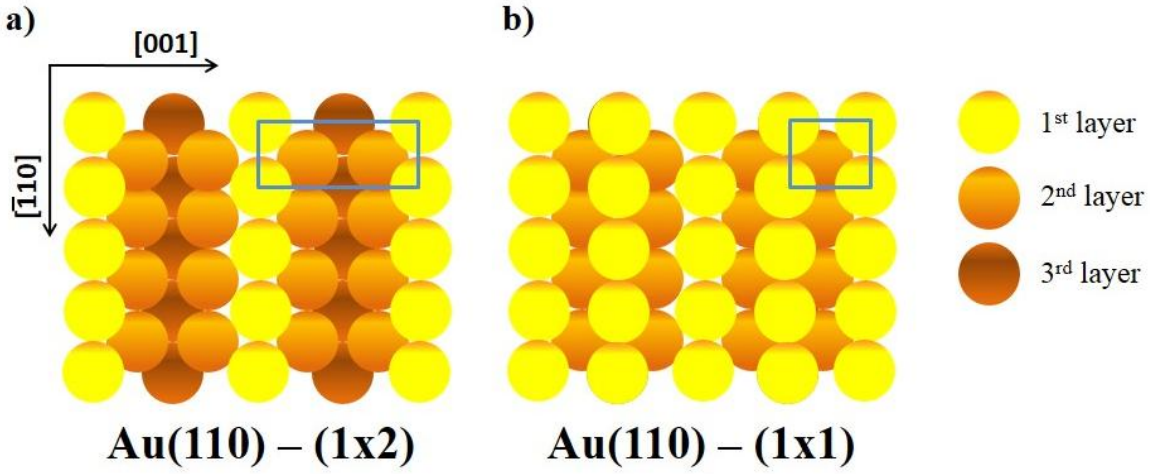

Figure 2.1 *Top view of the structural atomic model of Au(110) for the (1x2) reconstructed (a) and unreconstructed (b) surface in the first three atomic layers. Blue rectangles correspond to the (1x2) and (1x1) unit cells respectively.*

phase of disordering. This means that there is still some fraction of the (1x2) missing row on the surface at this stage. The edge diffusion along $[1\bar{1}0]$ direction increases significantly with temperature and the step edges are composed of a network of small segments [86] [87] increasing with temperature. Upon heating, the surface undergoes the phase transition according to the Ising universality class, with spontaneous formation of domain walls.

An atomic model of Au(110)-(1x2) and Au(110)-(1x1) is shown in Figure 2.1. Unit cells are highlighted in blue. Note that the (1x1) model corresponds to a hypothetical (1x1) ordered phase, and not to the disordered (1x1) phase observed above 670 K. In the missing row model of the (1x2) stable reconstruction, each second row of close packed atoms along the $[0\bar{1}1]$ direction is removed and the unit cell is doubled along the [001] direction. The distortion on the surface provides increased spacing on the first two layers, and double atoms rows in the second layer. A proper preparation of the clean (110) gold surface by sputtering and annealing leads to a sharp (1x2) single-domain LEED pattern at room temperature, as shown in a Figure 2.2.

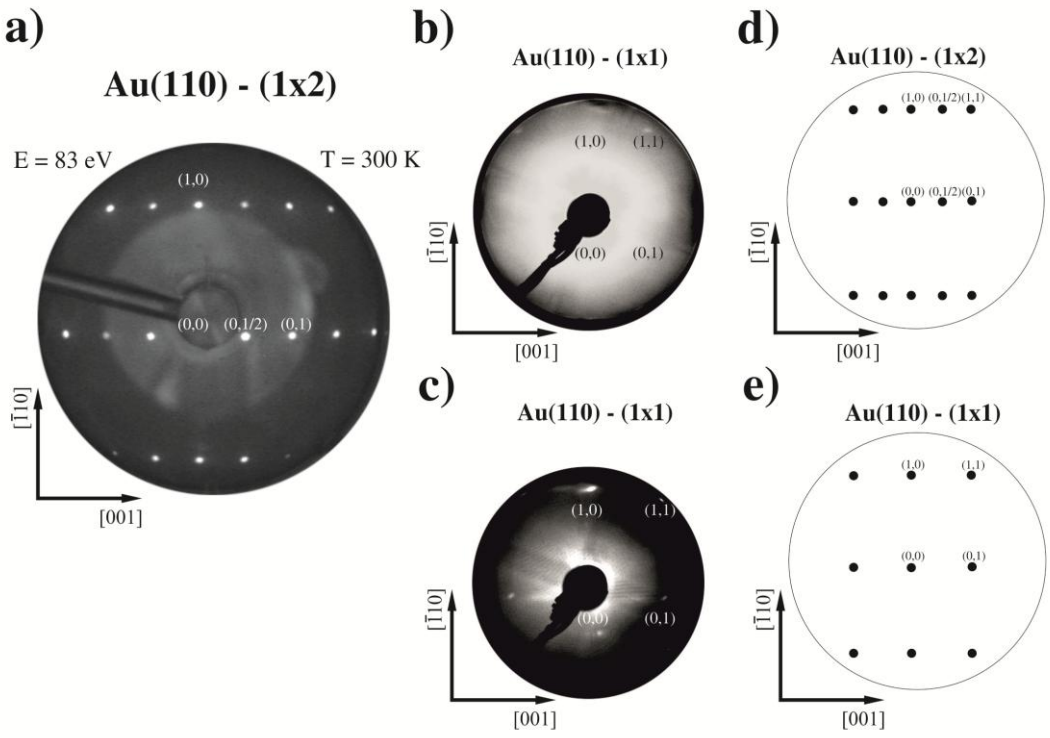

Figure 2.2 *LEED pattern of Au(110) a) (1x2) reconstructed surface at T = 300 K and E = 83 eV; b) (1x1) unreconstructed surface at high temperature (~700 K); c) (1x1) unreconstructed surface obtained by deposition of gold; d) LEED pattern model of Au(110)-(1x2); e) LEED pattern model of Au(110)-(1x1).*

The order-disorder transition leads to an intensity decrease of the ½ order spot related to the reconstruction, and reduces the structure to (1x1). Heating the crystal in front of the LEED apparatus shows the changes induced by the transition very easily (Figure 2.2.b). Increasing or decreasing the temperature triggers a switching of the LEED pattern in a fast and visible process.

A metastable (1x1) structure can be produced also using different methods. The first one is sputtering followed by a mild annealing, below the temperature needed to produce the missing row phase. Another possibility is evaporating Au on top of the reconstructed surface (Figure 2.2.c). Details on the temperatures and methods to prepare the metastable (1x1) phase and to observe the order-disorder phase transition appear in the Chapter 1 section 1.1.1.4.

It is an interesting question how the structural changes described above affect the surface electronic structure.

2.2 Electronic structure of Au(110)-(1x2)

First studies of the electronic structure of Au(110) using photoemission/or angle-resolved photoemission [51] [52] and theoretical calculations [53] were made in the early 80's. A study of the core levels and the intensity of the surface and bulk ratios showed a crystallographic dependence. f and d surface core level shifts depend on the surface reconstruction, due to the s-d rehybridisation [88]. Valence bands were characterized by the sp and d orbitals ($5s_{1/2}$, $5p_{3/2}$, $4f_{5/2}$, $5d_{3/2}$, $4f_{7/2}$, $5d_{5/2}$, $5p_{1/2}$, $6s_{1/2}$) [52] [55]. ARPES results identified the bulk bands, which follow the expected behaviour [54] [70], in agreement with theoretical calculations [52]. 5d electrons strongly contribute to the reconstruction and are important to stabilize the missing row structure (the bonding is stronger for 5d metals) [89]. The first identification of the surface states on Au(110) was made in the early 80's also [56] [70] [63]. A surface state has been also observed on (1x1) unreconstructed Au(110), obtained with a different surface treatment [45]. Theoretical studies find a surface state only for the (1x1) surface. Finally, the surface state of Au(110) should exhibit Rashba splitting [45] [68] [69], although no evidence was obtained in recent experiments [45].

2.2.1 Bulk Electronic Structure of Au(110)-(1x2)

The bulk electronic band structure of Au(110)–(1x2) has been characterized along XKΓ direction by normal emission ARPES using photon energies in the 19-85 eV range. The electron binding energies are converted into perpendicular momentum assuming a free-electron like final state band and an inner potential V_0 = 12 V.

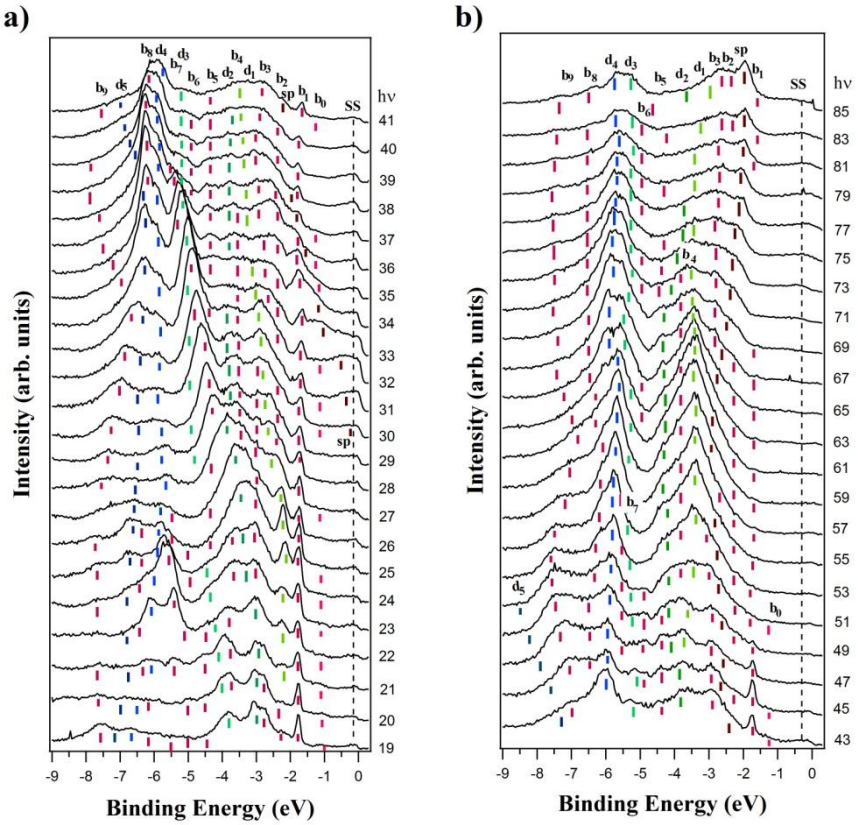

Figure 2.3 *Normal emission energy distribution curves for Au(110)-(1x2) and photon energies in the range 19 to 41 eV (a) and 43 to 85 eV (b). The dashed line corresponds to the surface state and vertical tics to bulk bands and density of states. Different colours correspond to experimental points belonging to following identified bulk bands or processes: Umklapp processes (pink), density of states (dark pink), sp band (brown), d band no. 1 (light green), d bands no. 2 and 3 (green), d bands no. 4 and 5 (blue).*

Experimental energy distribution curves (EDCs) for photon energies in the range 19 to 85 eV are shown in Figure 2.3a and b, while Figure 2.4 a and b collects the experimental data points together with theoretical bands from Ref. [55]. Upon inspecting the EDC's, it is clear that the sp band is crossing the Fermi edge for a photon energy of 30 eV and disperses rapidly

to around -2 eV BE. In addition, the d bands (labelled d_1 to d_5) are well defined and exhibit significant dispersion.

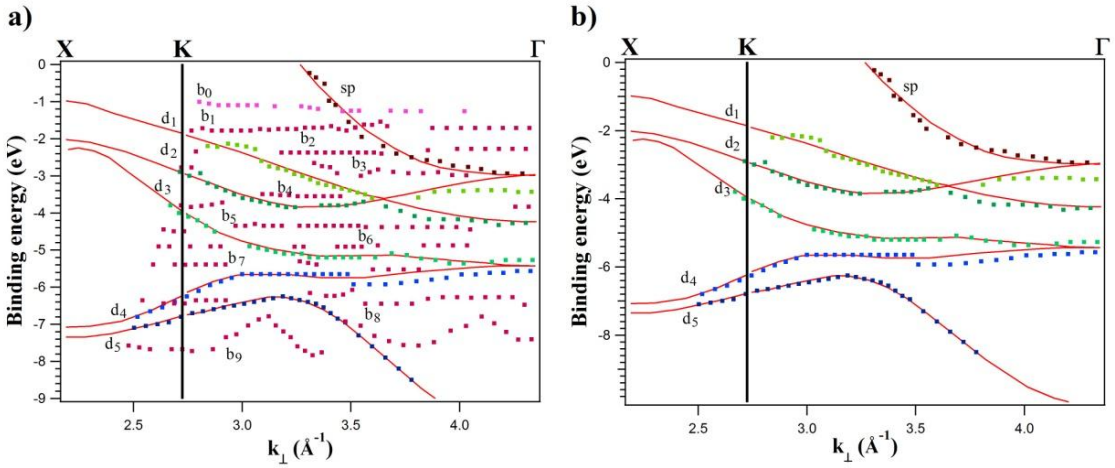

Figure 2.4 *Bulk band dispersion vs. momentum along XKΓ bulk direction (dots) and theoretical predictions of the band bulk structure of Au (continuous red lines) a) including extra bands corresponding to maxima of the density of states and Umklapp processes (pink dots); b) excluding extra bands. Theoretical bands are taken from reference [55].*

Comparing experimental results with a free electron final state calculation, most observed peaks agree well with theory (Figure 2.4b), but some bands cannot be explained by the free-electron final-state model. They exhibit no dispersion with momentum and are attributed to transitions not conserving the momentum (labelled b_1 to b_8), which are seen with highest intensity at the maxima of the density of states in k space, especially close to Γ point. On the contrary, band b_9 is dispersing with momentum and it does not correspond to a maximum of the density of states, like other bands. This band is assigned to an Umklapp process, which has been observed also for other noble metals like eg. Cu(110). The band observed is described as the secondary state of the vector $\vec{G}_{\bar{1}11}$ [90].

The small peak at -1.16 eV (labelled b_0, pink vertical ticks) corresponds to an Umklapp of the sp band and clearly shows the edge of the gap. The peak is visible for low photon energies (in the range 19-51 eV).

The non-dispersing peak near the Fermi energy is the surface state, whose properties are analysed in detail below.

Figure 2.5a shows the bulk Brillouin zone and the (110) surface Brillouin zone. The $\overline{X}$ symmetry point corresponds to the surface projection of the bulk X symmetry point, while the bulk L point is projected onto the $\overline{Y}$ symmetry point. The bulk W point is projected into the $\overline{S}$ point. Finally, the surface $\overline{\Gamma}$ point is the projection of the bulk Γ point along ΓΣK direction of the bulk Brillouin zone.

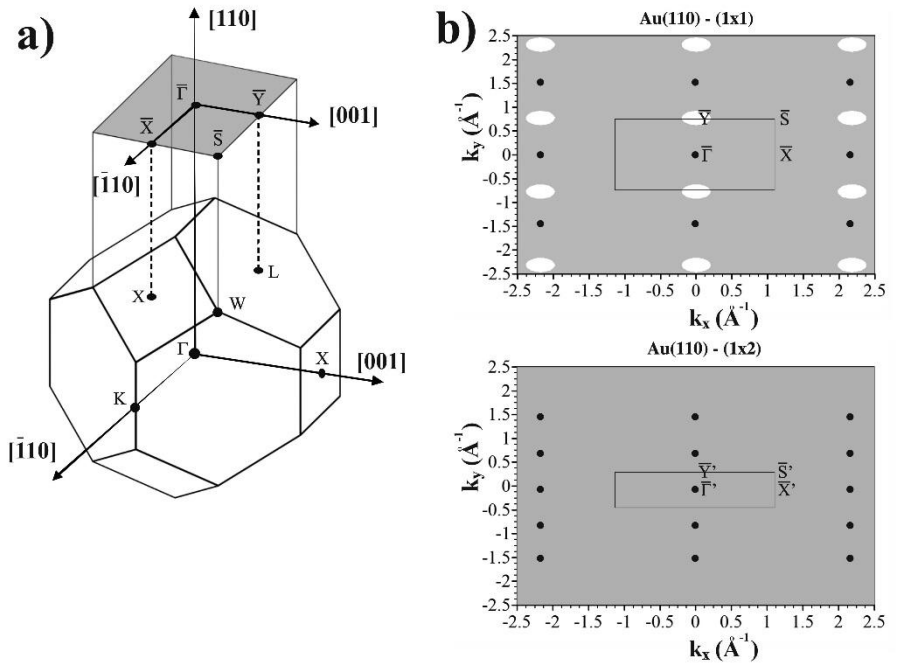

Figure 2.5 *a) Surface Brillouin zone of the (110) face with symmetry points highlighted and their relationship with the projection of bulk points. b) Surface Brillouin zone (SBZ) of the (1x1) surface (top) and (1x2) reconstructed surface (bottom). Shaded regions correspond to the surface projection of bulk bands, unshaded regions are absolute band gaps [16].*

The two dimensional surface Brillouin zone for Au(110)-(1x1) presents an absolute band gap at the $\overline{Y}$ point (Figure 2.5b). This gap corresponds to the (110) projection of the well-known avoided crossing band gap of noble metals near the L point. The projection of this gap along (111) directions hosts the also well-known Shockley surface state of (111) noble metal surfaces. Thus, the $\overline{Y}$ point gap can contain a surface state close to the Fermi energy, which has indeed been observed for Cu [56] and Ag [57]. In the case of Au(110), the (1x2) reconstruction folds the $\overline{Y}$ point into the $\overline{\Gamma}$ point. A new $\overline{\Gamma'}$ point appears at the location of the initial $\overline{Y}$ point ($k_{||} = 0.77$ Å^{-1}). The new $\overline{Y'}$ point is located halfway between the two $\overline{\Gamma'}$

points, at 0.37 $Å^{-1}$. The new $\overline{S}'$ point is also located halfway along the $\overline{XS}$ distance ($k_{\parallel}$ = 0.37 $Å^{-1}$). In turn, the new $\overline{X}'$ point coincides with the $\overline{X}$ point ($k_{\parallel}$ = 1.09 $Å^{-1}$). Due to this folding, the reconstructed surface has no absolute band gap.

In order to understand the experimental results, relativistic first–principles LDA slab layer calculations, including spin-orbit coupling (SOC) have been performed by E. Chulkov et al. [60]. Figure 2.6 shows the band structures of the unreconstructed (1x1) and the reconstructed (1x2) surfaces projected along the surface.

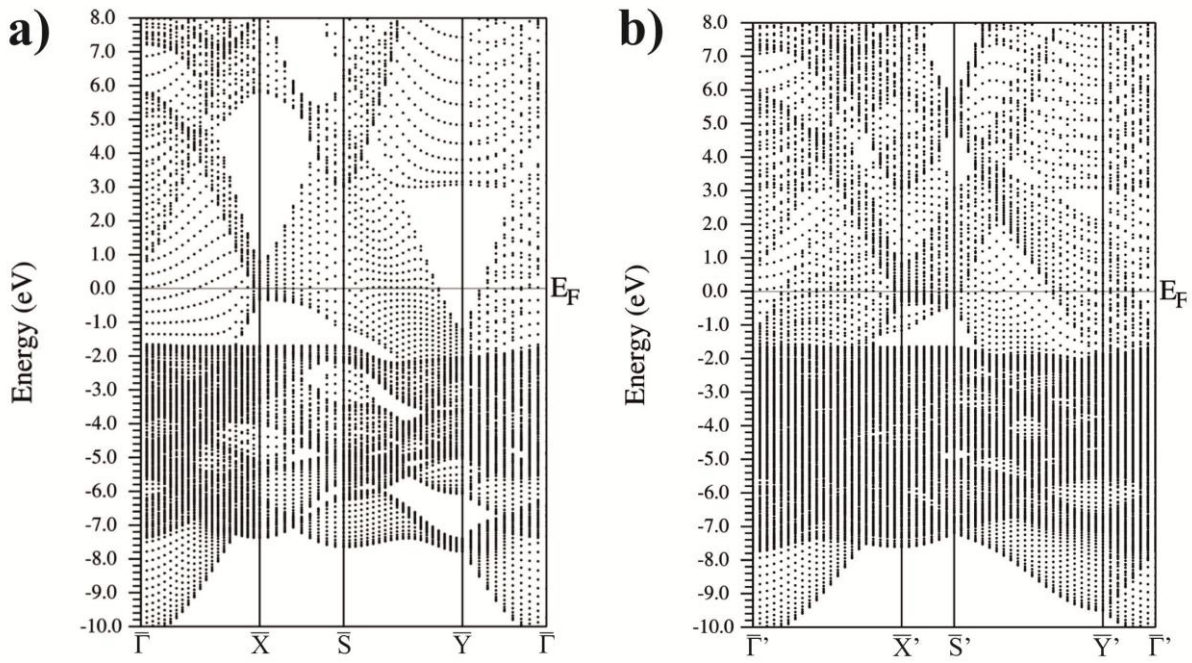

Figure 2.6 *a) Au(110)-(1×1) bulk band projection b) Au(110)-(1×2) bulk band projection [60].*

The stable reconstruction folds the $\overline{YS}$ direction into the $\overline{\Gamma X}$ direction, eliminating the band gap at $\overline{Y}$ point. There is an additional band gap below the Fermi energy around $\overline{X}$ and $\overline{S}$ point for the (1x1) surface. This gap is maintained in the (1x2) surface, but it becomes smaller. Below 7.5 eV BE, there is a large gap in most of the Brillouin zone (bottom of the valence band). That region was not studied in this work.

The sp band dominates the surface electronic structure of Au near the Fermi level. As only this band crosses the Fermi energy, it is responsible of the Fermi surface, which has an almost spherical shape (Figure 2.7a).

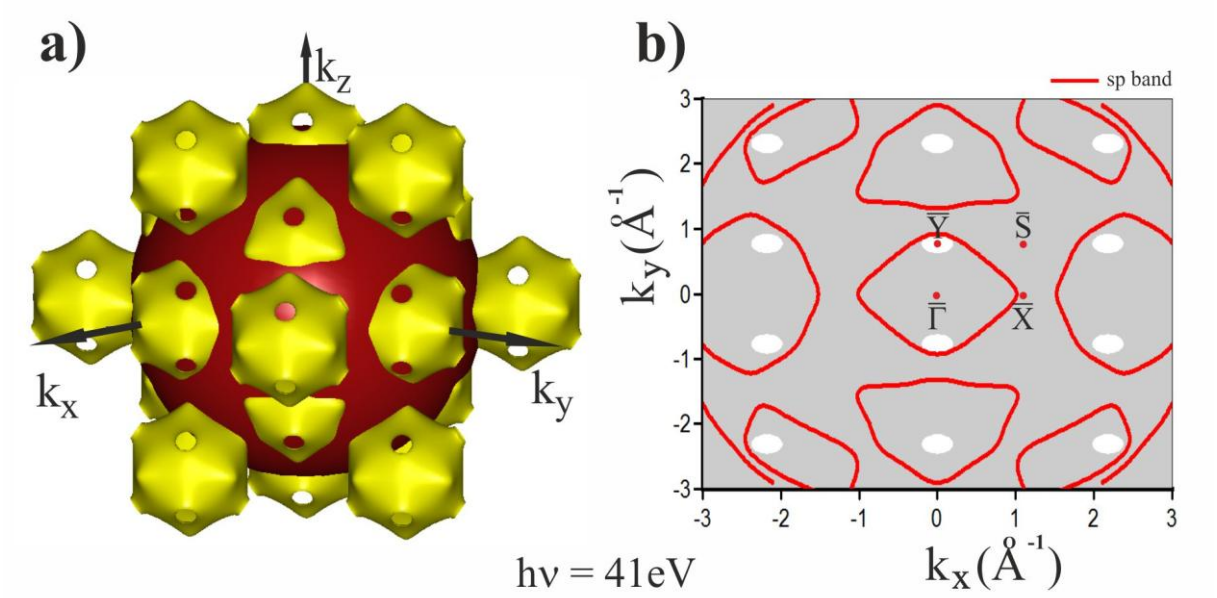

Figure 2.7 *a) Theoretical Fermi surface (yellow) in the repeated zone scheme for Au(110). The hemisphere (red) represents the distribution of initial states probed with a photon energy of 41 eV; b) surface projection for a photon energy of 41 eV [16]. The red contours correspond to the band crossing at the Fermi energy.*

The hybridisation gap is seen in the surface projection as absolute gaps. Projection of the almost spherical shape on the 110 face produces elliptical gaps. The semi sphere represents the distribution of initial states probed with a photon energy of 41 eV. The red lines represent contours of that distribution in the k_x –k_y momentum plane.

The electronic structure along the two main high symmetry directions of the rectangular Au(110)-(1x1) surface ($\overline{\Gamma Y}$ and $\overline{\Gamma X}$) has been analysed using a tight binding electronic structure calculation by ELAN code Ref. [91].

For a photon energy of 41 eV, the conduction band (sp orbital origin) has a maximum BE of approx. -1.71 eV at the $\bar{\Gamma}$ point. Theoretical calculations for the dispersion of this band along $\overline{\Gamma Y}$ direction are shown in Figure 2.8a. It crosses the Fermi level at $k_{||} = 0.93$ Å^{-1}. Bands 4 and 5 (of d orbital origin) appear below -2 eV BE. Their minimum/maximum BE is reached near the $\bar{\Gamma}$ point (not shown). The calculations show the absolute band gap around $\bar{Y}$ point. The width of the gap at the Fermi energy is $\Delta k_{||} = 0.3$ Å^{-1}. The bottom of this band gap lies at -1.05 eV BE. Figure 2.8c shows a simulated intensity map taking into account the bulk partial density of state (PDOS) of the initial and final states. The simulation by ELAN code can also show an intensity map including the effect of direct transitions.

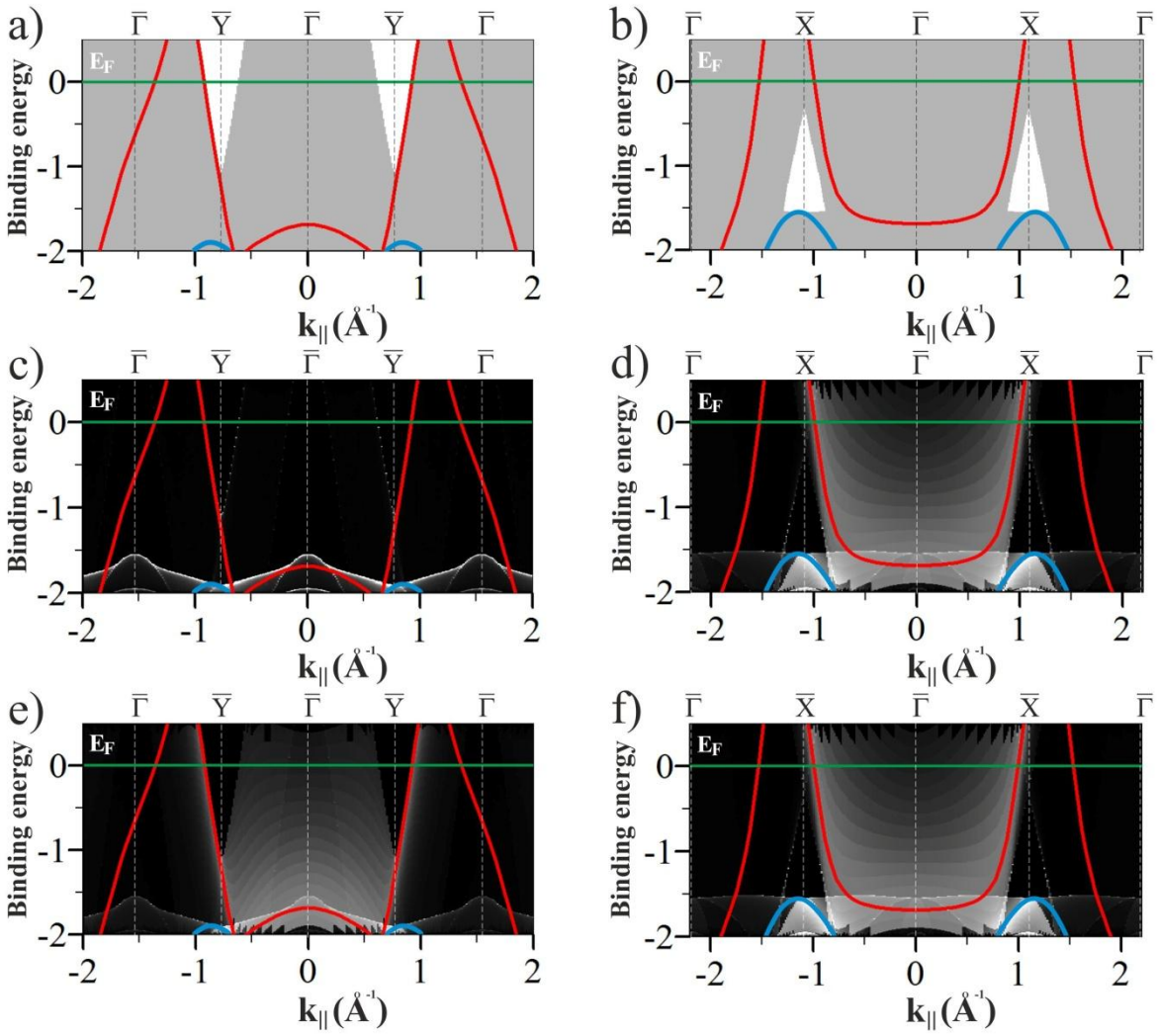

Figure 2.8 *Theoretical valence band electronic structure calculated by ELAN code for Au(110) along the two high symmetry directions for a photon energy of 41 eV: red lines correspond to the sp bulk bands and blue lines to d bands, a) $\overline{\Gamma Y}$ direction b) $\overline{\Gamma X}$ direction. The grey shaded region corresponds to the projection of bulk bands and the white regions are absolute band gaps; c) $\overline{\Gamma Y}$ direction and d) $\overline{\Gamma X}$ direction, including the partial density of bulk states; e) $\overline{\Gamma Y}$ direction and f) $\overline{\Gamma X}$ direction showing an intensity map that takes into account the initial and final state bands, as generated by ELAN code [91] based on [92].*

Figure 2.8e shows an intense area around the gap, with a stronger intensity on the right side of the gap at $\overline{Y}$ point (for positive parallel momentum), because the sp bulk band approaches the gap edge.

Along $\overline{\Gamma X}$ direction (Figure 2.8b), the sp bulk band disperses and crosses the Fermi level at $k_{\parallel} = 1$ Å^{-1}, close to the $\overline{X}$ point and also at $k_{\parallel} = 1.55$ Å^{-1} (close to next $\overline{\Gamma}$ point), as shown by calculations made using FLAN code (see Figure 2.7). A maximum of -1.69 eV BE is reached at $\overline{\Gamma}$ point.

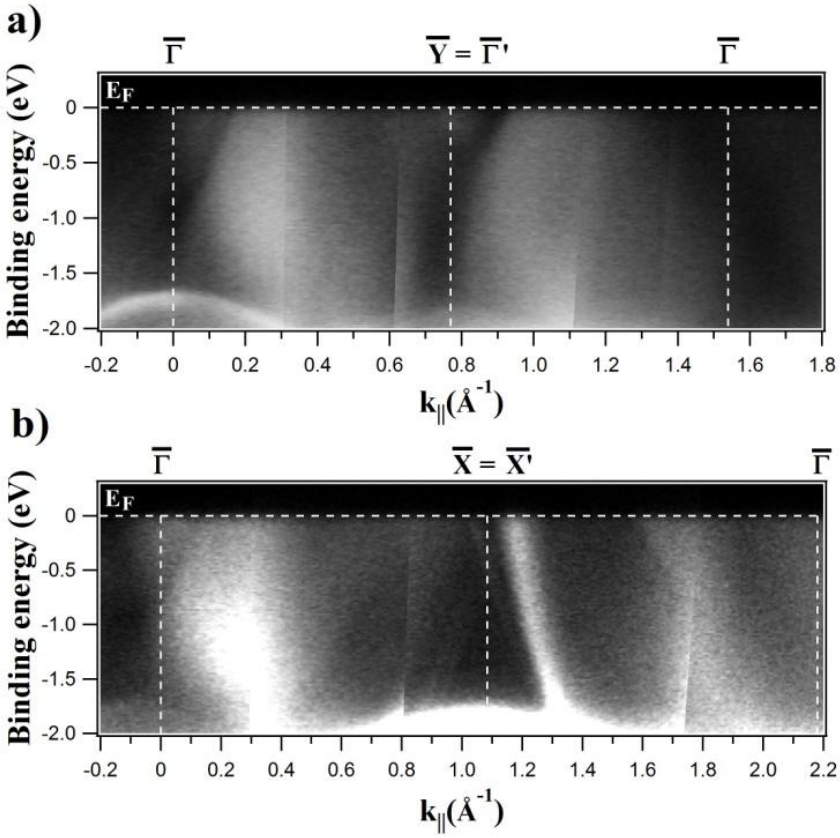

Figure 2.9 *Valence band electronic structure of Au(110)–(1x2) measured along the two main high symmetry directions (a) perpendicular to missing rows – $\overline{\Gamma' Y'}$ direction and (b) parallel to missing rows – $\overline{\Gamma' X'}$directions) for hν = 41 eV. Intensity is shown as a gray scale (brighter means higher intensity).*

The electronic structure of the Au(110)-(1x2) reconstructed surface along the two main high symmetry directions was characterized for several photon energies at room temperature. The valence band perpendicular to missing rows (along $\overline{\Gamma' Y'}$ direction) is presented in Figure 2.9a for hν = 41 eV and parallel to missing rows (along $\overline{\Gamma' X'}$ direction) in Figure 2.9b.

The sp bulk band is seen around $\overline{\Gamma'}$ with a maximum binding energy of –1.80 ± 0.02 eV (Figure 2.9a), for measurements along the $\overline{\Gamma' Y'}$ direction. The band disperses downwards

away from the $\bar{\Gamma}$ point, and upwards near the $\bar{Y}$ point (seen as the bright area on the right side of that point). The d band is seen for $k_{\parallel} = 0.80$ Å^{-1} (not shown in this figure) with a hole like dispersion. The band gap around $\bar{Y}$ point is observed as a darker area, and indeed the band gap shape is seen also around $\bar{\Gamma}$ point, due to the (1x2) folding. The gap edge is well defined by a contrast of intensity on the left and right side. As the bulk sp band is detected close to the right side of the gap for the photon energy 41 eV, the left edge of the gap is less defined than the right edge, where a stronger intensity contrast is seen between the occupied and unoccupied sides of the gap. For $\bar{\Gamma}$ and $\bar{Y}$ points, the k space width of the gap at the Fermi energy is 0.28 ± 0.01 Å^{-1} and 0.27 ± 0.01 Å^{-1}, respectively, and the minimum BE is -1.08 $\pm$ 0.01 eV and -0.91 $\pm$ 0.01 eV, respectively. These values can be compared to ELAN simulations shown in Figure 2.8a, and in particular to the gap area around $k_{\parallel} = 0.77$ Å^{-1}. Experimental values are very close to calculations. However, the (1x2) reconstructed surface should present no band gap (Figure 2.7b).

The sp bulk band crosses the Fermi energy at $k_{\parallel} = 0.99 \pm 0.07$ Å^{-1}and 1.50 ± 0.08 Å^{-1} along $\overline{\Gamma' X'}$ direction, for hν = 41 eV. Due to the width of the sp band, the crossing is not distinguished in Fig. 2.9. A d band is observed at $k_{\parallel} = 1.07 \pm 0.02$ Å^{-1} with a maximum BE of -2.08 $\pm$ 0.01 eV. Theoretical predictions from FLAN and ELAN simulations for Au(110)-(1x1) for both direction agree with these results. The prominent band crossing the Fermi energy near the $\bar{X}$ point is discussed in the next section.

2.2.2 Surface electronic structure of Au(110)-(1x2)

2.2.2.1 Surface electronic structure along $\overline{\Gamma Y}$

As described before, the absolute band gap around $\bar{Y}$ point of (110) noble metal surfaces, hosts a Shockley surface state of similar orbital origin as the well know (111) surface state [58]. This surface state has free electron like character. In the case of Au(110), the (1x2) surface reconstruction removes the absolute band gap. Experimental ARPES results dating from some years ago found intensity at the $\bar{Y}$ point that was attributed to a surface resonance of similar orbital origin, indicating that the surface state should survive the reconstruction. On the contrary, more recent ARPES experiments and theoretical calculations concluded that the Shockley surface state at the $\bar{Y}$ point lies above the Fermi energy for the (1x2) surface [45].

We have found a surface resonance at the $\bar{\Gamma}'$ point (Figure 2.10). We have monitored it for photon energies in the range from 29 to 50 eV. Its surface character has been demonstrated by the lack of the dispersion with $k_\perp$ (constant $k_{||}$ location for the whole photon energy range probed, not shown).

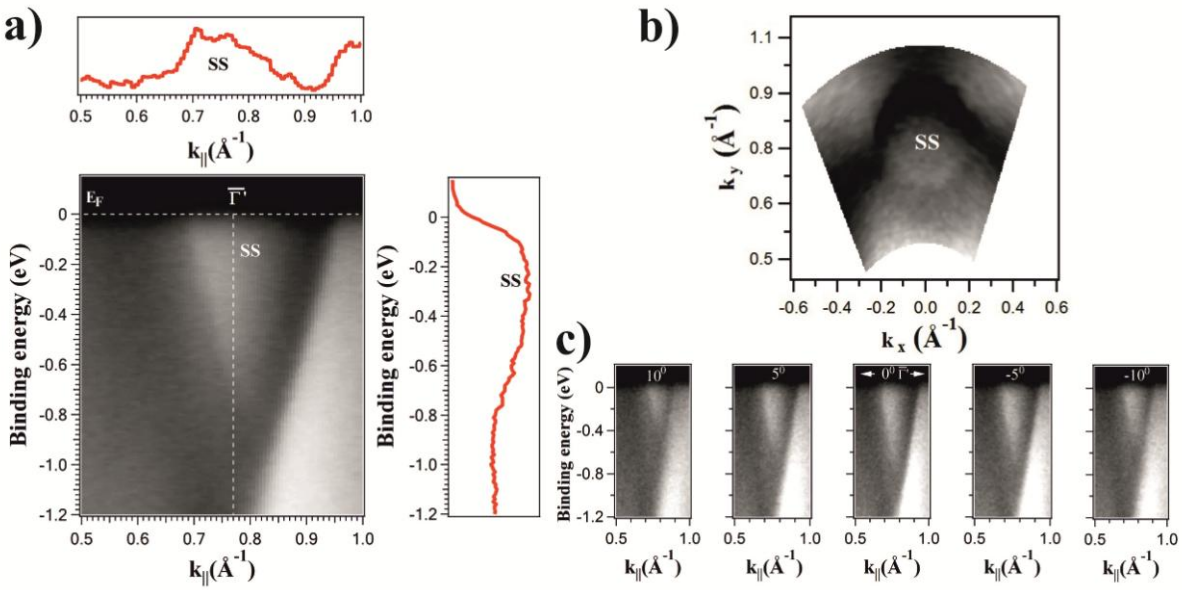

Figure 2.10 a) *Surface band dispersion around $\bar{\Gamma}'$ point along $\overline{\Gamma' Y}$ direction for $h\nu$ = 43 eV with EDC and MDC profiles, b) Fermi surface near $\bar{\Gamma}'$ point at $k_{||}$ = 0.77 Å^{-1} c) Surface band dispersion for selected azimuthal angles with respect to the $\overline{\Gamma Y}$ direction, for $h\nu$ = 44 eV. All measurements have been done at T = 300 K.*

The state is shown in more detail in Figure 2.10a for hν = 43 eV. It spans a range of 0.18 ± 0.01 Å^{-1} in reciprocal space at the Fermi energy, and the bottom of the band is found at 0.30 ± 0.01 eV. Figure 2.10a shows the surface state and the edge of the band gap, whose right side is imaged much more sharply, as the bulk sp band is detected on this side for the photon energy used (43 eV). Figure 2.10a shows both an EDC (crossing the bottom of the band) and an MDC (at the Fermi energy). The broad shape of the EDC suggests the existence of more than one state. Figure 2.10b shows a constant energy surface measured for the Fermi energy (Fermi contour). The elliptical shape of the gap is clearly distinguished, and the surface state band appears as an elliptical bright area located around the $\bar{\Gamma}'$ point.

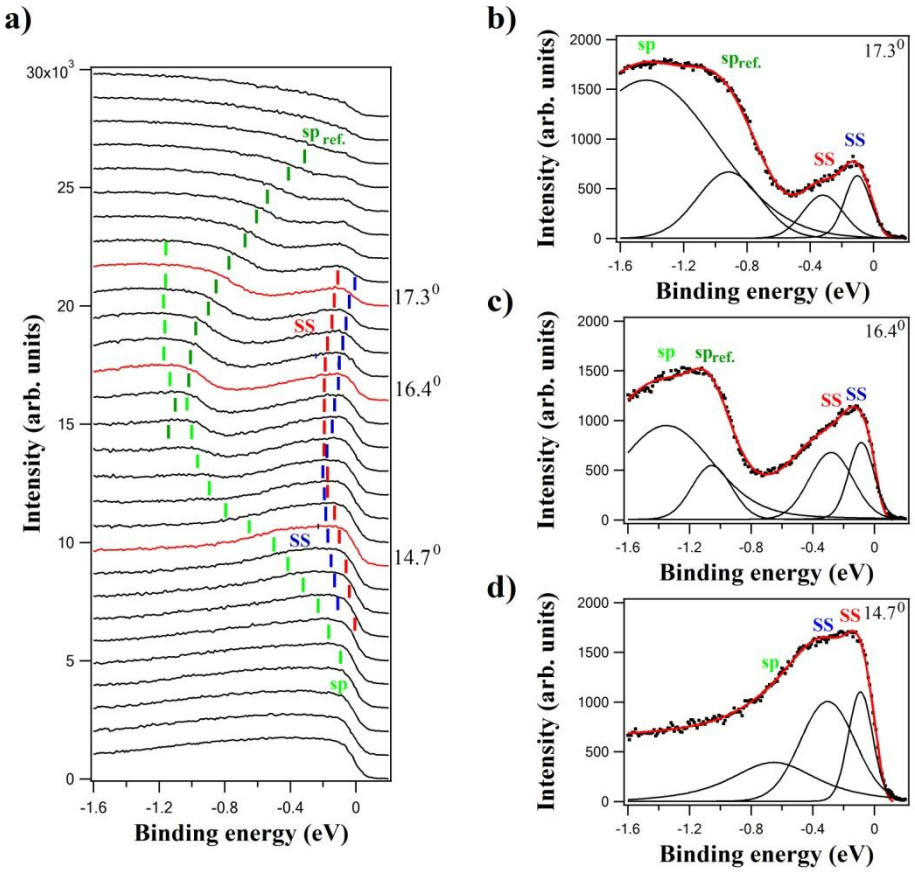

Figure 2.11 *a) EDC profiles for the resonance surface band dispersion at $\overline{\Gamma}'$ point for $h\nu = 35$ eV at T = 300 K. Green tics correspond to the sp bulk band, blue and red tics show the dispersion deduced from the fit of the two components found in the surface resonance band. Some emission angles are shown. The sp bulk band (labelled sp) is seen also as a weaker feature at the other gap edge ($sp_{ref.}$) b-d) Selected EDC profiles (highlighted in panel a)) showing the two peaks found around $\overline{\Gamma}'$ point.*

The surface band has been studied for a range of azimuthal emission angles with respect to the $\overline{\Gamma'Y'}$ direction (Figure 2.10c). Upon changing the azimuthal angle, different cuts of the surface band paraboloid were obtained, always showing a parabolic like shape as expected. As the azimuthal angle is larger, the bottom of the parabola becomes smaller, until it disappears for sufficiently large azimuthal angles. An analysis of the EDC profiles and of their dispersion shows that the main peak is asymmetric. This is very clear for emission angles slightly away from the band gap (Figure 2.11d). Although the experimental resolution was not sufficient to resolve sharply this peak, the line shape has been fit using two Voigt components, after subtracting a Shirley background and removing the Fermi function [93].

A plot the split band (experimental dots in BE vs. momentum) in shown in Figure 2.12. A parabolic fit to these experimental points reveals that the minimum binding energy of the two bands is -0.40 ± 0.05 eV and -0.20 ± 0.05 eV slightly off the $\bar{\Gamma}'$ point. The two components seen support that the spin-orbit split components at $\bar{\Gamma}'$ point are observed. The splitting is around 0.025 ± 0.002 $Å^{-1}$ in reciprocal space. A plot the split band (experimental dots in BE vs. momentum) in shown in Figure 2.12.

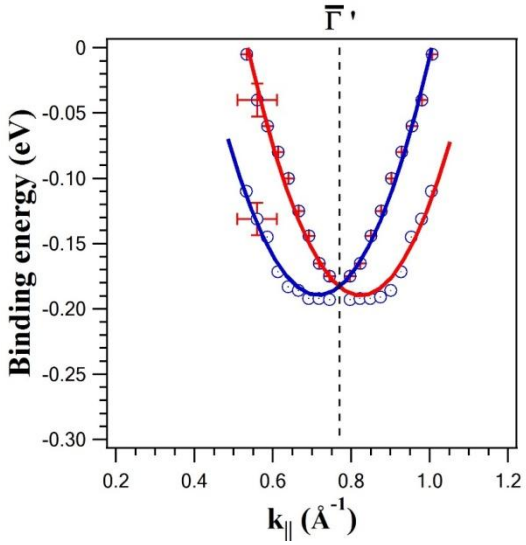

Figure 2.12 *Surface resonance band showing splitting around $\bar{\Gamma}'$ point for $h\nu = 35$ eV at T = 300 K (error bars shown are representative for all points). Continuous lines are a parabolic fit to the data points.*

The behaviour of the two bands shows an anisotropic Rashba splitting, in agreement with the predictions by M. E. Simon et al. [94]. These authors calculate a minimum binding energy of -0.37 eV and at 0.03 $Å^{-1}$ from $\bar{\Gamma}'$. Experimental results are close to that prediction, made for an unreconstructed surface. However, the BE values are 0.20 eV less than recent measurements [45] and other theoretical calculations [68]. In principle, at $\bar{\Gamma}'$ point there should be no gap and no surface state, as it is shown in Figure 2.6b. However, both a gap and a surface band are seen very clearly in the experiment. The expected lack of gap is due to the folding of the bulk bands with the periodicity of the surface reconstruction. However, if the folded bulk states are not seen with PES at the relevant photon energies used, or if the intensity of the folding is weak, a region with low density of states (following the shape of the gap) is still seen after the reconstruction. The surface state survives in this region as a surface resonance.

Folding into normal emission

Due to the (1x2) folding, the $\overline{Y}$ point is folded into the $\overline{\Gamma}$ point at normal emission, to become also a $\overline{\Gamma}'$ point. As this new point is equivalent to the $\overline{Y}$ point, a surface resonance is observed at a binding energy of -0.20 ± 0.05 eV (Figure 2.13a) in a broad range of photon energies (hν = 21 – 40 eV). The resonance is a result of the folding of the Shockley-type

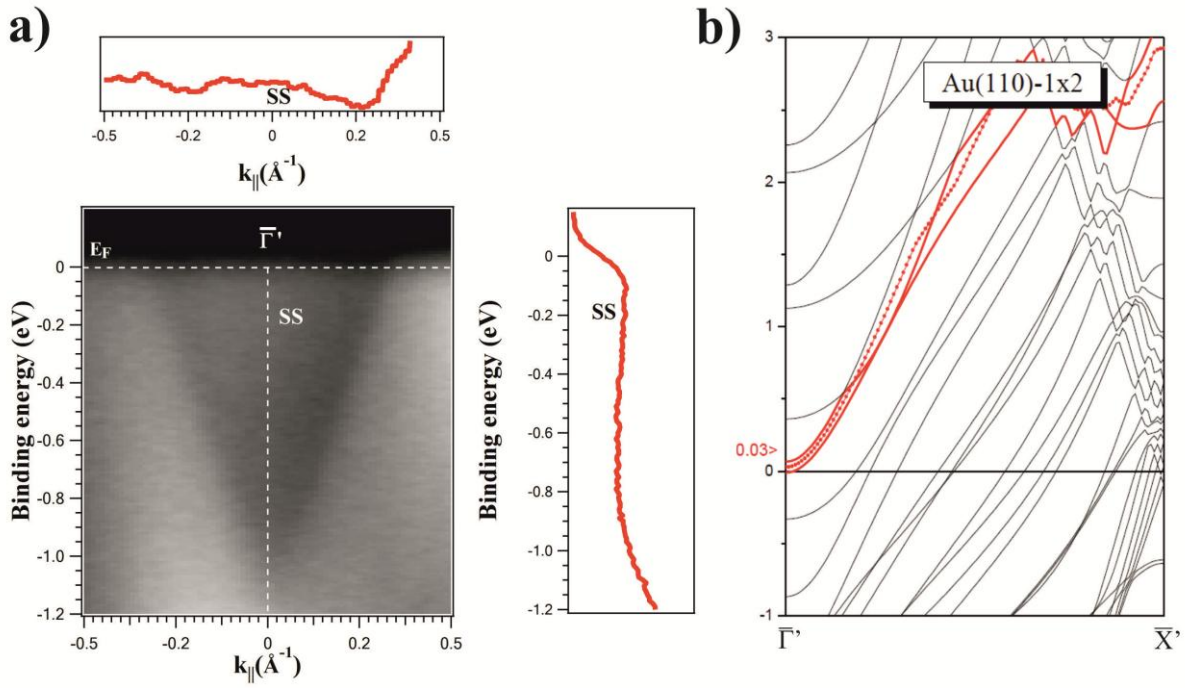

Figure 2.13 *a) Surface state band dispersion around normal emission for hν = 43 eV with EDC and MDC profiles measured at T = 300 K; b) 15 ML Au(110)-(1×2) slab calculation (red lines correspond to the Shockley surface state) [60].*

surface state into normal emission direction. The Fermi momentum is 0.15 ± 0.02 Å^{-1}. Both values are determined from Fig. 2.13 (MDC and EDC) and have relatively large error bars. Figure 2.13b shows the results of a calculation with optimized lattice parameter and surface relaxation for 15 ML Au(110)-(1x2) slab [60]. The Shockley surface state becomes unoccupied at $\overline{\Gamma}'$ point (Figure 2.13b), slightly above (0.03 eV) the Fermi level. The experimental observation of the surface resonance well below the Fermi energy allows us to discard that we are observing part of the unoccupied state, due to the convolution with the Fermi function. In turn, it reveals that the surface resonance appears filled for the surface studied.

Temperature dependence

The temperature dependence of the reconstructed surface was studied by monitoring the order-disorder phase transition. As a first approach, the critical temperature was determined based on an analysis of the LEED patterns, which switch from a (1x2) missing row reconstruction to a (1x1) structure (see Figure 2.2). The critical temperature found was 588 K. This value is lower (16% less) than the value quoted in Ref. [95]. We attribute this difference to the fact that the thermocouple could not be attached in a position sufficiently close to the sample, what gave a temperature difference of approx. 100 K. In a second stage, the Au(110) crystal was heated in front of the electron analyser and the effect of the phase transition in the surface electronic structure was probed.

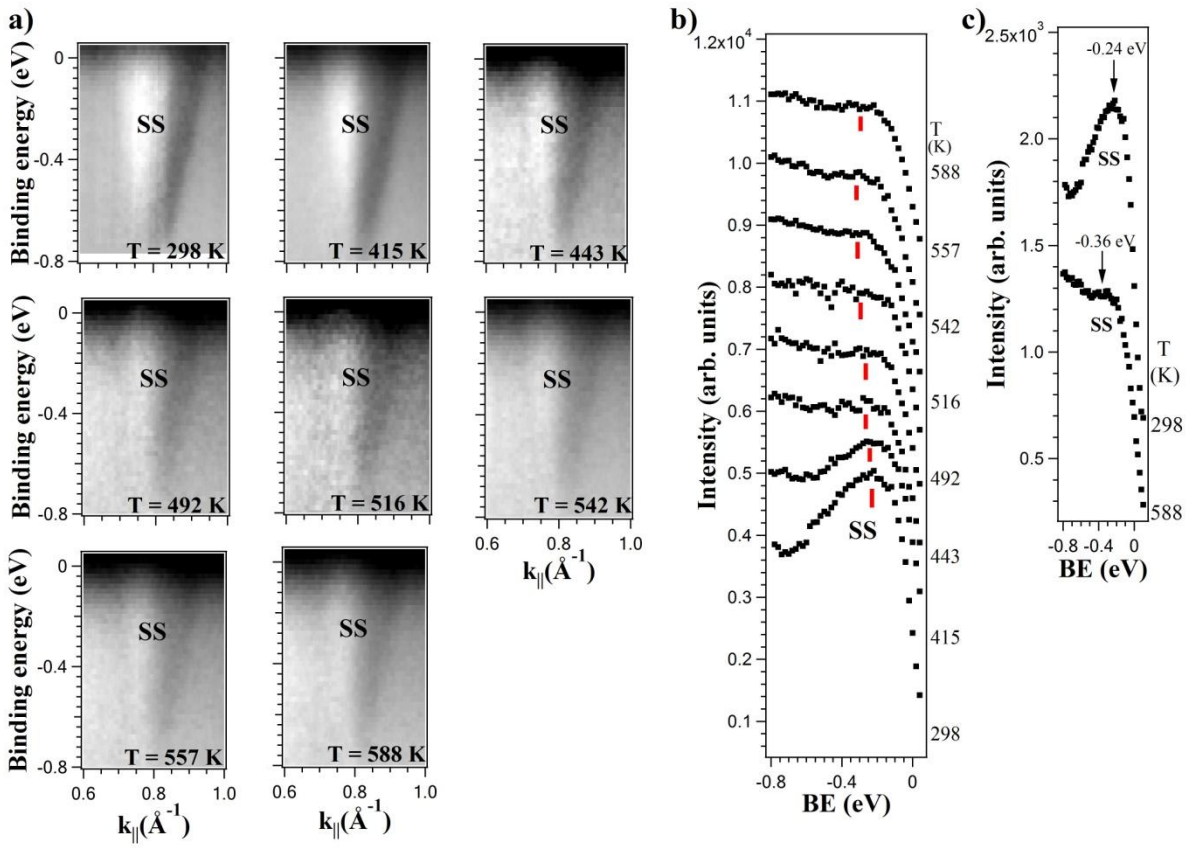

Figure 2.14 *a) Surface band dispersion around $\bar{Y}$ point ($\bar{\Gamma}'$ point) for $h\nu$ = 35 eV in the temperature range 298 K - 588 K; b) EDCs in the binding energy range of the surface state, at $k_{||}$ = 0.77 Å^{-1} for the same range of temperatures c) a comparison of EDC profiles of the surface state at T = 300 K and T = 588 K.*

Figure 2.14a shows the temperature dependence of the surface state around $\bar{\Gamma}'$ point. Upon increasing the temperature, the intensity of the surface state decreases and the surface state shifts slightly away from the Fermi energy (Figure 2.14b), until a value of -0.36 ± 0.03 eV BE at 588 K is reached (an energy shift of approx. 0.12 eV). At this point the surface state is much weaker, but it still exists at $\bar{\Gamma}'$ point (Figure 2.14c).

In the case of the Au(110)-(1x1) surface, obtained either by Au evaporation (see also below) or by heating above the order-disorder phase transition, the (1x2) folding disappears, and so does the surface resonance at normal emission. The comparison for both surfaces (reconstructed and unreconstructed) is presented in Figure 2.15. The surface state at $\bar{\Gamma}'$ point is clearly seen for a photon energy of 43 eV for the reconstructed surface. In the unreconstructed surface, the surface state becomes less resolved (Figure 2.15b), with high intensity only around $\bar{Y}$ point. EDC profiles show that the surface state is shifted up to 0.55 eV in binding energy. This value is close to the shift reported in Ref. [45] (0.59 eV) for the unreconstructed surface.

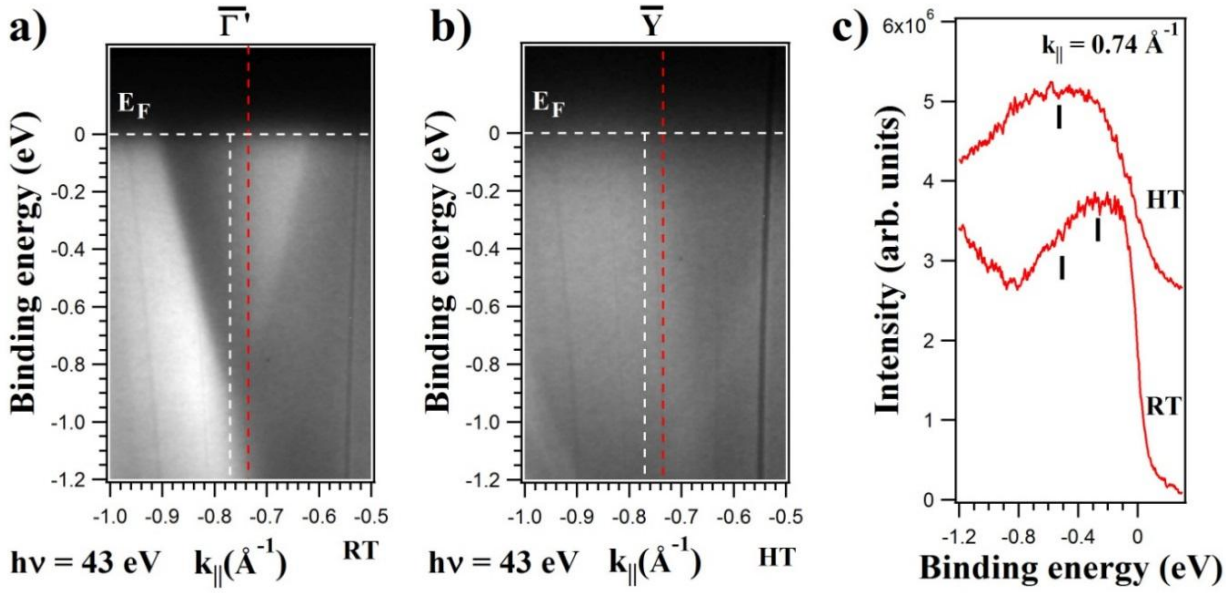

Figure 2.15 *a) Surface band dispersion around $\bar{\Gamma}'$ point (reconstructed surface), b) Surface band dispersion around $\bar{Y}$ point (unreconstructed surface) for $h\nu$ = 43 eV. EDC profiles at $k_{||}$ = 0.74 Å^{-1} (near $\bar{Y}$ point) for both reconstructions, corresponding to the red dashed lines in panels a) and b).*

Analysis of Au(110)-(1x1)

A (1x1) reconstruction can be obtained by two methods at RT. The first one is the evaporation of Au onto the (1x2) reconstructed Au(110) surface. The LEED pattern confirms the observation of a (1x1) superperiodicity (Figure 2.2c). The surface state band is observed with a higher binding energy (Figure 2.16).

For 21 eV photon energy, the shape of surface state is better resolved, but in general the intensity of the state is weak, as we do not expect to have large (1x1) domains. The minimum binding energy is -0.7 eV.

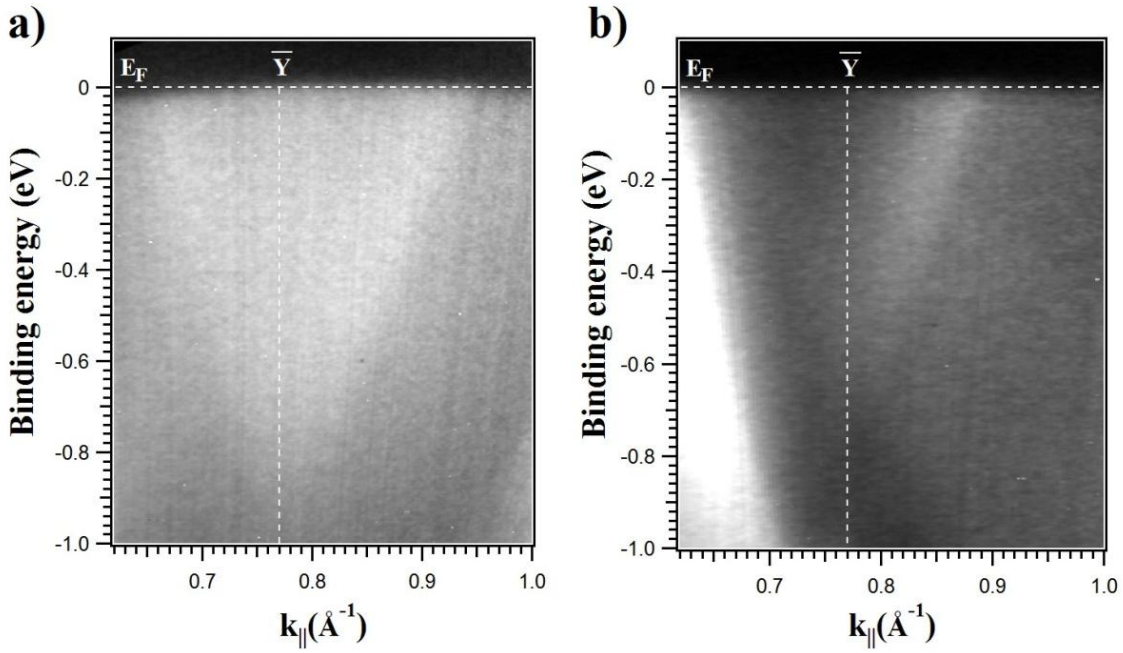

Figure 2.16 a) *Surface band dispersion around $\bar{Y}$ point for Au(110)-(1x1) at: a) $h\nu$ = 21 eV and b) $h\nu$ = 43 eV.*

The second method to produce a (1x1) surface at room temperature is to destroy the (1x2) reconstruction long range order by a mild Ar^+ sputtering (method described in section 1.1.1.4). The surface state at $\bar{\Gamma}'$ point (Figure 2.17a) disappears and even the sp bulk band is not observed after sputtering (Figure 2.17b).

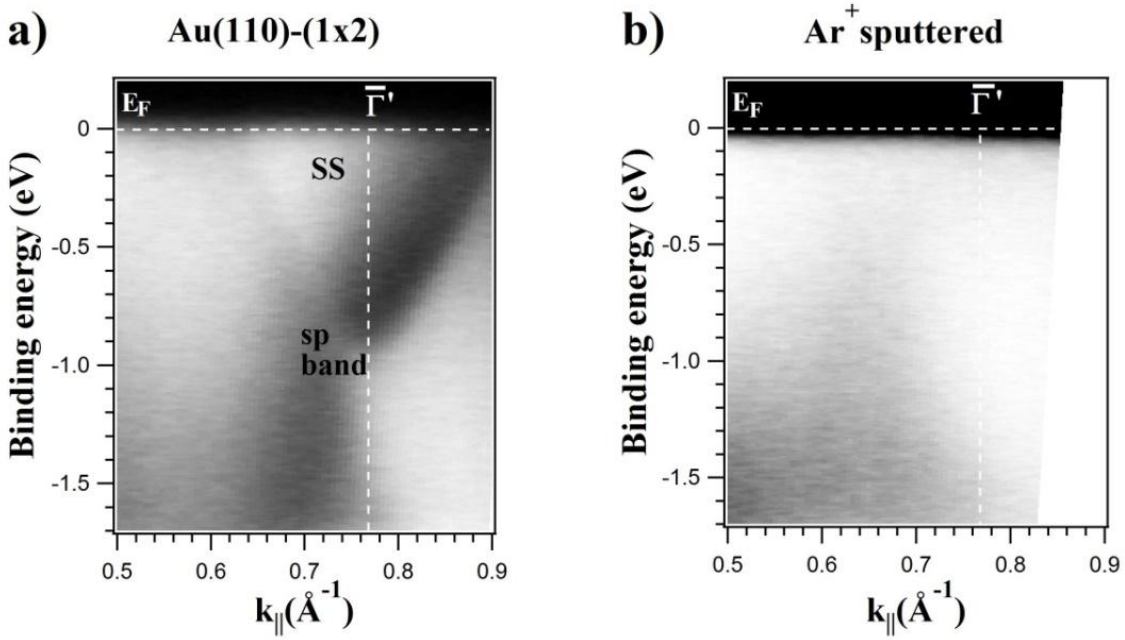

Figure 2.17 *Electronic band structure near the $\bar{\Gamma}'$ point for $h\nu$ = 35 eV a) for Au(110)-(1x2); b) after sputtering.*

2.2.2.2 Surface electronic structure along $\overline{\Gamma X}$

The Fermi surface of noble metals is entirely determined by the sp band. Figure 2.18 (left column) shows the projection of the initial states probed with different photon energies (yellow contours). The right column shows the corresponding 3D cuts of the initial state hemisphere and the Fermi surface (in the repeated zone scheme). For hν = 27 eV and 35 eV, the sp bulk band crosses the Fermi energy along $\overline{\Gamma X}$ direction in a single point, located at momentum values farther away than the $\bar{X}$ point. The sp band becomes occupied for increasing values of the momentum, and thus it disperses away from the Fermi energy as momentum increases. For photon energies of 35 eV and above, there is an additional contour near normal emission. For this contour, the sp band is occupied near normal emission.

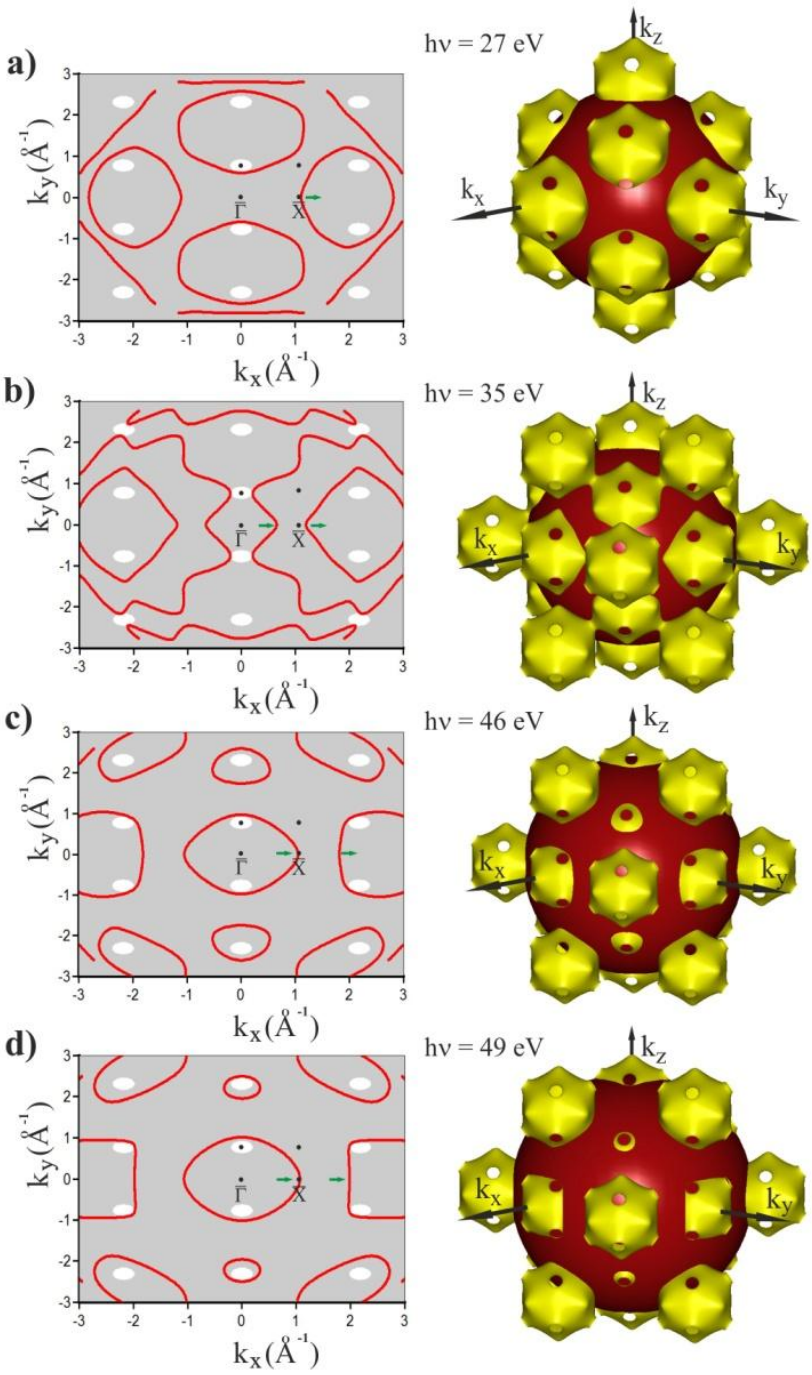

Figure 2.18 *Initial state contours (red) for different photon energies (left column) showing also the projection of bulk states. Green arrows correspond to the direction of movement of the sp band along $\overline{\Gamma X}$ direction. In the right column, 3D representation of the cut of the initial states hemisphere at each photon energy (red) and the Fermi surface (in the repeated zone scheme). All simulations have been generated using FLAN code [16].*

Figure 2.19 shows constant energy surfaces (including the Fermi surface) for Au(110) along the <110> direction. At the Fermi energy, the only absolute gaps are located around $\bar{Y}$ point. For deeper BEs, a band gap is seen along $\overline{XS}$ direction, formed by discontinuous segments between $\bar{S}$ and $\bar{X}$ points. Finally, below -1.4 eV a gap opens also at the $\bar{S}$ point, giving rise to the formation of a gap channel along $\overline{XS}$ direction.

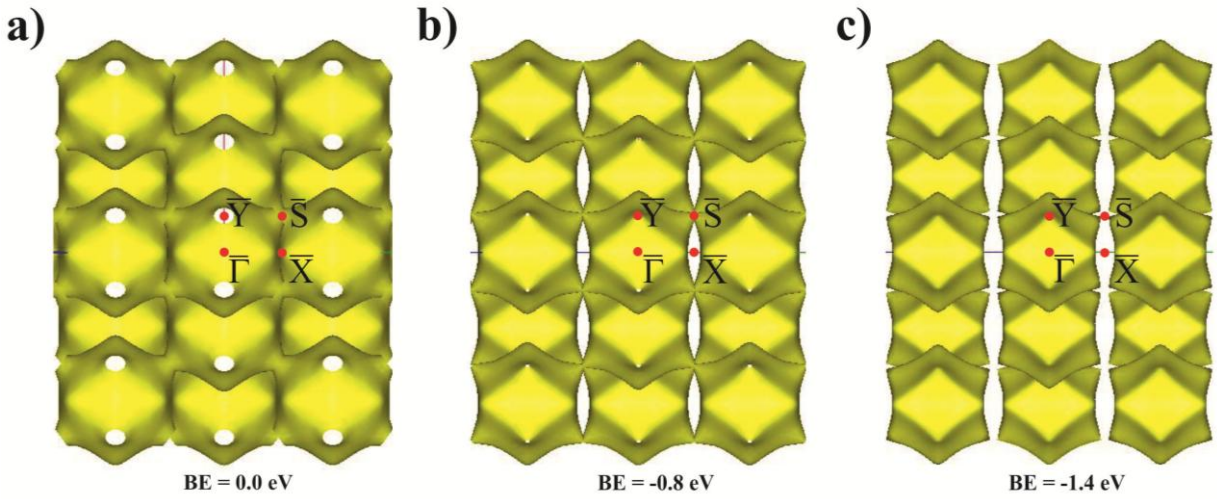

Figure 2.19 *Constant energy surfaces of Au(110) for different BE values: a) BE = 0.0 eV; b) BE = -0.8 eV; c) BE = -1.4 eV.*

Figure 2.20 shows ARPES results near the $\bar{X}'$ point. The Fermi momentum of the sp band is 1.20 ± 0.05 $Å^{-1}$ for hν = 43.5 eV at room temperature. Four additional bands (SS_1, SS'_1, SS_2, SS'_2) are observed. These bands are detected in a broad photon energy range (hν = 29 – 47 eV), see also Figure 2.20, and are symmetric with respect to the $\bar{X}'$ point. Figure 2.21 shows the photon energy dependence of the extra bands observed (panel a) and MDC cuts for the same energy range (panel b). Although the photon energy range shown is not large (40.8 to 44 eV), the bulk sp band exhibits a clear energy dispersion in the MDC cuts. On the contrary, the extra SS bands do not disperse with photon energy. The SS bands are seen sharper for larger photon energies than for smaller photon energies (see Figure 2.21a for hν = 43.5 eV). The splitting between SS_1 and SS'_1, and between SS_2 and SS'_2 does not depend

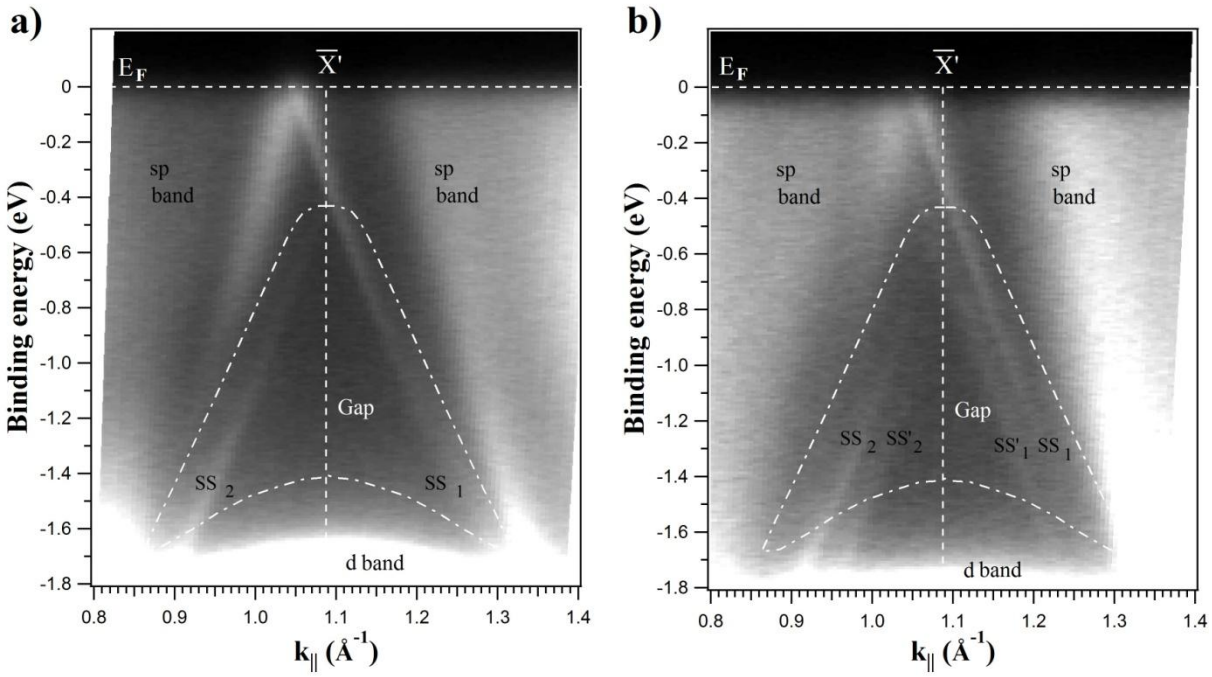

Figure 2.20 *Energy vs. momentum representation of the valence band of Au(110)–(1x2) around $\overline{X}'$ point for hv = 43.5 eV at T = 300 K. Besides the sp and d bands, additional bands (SS_1, SS_1', SS_2, and SS_2') are seen. A dash-dotted line highlights the absolute band gap for a (1x1) surface (from Ref [60]). a) Experiment made in a surface region with a weaker (1x2) reconstruction, b) experiment made in a surface region with a strong (1x2) reconstruction.*

on photon energy. Its value is 0.03 ± 0.01 $Å^{-1}$ for the MDC cut at -1.25 eV BE (Figure 2.21b). It was obtained by measuring the distance between the surface state experimental peaks fitted with Lorentzian components, as shown in Figure 2.22**.** In this figure, the sp band crosses the Fermi energy at 1.2 $Å^{-1}$.

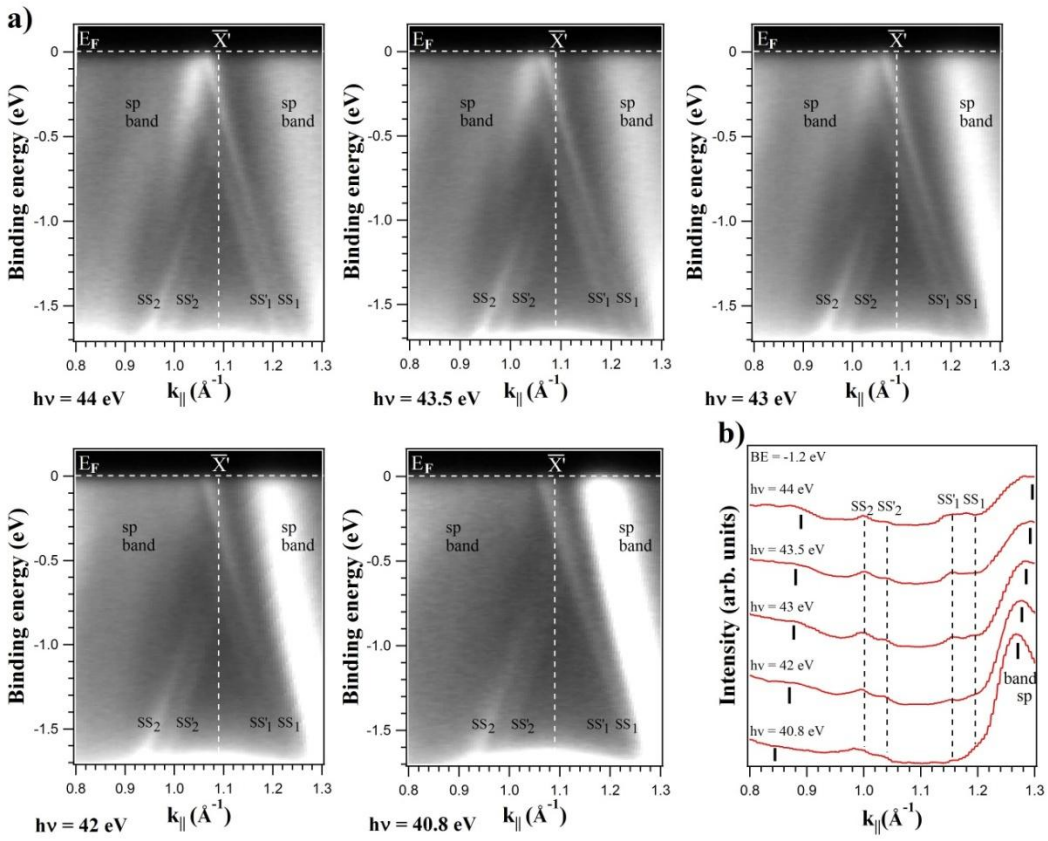

Figure 2.21 *a) Electronic band structure of Au(100)-(1x2) around $\bar{X}'$ point for several photon energies (hν = 40.8 – 44 eV) at T = 130 eV; b) MDC profiles for BE = -1.2 eV at T = 130 K.*

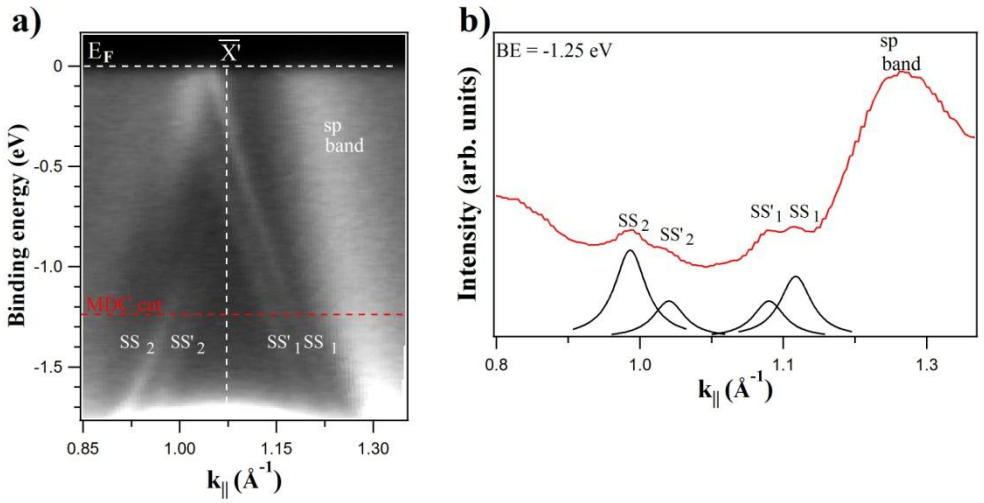

Figure 2.22 *a) Electronic band structure of Au(100)-(1x2) around $\bar{X}'$ point for hν = 43.5 eV; b) MDC profile for BE = -1.25 eV at T = 130 K. Peaks correspond to a fit of the line shape (see text for details).*

Figure 2.23 shows the temperature dependence of the splitting. The split-off bands SS'_1 and SS'_2 are seen much more clearly at low temperature, but they persist at RT. The MDC profiles at BE = -1.4 eV show that trend (Figure 2.23d). Interestingly, the extra bands SS_1 and SS_2 remain at high temperatures, but the splitting disappears at 588 K, when the surface structure reverts from (1x2) into a disordered (1x1) structure.

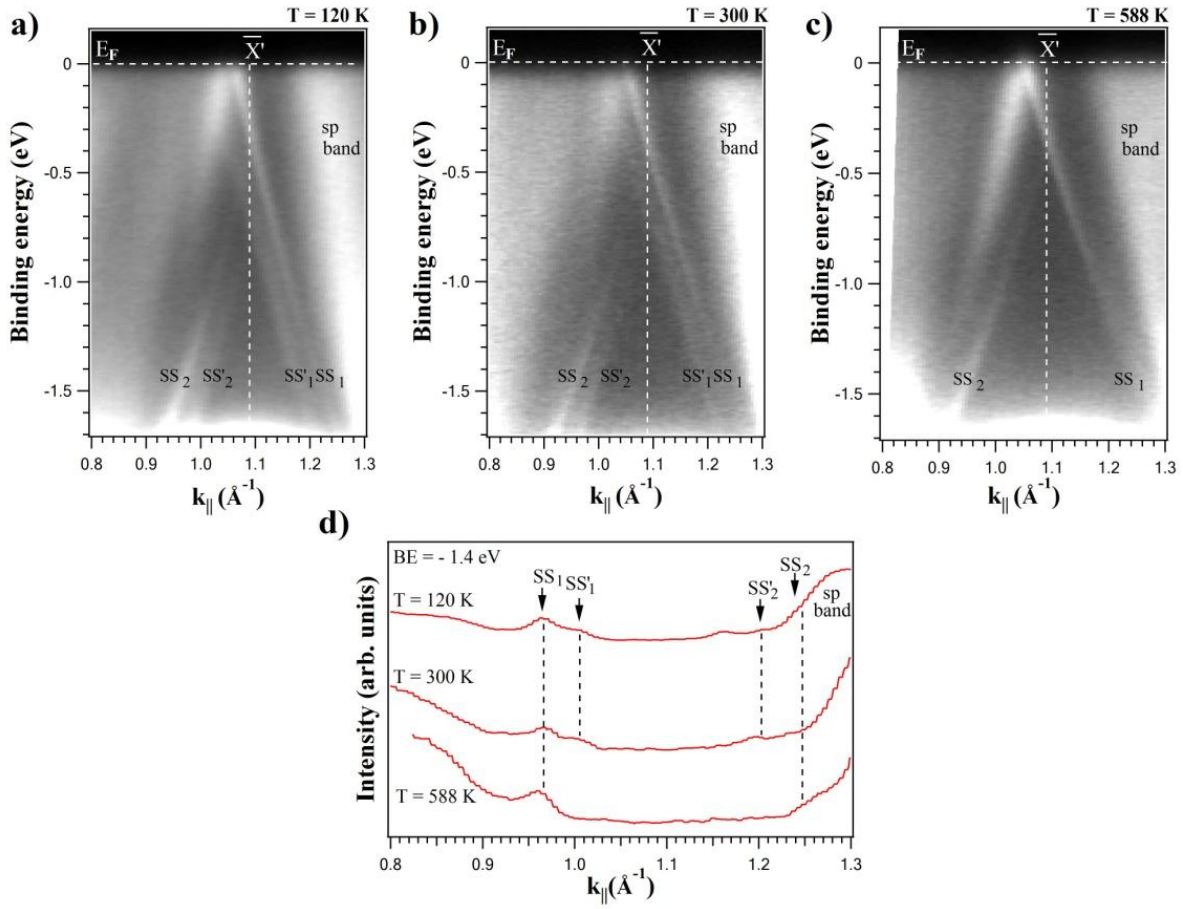

Figure 2.23 *BE vs. momentum representation for Au(110) around $\overline{X}'$ for hv = 43.5 eV: a) (1x2) reconstructed surface at T = 120 K; b) (1x2) reconstructed surface at T = 300 K; c) unreconstructed surface – (1x1) at T= 588 K.*

Figure 2.24 shows the band structure for selected azimuthal angles in the range 0º to 42º with respect to the $\overline{\Gamma'X'}$ direction at T = 130 K. Until 10º off, the extra bands remain almost unchanged in the momentum scale. The splitting along $\overline{\Gamma'X'}$ direction is 0.04 $Å^{-1}$ at -1.4 eV BE. The splitting becomes smaller as the azimuthal angle increases away from the $\overline{\Gamma'X'}$ direction. For instance, the value of the SS_1-SS_1' (SS_2 -SS_2') splitting is 0.025 $Å^{-1}$ for an angle

of 12º off. The splitting is visible up to 20º off. This angle corresponds approximately to the $\overline{\Gamma' S'}$ direction

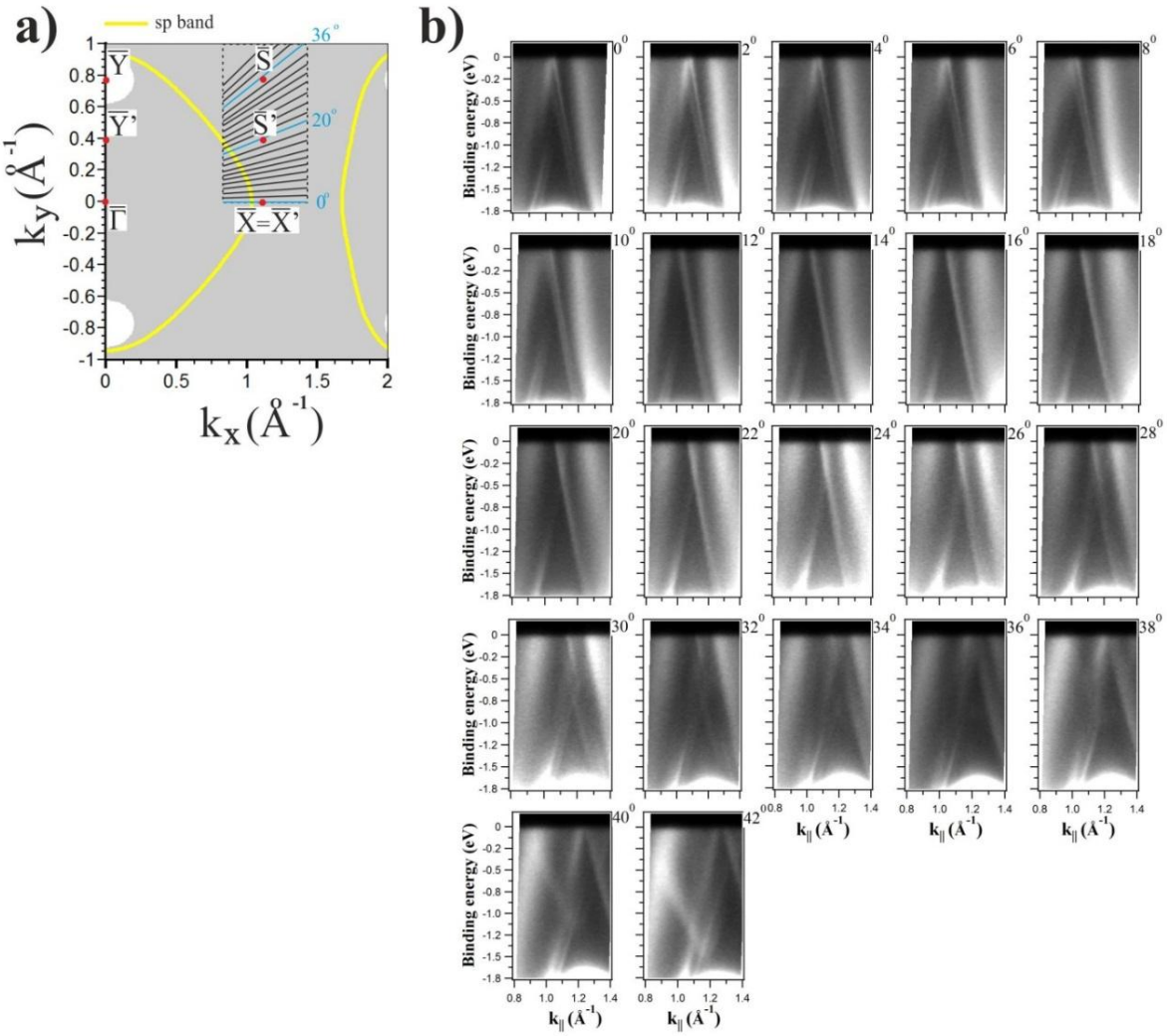

Figure 2.24 *Surface resonance bands for selected azimuthal angles with respect to $\overline{\Gamma' X'}$ point for $h\nu$ = 43.5 eV at T = 130 K.*

(19.6º), suggesting that the splitting disappears at the $\overline{S'}$ point. For even larger angles (i.e. when going again away from the $\overline{S'}$ point) the splitting reappears, reaching a value of 0.04 Å^{-1}. For azimuthal angles above 30º off, additional bands are detected. For 36º (35.5º correspond to the next $\overline{\Gamma' X'}$ direction, identical to $\overline{\Gamma S}$) an even larger splitting (0.07 Å^{-1}) is observed.

Figure 2.25 shows a constant energy surface for several binding energies at a photon energy of 43.5 eV. SS_1 and SS_2 are observed along $\overline{X' S}$ direction for -0.24 BE (Figure 2.25a). Lines highlight the dispersion of both states, which are split at $\overline{X'}$ and $\overline{S}$. Close to the $\overline{S'}$ point,

the states are coupled. Note that there is an absolute band gap below the Fermi level along that direction (Figure 2.19b and c).

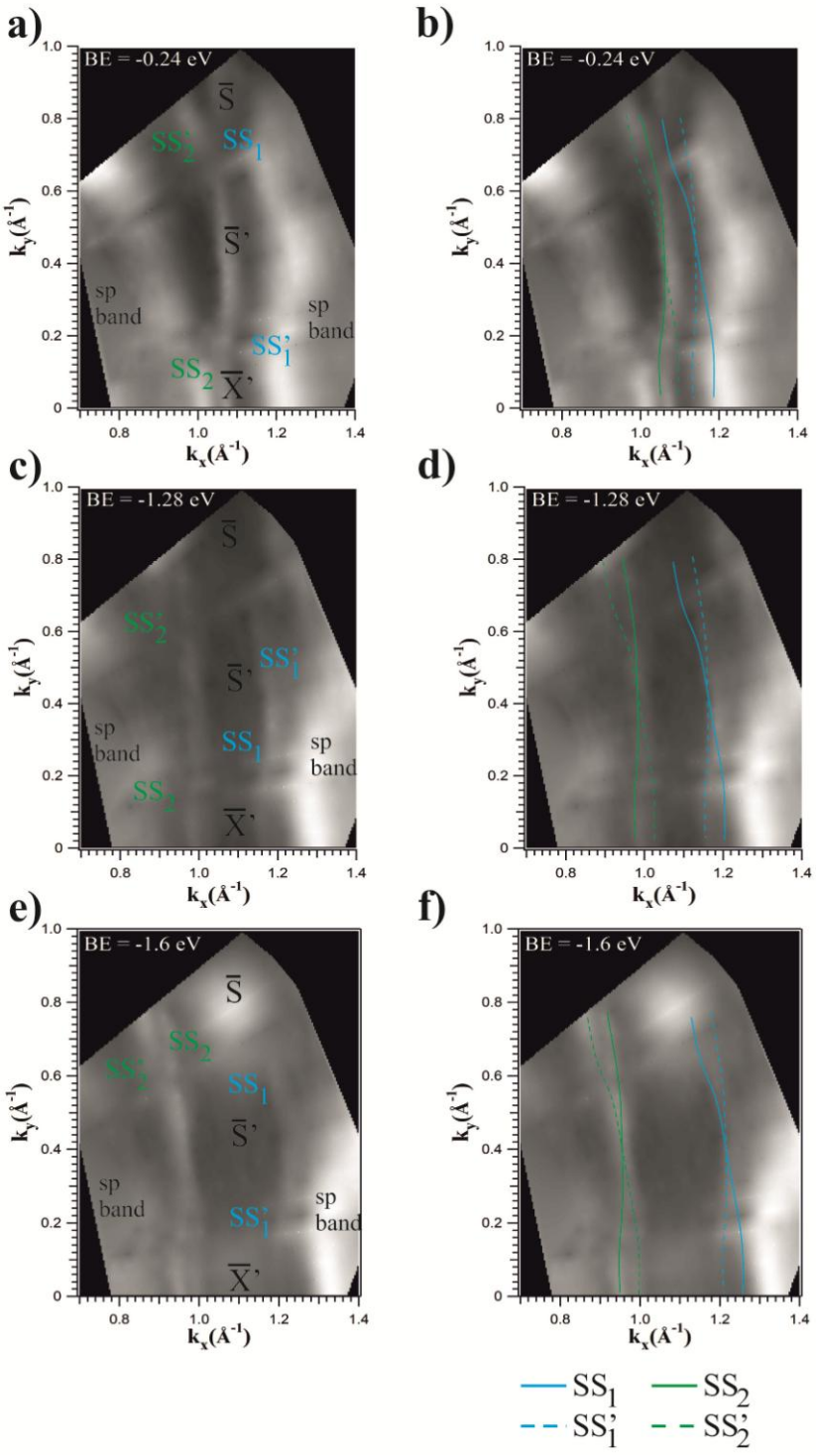

Figure 2.25 *Constant energy surfaces along $\overline{X'S}$ direction for hv = 43.5 eV and increasing BEs with schematic representations of the SS_1 (SS'_1) and SS_2 (SS'_2) bands topology along $\overline{X'S}$ direction.*

The splitting is better seen near the $\bar{X}'$ point for deeper BEs. It disappears near the $\bar{S}'$ point and reappears at the $\bar{S}$ point.

The band SS_1 at $\bar{X}'$ point disappears also after an ion treatment of the Au(110) crystal (method described in the chapter 1.1.1.4) that destroys the (1x2) long range order. After this treatment, only a broadened sp bulk band is observed (Figure 2.26a). After annealing the crystal, the band SS_1 is observed again (Figure 2.26b).

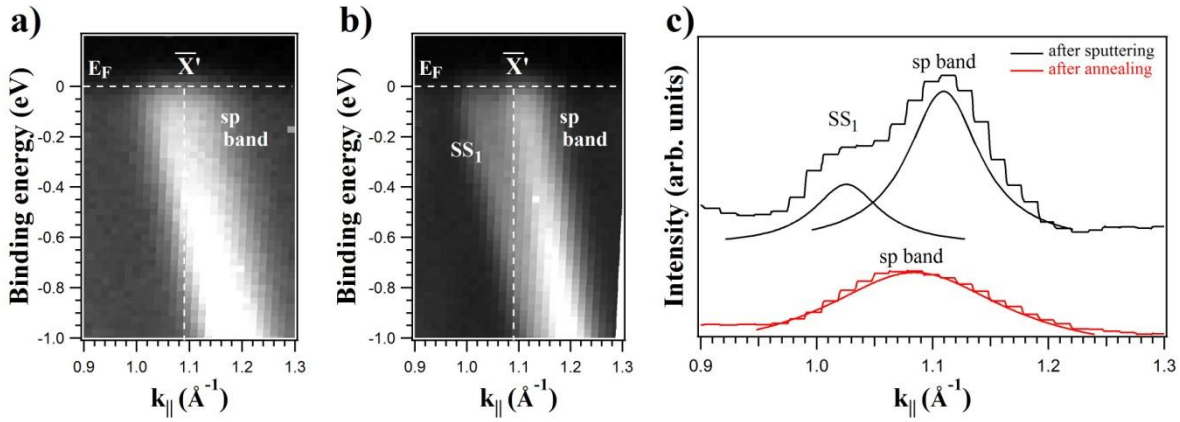

Figure 2.26 *Electronic band structure near the $\bar{X}'$ point for $h\nu$ = 33 eV a) after sputtering; b) after annealing c) MDC curves for both cases at the Fermi level (peaks correspond to a fitting of the experimental line shape with Lorentzian components). All measurements were obtained at T = 300 K.*

These observations are reinforced by an inspection of the corresponding MDC profiles. After sputtering, the MDC profile shows only the sp bulk state around $\bar{X}'$ ($k_{\|}$ = 1.08 Å^{-1}). The MDC profile of the annealed surface shows SS_1 and the sp bulk band close to the Fermi energy (Figure 2.26c). After annealing, SS_1 state crosses the Fermi edge at $k_{\|}$ = 1.03 Å^{-1}, and the sp bulk band is shifted 0.03 Å^{-1}.

2.3 Discussion

We consider first the electronic structure near the $\bar{Y}$ point. The Au(110) reconstructed surface should present no gap due to the folding induced by the superperiodicity. However, there is a clear area with a reduced density of states, so that the $\bar{Y}$ point surface state survives as a surface resonance at $\bar{\Gamma}'$ points. The surface resonance presents a parabolic dispersion, with the bottom at ~0.3 eV. This electronic state is folded with the periodicity

of the reconstruction, as it is seen for different photon energies at various $\bar{\Gamma}'$ points: $k_{\parallel} = 0$ Å^{-1}, $k_{\parallel} = 0.77$ Å^{-1}, and $k_{\parallel} = 1.54$ Å^{-1}. An analysis of the EDCs shows that there is more than one band, what is traced back to the existence of anisotropic Rashba splitting, in agreement with theoretical calculations. There is no evidence of splitting for $k_{\parallel} = 1.54$ Å^{-1}.

The loss of (1x2) superperiodicity induced by temperature destroys the folding. At high temperature, when (1x2) long-range order disappears, the surface resonance disappears also at $\bar{\Gamma}$ (or it becomes much weaker), but is still observed at $\bar{Y}$ point, being shifted only 0.12 eV. However, the surface resonance survives at 1.54 Å^{-1}. This finding suggest that, even if the LEED is (1x1), there are still (1x2) small regions or some degree of (1x2) ordering. In fact, large domains are not required in ARPES to observe band folding and high-temperature STM reveals still small regions of (1x2) domains on the surface at the phase transition temperature. The smaller value of the BE at higher temperatures suggests that the surface resonance domain size is smaller.

The deposition of Au induces also a (1x1) reconstruction. The surface resonance also vanishes in this case at $\bar{\Gamma}$ point. The surface resonance shifts to higher binding energies at $\bar{Y}$ point. Its minimum binding energy is close to the theoretical prediction.

We consider now the electronic structure near $\bar{X}'$ point. Here, theoretical calculations predict the opening of a gap and the existence of a channel along $\overline{X'S'}$ direction, both below the Fermi energy. Several bands (additional to the expected bulk sp band) are seen in the vicinity of the $\bar{X}'$ point. We attribute SS_1 (close to the right gap edge) and SS_2 (close to the left gap edge) to surface resonance bands split off from the gap edge. These two bands exhibit the expected symmetry with respect to the $\bar{X}'$ point and are surface sensitive. A possible bulk origin is definitely discarded in view of the lack of dispersion with photon energy. Both resonances are enhanced by the presence of the band gap (Figure 2.20 and Figure 2.19b and c), but also survive out of the gap region.

There are two possible explanations for the additional bands (SS_1' and SS_2'). It is worth mentioning that surface resonance bands analogous to SS_1 and SS_2 are also seen in Cu(110) and Ag(110) surfaces, but in these two cases the surface resonances present no additional splitting. The difference of Au(110) with Ag(110) and Cu(110) surfaces is that Au(110) is reconstructed (1x2) and is a heavier element, and thus spin-orbit coupling is more important. A first explanation for the origin of the splitting would thus be spin-orbit splitting of a Rashba origin. However, this idea is not in agreement with theoretical calculations [60],

which do not predict significant Rashba splitting for these bands. A second explanation is that they are due to the (1x2) folding combined with the specific dispersion features of SS_1, SS_2.

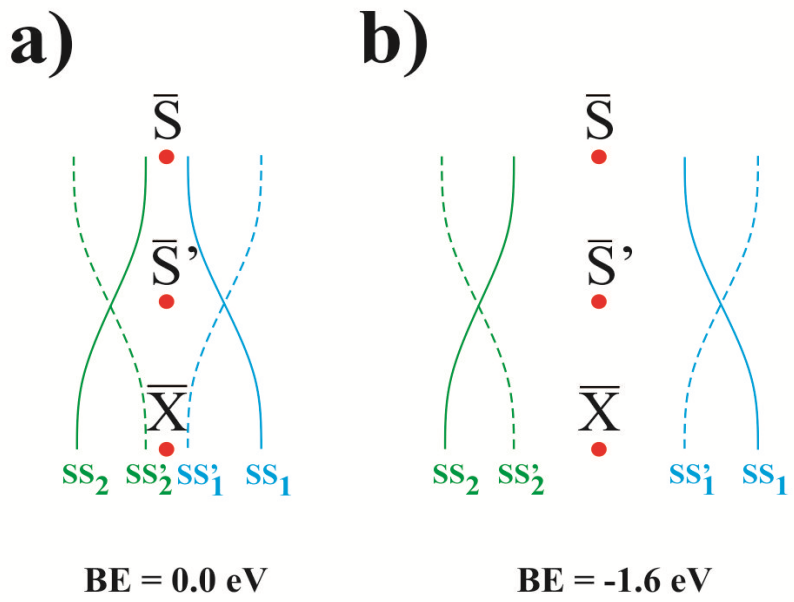

Figure 2.27 *a) A scheme of the band dispersion of SS_1 and SS_2 at 0 eV BE and b) the dispersion of SS_1, SS'_1, SS_2 and SS'_2 at -1.6 eV BE.*

This origin is supported by the sensitivity of the split bands to surface ordering and to the appearance of the (1x2) reconstruction. To understand the model proposed, we show in Figure 2.27 a scheme of the band dispersion of Fig. 2.25. We consider first the band SS_1 near $\overline{XS}$ direction and farther away from normal emission than $\overline{XS}$ direction. The Fermi contour of this band (and the corresponding constant energy surfaces for deeper BEs) is closer to the $\bar{S}$ point than to the $\bar{X}$ point, in the absence of (1x2) folding. Due to symmetry reasons, an equivalent band SS_2 is seen near $\overline{XS}$ direction, but closer to normal emission than $\overline{XS}$ direction. For the reconstructed surface, a new $\bar{S}'$ symmetry point is formed, half-way between $\bar{S}$ and $\bar{X}$ points, which become equivalent $\bar{X}'$ points. Both contours SS_1 and SS_2 are folded according to the new surface symmetry, giving rise to the appearance of the two close bands, SS_1' and SS_1' (dashed lines in Fig. 2.27). Note that due to the (1x2) symmetry, the two bands should be degenerate at $\overline{S'}$. The splitting found, together with the foreseen degeneracy at $\bar{S}'$ is in agreement with the angular dependence of the splitting seen in Figure 2.25.

2.4 Summary

The electronic structure of Au(110)-(1x2) along XKΓ direction presents good agreement with the free electron final state model with some exceptions explained from indirect transitions and Umklapp processes. An occupied Shockley surface state is identified at the $\bar{Y}$ point for the (1x2) surface. This state presents a free electron like behaviour and it is observed in each $\bar{\Gamma}'$ point, so that it is repeated with the surface periodicity. This Shockley surface state presents the features of a two-dimensional state and exhibits spin-orbit splitting. If the temperature increases above the order-disorder critical temperature, the surface reconstruction disappears and the surface state is not observed at $\bar{\Gamma}'$ anymore, but it survives as a weak feature near $\bar{Y}$ point. A metastable Au(110)(1x1) structure has been obtained using two preparation methods. In this structure, the binding energy of the Shockley surface state is close to the theoretical value for the unreconstructed surface. A surface resonance is observed at $\bar{X}'$ point, in agreement with previous findings for Cu(110) and Ag(110). The surface resonance is located inside or near the bulk band gap existing along $\overline{XS}$ direction below the Fermi level. For the (1x2) superstructure, the surface resonance is split near $\bar{X}'$ point in two electronic states (SS_1 and SS_2). These two split bands follow the shape of the band gap and are degenerate at $\bar{S}'$ point. The splitting of the surface resonance is due to the (1x2) folding, because the unreconstructed surface presents no splitting.

3. Surface states on vicinal Beryllium surfaces: two-dimensional quantum well states

A vicinal surface with monoatomic steps is an interesting example of quasi one-dimensional nanostructured system. Vicinal surfaces have been an active field of research in the past due to several reasons. On the one hand, they can be used as templates for the further growth of low dimensional nanostructures [96] [97] [98] [99] [100]. On the other hand, the high step density makes many vicinal surfaces active in heterogeneous catalysis [101] [102]. The electronic properties of noble metal vicinal surfaces have been a subject of attention in the last years [96] [97]. Most noble metal vicinal surfaces present intrinsic surface states, which can be manipulated by changing the step superperiodicity. These surfaces are good model systems to understand the properties of laterally nanostructured systems and to achieve an effective tailoring of their electronic behaviour [96] [97] [103] [104]. In the case of noble metal surfaces vicinal to the (111) direction [96] [97] it has been found that the wave function of the surface state switches from being localized at the terraces for small miscut angles (and larger terraces), to being delocalized along the optical surface for miscut angles larger than a critical value of approximately 7º. The origin of the switch (which affects the transport properties of the surface state), is attributed to the closing of the surface band gap along the (111) direction [97] [98]. This process permits the coupling between surface and bulk states via a step lattice vector, and bulk states hybridize with the surface state wave function, giving rise to a 3D surface resonance [96]. Group II metals (like Be and Mg) exhibit several prominent surface states with a large density of states, which in some cases is even larger than the bulk electronic density. In the case of (0001) surfaces, the surface state has an almost ideal two-dimensional character, since the bulk band gap is very large [105]. In the case of $(10\bar{1}0)$ surfaces, there are different kinds of surface states, as there are several band gaps in the electronic structure [106].

The main objective of this chapter is the investigation of the electronic properties of beryllium surfaces vicinal to the $(10\bar{1}0)$ direction for several miscut angles. First, the crystalline structure is characterized by using the LEED and STM techniques (Chapter 3.1). Then, the existence of surface states and their distribution in reciprocal space is analysed (Chapter 3.2). To this end, we have probed the two high symmetry directions of the surface. Several surface states have been observed and characterized at high symmetry

points, in particular near the $\bar{A}$ point [106] [107] [108]. In the last subsection we discuss the electronic states observed and their origin.

3.1 Crystalline structure of vicinal hcp surfaces: the case of beryllium.

Beryllium is a metal belonging to the IIA group (alkaline earth metals). Be crystallizes in the hexagonal close packed structure (hcp). The hcp structure is characterized by the stacking of two different atomic layers with different registry, as shown in Figure 3.1. Each layer is formed by a hexagonal atomic arrangement.

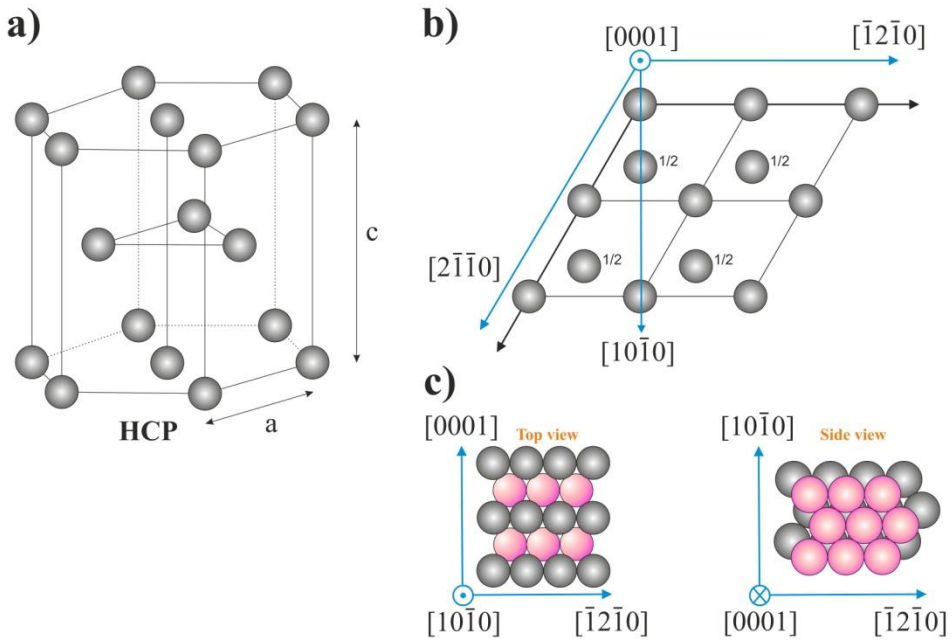

Figure 3.1 *a) Conventional unit cell of the hexagonal close packed lattice, side view. For Be, a = 2.29 Å and c = 3.58 Å; b) Same, top view; c) Model of the* $(10\bar{1}0)$ *surface.*

The real space lattice parameters of the $(10\bar{1}0)$ surface are c = 3.58 Å along [0001] direction and a = 2.29 Å along $[1\bar{2}10]$ direction [109]. The first layer of Be$(10\bar{1}0)$ consists of the closed packed rows along the $[1\bar{2}10]$ direction.

The samples used for this work are crystals vicinal to the $(10\bar{1}0)$ face, with nominal miscut angles of 2.95º, 4.48º, 6.06º, and 9º along the [0001] surface direction, which corresponds to the long side of the surface rectangular unit cell in real space. Figure 3.2 shows several vicinal $(10\bar{1}0)$ surfaces with the nominal miscut angles used in this work.

An important feature of the hcp lattice is that, at variance with the fcc lattice, there are two possible surface terminations, related to the two different step heights: 0.66 Å (h_1 – called "short") and 1.32 Å (h_2 – called "long"). This feature is traced back to the specific stacking of atomic planes in hcp crystals, which always gives rise to the exposure of two different terminations for vicinal surfaces (see also Figure 3.1).

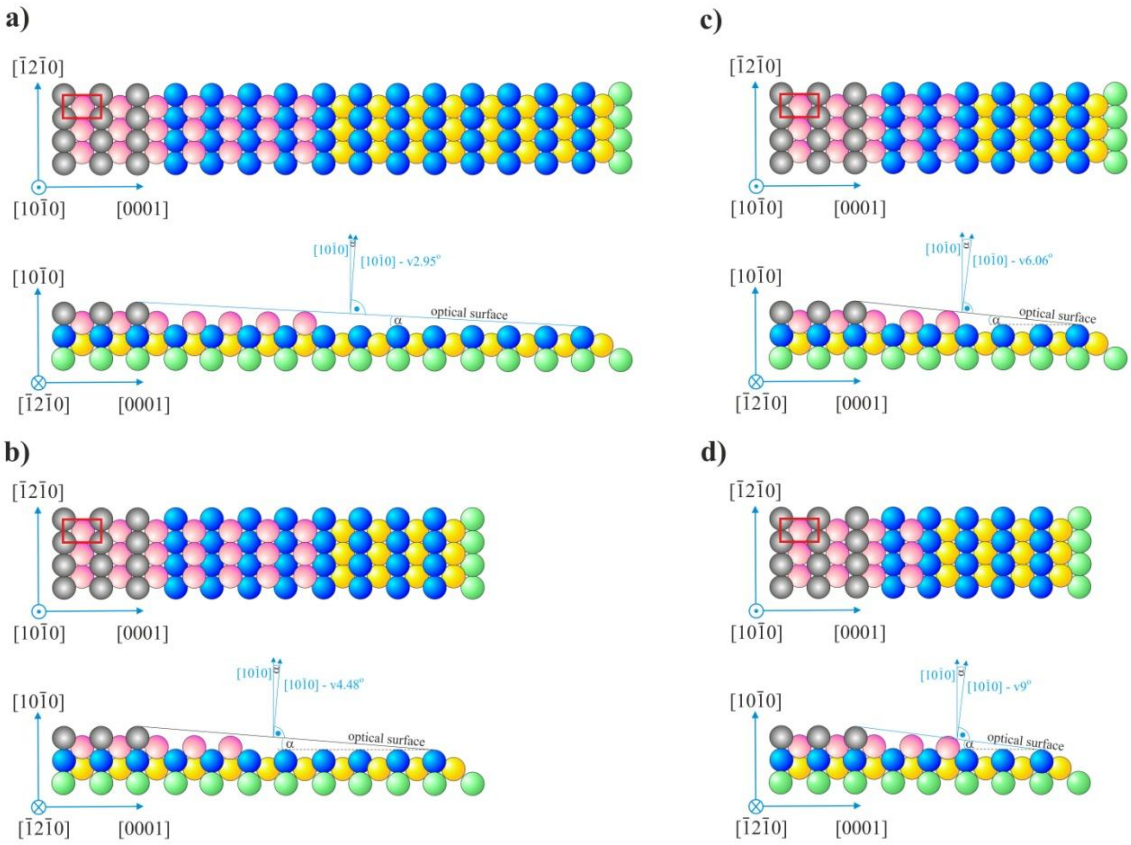

Figure 3.2 *Atomic models of selected vicinal Be*$(10\bar{1}0)$ *surfaces for the nominal miscut angles used in this work including a top view (the red rectangle is a* $(10\bar{1}0)$ *unit cell) and a side view, showing the angle between the optical surface and the* $(10\bar{1}0)$ *terraces, for a) 2.95º miscut; b) 4.48º miscut; c) 6.06º miscut; d) 9º miscut.*

As vicinal hcp surfaces may exhibit two types of terminations, these types are present in the case of the $(10\bar{1}0)$ surface, with two types of terraces of widths L_1 and L_2, corresponding to the two types of steps. Only the total terrace length $L = L_1 + L_2$ is determined by the miscut angle, as L determines the surface superperiodicity. Table 3.1 collects the relevant parameters for the samples used.

Sample No.	Crystal	Nominal miscut angle [degrees]	Real miscut angle [degrees]	$L_{tot.}$ [Å]	$L_{tot.real}$ [Å]
1	$Be(10\bar{1}0) - v2.95^{\circ}$	2.95	2.3±0.5	38.5	49.3
2	$Be(10\bar{1}0) - v4.48^{\circ}$	4.48	5.4±0.5	25.4	21.0
3	$Be(10\bar{1}0) - v6.06^{\circ}$	6.06	6.0±0.5	18.8	18.9
4	$Be(10\bar{1}0) - v9^{\circ}$	9.00	-	12.7	-

Table 3.1 *Structural parameters of* $Be(10\bar{1}0)$ *surfaces vicinal along [0001] direction.*

Four different crystals were cut from a Be single crystalline rod of cylindrical shape. As the natural growth direction in hcp crystals is $[11\bar{2}0]$, the $(10\bar{1}0)$ direction lies at 90º from the rod axis. Cutting and polishing Be crystals to a high degree of perfection is extremely difficult. On the one hand, the natural grain size of Be single crystals is rather small, giving rise to a poor natural quality of single crystalline specimens, with an average orientation error of 0.5º. On the other hand, polishing vicinal crystals to a high degree of accuracy usually requires several cycles of polishing and orientation using the Laue technique. As Be powder is toxic, this process has to be undertaken in an automatic setup with controlled atmosphere and prepared to filter toxic particles in the exhaust pipes. At the moment, such facilities are only available in environments prepared to cut such materials as transuranides, what restricts the use of the facility to a fixed time slot. Thus, the accuracy of the miscut angle of Be vicinals is much lower than corresponding values obtained for other materials. In Table 3.1, the vicinal Miller indexes of the orientation correspond to the nominal miscut angles. The nominal orientation of each crystal was checked using the Laue technique, and the real miscut angle of the final crystals was determined in this way. The difference between the nominal angle and the actual angle achieved can reach even 1º. A smaller miscut angle gives rise to larger terraces on the surface. If the miscut angle increases, then the size of terraces decreases (see also the model in Figure 3.2). As there is no information in the literature about the nature and ordering of terraces in vicinal Be crystals, the selected miscut angles do not necessarily correspond to stable step superperiodicities. Step bunching or faceting could take place, destroying the expected average surface shown in the

ideal models of Figure 3.3 Thus, the actual distribution of steps at the surfaces has to be determined in each case using LEED and/or STM.

Each sample was carefully studied using LEED to determine the long-range ordering of the step distribution. The LEED pattern for the flat surface $(10\bar{1}0)$ has a rectangular symmetry (Figure 3.3a). In addition to this, the pattern for vicinal surfaces shows extra spots along [0001] direction, indicating the existence of a superperiodicity in the vicinal surface. Some of the spots are fairly sharp (Figure 3.3, panels c or f), but some are blurred (panel d), indicating different degrees of order in the superlattice.

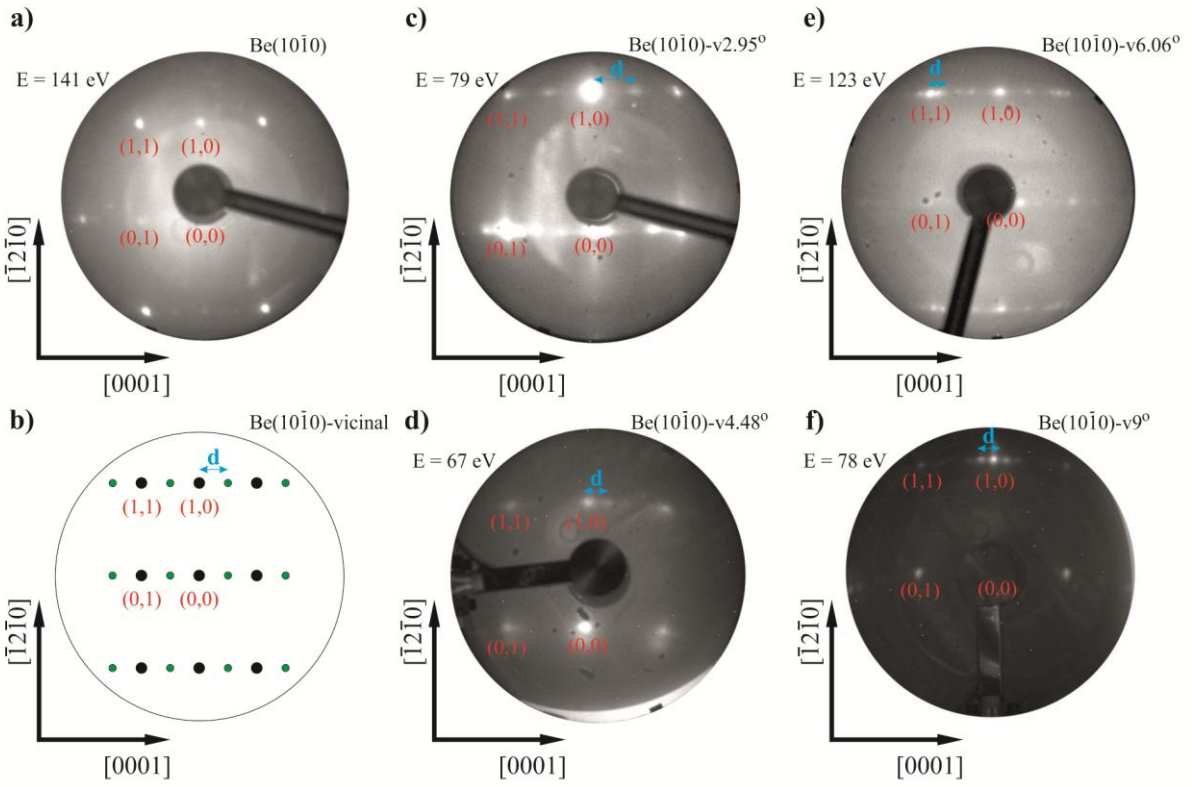

Figure 3.3 *LEED patterns for several crystals: (a) $Be(10\bar{1}0)$, (b) LEED pattern model of vicinal $Be(10\bar{1}0)$, (c) $Be(10\bar{1}0) - v2.95^{\circ}$, (d) $Be(10\bar{1}0) - v4.48^{\circ}$, (e) $Be(10\bar{1}0) - v6.06^{\circ}$, (f) $Be(10\bar{1}0) - v9^{\circ}$ measured at room temperature.*

A summary of the periodicities of the extra spots is shown in Table 3.2. A detailed analysis of the periodicities present in the LEED patterns observed for each crystal was performed as part of this work. In general, an analysis of the profiles along the [0001] direction can determine the distance between the spot (01), corresponding to the (1x1) unit

cell, and extra spots around that spot. In most cases, several superperiodicities coexist in the LEED pattern of each vicinal

Crystal	Average terrace size		LEED		Number of unit cells
	Nominal (Å)	Laue (Å)	Superperiodicity ($Å^{-1}$)	Terrace size (Å)	
$Be(10\bar{1}0) - v2.95^{\circ}$	38.5	49.3	Diffuse spots	-	
$Be(10\bar{1}0) - v4.48^{\circ}$	25.4	21.0	0.28 ± 0.02	22 ± 2	6
$Be(10\bar{1}0) - v6.06^{\circ}$	18.8	18.9	0.36 ± 0.05	18.78 ± 2	5
$Be(10\bar{1}0) - v9^{\circ}$	12.7	-	0.43 ± 0.06	14.6 ± 1	4
			0.24 ± 0.06	25.9 ± 1	7

Table 3.2 *Periodicities observed* in the *LEED patterns for the vicinal Beryllium surfaces studied.*

surface, indicating that the superperiodic step distribution is not unique, and that there are domains large enough to be observed by LEED. Table 3.2 collects the main superperiodicities observed and the corresponding experimental distance between steps (terrace size) calculated from them (minor superperiodicities are not included). Note that the nominal terrace size is calculated from the nominal miscut angle and the Laue terrace size from the actual miscut angle measured. This value is determined from the bulk miscut orientation, and thus it represents the expected average terrace size. However, the actual surface may present different distributions of terrace sizes if the average value does not correspond to a minimum of the surface energy. Actual terrace sizes observed are determined from the LEED analysis. In fact, as mentioned above, besides these main periodicities, other minority superperiodicities are also observed in the LEED. Smaller additional spots along $[1\bar{2}10]$ direction were also observed in some cases, which may indicate a small amount of faceting.

3.2 Surface states on high-symmetry beryllium surfaces

The surface Brillouin zone of Be$(10\bar{1}0)$ is rectangular (Figure 3.4a). The miscut angles along [0001] direction (perpendicular to steps), are along $\overline{\Gamma A}$ direction (Figure 3.4b). The superperiodicity induced by the step superlattice corresponds to 0.16, 0.25, 0.34, and 0.5 Å^{-1}. As the substrate $\bar{\Gamma} - \bar{\Gamma}$ distance is 1.754 Å^{-1}, the step superlattice corresponds approximately to 11, 7, 5, and 4 times the substrate superlattice. The new Brillouin zone created on

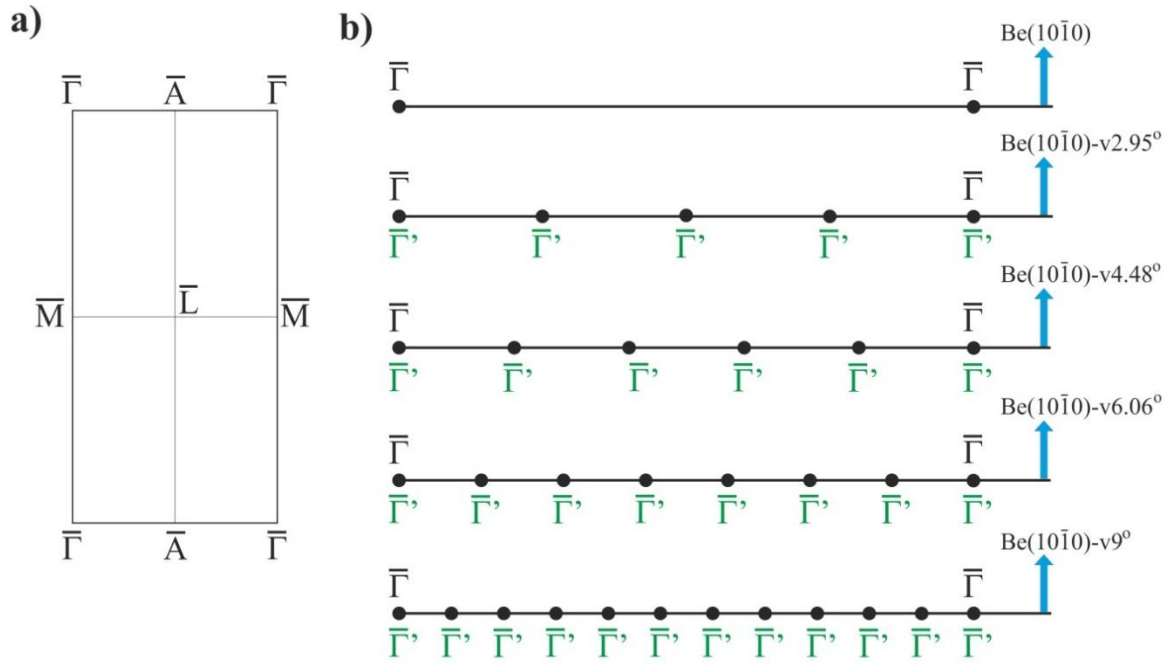

Figure 3.4 *a) Reciprocal space lattice of Be$(10\bar{1}0)$ surface, 2D Surface Brillouin Zone ($\overline{\Gamma A}$ = 0.877 Å^{-1} and $\overline{\Gamma M}$ = 1.375 Å^{-1}), b) Representation of the superperiodicity along $\overline{\Gamma A}$ direction, which corresponds to [0001] direction, for the flat surface and several vicinal surfaces, assuming nominal terrace lengths.*

the surface (due to the miscut) contains new symmetry points (primed), whose number and distribution depends on the step superlattice. New $\bar{\Gamma}'$ and $\bar{A}'$ points (located halfway between the $\bar{\Gamma}$ or $\bar{\Gamma}'$) appear. Depending on the actual new superperiodicity, a new $\bar{A}'$ point may or may not coincide with the old $\bar{A}$ point. $\overline{\Gamma M}$ direction ($[1\bar{2}10]$) corresponds to the direction along the steps. As the $(10\bar{1}0)$ face exhibits several surface states of different orbital origin (see below), it constitutes a good playground to understand the influence of the step superlattice on surface states.

3.2.1 Electronic structure of flat Beryllium surface

Flat beryllium surfaces have been studied since many years [106] [110] [111] [112]. The electronic structure of atomic Be (atomic number 4) is very simple: $1s^2 2p^2$. The electronic structure of bulk Be is dominated by the fraction of 1s electrons promoted to the 2p state [113]. The promotion is related to the actual position of the Fermi level in the density of states: bulk band calculations show that the Fermi level is situated in a dip of the density of states. On the other hand, the electronic structure of several high symmetry surfaces of Be has been investigated in detail [106] [114], and it has been found that the (0001) and $(10\bar{1}0)$ surfaces present several different surface states, accommodated in the different bulk band gaps of these surfaces. Due to the reduced bulk density of states, the electronic density of some of these surface states at the Fermi energy exceeds the bulk density of states at this energy. So, we may say that the surfaces of Be are more metallic than the bulk. The electronic structure of Be(0001) surface has received ample attention because it has a large and deep bulk band gap centred at $\bar{\Gamma}$, where a prominent surface state is observed. This state is described as a 2D electron gas. This surface state has been visualized in STM by the high amplitude of Friedel oscillations resulting from scattering of the surface electrons with defects and impurities [115]. The electron-phonon coupling constant has been determined from the dependence of the surface state line width with temperature [116]. Also the Be 1s core level has been analysed. It presents a complex line shape, due to the excitation of optical phonons in the photoemission process [116]. Moreover, large core level shifts have been observed experimentally and have been attributed to the different surface layers [117] [118]. Due to the large electron-phonon coupling constant, the beryllium surface is a good candidate to drive 2D superconductivity [119].

The electronic structure of the surface of $Be(10\bar{1}0)$ surface has been also the subject of several studies [106] [110] [111] [120] [121]. ARPES measurements for this surface have found several surface states in the gaps of the projected bulk density of states (Figure 3.5) [106]. The electronic states found are in good agreement with theoretical predictions [106] [121]. For normal and near normal emission ($\bar{\Gamma}$ area) there is a prominent surface resonance (SR), related to the bulk electronic states at the edge of the gap. It has sp_z character and behaves as an almost ideal 2D electron gas. From a fit to its parabolic dispersion an effective mass of 1.17 m_e is obtained, close to literature results for Be(0001).

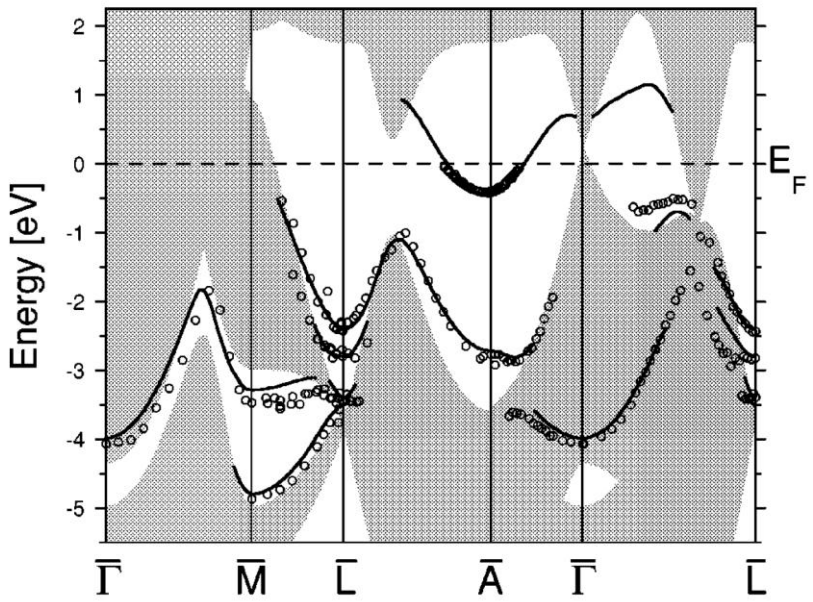

Figure 3.5 *Surface band structure of Be*$(10\bar{1}0)$ *along high symmetry directions, from Ref. [106].*

Two surface states are identified at the $\bar{M}$ point [106], with BEs of -3.3 and -4.8 eV, respectively. The first one coincides with the prolongation of the SR, and it has a p_x symmetry. A charge density maximum (CDM) of this state is located between the first and second atomic layers of the crystal. The second electronic surface state is related to a CDM at the third atomic layer, and it has the same symmetry as the upper state. Four surface states are found along $\overline{\Gamma L}$. All have p_x-p_y symmetry. Two Shockley like states (S1, S2) are found near $\bar{A}$ point. The state closer the Fermi edge (S1) state has s-p_z character, and its minimum BE is -0.46 eV, with an effective mass of 1.37 m_e. S1 state is localized at the top surface layer and it is nearly free electron like. The second electronic state (S2) has a binding energy of -2.7 eV at the $\bar{A}$ point, and its main orbital contribution is p_y. Its CDM comes mainly from the first layer (50%) and the rest from lower layers [122]. The electron phonon (e-p) coupling of the surface states S1 and S2 around $\bar{A}$ has been determined also [111]. Both states present a temperature dependent shift related to e-p coupling, but their behaviour is different. S1 state is 2D localized, due to a high e-p coupling. In turn, S2 is not purely 2D localized in the surface layer [111]. The surface state provides backbonding of the underlying atomic layer and it contributes to the large inward contraction of the surface [109]. The good knowledge achieved on the flat Beryllium surface offers favourable conditions to study an almost perfect two dimensional electron gas, and creates an ideal background to probe the effect of steps in its properties, exploiting the individual character of these states.

3.2.2 Electronic structure of vicinal Beryllium surface

In the case of a vicinal surface, new symmetry points appear between $\bar{\Gamma}$ points along the miscut direction. The two high symmetry directions were studied: $\overline{\Gamma A}$ (perpendicular to steps – $[0001]$ direction) and $\overline{\Gamma M}$ (along steps – $[1\bar{2}10]$ direction). Along both directions several surface states are seen close to the Fermi energy in the case of the flat surface $(10\bar{1}0)$, which are expected to be modified by the new periodicity. We foresee that the electronic structure will be affected by the periodic step potential, eventually leading to confinement effects. We present here the surface electronic structure found for the 4 different miscut angles (2.95, 4.48, 6.06, and 9 degrees).

3.2.2.1 Surface states on vicinal Beryllium surfaces

The spectra of the valence band of the vicinal beryllium surfaces (2.95º, 4.48º, 6.06º, and 9º) at normal emission (NE, $k_{\parallel}$ =0 Å $^{-1}$) are presented in Figure 3.6. It shows a previously reported [105] surface resonance (SR) for several photon energies. The minimum BE for the SR state is -4.00 ± 0.03 eV (for 2.95º miscut), -3.70 ± 0.03 eV (for 4.48º miscut), -4.02 ± 0.05 eV (for 6.06º miscut), and -3.95 ± 0.05 eV (for 9º miscut). T. Balasubramanian et al. [106] have reported a minimum BE of E_{min} = -4.07 ± 0.04 eV for the flat Be$(10\bar{1}0)$ surface in NE. Theoretical calculations predict a band gap just below the SR near $\bar{\Gamma}$. As the SR lies right at the edge of the gap, the intensity is high. In the rest of the BE scale there is no other band gap (subchapter 3.2.1), but between the SR state and the Fermi energy, there are several additional peaks, whose position and intensity depends on the vicinal surface. For the different miscut angles (2.95º, 4.48º, 6.06º, and 9º) these additional peaks are detected in normal emission in a wide range of the photon energies (15-75 eV) (see Figure 3.6). The intensity of the peaks changes with photon energy, which can be due to different reasons (final step superlattice diffraction effects in the perpendicular momentum, energy dependent cross sections). However, the BE of many of the peaks does not change with photon energy, suggesting a surface origin. A detailed analysis and interpretation and presented in the following sections.

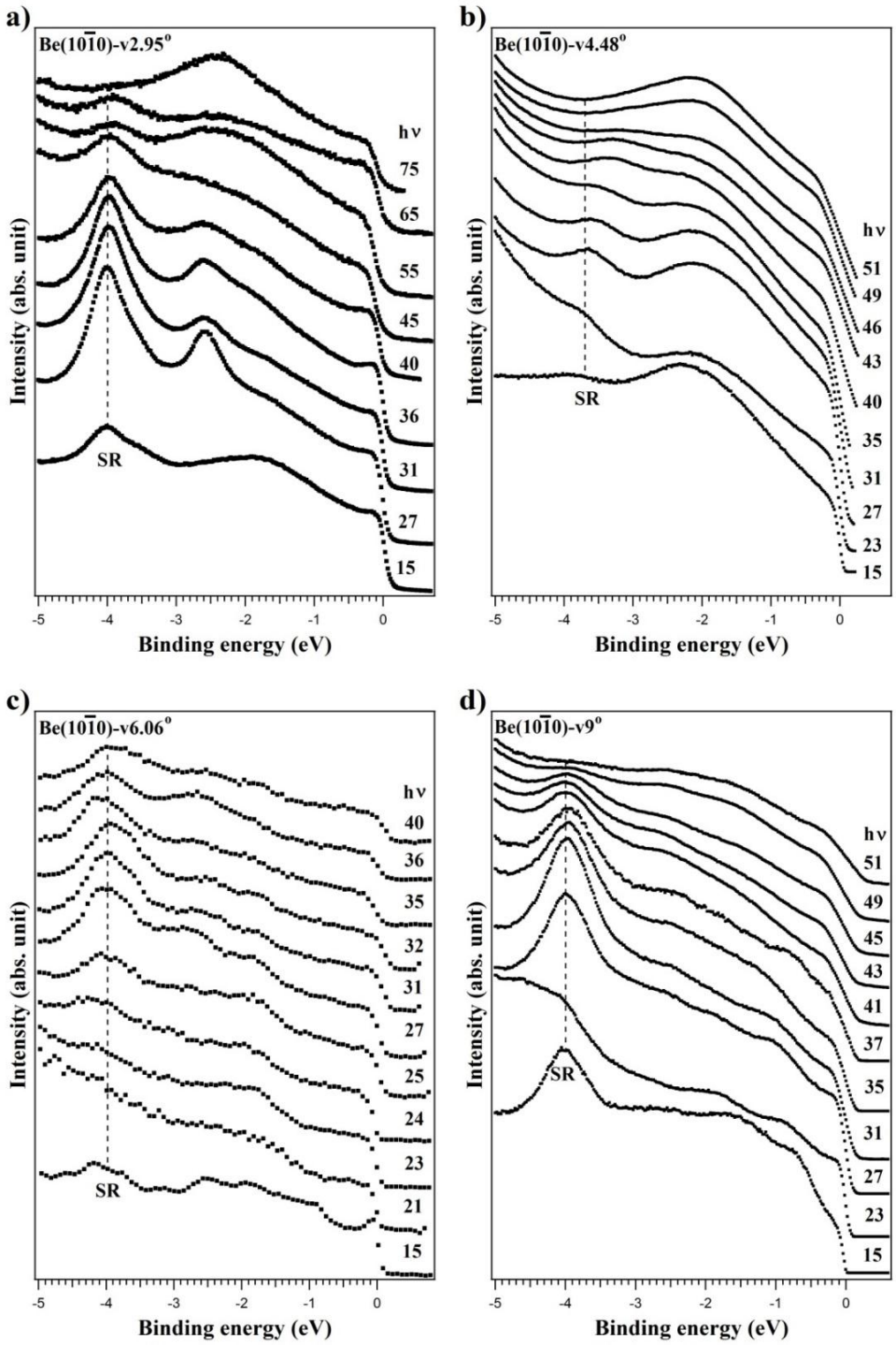

Figure 3.6 *Energy distribution curves for vicinal beryllium surfaces at normal emission for different photon energies.*

At the $\bar{A}$ point, there is a gap from the Fermi energy to -3.5 eV BE, which contains two high intense surface states. Their minimum BE changes with the miscut angle (Table 3.3 and Figure 3.7), so that going to larger miscut angles, the BE tends to decrease.

Crystal	S1 (eV)	S2 (eV)
$Be(10\bar{1}0)$	-0.38 ± 0.04	-2.73 ± 0.04
$Be(10\bar{1}0) - v2.95^{\circ}$	-0.32 ± 0.05	-2.63 ± 0.05
$Be(10\bar{1}0) - v4.48^{\circ}$	-0.30 ± 0.05	-2.62 ± 0.05
$Be(10\bar{1}0) - v6.06^{\circ}$	-0.27 ± 0.07	-2.60 ± 0.07
$Be(10\bar{1}0) - v9^{\circ}$	-0.21 ± 0.05	-2.55 ± 0.05

Table 3.3 *Surface states at $\bar{A}$ point for the different miscut angles.*

The energy shift of S1 and S2 to lower values is presented in Figure 3.7a at the $\bar{A}$ point. For each crystal, the EDC correspond to the extreme BE values (maximum or minimum) for states S1 and S2. The dispersion of S1 and S2 states around the $\bar{A}$ point for a vicinal beryllium surface with miscut angle 6.06º at hν = 24 eV is shown Figure 3.7b.

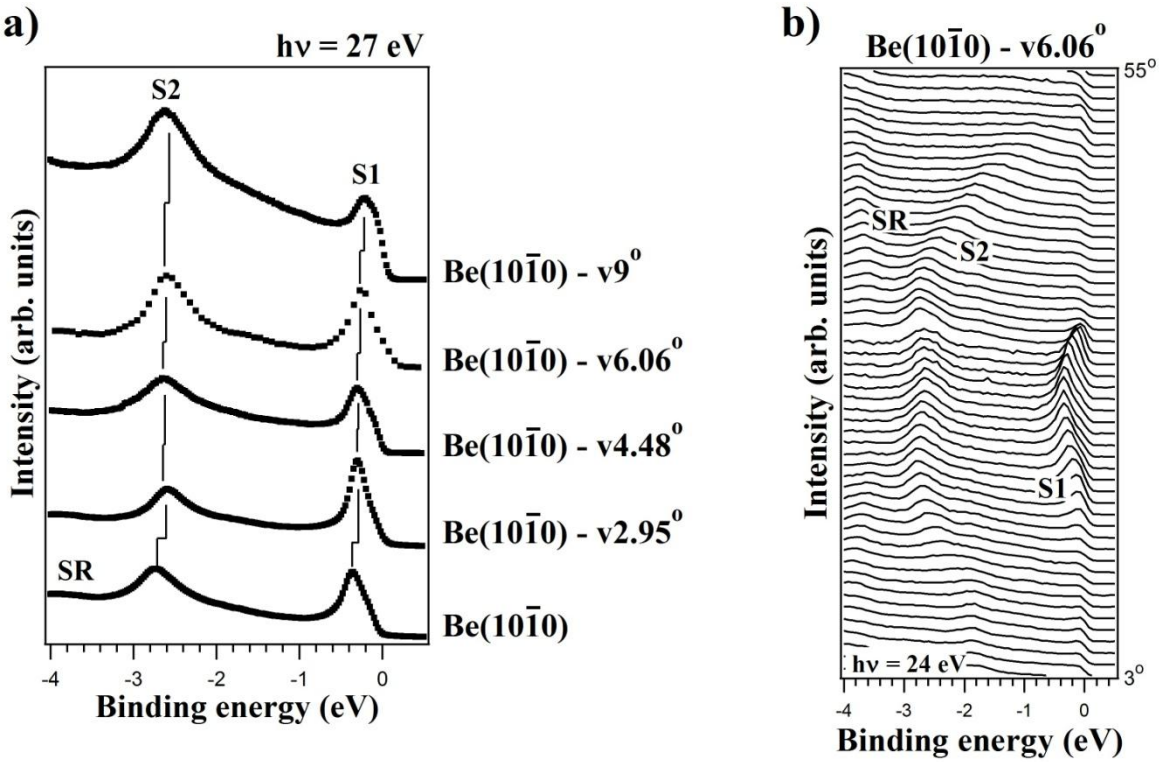

Figure 3.7 *a) Energy distribution curves at the $\bar{A}$ point for photon energy 27 eV. Vertical lines highlight the shift of the surface states for different vicinal beryllium surfaces; b) Surface band dispersion of S1 and S2 states around the $\bar{A}$ point for 6.06º miscut at hν = 24 eV.*

Figure 3.8 shows a structure plot, where the parallel momentum at which the minimum of the surface band S1 is reached is represented vs. the perpendicular momentum. As the parallel momentum is a conserved magnitude (when measured with respect to the surface plane relevant for the wave function), this plot reveals which is the conservation plane involved. Thus, in the case of Figure 3.8a the parallel momentum with respect to the optical surface is not a conserved magnitude, as it changes with the perpendicular momentum. In turn, when the parallel momentum is measured with respect to the terrace orientation the experimental points follow a vertical line, indicating that the parallel momentum thus defined is a conserved magnitude, and that the terrace plane is the relevant plane for the wave function. Finally, at the $\overline{M}$ point, the gap extends between -3 and -5 eV BE. The gap contains two surface states. The shallower one is seen at -3.3, -3.5, and -3.6 eV BE for miscut angles of 2.95, 4.48º, 6.06º, and 9º, respectively.

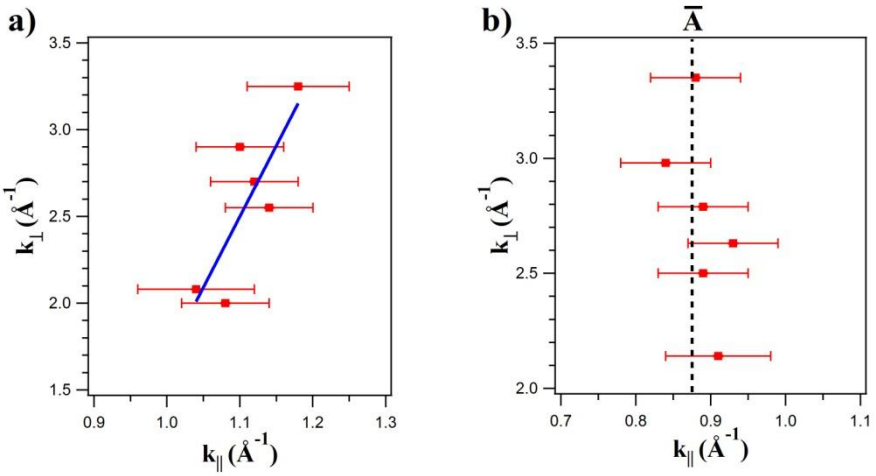

Figure 3.8 *Structure plot showing the parallel momentum at which the minimum of the surface band S1 is reached vs. the perpendicular momentum. a) parallel momentum is referred to the optical surface (the blue line is a linear fit to the data) b) same, but with parallel momentum referred to the terrace orientation ($\bar{A}$ point is taken from Ref. [106]).*

3.2.2.2 Electronic structure along $\overline{\Gamma A}$ direction

Energy vs. momentum representations along $\overline{\Gamma A}$ direction, which corresponds to dispersion perpendicular to the steps, are shown in Figure 3.9 for four Be vicinal surfaces. All drawings are corrected, so that angles are referred to the terrace direction. The most intense

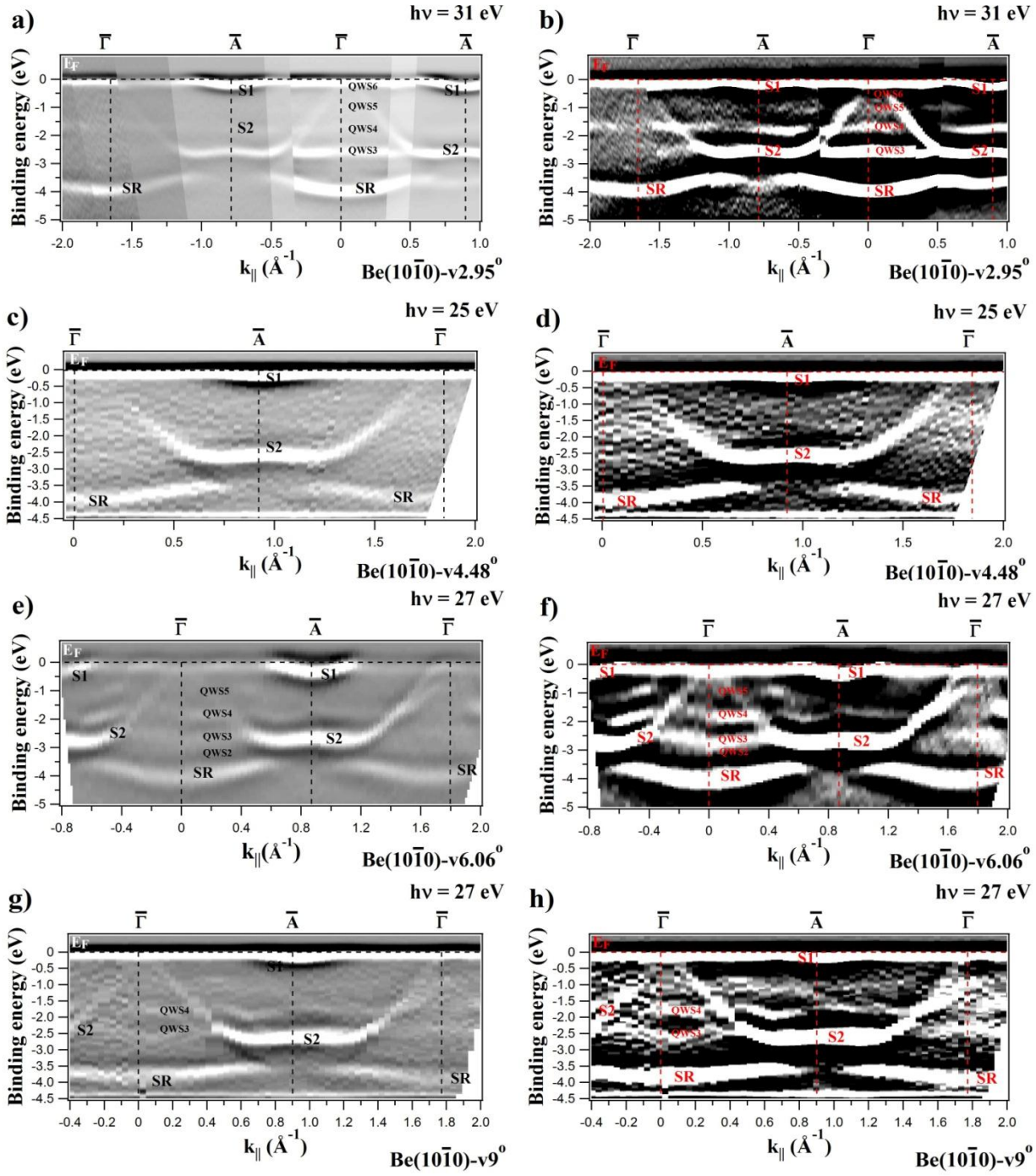

Figure 3.9 *Energy vs. momentum plots along the direction perpendicular to steps ($\overline{\Gamma A}$) for $Be(10\bar{1}0) - v2.95^{\circ}$ at hν = 31 eV, $Be(10\bar{1}0) - v4.48^{\circ}$ at hν = 25 eV, $Be(10\bar{1}0) - v6.06^{\circ}$ at hν = 27 eV, and $Be(10\bar{1}0) - v9^{\circ}$ at hν = 27 eV. Left column, second derivative data with no filtering; right column, same data with a noise filter and increased contrast. This treatment enhances the observation of weak features, like the QWS.*

band is the SR state, seen near -4 eV BE for NE and dispersing with quasi-parabolic shape along $\overline{\Gamma A}$ direction, as it was observed for the flat surface $Be(10\bar{1}0)$ [111]. At the $\bar{A}$ point, the S1 band is seen very close to the Fermi energy and crossing near $\bar{A}$, also in agreement with previous reports for the flat surface [106] [108]. S1 disperses with an effective mass of 1.37 m_e in a narrow range of reciprocal space (±0.02 $Å^{-1}$).

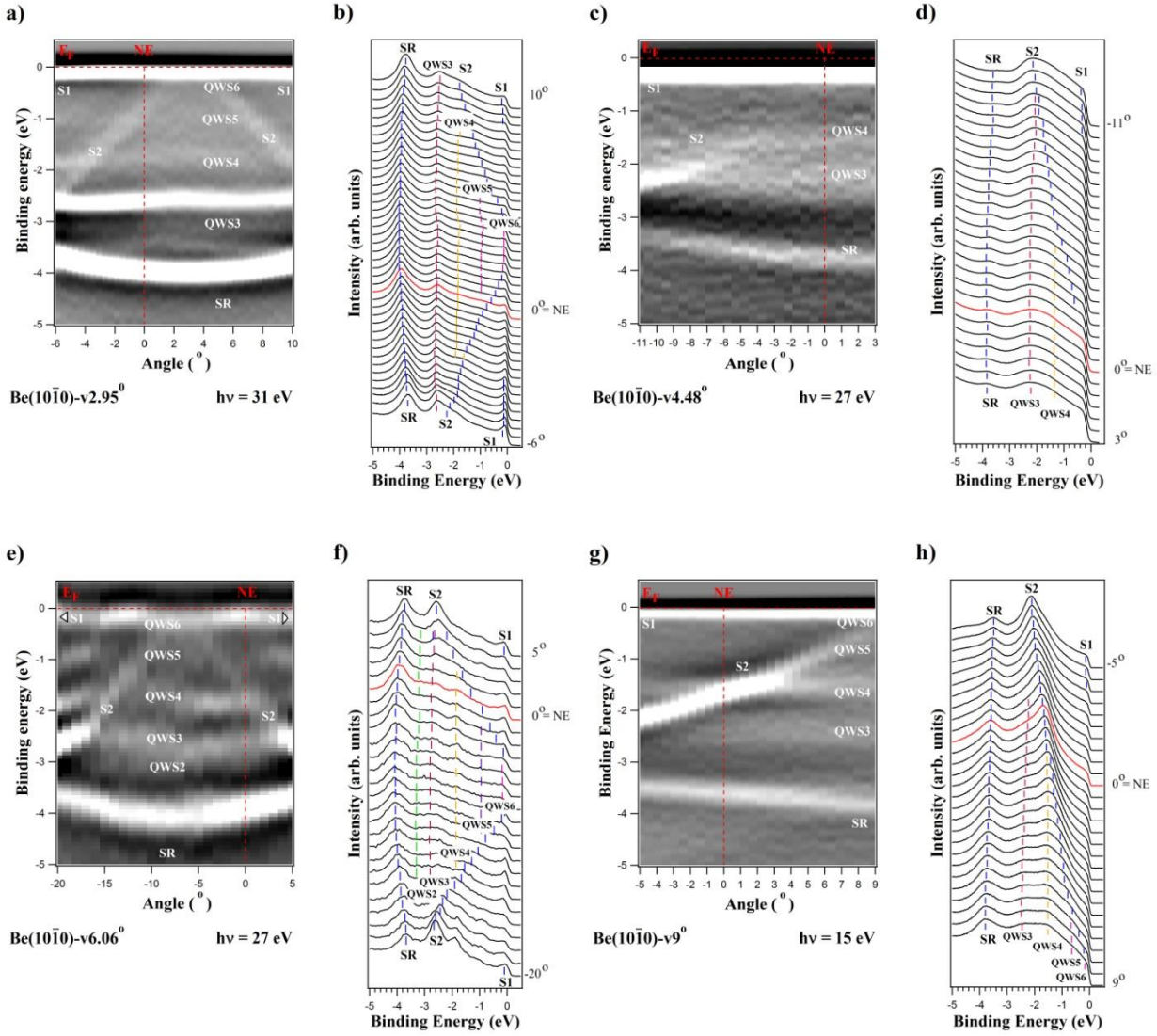

Figure 3.10 *Band dispersion perpendicular to the steps ($\overline{\Gamma A}$ direction) for* $Be(10\bar{1}0) - v2.95^{\circ}$*(a,b),* $Be(10\bar{1}0) - v4.48^{\circ}$ *(c,d),* $Be(10\bar{1}0) - v6.06^{\circ}$*(e,f),* $Be(10\bar{1}0) - v9^{\circ}$*(g,h). Each state is denoted with a different colour: blue tics – SR, S2, S1; green tics – QWS2 state; dark red tics – QWS3 state; yellow tics – QWS4 state; violet tics – QWS5 state; pink tics – QWS6 state. Angles in this figure refer to the average optical surface.*

The second surface state S2 has quasi-parabolic shape and arms approaching the Fermi energy near $\bar{\Gamma}$ and crossing it.

Between the SR state minimum and the Fermi level, several new states are observed around $\bar{\Gamma}$ point, labelled as QWS1, QWS2, QWS3, QWS4, QWS5, QWS6 in Figure 3.9a. These bands do not disperse along $\overline{\Gamma A}$ in the reciprocal momentum region where they are observed. For different photon energies, some of the bands are more intense.

Figure 3.10 shows a closer view of the dispersion of the new states perpendicular to the steps (along $\overline{\Gamma A}$ direction) for the different miscut angles.

3.2.2.3 Electronic structure along $\overline{\Gamma M}$ direction.

Energy vs. momentum representations along $\overline{\Gamma M}$ direction, which corresponds to dispersion along the steps, are shown in Figure 3.11 for four Be vicinal surfaces. The measurements were done for several photon energies, although only data at 31 eV photon energy are shown here. The most intense band is the SR state, seen near -4 eV BE for NE and dispersing with parabolic shape along $\overline{\Gamma M}$ direction. The arms of the parabola have a maximum radius of 0.93 $Å^{-1}$. Around $\bar{\Gamma}$ point, several additional minima closer to the Fermi energy are seen, the first one being at -3 eV BE at $\bar{\Gamma}$. All the additional bands seen at $\bar{\Gamma}$ are also seen in measurements along $\overline{\Gamma A}$ direction. However, the dispersion of these bands along $\overline{\Gamma A}$ was flat, while they have parabolic dispersion along $\overline{\Gamma M}$. The vicinal character of the surface does not affect this free-electron dispersion along the step direction. The intensity of these states depends on the photon energy, as mentioned in the previous subsection.

As expected for one-dimensional confinement, the new states present a different dispersion along the steps and perpendicular to them. This is highlighted in Figure 3.12, which shows a closer view of the dispersion of the new states along steps ($\overline{\Gamma M}$ direction) for the different miscut angles.

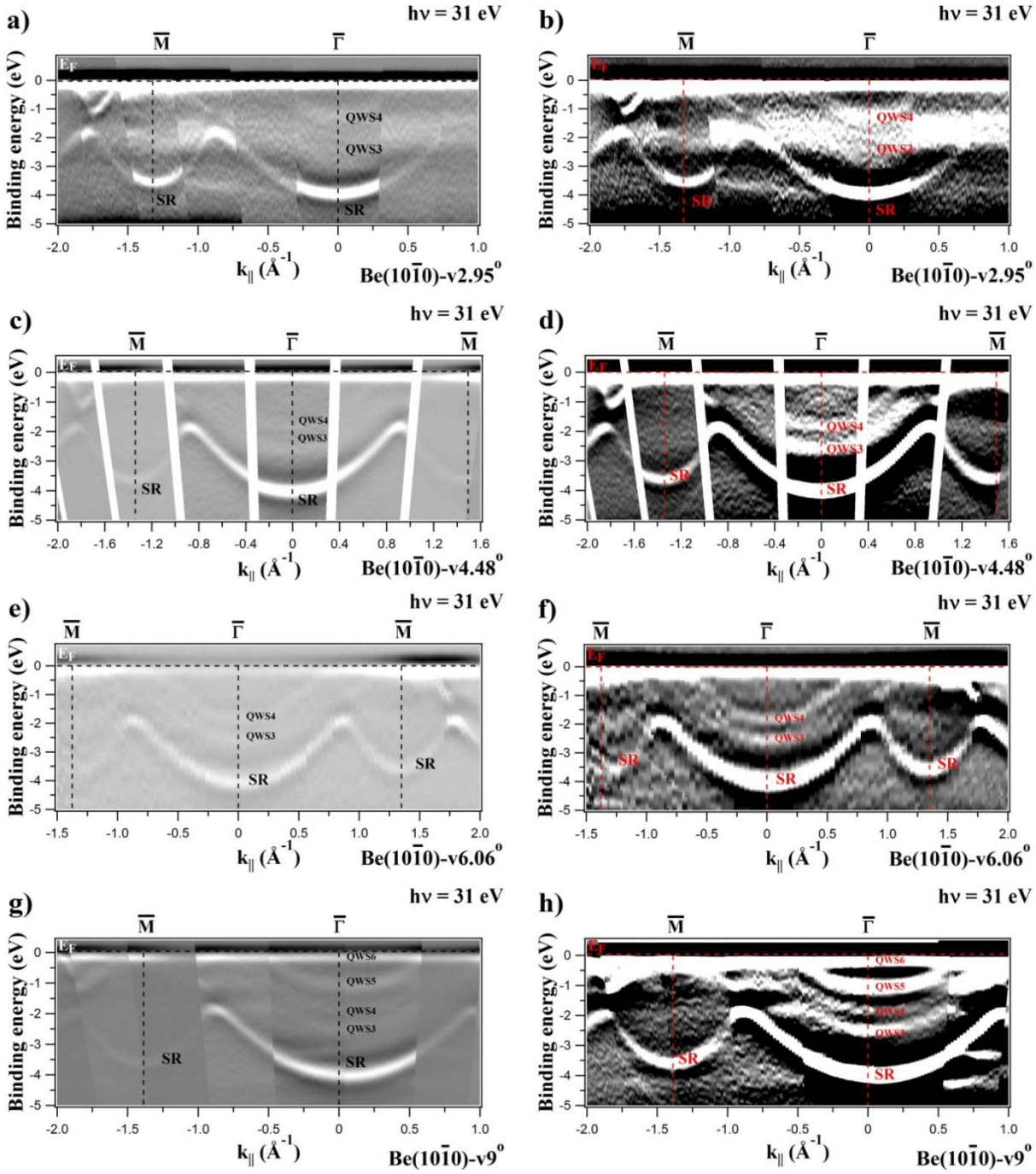

Figure 3.11 *Electronic band structure along steps ($\overline{\Gamma M}$ direction) at $h\nu$ = 31 eV for: $Be(10\bar{1}0) - v2.95^{\circ}$ (a), $Be(10\bar{1}0) - v4.48^{\circ}$(c), $Be(10\bar{1}0) - v6.06^{\circ}$(c), and $Be(10\bar{1}0) - v9^{\circ}$(g). Left column, second derivative data with no filtering; right column, same data with a noise filter and increased contrast. This treatment enhances the observation of weak features, like the QWS.*

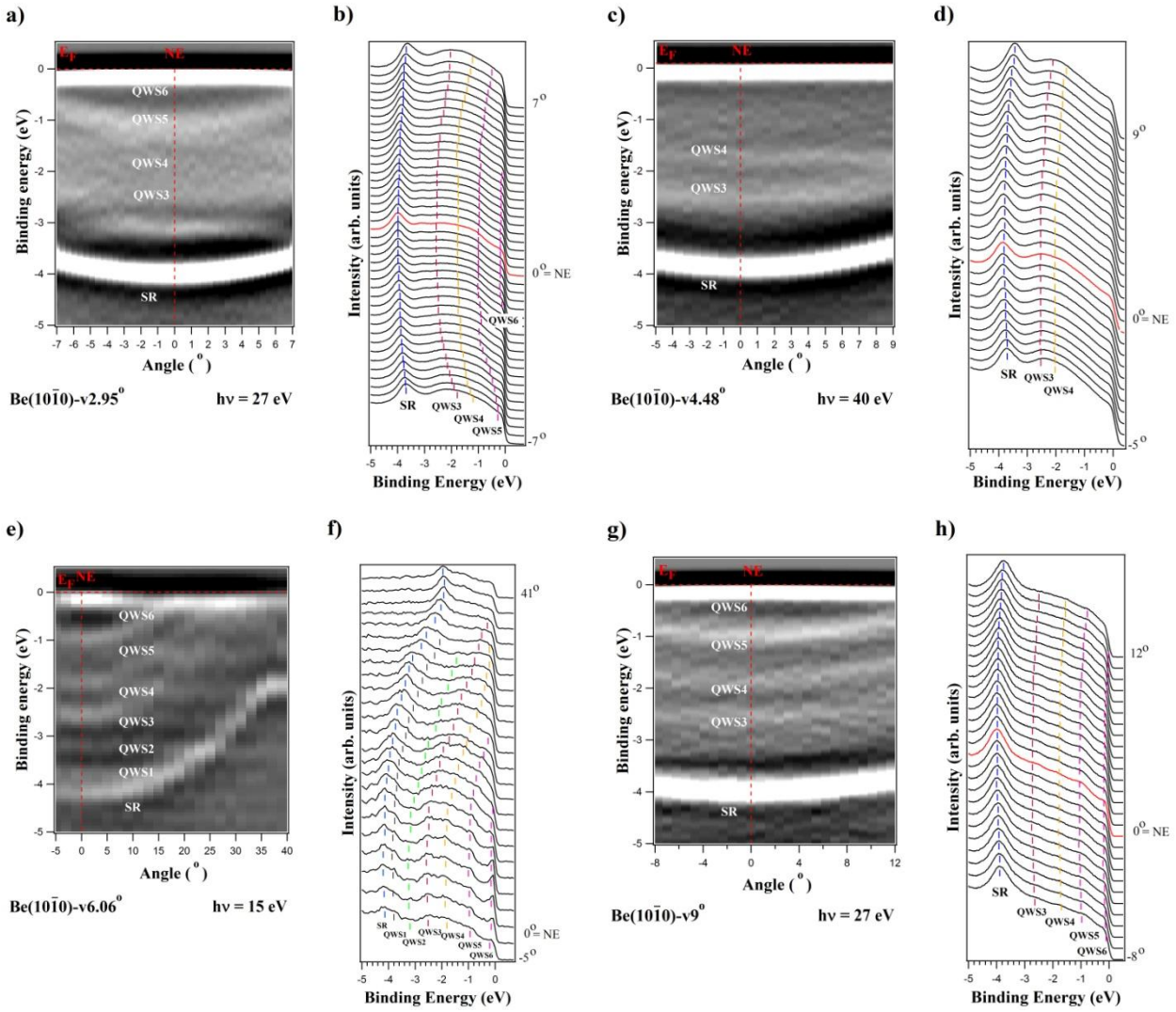

Figure 3.12 *Band dispersion along the steps ($\overline{\Gamma M}$ direction) for* $\mathrm{Be}(10\bar{1}0) - v2.95^{\circ}$*(a,b),* $\mathrm{Be}(10\bar{1}0) - v4.48^{\circ}$ *(c,d),* $\mathrm{Be}(10\bar{1}0) - v6.06^{\circ}$*(e,f),* $\mathrm{Be}(10\bar{1}0) - v9^{\circ}$*(g,h). Each state is denoted with a different colour: blue tics – SR, S2, S1, grey tics – QWS1 state, green tics – QWS2 state, dark red tics – QWS3 state, orange tics – QWS4 state, violet tics – QWS5 state, pink tics – QWS6 state.*

Figure 3.13 shows the region of 22-42º emission angle along $\overline{\Gamma M}$ at hν = 15 eV (range of 0.6 – 1.2 $Å^{-1}$ in reciprocal momentum scale). The minimum of the new band QWS2 does not coincide with the maximum of the SR band. The deviation is 0.072 ± 0.032 $Å^{-1}$.

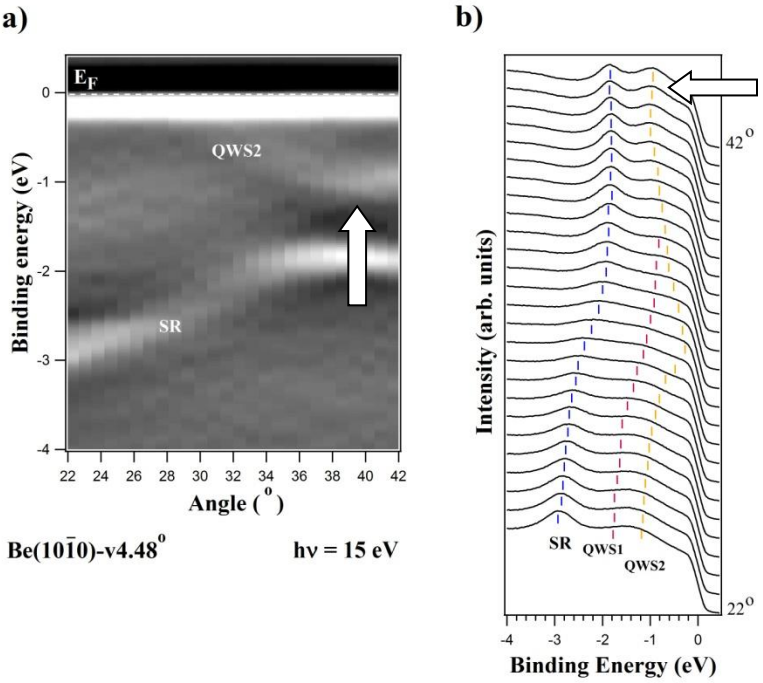

Figure 3.13 *Dispersion of the QWS2 in the half of the* $\overline{\Gamma M}$ *direction with a shifted minimum for* $Be(10\bar{1}0) - v4.48^{\circ}$ *at 15 eV.*

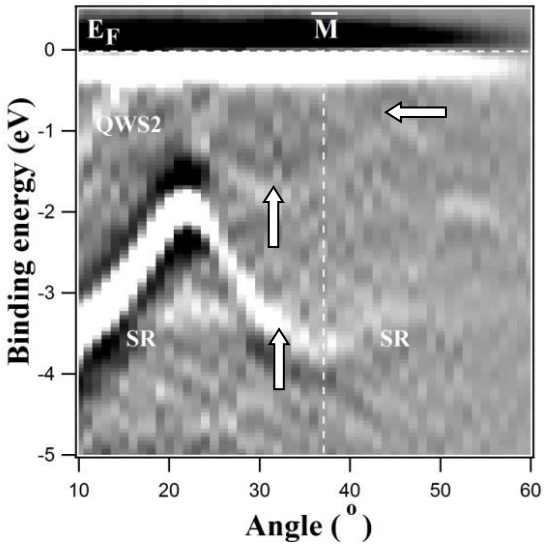

Figure 3.14 *Dispersion of the surface resonance band (SR) and of a QWS band above around the* $\bar{M}$ *point at* $h\nu$ *= 31 eV for* $Be(10\bar{1}0) - v6.06^{\circ}$.

Figure 3.14 shows the minimum of the SR band at the $\bar{M}$ point at -3.5 eV BE (shown for 6.06º and seen also for 2.95º, 4.48º, and 9º miscut). The band is very intense and it is seen for most photon energies. For some photon energies, a second weak minimum of a QWS band is also seen (Figure 3.14). For selected photon energies, the QWS band is seen for a range

of reciprocal space. Its dispersion mimics the behaviour of the SR band (Figure 3.14). There is an apparent shift in the angular scale, which does not appear in momentum representation. The minimum binding energy is around -1.5 eV (for the two vicinal surfaces: $\mathrm{Be}(10\bar{1}0) - v6.06^{\circ}$ $\mathrm{Be}(10\bar{1}0) - v9^{\circ}$).

For hν = 40 eV an additional band is seen crossing the Fermi level at $\bar{\mathrm{M}}$ for $\mathrm{Be}(10\bar{1}0) - v6.06^{\circ}$ (Figure 3.15a). It disperses with photon energy along $\overline{\Gamma\mathrm{M}}$.

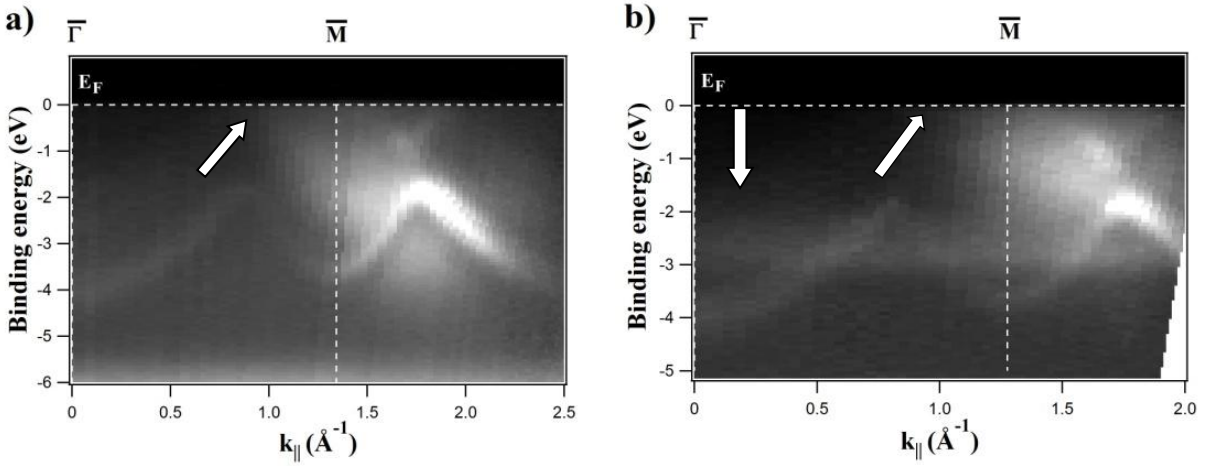

Figure 3.15 *Bulk bands along the $\overline{\Gamma\mathrm{M}}$ direction: a) the bulk band crossing the Fermi level at half distance of that direction for $h\nu$ = 40 eV and $Be(10\bar{1}0) - v6.06^{\circ}$; b) the bulk band at BE -2.8 eV for $h\nu$ = 36 eV. All bulk bands were observed for $Be(10\bar{1}0) - v6.06^{\circ}$.*

It corresponds to a bulk band of beryllium. Also, another bulk band appears at -2.8 eV BE for hν = 36 eV with a straight dispersion along that direction (Figure 3.15b).

3.3 Discussion

The electronic structure observed can be interpreted considering the vicinal character of the surfaces. The minimum of the SR band is not in the optical normal emission, but in the terrace direction. The same effect is seen for the minimum of S1 surface state. This behaviour indicates that the electron wave function is referred to the terrace direction, and not to the average optical surface.

Several new electronic states are seen at $\bar{\Gamma}$ point, between the SR state and the Fermi edge. Their absolute intensity is moderate, but they are well visualized in second derivative

images. These states do not disperse with photon energy. Only their intensity changes, what can be attributed to different reasons, like final state step superlattice diffraction effects or energy dependent cross sections. Different states with different BEs are seen for each vicinal surface. Their most important feature is that they do not disperse with parallel momentum along the direction perpendicular to steps. In turn they exhibit a parabolic dispersion with parallel momentum along the steps. These features mean that the new electronic states are delocalized along the terraces, but confined by the step superlattice.

All the described properties of the new states are in agreement with the formation of one dimensional quantum well states (QWS) related to the quantization of SR band in stepped surfaces. Perpendicular to the steps, the quantum well states are not dispersing in the range ±0.2 $Å^{-1}$ from the $\bar{\Gamma}$ point (Figure 3.10). Along steps, the quantum well states exhibit free electron like dispersion at least in a range of ±0.6 $Å^{-1}$ from $\bar{\Gamma}$ point (Figure 3.12). Thus, the electrons are confined along $\overline{\Gamma A}$ direction and delocalized along $\overline{\Gamma M}$ direction. Their intensity depends on photon energy.

It is well known that two-dimensional quantum well states can be experimentally realized in thin films [115] [123] [124] [125] [126] due to the vertical confinement of electrons. One dimensional (1D) quantum well states have been observed in vicinal surfaces [127] [128] due to the lateral confinement of the electrons by the step superlattice. Figure 3.16 presents a schematic representation of quantum well states (QWS) totally confined in a terrace. Steps represent a barrier for the electrons. Note however that in Figure 3.16 QWSs are confined in a terrace with two different kinds of steps, what is at variance with the behaviour described for noble metal surfaces. As already mentioned, this is related to the nature of the stacking in the hcp lattice, which gives rise to two different kinds of steps. Due to the two different steps, the structural periodicity is achieved for a terrace such as shown in Figure 3.16. Note however that ARPES provides no direct evidence about the nature of the steps in vicinal Be surfaces. It is possible that in fact double height steps are formed or that the two different steps are locally bunched. It is also possible that there is a large difference in transmission coefficient for each of the two types of steps, so that one type would be mostly transparent to electrons, and the other type would be mostly reflecting the electrons. In any case, we conclude (see below) that the effective periodicity generating the QWS is the total terrace length. In the extreme case of confinement, electrons may be totally trapped in the well between two steps, generating a series of quantum well states. Due to the lateral confinement, the QWS do not disperse in the direction perpendicular to the steps (flat bands) and are delocalized along the (parabolic dispersion).

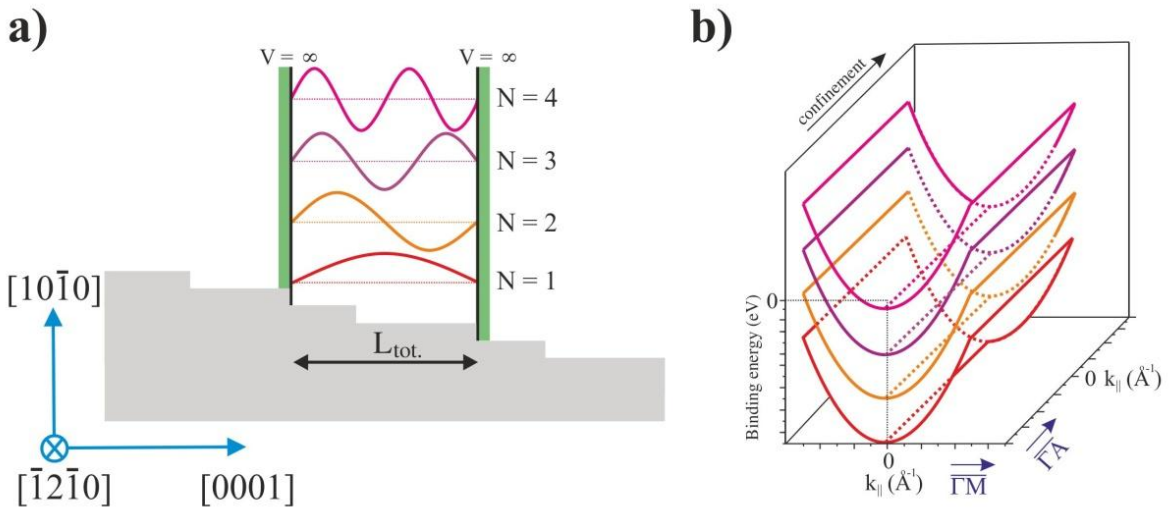

Figure 3.16 *Scheme of the electron wave functions in an infinite potential well, (a) schematic representation of the formation of 1D QWS in a beryllium vicinal surface. (b) 2D dispersion of 1D QWS showing confinement along $\overline{\Gamma A}$ direction and dispersion along $\overline{\Gamma M}$.*

In view of the qualitative observation of this kind of behaviour, we assume as a first approach a full confinement by the steps. In this case, the expression giving the binding energies of QWS in an infinite well can be used:

$$E_N = E_0 + \frac{\hbar^2}{2m^*}\frac{\Pi^2}{d^2}N^2 \qquad \text{Eq. 3.1}$$

where: E_N – n-energy of the quantum well state.

N – number of quantum state, N=1,2,3…N.

E_0 – initial energy, it corresponds to the minimum of the surface resonance.

$\hbar$ - Planck's constant.

m^* - effective mass of the surface resonance band.

d – width of quantum well/width of terrace.

Table 3.4 collects the QWS seen for each vicinal BE surface. Note that the QWS seen for the two smaller angles (2.95º and 4.48º) are weaker and less defined, and in some cases are only distinguished in second derivative images. On the other hand, LEED patterns for these

surfaces show diffuse spots. Due to this fact we did not try to fit these QWS with the model above.

Crystal	Terrace size (Å, LEED)	QWS1 (eV)	QWS2 (eV)	QWS3 (eV)	QWS4 (eV)	QWS5 (eV)	QWS6 (eV)
$Be(10\bar{1}0) - v2.95^{\circ}$				-2.5 ± 0.05	-1.80 ± 0.05	-0.93 ± 0.03	-0.18 ± 0.03
$Be(10\bar{1}0) - v4.48^{\circ}$				-2.39 ± 0.04	-1.74 ± 0.05		
$Be(10\bar{1}0) - v6.06^{\circ}$		-3.78 ± 0.07	-3.15 ± 0.07	-2.78 ± 0.04	-1.68 ± 0.05	-0.89 ± 0.03	-0.14 ± 0.03
	d = 18.76 Å	[N=1, -3.9]	[N=3, -3.2]	[N=4, -2.57]	[N=5, -1.76]	[N=6, -0.76]	-
$Be(10\bar{1}0) - v9^{\circ}$			-3.2 ± 0.05	-2.69 ± 0.05	-1.75 ± 0.04	-1.03 ± 0.04	-0.17 ± 0.03
	d = 14.6 Å		[N=2, -3.35]	[N=3, -2.6]	[N=4, -1.56]	-	[N=5, -0.21]
	d = 25.9 Å		[N=4, -3.19]	[N=5, -2.76] [N=6, -2.24]	[N=7, -1.62]	[N=8, -0.91]	[N=9, -0.10]

Table 3.4 *Quantum well states detected for the different vicinal surfaces compared to expected values for an infinite well model using the LEED terrace width.*

Periodicities deduced from LEED (see Table 3.2 for more details) appear in the first column. The other columns collect experimental values and calculations made using Eq. 3.1 (in brackets) for an infinite well and the terrace size obtained from LEED patterns (Table 3.2). The agreement is satisfactory for the 6º crystal, where all experimental QWS are reproduced using a single terrace size, although the N = 2 value is not observed. The agreement is also satisfactory for the 9º crystal, where most QWS are explained using the two terrace sizes seen in LEED. The agreement is not perfect, but this is not surprising as the model is based on the assumption of an infinite potential well and a perfectly regular terrace distribution.

We conclude that QWS are observed for two of the four sample orientations used. Their binding energies are reasonably explained from an infinite potential well model. The two other orientations analysed (corresponding to the largest terrace sizes) did show QWS, but the quality of the LEED patterns was not sufficient to determine the average terrace size and to explain the binding energies seen using a simple model.

3.4 Summary

A rectangular LEED pattern is observed for all samples, in agreement with a vicinal $(10\bar{1}0)$ surface. Split spots appear predominantly along $\overline{\Gamma A}$ direction, indicating an overall good and regular step superlattice. Weaker spots along $\overline{\Gamma M}$ direction indicate a minor contribution of facets and/or imperfections.

Photoemission spectroscopy is used to characterize the electronic structure of the vicinal beryllium surfaces. Monitoring of the core levels indicates a good degree of cleanliness. Scans along steps and perpendicular to steps for several photon energies allowed us to obtain an almost a full characterization of the surface electronic structure.

We identified the surface resonance band (SR), which also exists at the flat $(10\bar{1}0)$ surface. The surface state at the $\bar{A}$ point lies at shallower binding energies than for the flat surface, as expected for confinement by the step superlattice. An analysis of the position of the minimum of this surface state and of the SR vs. photon energy reveals that the electron wave function is referred to the terrace direction and not to the average optical surface.

At the $\bar{\Gamma}$ point, we observe additional electronic states identified as QWS. As an expected, the QWS do not disperse along $\overline{\Gamma A}$ direction and exhibit a free electron like behaviour along $\overline{\Gamma M}$ direction.

Most of the QWS observed for the 9º and 6º vicinal samples could be explained using a simple infinite well model

4. Surface electronic structure of A_{III}–B_V semiconductors and its temperature dependence

A_{III}-B_V semiconductors like gallium arsenide (GaAs), indium arsenide (InAs), and indium antimonide (InSb), are currently used in many applications, as data communication technology, solar energy conversion, thermal imaging, lighting, and others [129]. Particular milestones are the hybrid InSb-Si transistor, anticipated as future extension of silicon based MOSFET technology [130] [131] and devices operating in terahertz frequency domain [132] [133].

Recent findings have also demonstrated the large potential of these materials in other areas, e.g. as substrates for growth of magnetic structures [134], or for assembling of molecular nanostructures [135] [136] [137]. Besides those important applications, the surfaces of A_{III}-B_V semiconductors are by themselves low dimensional systems with a rich physical phenomenology [138]. In particular, the (001) face, frequently used in device technology, displays several different stoichiometry-dependent reconstructions (surface phases), whose properties have been investigated for a long time [139]. Several of those properties are well understood, but the comprehension of other features is a matter of current work [140] [141]. The c(8x2) surface phase is found for (001)-oriented InSb, InAs and GaAs, prepared either by annealing of molecular-beam-epitaxy (MBE)-grown surfaces or by ion sputtering and annealing of epiready wafers [21]. This reconstruction has been the subject of a continued interest and there exists a widely accepted model (the so-called ζ–model) describing its structure. The ζ-model was proposed independently by Lee et al. [142] and Kumpf et al. [143] [144], and was confirmed later on by different experimental techniques [145] [146] [147] [148]. According to the ζ–model the surface top bilayer has a symmetry close to (4x1) and the dominant features on the surface are A_{III}-atom rows running parallel to the [110] direction. The c(8x2) superstructure is due to A_{III}-atom dimers in the second bilayer of the crystal.

The ζ–model contains a significant number of vacancies [143] [144], whose concentration depends on the specific substrate (InSb, InAs or GaAs). STM work has found that the surface of InSb(001) exhibits important structural changes upon decreasing the temperature [146], which are traced back to temperature induced vacancy ordering [147] [149] [150] [151].

In this chapter a full surface electronic structure characterization of the selected A_{III}-B_V semiconductors is presented, namely InSb and InAs (001) faces with a c(8x2) reconstruction. In the section 4.1, the crystalline structure of these semiconductors and of the c(8x2) reconstruction is described. Next section is devoted to the surface and bulk electronic band structure of high-quality samples, characterized at room temperature and down to 5 K. Several different surface states are identified and their relationship with the c(8x2) reconstruction is described. The temperature dependence of the surface electronic band structure is also analysed, taking into account previously reported structural modifications of the surface [147] [148] [152]. In the case of InAs, the properties of the quantum well states formed in the surface accumulation layer are also described. The conclusion for both semiconductors is summarized in the subsection 4.2.3 and section 4.4.

4.1 Crystalline structure of A_{III}-B_V semiconductors and their c(8x2) surface reconstruction

A_{III}-B_V semiconductors have been widely studied and their properties are well known due to their many technological applications in fields like electronics and optoelectronics. The way of growing the crystals and their preparation is common. A_{III}-B_V semiconductors are synthesized using elements from 3rd (Ga, In, etc.) and 5th (As, Sb) group of the periodic table. A_{III}–B_V crystals present the zincblende structure (Figure 4.1a). The structure has a cubic, closely packed (face centred) array of B_V – atoms and A_{III} – atoms are located in tetrahedral (1/2 occupied) sites, giving a conventional unit cell with 4 A_{III} – atoms (red balls) and 4 B_V – atoms (blue balls). Each B_V – atom is surrounded tetrahedrally by 4 A_{III} – atoms.

The 001 face of the zincblende structure (Figure 4.1b) has a square surface unit cell with a lattice constant a_{InSb} = 6.4794 Å for InSb and a_{InAs} = 6.0584 Å for InAs. The (100) face of A_{III}-B_V semiconductors presents a rich surface phase diagram, with several different, stoichiometry-dependent reconstructions (surface phases) [138]. The different phases appear depending on the preparation conditions. Thus, the c(8x2) surface reconstructions, typical for the investigated semiconductors, can be obtained by ion sputtering and annealing of the crystal [21]. The (100) face can be prepared using other methods (e.g. molecular beam epitaxy), which usually lead to other type of surface reconstructions [153] [154]. A structural model of the c(8x2) reconstruction was presented simultaneously by Lee [142] and Kumpf

[143]. This so called "ζ–model" (Figure 4.2) is based on the existence of subsurface A_{III} dimers.

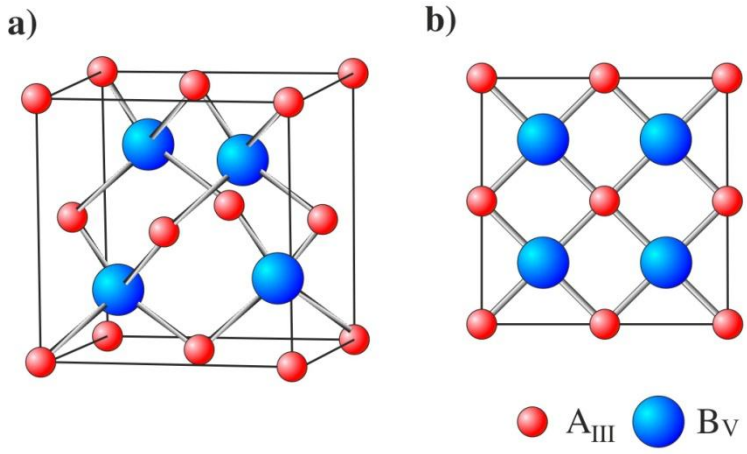

Figure 4.1 *a) Ball model of the zincblende structure of A_{III} – B_V crystals; b) (001) face of the zincblende structure.*

The structure contains two different chains of surface atoms along the [110] direction (vertical direction in Figure 4.2). In the first chain B_V – atoms are located at bulk positions (Sb7,8); on top of that chain, an additional chain of A_{III} – atoms (In1) running parallel to [110] direction, are bond with B_V – atoms (Sb6). In the second chain B_V atoms are shifted with respect to B_V bulk position.

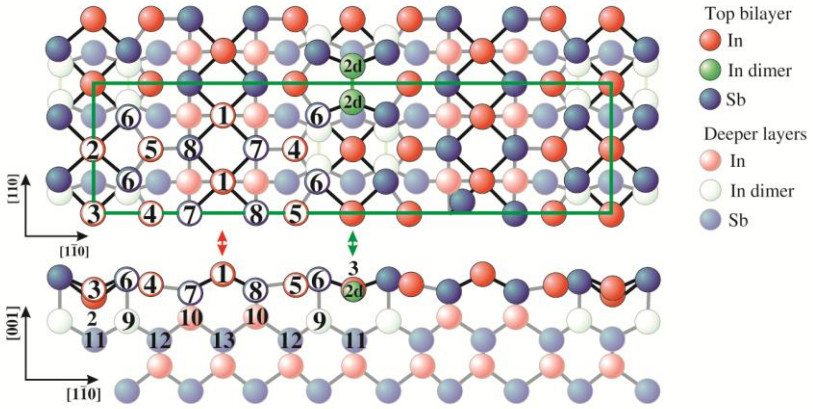

Figure 4.2 *Structural ζ-model for a c(8x2) reconstruction of the (001) face of A_{III} – B_V semiconductors (A_{III} – atoms in red, B_V – atoms in violet, A_{III} dimers in green). Numbers refer to specific types of atoms in the reconstruction, according to the labelling made in Ref. [143].*

The resulting surface top bi-layer has a (4x1) unit cell. Each A_{III} – atom in the second bi-layer has two bonds to B_V – atoms at the surface. The c(8x2) superstructure is due to A_{III} – atom dimers (In6) in the second bi-layer of the crystal. The final surface structure is obtained by repetition of the basic (4x2) unit [143]. In addition to this, there are A_{III} dimers in the first bilayer (In2d).

The model described above has been confirmed by several experiments [143] [145] [146] [155] [156] [157]. In particular, STM investigations support clearly an A_{III} – atom termination of the c(8x2) surface, forming one dimensional rows along [110] direction (Figure 4.3).

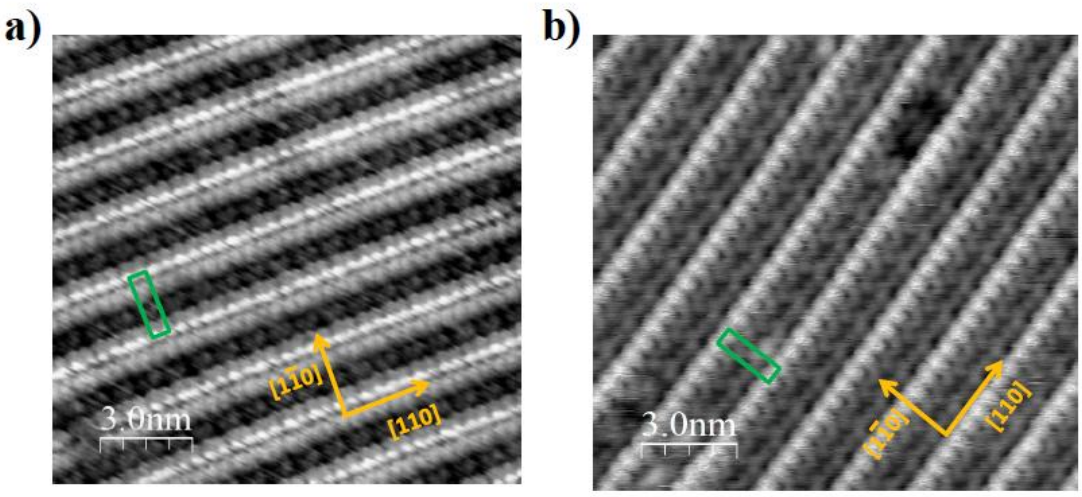

Figure 4.3 *a) STM image of InSb(001)-c(8x2) surface obtained at room temperature (image area 30x30 nm^2, scanning parameters: V_b = -0.75 V, I = 100 nA). b) STM image of InAs(001)(4x2)-c(8x2) surface obtained at room temperature (image area 30x30 nm^2, scanning parameters: V_b = -0.7 V, I = 100 nA) (green rectangles indicate unit cells of the patterns).*

The grey protrusions (clearly seen in the Figure 4.3) located in between bright chains of dot-like corrugations are B_V atom dangling bond states. STM images of the surface with various bias voltages provide different contrasts [158]. Most changes are seen in the low range of voltages, revealing the positions of atoms denoted by numbers 3-4-5 (In) and/or the bonds 4-7, 5-8 (numbers refer to Figure 4.2 and the structural model of Ref. [143]). Calculations also show that these atoms could be imaged at low voltages [148].

Recent STM studies of the InSb(001)-c(8x2) surface recorded a temperature – induced reversible phase transition at temperatures below 180 K [152]. The low temperature (LT) STM images indicate that the surface structural periodicity doubles along [110] direction in comparison to room temperature.

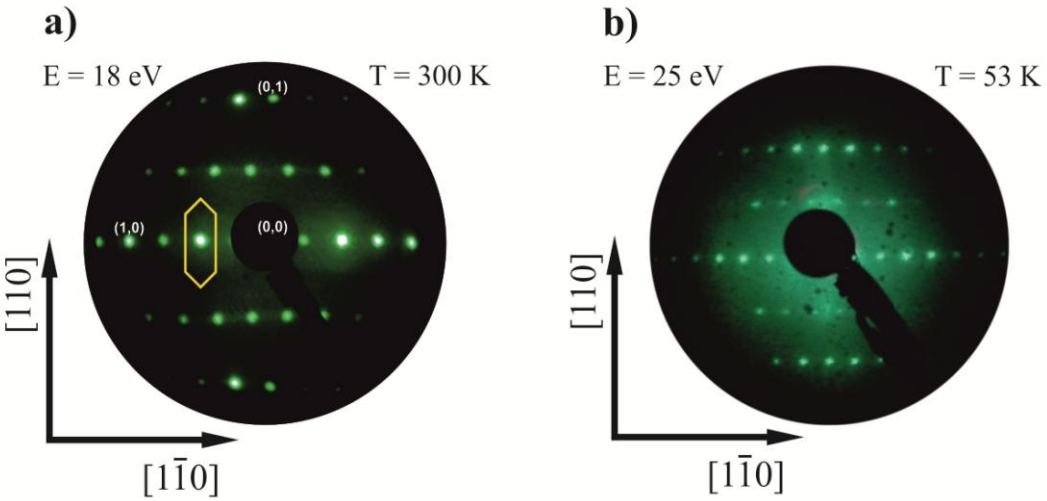

Figure 4.4 *LEED patterns of InSb(001)-c(8x2) for a) E = 18 eV taken at 300 K and b) E = 25 eV taken 53 K. The Brillouin zone of the c(8x2) reconstruction is highlighted.*

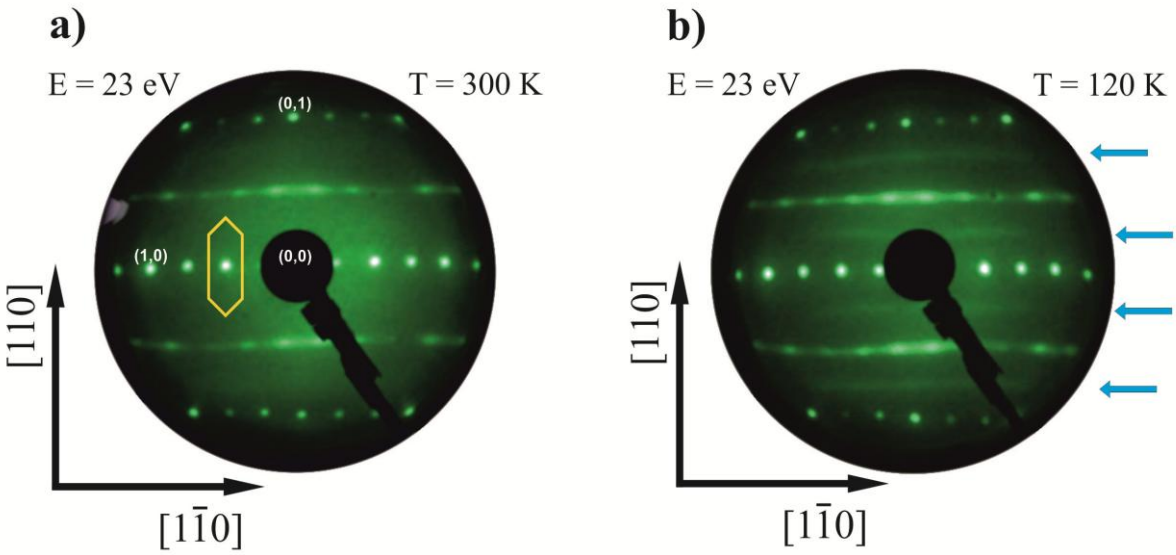

Figure 4.5 *LEED pattern of InAs(001)(4x2)-c(8x2) for E = 23 eV taken at a) 300 K and b) 120 K (blue arrows correspond to the new periodicity). The Brillouin zone of the c(8x2) reconstruction is highlighted.*

The c(8x2) superstructure was studied at room and at low temperature using low energy electron diffraction (LEED). Patterns (Figure 4.4 and 4.5) for InSb(001)-c(8x2) and InAs(001)(4x2)-c(8x2), show sharp four-fold symmetry spots in the $[1\bar{1}0]$ direction. In the case of InAs(001)(4x2)-c(8x2), a streaking of the two-fold symmetry spots along the [110] direction is observed, which is due to the coexistence of (4x2) and c(8x2) superstructures (Figures 4.4 and 4.5).

In the case of InSb(001)-c(8x2) cooled down to 53 K, no changes of the c(8x2) single-domain LEED pattern could be observed (Figure 4.4b). On the contrary, in the case of InAs(001)(4x2)-c(8x2), an additional fourfold periodicity is observed along [110] direction in the form of weak streaks, as shown in Figure 4.5b.

The phase transition observed for these reconstructions by LTSTM studies and the formation of the extra periodicity along [110] direction found in LEED patterns, are expected to induce changes in the surface electronic structure.

4.2 Electronic structure of A_{III}-B_V semiconductors

That main objective of this study is to understand the electronic properties of the InSb(001)-c(8x2) and InAs(001)4x2-c(8x2) reconstructed surfaces in a broad temperature range from room to low temperature. To this end, the bulk and surface electronic states are characterized along the two high symmetry directions.

ARPES is sensitive to the momentum distribution of energy states in the Surface Brillouin Zone (SBZ). The SBZ of a A_{III}-B_V(001) crystal with a centred c(8x2) superstructure is shown in Figure 4.6. Blue points represent $\bar{\Gamma}_{c(8x2)}$ points. The periodicity along $\bar{\Gamma}\bar{J}'$ direction ($[1\bar{1}0]$ crystal direction) is x8, but the centred SBZ presents a x4 periodicity due to partial extinctions. The periodicity along $\bar{\Gamma}\bar{J}$ direction ([110] crystal direction) is x2, but again the SBZ presents only x1 periodicity. The distance between $\bar{\Gamma}_{c(8x2)}$ points along $\bar{\Gamma}\bar{J}$ is much larger than along $\bar{\Gamma}\bar{J}'$.

Note however that in the case of a (4x2) lattice or of an extra x2 superperiocicity along the [110] direction (as observed in the case of InAs(001), an extra $\bar{\Gamma}$ point should appear (coinciding with the $\bar{J}_{1x1}$ point in Figure 4.7). For InSb(001), the distance $\bar{\Gamma}\bar{J}_{1x1}$ and $\overline{\Gamma J'}_{1x1}$ is 0.686 $Å^{-1}$ and for InAs(001) is 0.733 $Å^{-1}$ at 300 K. This model helps to understand the band structure of InSb and InAs.

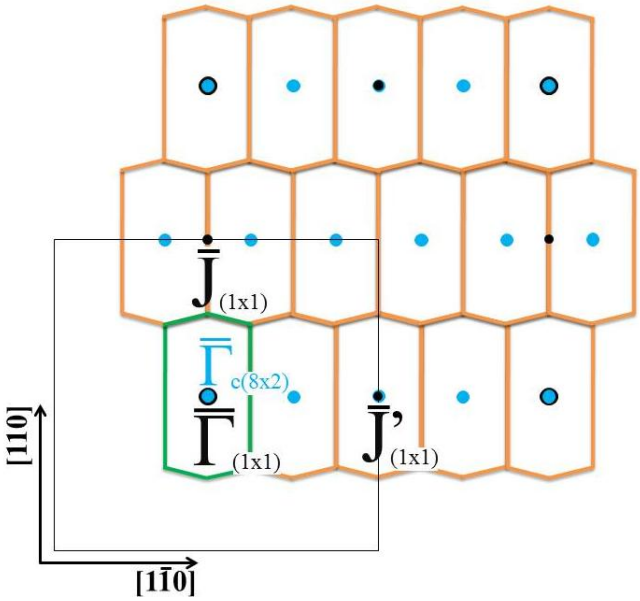

Figure 4.6 *Reciprocal space of the c(8x2) reconstructed surface showing the (1x1) surface Brillouin zone (black squares) and c(8x2) Brillouin zone (hexagons). Black/blue points correspond to $\bar{\Gamma}$ points of the (1x1)/c(8x2) lattices.*

The electronic structure of bulk InSb(001) was first investigated in 1983 by H. Höchst [159] and I. Hernández–Calderon [160] and few years later H. U. Middelmann [161], using photoemission and RHEED (reflection high energy electron diffraction). In 1995 the first systematic angle resolved photoemission spectra of InSb(001)-(4x1) were obtained. Three surface state bands were identified an related to the (4x1) reconstruction [162].

In the case of InAs(001), first ARPES investigations started in 1997 [163]. This work characterized the bulk band structure along ΓX bulk direction. Three groups of surface bands were identified for (2x4) and (4x2) reconstructions. These reconstructions form intrinsic electron accumulation layers, which are specific of each reconstruction. The reconstruction c(8x2) was studied in 2001 [164]. Different experiments have supported the existence of a charge accumulation layer on this superstructure, like core level photoemission [164], and high-resolution electron energy loss spectroscopy (HREELS) [165].

4.2.1 Bulk band structure structure of InSb(001)-c(8x2)

The bulk electronic band structure of InSb(001)-c(8x2) has been characterized along ΓX direction by normal emission ARPES using photon energies in the range 10-47 eV. This range covers ~90% of the Brillouin zone along ΓX. The electron binding energies are converted into perpendicular momentum assuming a free-electron like final state band

and an inner potential V_0 = 5.5 V (measured with respect to the Fermi energy) [159] [143] [150]. The experimental energy distribution curves (EDCs) are shown in Figure 4.7a and b, while Figure 4.7c collects the experimental data points together with theoretical bands from Ref. [166]. A comparison with previous findings [159] [143] [150], allows us to determine Γ_6

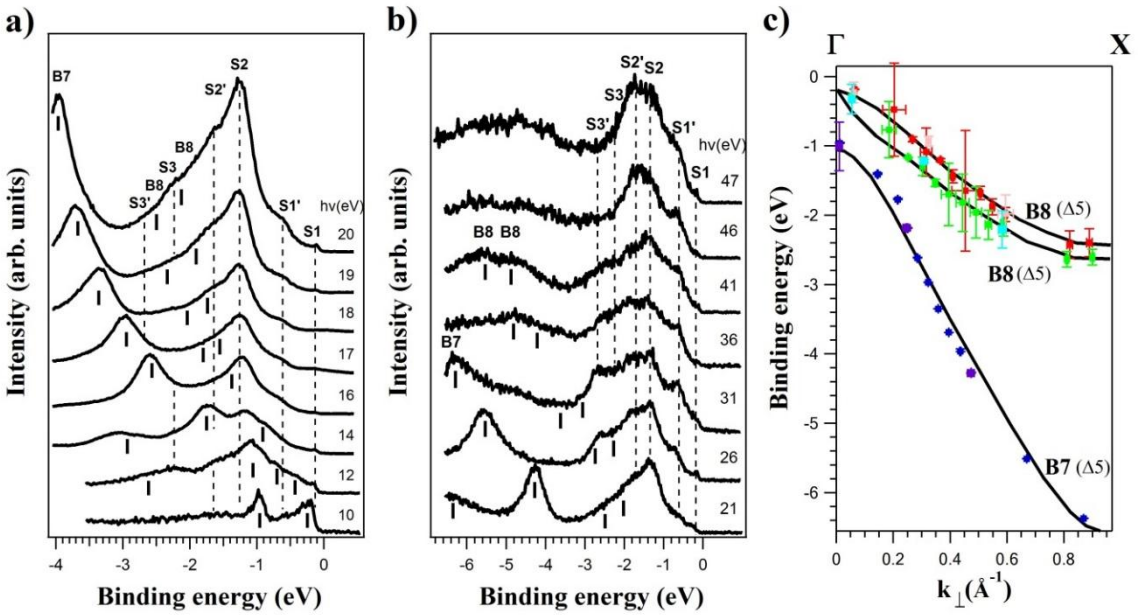

Figure 4.7 *Energy distribution curves along ΓX direction for photon energies in the range 10 to 20 eV (panel (a)) and 21 to 47 eV (panel (b)). Dashed lines correspond to surface states and vertical tics to bulk bands. Note that surface states are not seen at all energies with comparable intensity. (c) Bulk band dispersion versus momentum along ΓX direction from the experimental EDC's from panels (a) and (b). Bands are labelled as B7 and B8, according to their order in the valence band sequence. Colours highlight different data sets. Continuous lines are theoretical calculations from Ref. [166].*

(-12 eV, not shown), Γ_7 (-0.6 eV), and Γ_8 (-0.11 eV), corresponding to the valence band maximum). B7 band at Γ_7 is the spin-orbit split off band, while B8 band at Γ_8 is split in the well-known light and heavy hole bands away from Γ point.

4.2.2 Surface band structure of InSb(001)-c(8x2)

Figure 4.7a,b shows that, besides identified bulk bands, there are different additional peaks that do not disperse with photon energy. As they are also sensitive to surface ordering and reconstruction (not shown), they are assigned to surface bands. Related peaks can be grouped into: S1 group (S1, S1'), S2 group (S2, S2'), and S3 group (S3, S3'). Some of them are more intense for off-normal detection, or can be observed only for certain detection conditions (emission angle, photon energy). A more detailed description of the most relevant surface peaks is provided below.

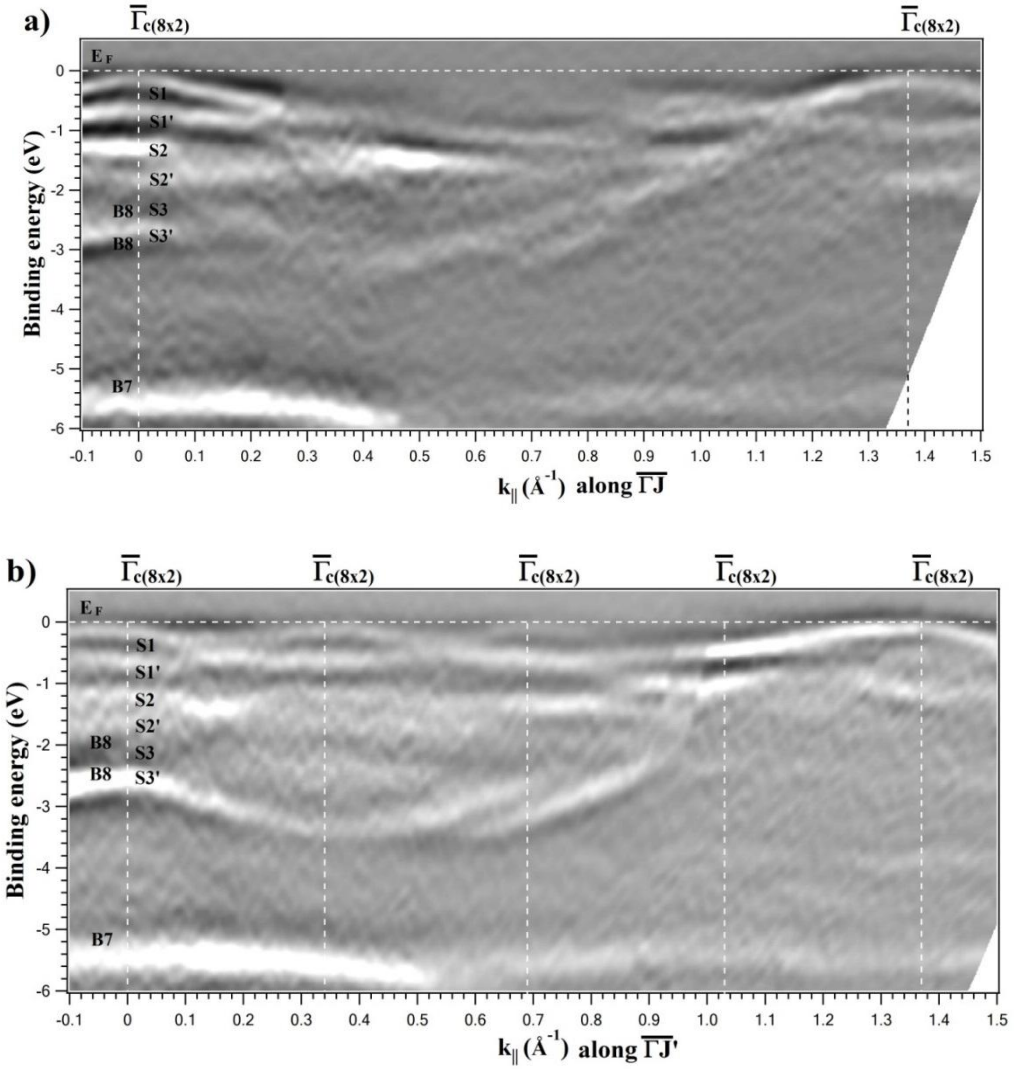

Figure 4.8 *Second derivative ARPES intensity distribution vs. binding energy along a) $\overline{\Gamma J}$ and b) $\overline{\Gamma J'}$ surface directions for hv = 26 eV. Surface and bulk bands are labelled near $\overline{\Gamma}$ point.*

Figure 4.8 presents an overview of the electronic band structure measured at 300 K with hν = 26 eV along the two high symmetry directions $\bar{\Gamma}\bar{J}$ and $\bar{\Gamma}\bar{J}'$. The spin-orbit split off band B7 is seen at ~3 eV from the heavy and light hole bulk bands B_8 at $\bar{\Gamma}$. Bulk bands present the same dispersion behaviour along the two symmetry directions probed, as the two directions are equivalent in the bulk. Three different groups of the surface states are highlighted in Figure 4.8 as S1 group (peaks S1 at -0.1 eV and S1' at -0.7 eV), S2 group (peaks S2 at -1.3 eV and S2' -1.6 eV), and S3 group (peaks S3 at -2.2 eV and S3' at -2.6 eV).

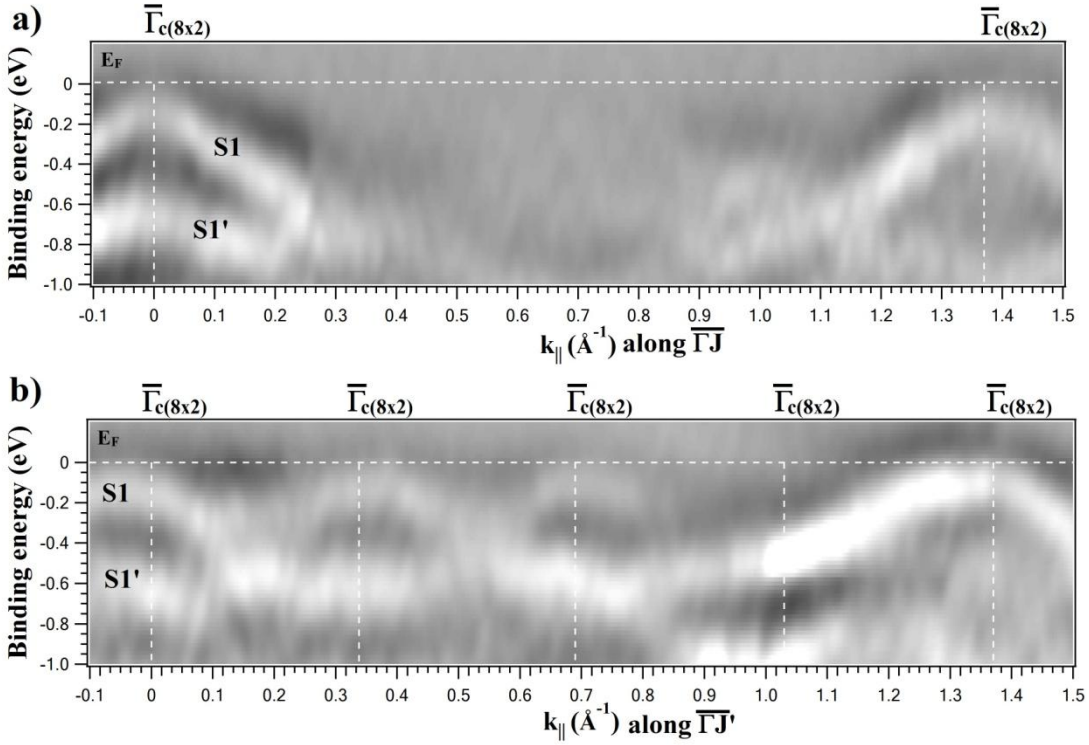

Figure 4.9 *Second derivative ARPES intensity distribution vs. binding energy showing in detail the dispersion of S1 and S1' surface states along a) $\bar{\Gamma}\bar{J}$ and b) $\bar{\Gamma}\bar{J}'$ surface directions for hν = 26 eV.*

The most prominent surface state is S1. It has a binding energy of -0.11 eV at $\bar{\Gamma}$ and it is sensitive to the reconstruction superperiodicity. Figure 4.9 shows that S1 is repeated once at the next $\bar{\Gamma}_{c(8x2)}$ point along [110] direction (panel a), and four times along $[1\bar{1}0]$ direction (panel b), in agreement with the expected superperiodicities derived from the symmetry of the surface reconstruction. The surface state S1 approaches the Fermi energy at $\bar{\Gamma}\bar{J}_{c(8x2)}$ points, but there is no detectable crossing. Thus, the c(8x2) reconstruction remains semiconducting. Furthermore, the bulk band edge measured at 10 eV and the edge of S1

(measured at 16 eV and higher photon energies), coincide and so there are no occupied surface states in the band gap.

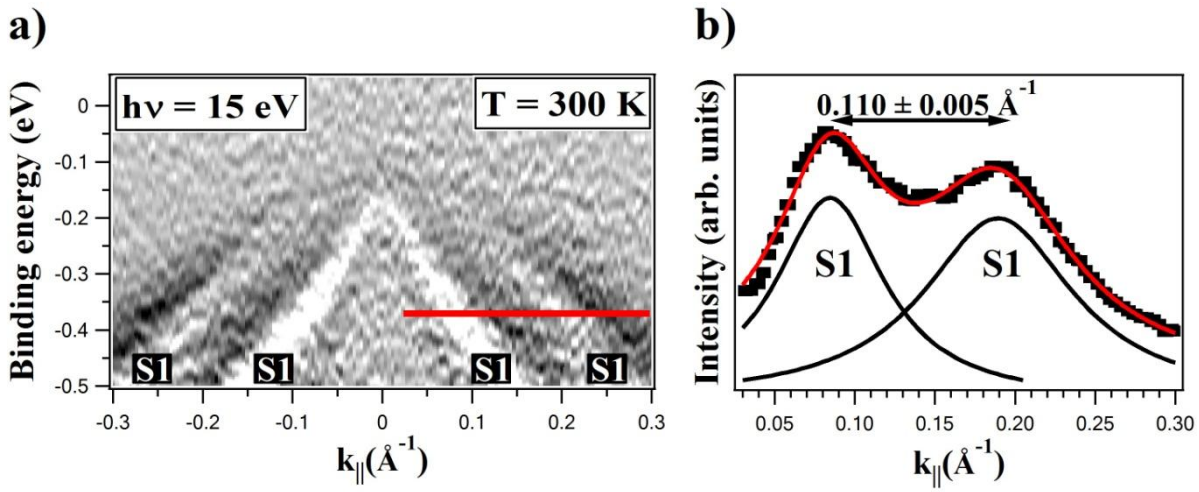

Figure 4.10 *a) ARPES intensity distribution versus binding energy and parallel momentum along $\overline{\Gamma J}$ showing the splitting of S1 surface state at T = 300 K. b) Momentum distribution curve corresponding to the red line in panel a) (BE = -0.35 eV).*

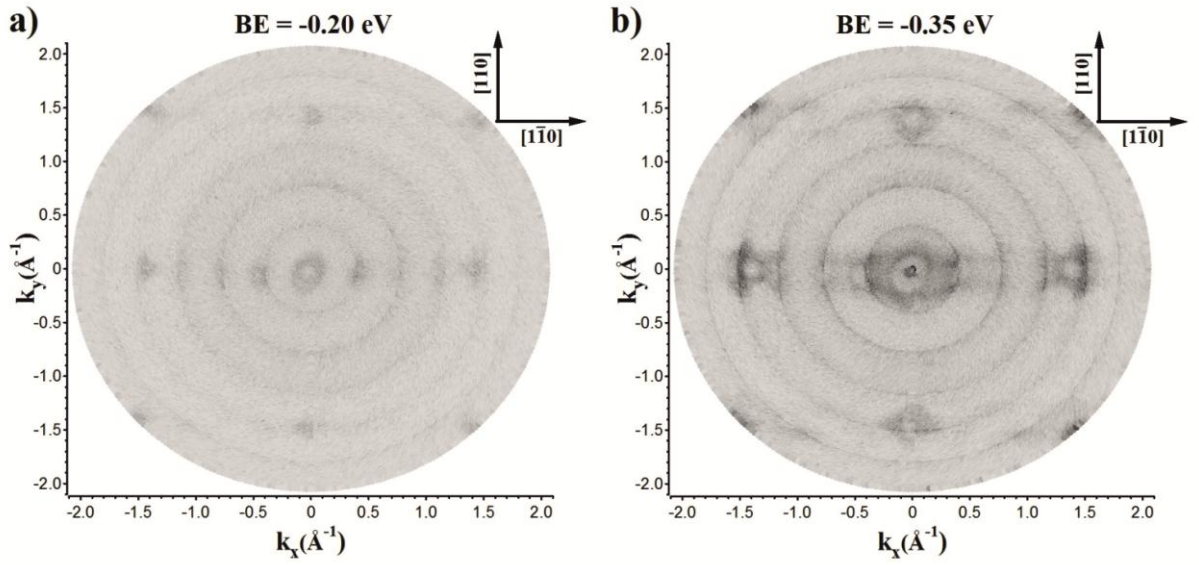

Figure 4.11 *Constant binding energy surfaces (photoemission intensity vs. parallel momentum), measured with hν = 26 eV for BE = -0.20 eV and BE = -0.35 eV. Note the inverted grey scale (dark/light corresponds to higher/lower intensity).*

Figure 4.10a shows a high-resolution binding energy vs. parallel momentum image for a photon energy of 15 eV. Surface state S1 appears now broader for off-normal emission

angles, and for large enough angles it is split into two different bands. The splitting is negligible at $\bar{\Gamma}_{c(8x2)}$ points, and larger at the c(8x2) zone edges. A momentum distribution curve (MDC) of this surface state (Figure 4.10b) highlights the splitting in reciprocal space (0.1 $Å^{-1}$ for -0.35 eV BE). The splitting is more pronounced along $\bar{\Gamma}\bar{J}$ than along $\bar{\Gamma}\bar{J}'$ (not shown).

Figure 4.11 shows constant energy maps for binding energies of -0.20 eV and -0.35 eV, i.e. in both cases very close to the minimum binding energy of the surface state S1. S1 is imaged as a circular spot, repeated four times along $[1\bar{1}0]$ direction. As constant energy images are neither symmetrized nor processed, small deformations due to the acquisition method (following concentric circular sectors) are seen. Interestingly, there are no additional $\bar{\Gamma}_{c(8x2)}$ points along [110] direction, as no extra spots are detected along this direction. However, extra spots at other locations are not observed either, and so the constant energy map of Figure 4.11 reflects an apparent (4x1) periodicity. The surface states observed with ARPES are compared with the density of states determined from STS measurements in Figure 4.12, which shows a differential conductance spectrum for both negative and positive sample bias.

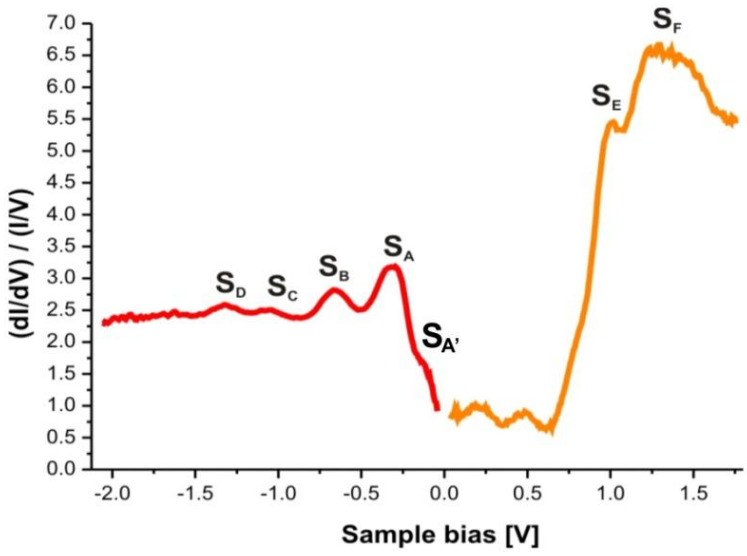

Figure 4.12 *Differential conductance spectrum of the InSb(001)-c(8x2) surface. Different peaks are identified in the occupied and unoccupied parts of the electronic structure (The gap measure in the figure is wider than expected, due to the tunnelling currents being either below the noise level or below the resolution of analogue-digital converter in the system).*

A direct comparison of the occupied part of the density of states with ARPES results in the normal emission region reveals an excellent agreement for the different peaks detected (values from ARPES in brackets): $S_{A'}$ at -0.11 eV (-0.11 eV, S1), S_A at -0.3 eV (-0.2-0.3 eV, S1 split-off band), S_B at -0.65 eV (-0.70 eV, S1'). S_C (-1.03 eV) and S_D (-1.31 eV) can be associated to S2 (-1.3 eV) and S2' (-1.6 eV) but the agreement is worse.

As surface bands in semiconducting surfaces are fairly localized, they can be traced back to filled surface bond states. The same analysis can be done for deeper lying peaks, but it becomes less straightforward, as all shallower states will contribute to the STM images. Images relevant for the identification of the surface bands have been recorded at low bias voltage. Figure 4.13 shows two filled-states STM images taken at 300 K with bias voltages of -0.5 V and -0.3 V. Parallel rows along [110] direction are the most important features. For -0.5 V each row contains a central brighter stripe, which corresponds to In1 atoms, while the darker sides are related to In4 and In5 atoms. Upon decreasing the voltage to -0.3 V there is a significant change in the image, as the central bright stripe is not seen anymore and the darker sides, attributed to In4 and In5, become brighter. The distance between the brighter spots and the centre of the row is ~5 Å. One every two atoms from the side rows is imaged brighter, and in most images only those brighter atoms are distinguished, producing the impression of an extra superperiodicity along the side rows ([110] direction). Based on all these features, the brighter spots could be identified as either In4 or In5 atoms. This would assign the bonds In4-Sb7 and In5-Sb8 to the surface state S1, with possible additional contributions. This assignment is confirmed by measuring the I(V) spectra locally on the 61x153 point grid over the surface space 25 nm x 10 nm (Figure 4.14). Different tunnelling conductance distributions are extracted from the data for the electron energies corresponding to the peaks marked as S_A and S_B on the filled states side as well as S_E and S_F on the empty state side (Figure 4.12). In agreement with the previous assignment, the brighter spots constituting the S_A pattern are identified with either In4 or In5 atoms [143] [144] [147], and the bonds In4-Sb7 and In5-Sb8 correspond to the surface state S1. There are no clear periodic features associated to S_B state, which may indicate that this state is more delocalized, or that it is related to the specific local features on the In1 row (non periodic) seen in the Figure 4.14, but an identification with specific atomic bonds is difficult. The S_E empty state is identified with the In2d dimer and finally the S_F empty state is identified with In1 atom rows [144] [152].

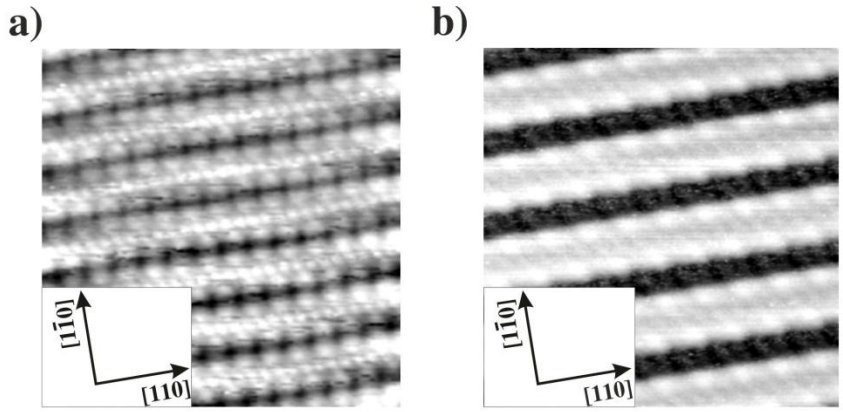

Figure 4.13 *Filled-state STM images of the InSb(001)-c(8x2) surface at RT. The tunnelling parameters are: a) -0.5 V, 200 pA, 13 nm x 13 nm b) -0.3 V, 60 pA, 8 nm x 8 nm.*

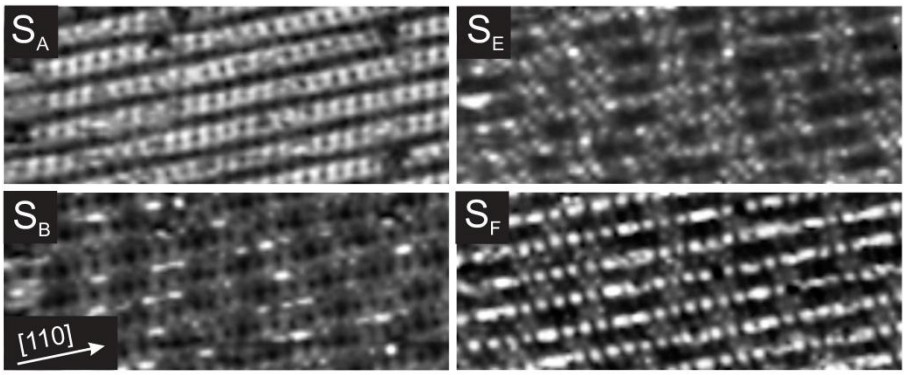

Figure 4.14 *Maps of the differential tunnelling conductance distribution for the electron energies defined by peaks S_A, S_B, S_E and S_F of the spectrum shown in Figure 4.14 (25 nm x 10 nm). The crystal temperature is 77 K.*

4.2.3 Temperature dependence of InSb(001)-c(8x2) electronic structure

The analysis of the electronic structure temperature dependence is based on the previous reports about the formation of ordered low-temperature phases at the same and related surfaces [144] [152].

Figure 4.15 and Figure 4.16 show high-resolution grey scale images of the valence band area closest to normal emission, both at 300 K and 5 K, for hν = 10 and 15 eV, respectively. Due to the reduction of thermal broadening, some peaks are seen sharper upon cooling. Besides this effect and an overall shift of the spectrum towards the Fermi energy (see

Subchapter 4.2.4), cooling to 5 K does not produce any significant changes in the valence band electronic structure.

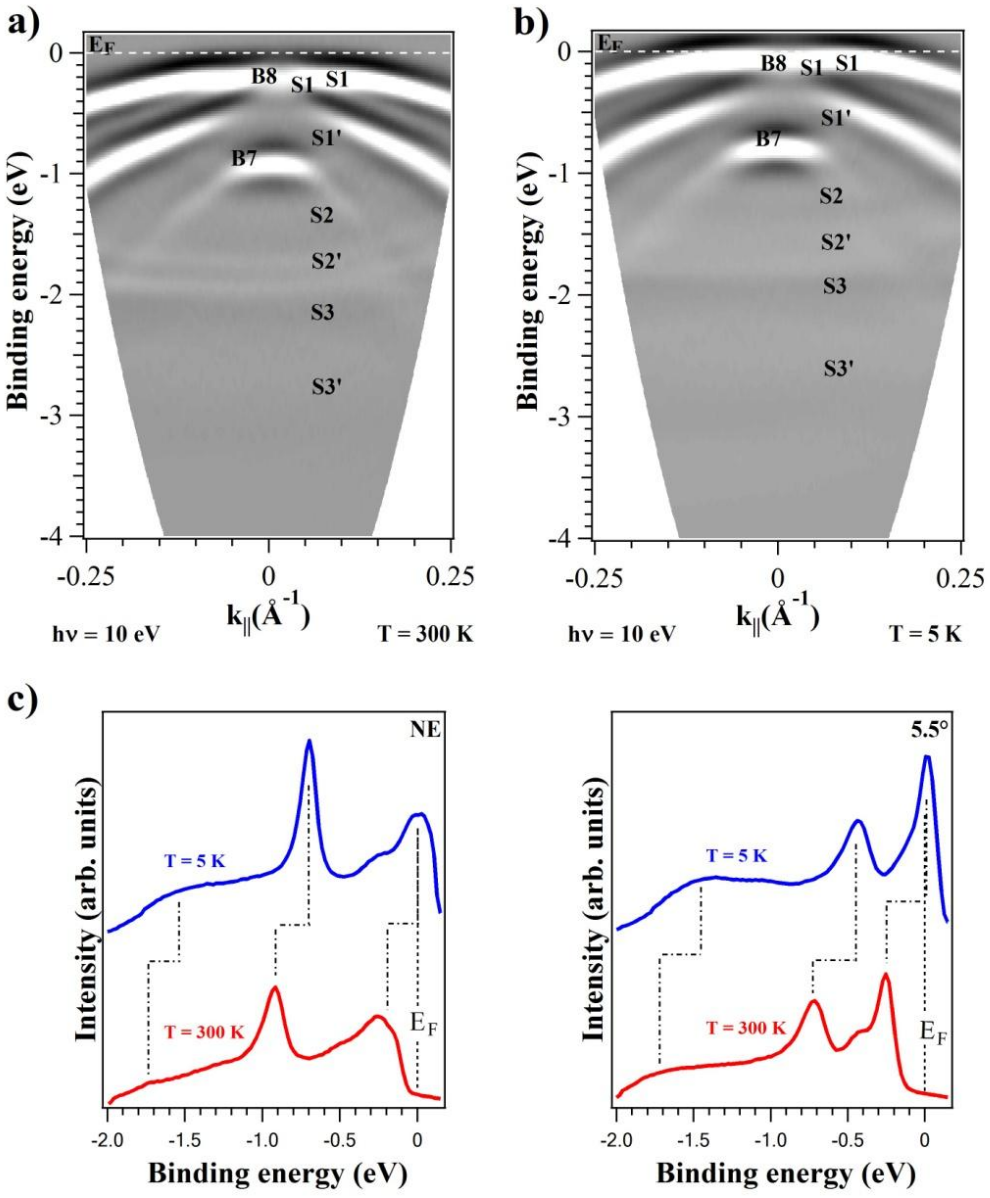

Figure 4.15 *Second derivative ARPES intensity distribution vs. binding energy and parallel momentum along $\overline{\Gamma J}$ for $h\nu$ = 10 eV at a) 300 K and b) 5 K. Labels refer to identified bulk and surface states. No significant changes are detected, except a uniform shift of the band structure to lower binding energies at low temperature. Panel c): selected EDCs from the data shown in panels a) and b) for normal emission (NE, left) and 5.5° emission angle (right) comparing spectra taken at 300 K and 5 K.*

STM images have shown that vacancy mobility diminishes with temperature, so that vacancies become localized and ordered at low temperature [158], although no new periodicities are seen in the LEED images.

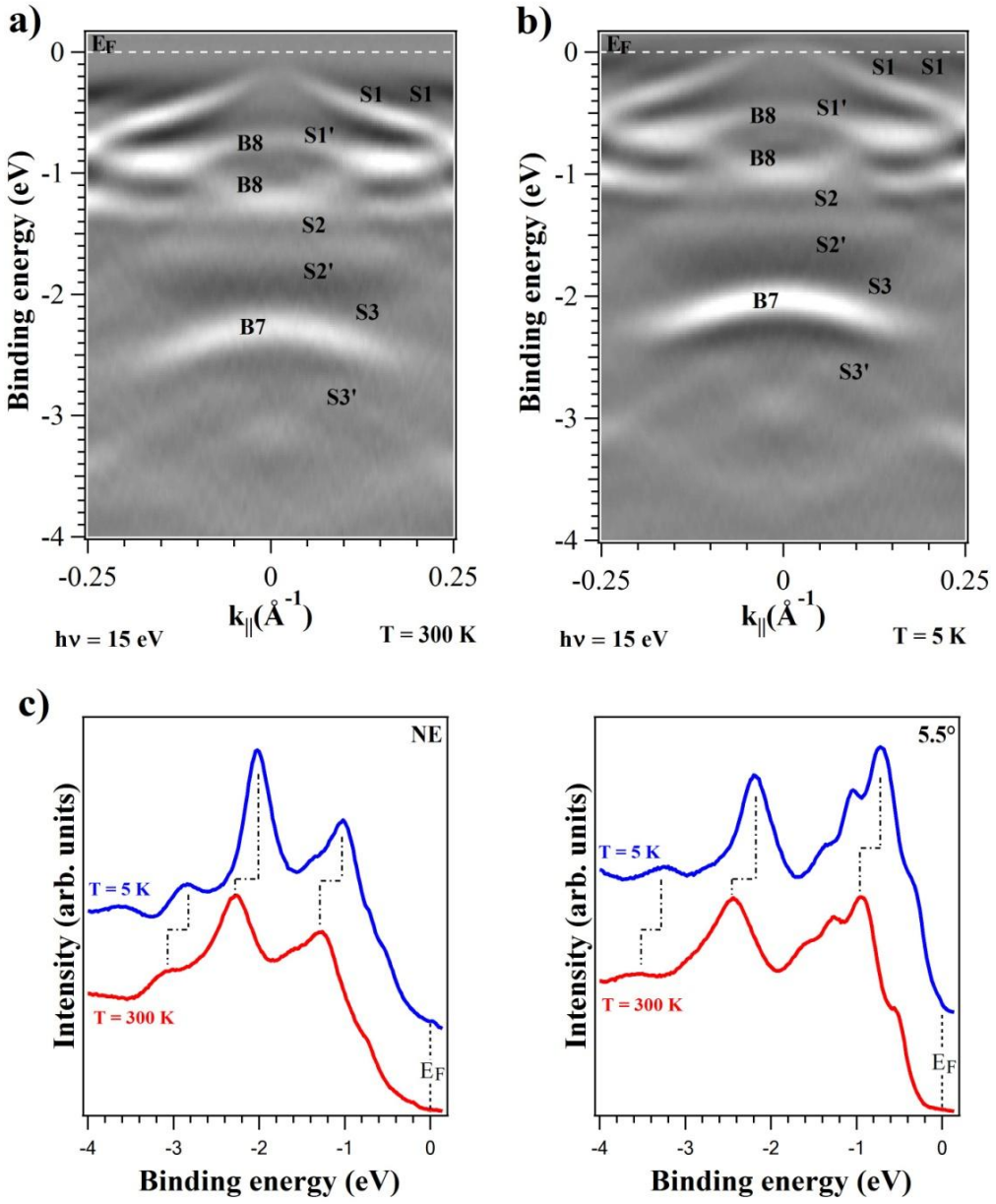

Figure 4.16 *Second derivative ARPES intensity distribution vs. binding energy and parallel momentum along $\overline{\Gamma J}$ for $h\nu$ = 15 eV at a) 300 K and b) 5 K. Labels refer to identified bulk and surface states. No significant changes are detected, except a uniform shift of the band structure to lower binding energies at low temperature. Panel c): selected EDCs from the data shown in panels a) and b) for normal emission (NE, left) and 5.5^o emission angle (right) comparing spectra taken at 300 K and 5 K.*

The lack of changes in the ARPES date, seen to detail in Figures 4.15 and 4.16, is in agreement with these results.

While the ordering process gives rise to modification in the STM images [158], no relevant differences are seen in ARPES, because the photoemission process is much faster than the diffusion of the atomic vacancies, and thus photoemission probes substantially the same structure at both temperatures.

4.2.4 Discussion

The electronic structure of c(8x2) reconstructed (100) surfaces of III-V semiconductors has been analysed theoretically for GaAs(001) [142] [156], and for InAs(001) [167]. In all cases, the calculations were made for a (4x2) unit cell containing one In2d (Ga2d) dimer and no In3 (Ga3). An energy vs. momentum dispersion relationship was calculated in Refs. [156] and [167]. Several filled surface states were found around $\bar{K}$ point, and along both $\bar{K}J$ and $\overline{KJ'}$ directions. As S1 is observed mainly near $\bar{\Gamma}_{c(8x2)}$ points, S1 cannot be identified with any of these predicted surface states [167]. Concerning experiments, only the In-rich InSb(001)-(4x1) reconstruction has been investigated using ARPES [162]. This phase exhibits two surface states S1 and S2. S1 presents a fourfold periodicity along $\overline{\Gamma J'}$ and onefold along $\bar{\Gamma}\bar{J}$, the same of S1 in the c(8x2). In turn, the BEs of the surface states in the (4x1) phase are shifted by -0.2 eV to larger values. As the valence band edge is not shifted, the different BEs reflect a specific feature of the reconstruction. Both the c(8x2) reconstruction studied in this work and the (4x1) reconstruction are obtained using a similar preparation technique. Indeed, the c(8x2) structure contains the (4x1) periodicity that is observed for the topmost surface state S1, as described above. While a definite statement would require a detailed structural analysis of the (4x1) reconstruction, it is probable that it corresponds to a c(8x2) not completely ordered, which would explain the several common features among the electronic structures of both phases. S1 is observed with ARPES in most of the (1x1) Brillouin zone as a fully occupied band. It is centred at $\bar{\Gamma}_{c(8x2)}$ points, and it disperses downwards from the symmetry points. Constant energy surfaces (see Figure 4.11) reveal a (4x1) symmetry, identical to the symmetry of the filled states from the topmost layer [158]. Indeed, this feature reflects that the full c(8x2) periodicity of the ζ-model is due to the second layer dimers (In9 atoms). As S1 state is due to filled last-layer bonds, any structural effect related to second layer atoms must be small, and the symmetry of the

relevant periodic potential is only (4x1). A comparison with STM images taken at voltages below -0.5 V (Figure 4.13) allows us to assign S1 to filled In4-Sb7 and In5-Sb8 bonds. These two families of bonds (In4-Sb7 and In5-Sb8) are not identical, due to the distribution of subsurface dimers. The appearance of two surface bands of close dispersion is expected, in good agreement with the ARPES experimental observation of the splitting of S1 in two nearly dispersing bands (Figure 4.10), when going away from $\bar{\Gamma}_{c(8x2)}$.

We analyse in the following the origin of the energy shift observed upon cooling. The chemical potential is located at room temperature 0.11 eV above the edges of both the valence band and the surface state S1. Both edges are distinguished in the experiment by using different photon energies (see Figures 4.7, 4.15, and 4.16), as the top of the valence band is probed by ARPES for a photon energy of 10 eV, while for higher photon energies (e.g. 14-16 eV) the top bulk band is below the edge and only the surface state S1 is detected. As the width of the InSb band gap is 0.18 eV at room temperature, this means that the chemical potential is above the centre of the gap, and as established above there is no band bending (Figure 4.17a).

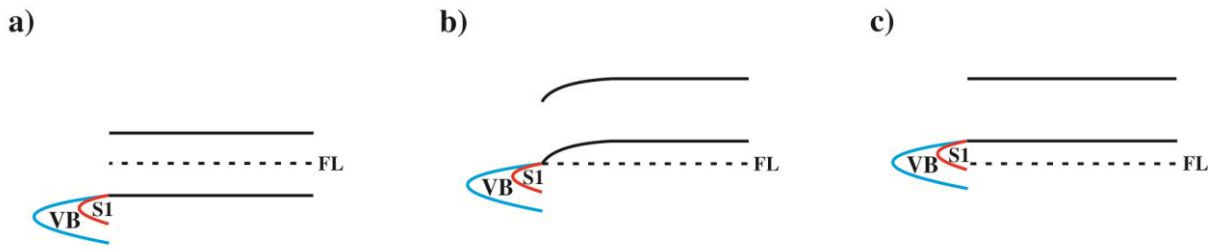

Figure 4.17 *Schematic representation of the surface bands and the band bending changes detected: a) room temperature, b) low temperature, no UV illumination, c) low temperature under UV illumination.*

The contribution of thermal excited electron-hole pairs is very important in the case of InSb, due to the small value of the gap [168]. Also the effective masses of electrons in the conduction band (m_c) and holes in the valence band (m_v) are very different (m_c = 0.014, m_v = 0.430). Due to these features, the chemical potential is closer to the band of light carriers. Indeed, the position of the intrinsic chemical potential in the bulk at 300 K is 0.157 eV from the top of the valence band. In addition, the effect of impurities can be estimated. Taking into consideration the experimental value of the chemical potential at the surface (μ = 0.11 eV) and the value expected for an intrinsic crystal (μ_i = 0.157 eV), the

difference is $\mu - \mu_i = -0.047$ eV, which is consistent with a concentration of acceptor impurities of $1x10^{17}$ cm^{-3}. This value is compatible within accuracy with the expected crystal doping, confirming that there is no band bending at the surface. This finding is consistent with the binding energies of In and Sb core levels (not shown). The Fermi level position and band bending can be compared to results obtained for InSb(001) with the different reconstructions, preparation methods and doping. As the band bending is sensitive to the surface termination, broad range of values has been found before. Olsson et al. [162] found the Fermi level 0.15 eV above the VBM for an undoped ($3x10^{15}$ cm^{-3}), (4x2) reconstructed crystal. Höchst et al. [159] found the Fermi level close the CBM, without band bending, for a (2x4) crystal. John et al reported a position 0.10–0.15 eV above the CBM for a c(8x2) surface [169]. Finally, Schweitzer et al. [170] using HREELS reported a pinning position of the Fermi level near the top of the VBM for the p doped ($2x10^{14}$ cm^{-3}) InSb(001), close to the results shown here.

We consider now the thermal induced shift of the chemical potential. The shift is 0.23 eV and is a rigid displacement of the whole band structure towards the Fermi level, so that part of it becomes apparently located above the Fermi energy (Figures 4.15 and 4.16). The shift is fully reversible with temperature. As the sample is always grounded during ARPES measurements, the sample Fermi level is determined by the ground level of the apparatus, and the apparent shift of the bands is equivalent to a change of the position of the sample chemical potential with temperature. There are two processes that contribute to such a shift [171]. The first one is the well-known freezing of thermal carriers upon decreasing the temperature. The second is the stabilization of a surface photovoltage induced by the photoemission process. Both effects are analysed separately.

The sample is nominally an intrinsic semiconductor, but in view of the shift of the chemical potential towards the valence band at low temperatures, impurities are of p type. The thermal induced shift is very intense in the case of InSb, due in part to the small binding energies of impurities and the densities of states of the valence and conduction bands [168]. In the case of donor impurities, even a sample with a small 10^{15} cm^{-3} doping becomes degenerate below ~100 K, i.e. the chemical potential is above the conduction band. In the case of acceptor impurities in the concentration level of the sample, the bulk chemical potential is below the valence band for $T < 30$ K. However, the chemical potential at the surface should be pinned by the surface states located just below the top of the valence band, which gives rise to a downwards band bending at low temperatures (Figure 4.17b).

The second effect considered is the stabilization of a surface photovoltage (SPV). When ARPES is used to probe semiconducting surfaces UV radiation stabilizes a temperature-dependent SPV, which shifts uniformly both the core levels binding energies and the valence band [172] [173] [174] [175] [176]. The effect is due to light-induced electron-hole pair formation, giving rise to accumulation of one of the carrier types at the surface (electrons or holes, depending on the sample doping). The sign of the shift depends on the initial band bending. As bands become flat after SPV formation, the shift is towards the Fermi energy for initial downwards band bending (in general, for p doped samples), and away from the Fermi energy for initial upwards band bending (in general, for n doped samples). As electron-hole recombination is reduced at low temperature, the effect becomes also more important upon cooling down. It is furthermore enhanced in the case of low densities of carries (low doping) and to a lesser extent by an intense photon flux (more details on the SPV process can be found in Refs. [174] [175]). The sign of the shift detected, and the fact that occupied bands are observed above the bulk chemical potential, are unequivocal indications of a SPV.

In the absence of UV light illumination, the formation of a band bending with downwards bent bands (Figure 4.17b), as described in the previous paragraph, would be the only process observed. However, once the band bending is established, and due to the formation of electron-hole pairs induced by ultraviolet light, the bands become again flat and part of the band structure is shifted above the bulk chemical potential (Figure 4.17c). Based on the total shift between room temperature and 5 K (0.23 eV), the position of the bulk chemical potential is 0.12 eV below the valence band maximum at 5 K. An specific feature of the InSb(001)-c(8x2) surface is that both effects (temperature induced shift of the chemical potential and SPV) significantly contribute to the total shift observed, which is larger than the band gap at 300 K.

A visual inspection of Figure 4.16 reveals that InSb(001)-c(8x2) is semiconducting, as the surface state S1 approaches the Fermi energy at $\bar{\Gamma}$, but it never crosses it. STM experiments [146] have revealed that the surface undergoes a phase transition upon decreasing the temperature, which is explained by the ordering of mobile vacancies at low temperature. ARPES experiments show that these changes do not affect the electronic structure, which remains all the time semiconducting. This feature deserves some comments. Lee et al. [142] have analysed the ζ (4x2) cell, which includes one In 2d dimer, and no In1, In2, or In3 atoms. This situation is close to the experimental findings for GaAs(001) [143]. In any case, the c(8x2) unit cell would be obtained by repeating the (4x2) cell so that

the results would apply to it as well. The Lee et al. conclusion was that the (4x2) unit cell is semiconducting, as it has an even number of electrons and thus there are no unsaturated dangling bonds. A semiconducting character is an important feature contributing to the stability of a surface, as there is a smaller contribution of the electronic energy. The experimental ARPES results presented in this work show that InSb(001) c(8x2)-reconstructed surface is also semiconducting. However, STM results [146] have shown that the structure is more complex than the model proposed in Ref. [142]. A detailed analysis on the basis of the number of dangling bonds does not seem possible here, but we can calculate the number of electrons in the top surface layer, on the basis of the statistical study made for InSb(001) using surface X-ray diffraction [143] [144]. This work reports occupations of (57 ± 1)% (In1), (72 ± 2)% (In2), (28 ± 1)% (In 2d), and 100% (In3). An electron-counting analysis reveals that we expect to obtain a semiconducting surface for 50% (In1), 66% (In2), 25% (In 2d), and 100% (In3), which are very close to experimental values, and in most cases within the accuracy of the surface X-ray results. These findings are fully coherent with our current views on the studied structure.

4.2.5 Conclusions

The electronic structure of InSb(001)-c(8x2) sheds light into several different interesting properties of the surface, in particular the relationship between the structure and the dangling bond distribution. The S1 surface state has been identified as a filled bond state specific to the ζ-structure model, which also explains the observed splitting. Also in agreement with this model, we find that the c(8x2) structure is semiconducting. A large overall shift of the band structure at low temperatures is explained from a combination of low temperature freezing of thermal carriers and UV radiation induced SPV. The results obtained give insight in to several different properties of InSb(001)-c(8x2), in particular the relationship between the structure and the dangling bond contribution.

4.2.6 Bulk band structure of InAs(001)(4x2)–c(8x2)

The bulk electronic band structure of InAs(001)(4x2)-c(8x2) has been investigated at normal emission with photon energies in the range 10-21 eV (Figure 4.18a,b). Figure 4.18c shows the experimental EDC's, and the experimental points vs. perpendicular momentum (using an inner potential of V_0 = 9.5 eV). Binding energies are referred to the Fermi energy.

We identify B7 (-1.1 eV) and B8 (-0.5 eV), Δ5 spin split bands, which correspond to two non-degenerated subbands (these are the heavy holes and light holes Δ5 bands). The experimental spin-orbit splitting at Γ point is 0.6 eV. Comparing to the results for InSb(001) with the same reconstruction, these findings exhibit many similarities, as the number of bands and their general topology are nearly the same. The experimental results have been compared with theoretical predictions [159] [166]. The agreement is satisfactory (Figure 4.18c).

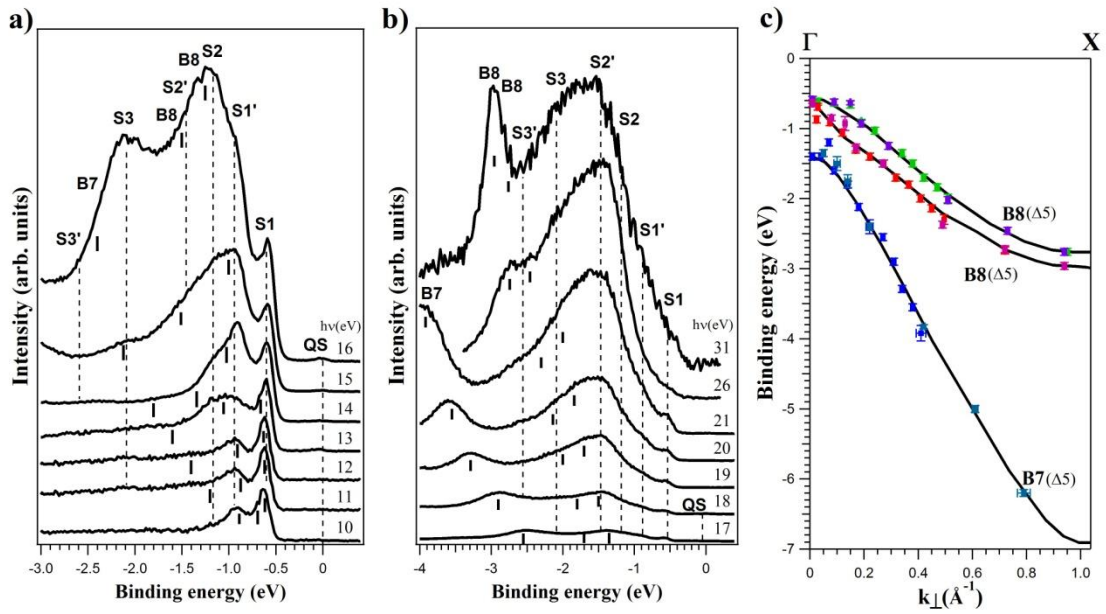

Figure 4.18 *Energy distribution curves along ΓX direction for photon energies in the range 10 to 20 eV (a) and 21 to 47 eV (b). Dashed lines correspond to surface states and vertical tics to bulk bands. (c) Bulk band dispersion vs. momentum along ΓX direction from the experimental EDCs in panels a) and b). Bands are labelled as B7 and B8, according to their order in the valence band sequence. Colours highlight different data sets. Continuous lines are theoretical calculations from Ref. [166].*

4.2.7 Surface electronic structure of InAs(001)(4x2)–c(8x2)

EDCs InAs(001)(4x2)-c(8x2) are presented in Figure 4.18. Besides identified bulk bands along the ΓX direction, there are different additional peaks that do not disperse with photon energy in the range 10 – 21 eV (notoriously, peak S1). As these peaks are also sensitive to surface ordering and the reconstruction superperiodicity, we identify them as surface bands: S1 group (S1, S1'), S2 group (S2, S2'), and S3 group (S3, S3'). Some of these peaks (S1' and S3' states, P. de Padova's notation n_1 and n_2 or S2' as A1 in M. C. Håkansson)

have been detected before for InAs(001)(4x2)-c(8x2) [177] and InAs(001)(4x2) [163]. They present a correlation between peak intensity and photon energies, explained as a strong resonant effect at photon energies corresponding to the bulk bands located at high symmetry points, like Γ and X [178].

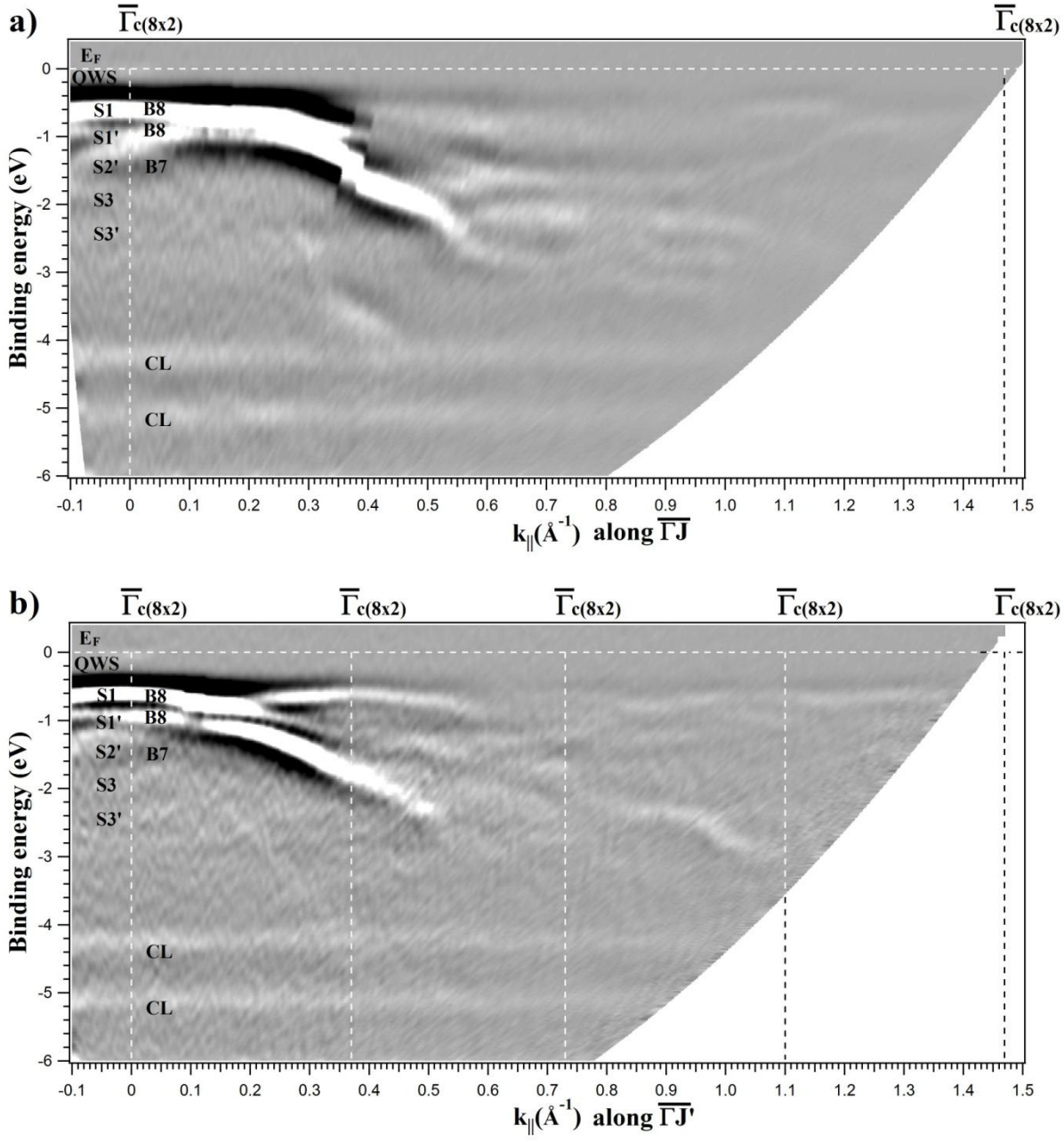

Figure 4.19 *Energy vs. momentum dispersion for the electronic bands of InAs(001)(4x2)-c(8x2) along a) $\overline{\Gamma J}$ direction and b) $\overline{\Gamma J'}$ direction for hν = 13 eV and T = 300 K (brighter means higher intensity).*

All these surface states are below the VBM, and thus they should be considered more properly as surface resonances. However, due to the localized nature of the bonds in semiconducting surfaces, these electronic states are distinguished well. In addition to these states, a new metallic state (QWS) is observed close to the Fermi level. This state is related to the formation of a surface accumulation layer in the pristine surface of InAs(001), as already reported for this crystal [164] (see section 4.2.9 for a detailed description).

The dispersion of the bulk and surface bands has been recorded along the two InAs(001) (1x1) high symmetry directions ($\bar{\Gamma}\bar{J}$ and $\overline{\Gamma J'}$), and is shown in Figure 4.19, measured at 300 K. The spin-orbit split off band is seen at 1.5 eV from the heavy and light holes bulk bands at $\bar{\Gamma}$ for hν = 16 eV. The dispersion behaviour of the bulk bands is very similar for both directions (along [110] and [1$\bar{1}$0]), as both are equivalent in the bulk for a cubic crystal and a square surface.

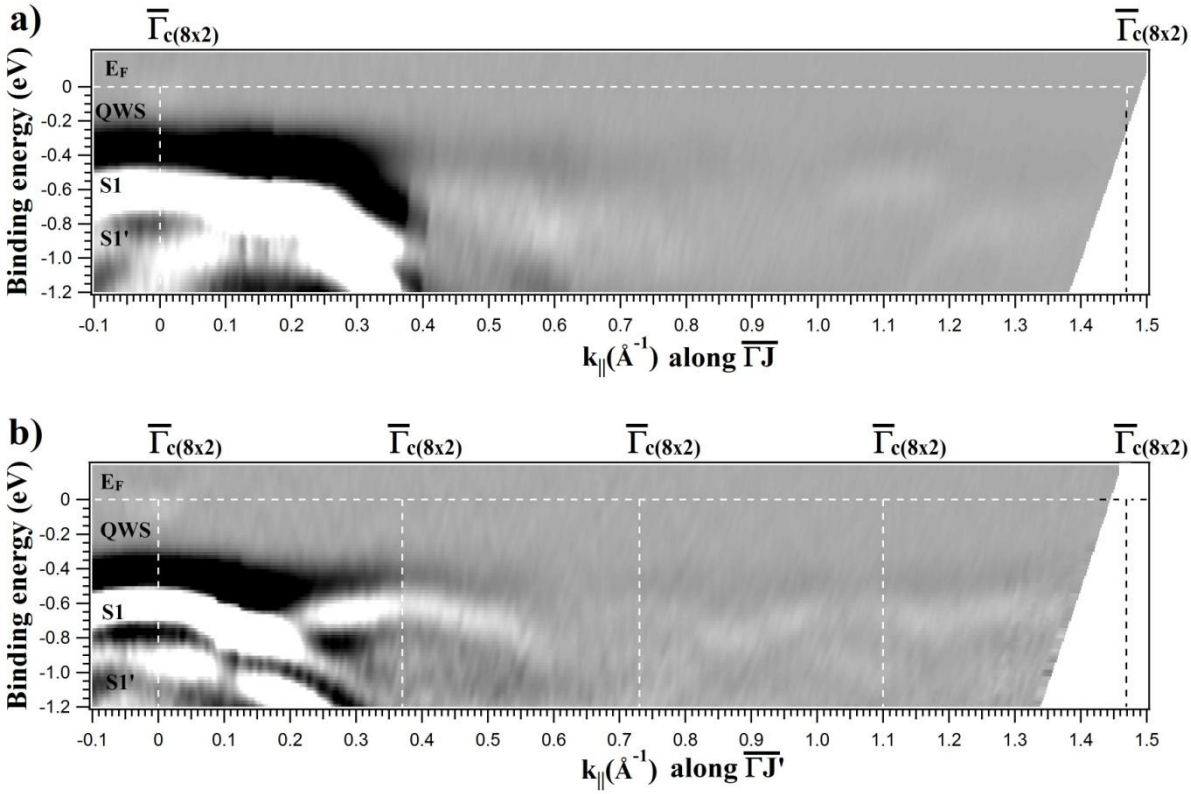

Figure 4.20 *Electronic band structure of InAs(001)(4x2)-c(8x2) along: a) $\overline{\Gamma J}$ direction, b) $\overline{\Gamma J'}$ direction for the hν = 13 eV at temperature T= 300 K.*

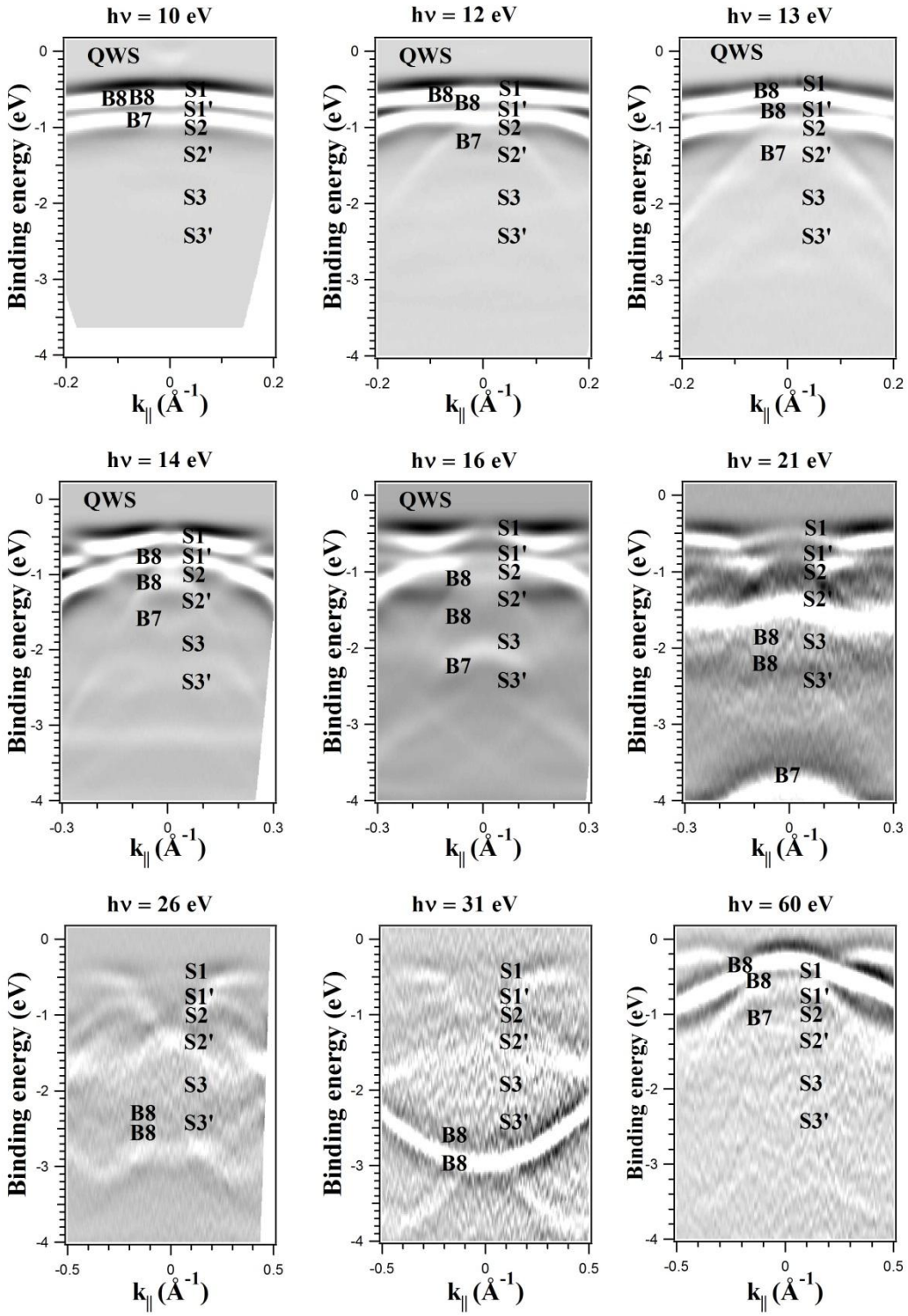

Figure 4.21 *Second derivative ARPES intensity distribution vs. binding energy and parallel momentum along $\overline{\Gamma J}$ for the photon energy range 10 - 60 eV at 300 K.*

On the other hand, there are also two bands (labelled as CL) that are not dispersing vs. momentum (BEs = -4.2 eV and -5.0 eV), which probably correspond to the In4d core level, excited with the second order of the monochromator.

Three different groups of surface states are identified: S1 group (peaks at -0.57 eV and -0.92 eV); S2 group (peaks at -1.5 eV and -1.7 eV); and S3 group (peaks at -2.09 eV and -2.59 eV). The same number of states is identified for InSb(001)-c(8x2) for the same reconstruction. These surface bands disperse along $\bar{\Gamma}\bar{J}$ and $\overline{\Gamma J'}$ direction. However, some surface bands are superimposed with bulk bands, and its actual periodicity is difficult to distinguish. The most evident case is S1 group. It is most sensitive to the reconstruction formed on the surface, and it exhibits no extra periodicity along $\bar{\Gamma}\bar{J}$ direction and 4-fold superperiodicity along $\overline{\Gamma J'}$ (Figure 4.20).

The distance between the repetition points (corresponding to $\bar{\Gamma}_{c(8x2)}$ points) in the momentum space is $k_{||} \approx 0.37$ Å^{-1} along $\bar{\Gamma}\bar{J}'$ direction, and $k_{||} \approx 1.47$ Å^{-1} along $\bar{\Gamma}\bar{J}$ direction, in agreement with the c(8x2) superstructure for this crystal.

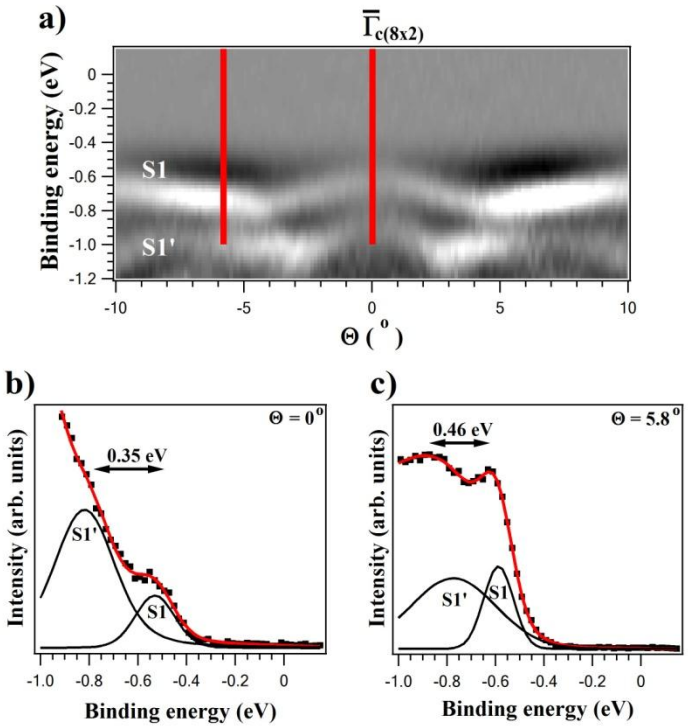

Figure 4.22 *a) S1 Surface state band dispersion along $\overline{\Gamma J'}$ direction for hν = 21 eV, red lines correspond to EDC profiles at normal emission (b) and $\theta = 5.8^{o}$ (c).*

Figure 4.22a shows a detailed view of the area near the top of the valence band for hν = 21 eV. Both S1 and S1' surface bands are resolved in great detail for this photon energy. Energy distribution curves show the surface states at the $\bar{\Gamma}_{c(8x2)}$ point (normal emission) and the zone edge at 0.18 Å^{-1} ($\theta = 5.8^{o}$) along $\overline{\Gamma J'}$ direction. The distance between the two

states is 0.35 ± 0.02 eV for the centre zone gap and 0.46 ± 0.03 eV for the zone edge (Figure 4.22b).

For the other surface states, the distance between S2 and S2' is ~0.28 eV and the distance between S3 and S3' is ~0.5 eV. Their distance at the zone edge is difficult to determine.

4.2.8 Temperature dependence of InAs(001)(4x2)–(8x2) structure

The analysis of the surface electronic structure of InAs(001)(4x2)-c(8x2) at low temperature is very interesting in view of the formation of an extra periodicity [152], in agreement with our LEED results (Figure 4.5), which find a doubling of periodicity along (110) direction at low temperature.

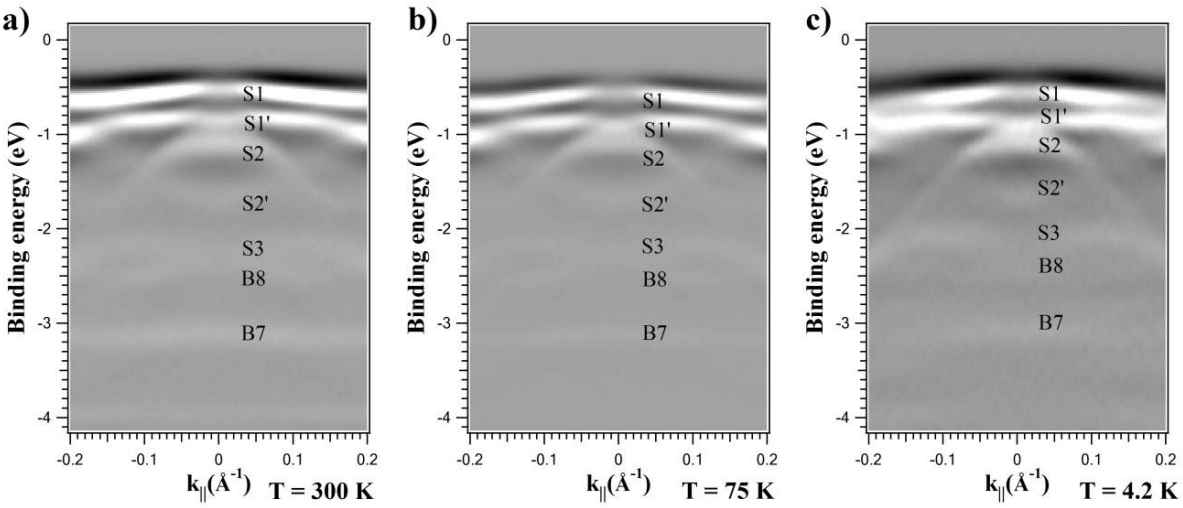

Figure 4.23 *Energy vs. momentum dispersions of InAs(001)(4x2)-c(8x2) around $\bar{\Gamma}$ point for different temperatures a) T = 300 K, b) T = 75 K and c) T = 4.2 K for hν = 14 eV (brighter means higher intensity).*

Figure 4.23 shows ARPES spectra around normal emission ($\bar{\Gamma}$ point) recorded at different temperatures. The electronic structure is better resolved upon decreasing the temperature, but there is no significant shift in binding energy, as it is the case for InSb in Figure 4.15 and Figure 4.16. A detailed study of the surface components of the As 3d core level using hν = 110 eV finds a very small shift of ~0.06 eV between RT and 4.2 K, in the direction of higher energy (away from Fermi level).

The electronic band structure along $\bar{\Gamma}\bar{J}$ direction was studied at different temperatures ranging from 300 K to 4 K. Figure 4.24 shows a greyscale representation of the bands measured at 300 K and 4.2 K. There are no significant changes of the electronic structure along this direction, meaning that the phase transition does not affect the electronic structure at temperatures below 300 K.

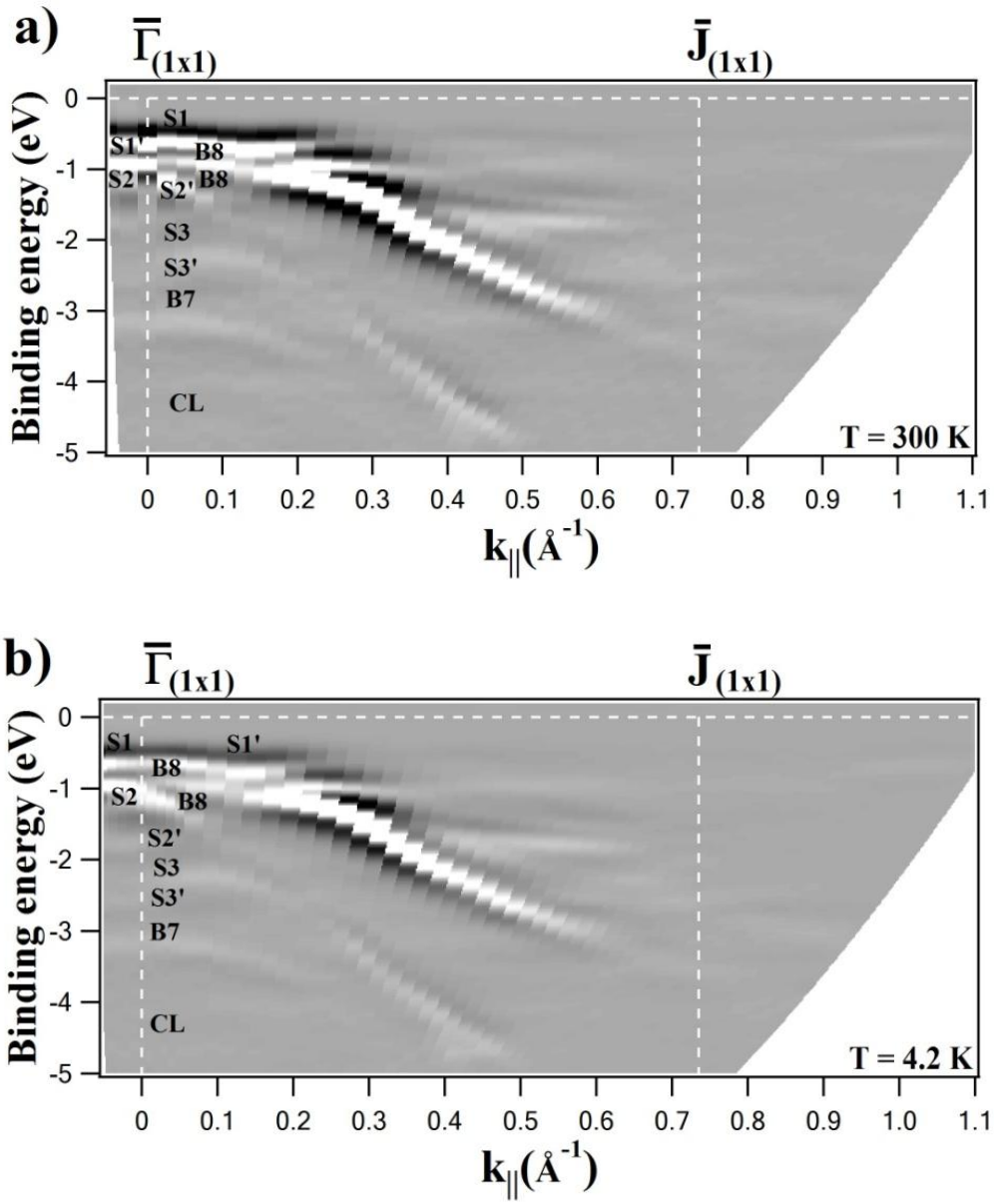

Figure 4.24 *Energy vs. momentum dispersion of InAs(001)(4x2)-c(8x2) along [110] (hv = 14 eV) at: a) T = 300 K b) T = 4.2 K (brighter means higher intensity).*

It could be expected that the same or close effects as described before for InSb(001) are also seen for InAs(001) [148] [179]. However, the existence of a metallic state at the Fermi energy prevents the observation of SPV effects for this surface.

4.2.9 The conduction band of InAs(001)(4x2)–(8x2) surface

4.2.9.1 Fermi level pinning and band bending

Semiconductors are covalently bonded compounds. At the surface, dangling bonds give rise to surface states. They are frequently influenced by the presence of a reconstruction. We summarize in the following the most relevant aspects related to InAs from this ample and complex subject. We follow the arguments put forward in Ref. [179]. Ionized surface states in the band gap (gap states) are crucial to explain the Fermi level pinning at semiconductor free surfaces. Surface states are spatially localized at the surface, with wave functions exponentially decaying into the bulk. Due to their localized nature, their character contains contributions from large portions of the surface Brillouin zone. Surface states have predominantly either valence band (donor) character or conduction band (acceptor) character. The crossover from donorlike to acceptorlike states is referred to as branch-point energy (E_B), which lies close to the middle of the average or dielectric gap, at the mean-value point [180] [181] [182]. Charge neutrality is satisfied when all donorlike states are occupied and all acceptorlike states are empty, and occurs ideally, when the Fermi level lies at E_B. Owing to this fact, E_B is often referred to as Charge Neutrality Level (CNB). Due to the intrinsic properties of surface states (large screening lengths, discrete instead of continuous character), the Fermi-level pinning can occur away from E_B. In most semiconductors, E_B lies at the middle of the band gap.

The properties of GaAs can be used to show the role of E_B in the formation of the space-charge layer. The bulk Fermi level of n-type GaAs lies at E_B (see Figure 4.25). If occupied acceptorlike surface states exist, upward band bending will occur and a depletion layer is formed at the surface with the pinned surface Fermi level lying close to E_B, which for GaAs lies close to the midgap position. In the absence of surface states, flat bands occur, i.e., there is no band bending due to the absence of ionized surface states. Such a situation is observed for a cleaved (110) nonpolar surface of GaAs.

Figure 4.25 shows the band line-up for several semiconductors. The cation acts to push the CBM downwards, but as the spin-orbit splitting increases the VBM is pushed upwards.

The location of E_B high above the CBM for InAs generally results in the formation of an accumulation layer, due to the bulk Fermi level lying below E_B. As mentioned above, charge neutrality is achieved when the surface Fermi level is pinned close to E_B, and the band bending is compensated by the remaining unoccupied donorlike surface states. However, if the bulk Fermi level of InAs would lie above E_B, then the situation would be the same as for n-type GaAs, and a depletion layer would appear. We note that the position of E_B is not unusually high for InAs, in turn, the CBM is extremely low. The position of E_B is universal for all covalent and weakly ionic semiconductors, lying approximately 4.9 eV below the vacuum level [183] [184]. The position of the CBM is determined by the location of the minimum of the conduction band at the Γ point (see Figure 4.25b). In turn, the position of E_B takes into account the position of the maximum density of states in the conduction band, which lies much higher due to the large density of states at the L point. This feature is rather unusual and is specific of InAs.

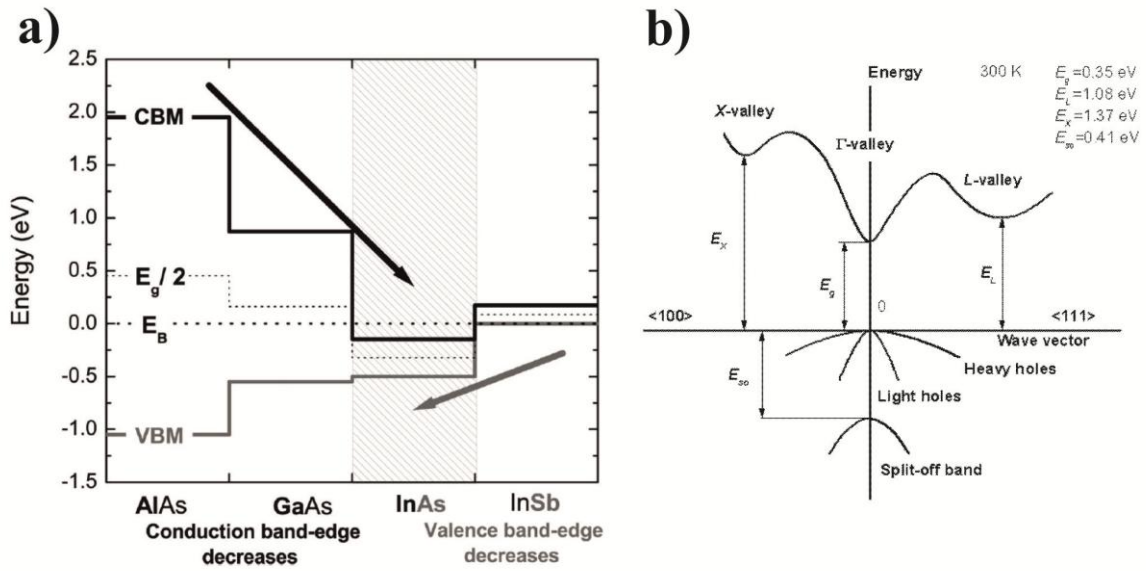

Figure 4.25 *a) The band line-up of the AlAs, GaAs, InAs, and InSb referred to the calculated positions of the branch-point energy (E_B) (dotted line) [185]. The figure shows also the position of the midgap (Eg/2) (dotted thin line) b) schematic band structure of InAs showing the positions of the conduction band minimum (CBM) in different high-symmetry points, with respect to the valence band maximum (VBM) [186].*

4.2.9.2 Temperature dependence of the Fermi energy

The value of the band gap of InAs changes with temperature as shown in Figure 4.26a. The position of the Fermi energy will change with temperature also, depending on the density the carriers and its type. Note that for moderate doping levels and low temperatures, the Fermi level can be located outside the band gap, and InAs becomes degenerate.

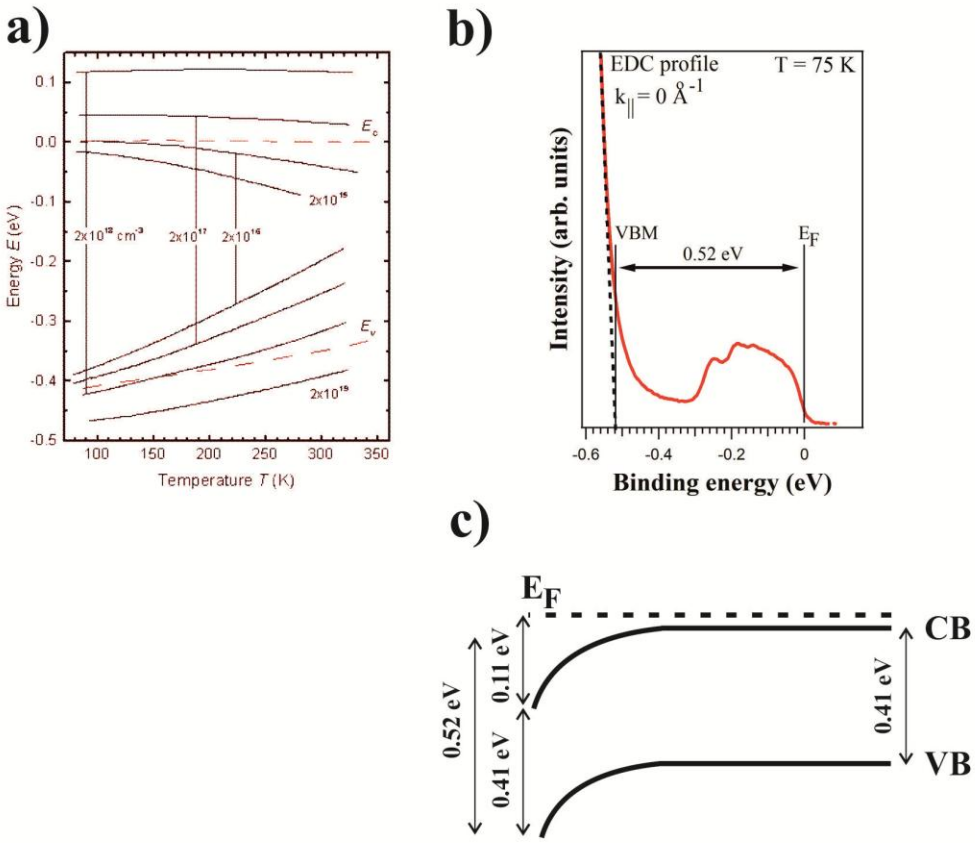

Figure 4.26 *a) Position of the Fermi level versus temperature referred to the CBM, for different concentrations of shallow donors and acceptors [186]. b) Experimental position of the VBM with respect to the Fermi level for InAs(001)(4x2)-c(8x2) at 75 K. c) Schematic representation of the observed band bending of InAs(001)(4x2)-c(8x4) and formation of a charge accumulation layer (values at 5 K). The Fermi level is pinned slightly above (< 2 meV) the conduction band.*

4.2.9.3 Surface band bending

The VBM is determined from measurements of the valence band at $\bar{\Gamma}_{c(8x2)}$ point for a low photon energy of 10 eV, which corresponds to the Γ point (Figure 4.18). The Fermi energy is measured in a Ta foil in electrical contact with the sample and close to it. All binding energies are referred to the Fermi energy. The VBM is located 0.52 eV at T = 75 K (Figure 4.26b). Considering that the band gap is 0.36 eV (0.42 eV) for 300 K (5 K), the band structure is affected by a downward band bending. Taking into account that the InAs(001)(4x2)-c(8x2) crystal used is nominally undoped, with a carrier concentration of donors of 3 x10^{16} cm^{-3}, the VBM is at 0.42 eV from the Fermi level in the bulk at 75 K, which lies slightly above the CBM. The CBM lies at 0.11 eV below the Fermi energy at 75 K and the surface presents a charge accumulation layer, as shown in Figure 4.26c.

4.2.9.4 Accumulation layer

The existence of an accumulation layer in InAs(001) reconstructed surfaces has been observed by HREELS [165]. Core level and valence band photoemission also supported the existence of free charge at the surface [164]. The existence of an accumulation layer on the InAs(001)(4x2)-c(8x2) surface is evidenced now by ARPES experiments in the near normal-emission area (around $\bar{\Gamma}$). A new conducting band close to the Fermi level is observed in a narrow range around normal emission in Figure 4.27. The width of the new state is 0.1 $Å^{-1}$ in k-space, with a minimum binding energy of ~0.13 eV.

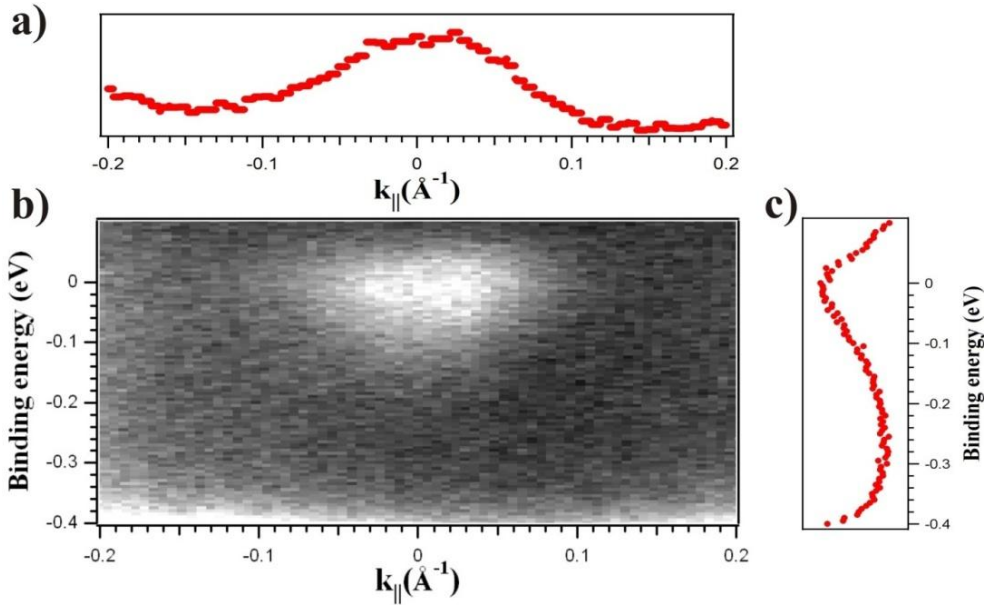

Figure 4.27 *Conduction band of InAs(001)(4x2)-c(8x2) surface along $\overline{\Gamma J}$ direction for hν = 13 eV and T = 300 K (b); MDC profile at the Fermi energy (a); EDC profile for normal emission (c).*

Although the data in Figure 4.27 are taken with low angle resolution, they are useful both to locate the electronic states in reciprocal space and to determine their energy dependence.

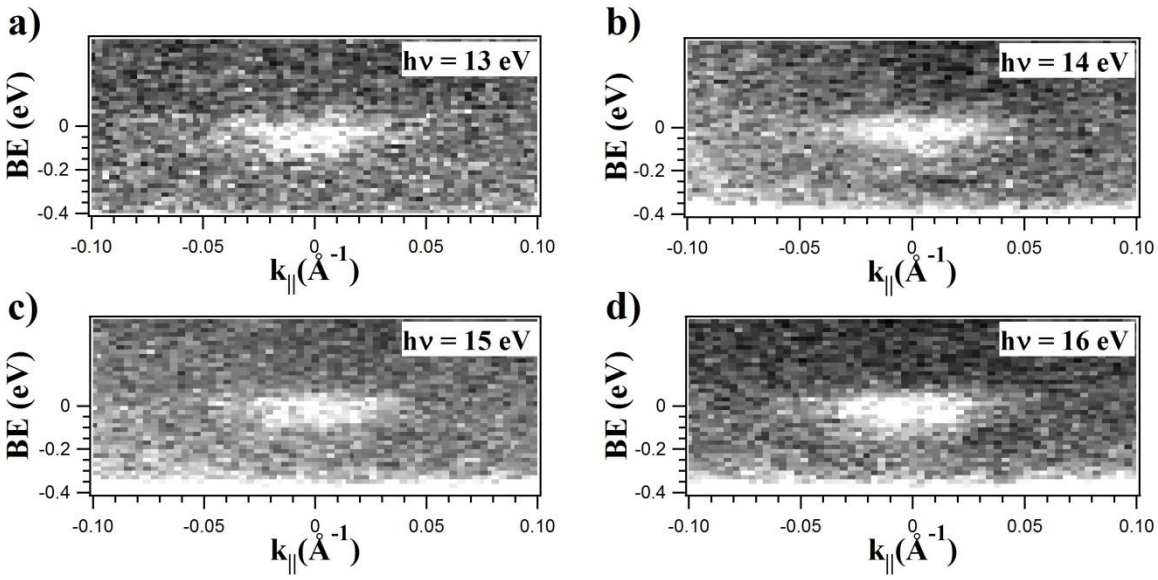

Figure 4.28 *Conduction band of InAs(001)(4x2)-c(8x2) structure along $\overline{\Gamma J}$ for selected photon energies a) 13 eV, b) 14 eV, 15 eV, d) 16 eV at 300 K.*

The electronic states detected near the Fermi energy have been probed for several photon energies in the range 10 to 47 eV (Figure 4.28). The conduction band is appearing for hν = 10 eV and disappearing for hν = 16 eV. Then, a flat band around 0.15 eV is seen for hν = 17 eV (not shown). For higher photon energies, the electronic states are seen with decreasing intensity until they disappear above 19 eV.

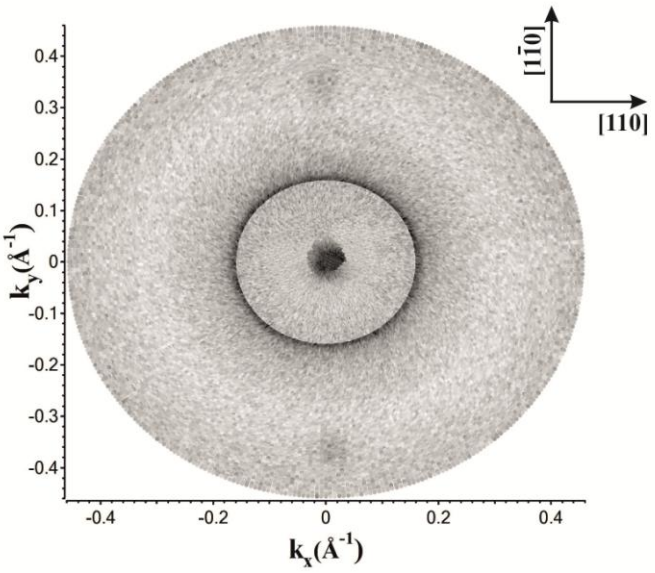

Figure 4.29 *The Fermi surface map of InAs(001)(4x2)-c(8x2) at hv = 13 eV.*

The new band is localized in reciprocal space, as shown by the Fermi Surface Map (FSM), which provides the distribution in reciprocal space of the electronic state. Figure 4.29 shows a contour of the new band around normal emission. Two replicas of this contour are seen (top and bottom) at 0.37 Å^{-1} from normal emission, corresponding to $\bar{\Gamma}_{c(8x2)}$ along $\overline{\Gamma J'}$ direction.

4.2.10 Conduction bands at low temperature for InAs(001)(4x2)-c(8x2) surface

The band structure shown in Figure 4.26c describes a situation where a surface accumulation layer is formed. The conduction band is partially occupied at the near surface region. The corresponding electronic states are confined in the direction normal to the surface by the band bending potential, giving rise to the formation quantum well states. Each of these states behaves as a two dimensional electron gas (2 DEG). The density of states in the 2DEG can be calculated adding the contributions of all occupied QWS. For each state, the density can be calculated from $N_{2D} = k_F^2/2\pi$, where k_F is the Fermi wave vector. For the measured sample of InAs(001) we obtain $N_{2D} = 6.6 \times 10^{12}$ cm^{-2}.

The existence of an accumulation layer at the surface if InAs(001) was evidenced long time ago with different techniques [165] [187] [188], even on oxidized InAs(001) [189], and more recently using ARPES [190]. Although there were some indirect evidences

of the existence of subbands (QWS) within the accumulation layer [191], their existence was demonstrated by ARPES in the case of InAs(110) [192], where the asymmetric line shape of the valence band evidence the existence of several QWS subbands. More recently, high-resolution ARPES experiments on InN [193] have directly shown the existence of two QWS at 60 K. Later on, QWS have been observed also for CdO(100) [194] [195], and doped InAs(111) [195].

In the case of InAs(001)(4x2)-c(8x2), high resolution ARPES experiments performed at Cassiopée Beamline from RT to 5 K show that the valence band electronic states of the accumulation layer present a complex line shape. Figure 4.30 shows results taken with hν = 10 eV, i.e. near the VBM for three different temperatures. The main effect of cooling is an increase of the resolution, due to freezing of phonon broadening. However, cooling of the crystal down to 4.2 K reduces significantly the lifetime of the clean surface,

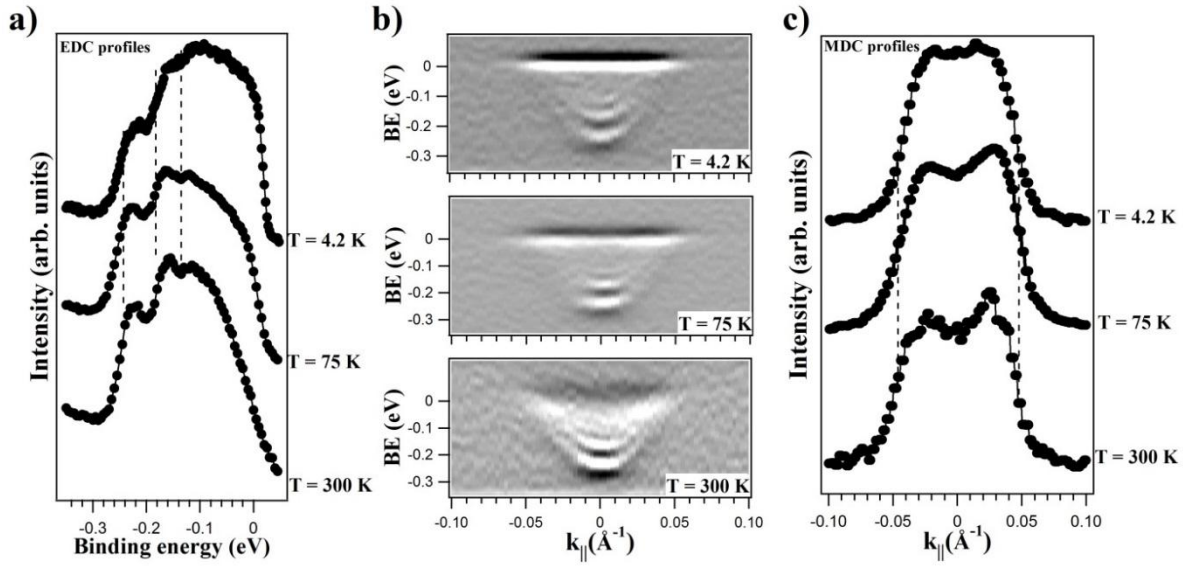

Figure 4.30 *a) EDC profiles for normal emission and hν = 10 eV; b) InAs(001)(4x2)-c(8x2) conduction band in a BE vs parallel momentum gray scale representation along $\overline{\Gamma J}$ direction; c) MDC profiles from panel a) at BE = -0.01 eV. In all cases, data at three temperatures (T = 300 K, 75 K, 4.2 K) are shown.*

due to condensation of residual gases, so that the real resolution in the spectrum after a minimum accumulation time worsens. Due to this fact, most of the analysis has been done using spectra taken at higher temperatures (in general, 75 K). As the accumulation layer is metallic, the temperature induced increase of resolution is apparent in the width of the Fermi edge, as shown in Figure 4.30a). The width of the Fermi edge narrows significantly between 300 K and 4.2 K, reaching 0.020 ± 0.008 eV at 4.2 K (limited by the resolution set in the

analyser). The gray scale images in Figure 4.30b) show very clearly that the conduction band for InAs(001)(4x2)-c(8x2) along $\bar{\Gamma}\bar{J}$ direction contains more than one band. At least three states are distinguished without further analysis at 300 K and 75 K.

The EDC for hν = 10 eV at 75 K is shown in more details in Figure 4.31. Here, the enlarged scale allows one to extract some conclusions. First, there are at least three peaks seen with a naked eye in the spectrum (highlighted with tics). Second, the shape of the spectrum is remarkable, as the deeper lying state (at ~ -0.25 eV BE) appears to be less intense than the second one (at ~ -0.17 eV BE).

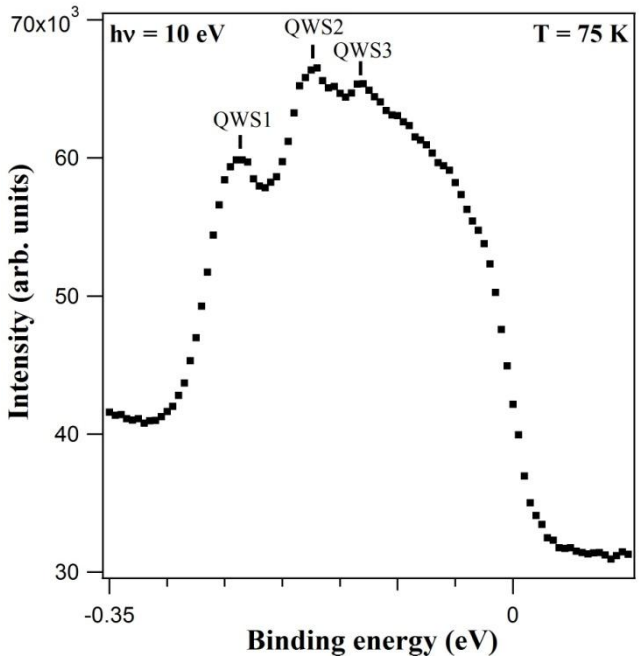

Figure 4.31 *EDC profile at normal emission, hν = 10 eV and T = 75 K. Three peaks are highlighted with tics.*

This is at variance with previous observations made with lower energy or angular resolution for InAs of with analogous experimental conditions for similar accumulation layers [193] [195], where the deepest lying QWS is always the most intense one. The rest of the spectrum line shape is not sufficiently resolved to perform a direct deconvolution. Owing to this fact, we did not attempt to obtain a deconvolution of the line shape in different spectral components based on the experimental line shape only, as the result would not be unique.

Band gap – E_g	0.405 eV
Varshni parameter – α	0.25 meV/K
Varshni parameter – β	75 K
Surface carrier density – N_{ss}	$3.63x10^{12}$ cm^{-2}
Bulk carrier density – N_b	$3x10^{16}$ cm^{-3}
Band effective mass – m_0^*	$0.021m_e$
Spin – orbit splitting –Δ_{so}	0.381 eV

Table 4.1 *InAs parameters used in the theoretical calculation.*

Thus, in order to understand the origin of the unexpected line shape and to perform a judicious deconvolution, quantitative calculations on the foreseen electronic states of the accumulation layer have been made by J. Lis [196]. The calculations are based on the Poisson-Schrödinger coupled equations within a modified Thomas-Fermi approximation to take into consideration the one electron potential V(z) and a depth-dependent electron density. Kane's **k°p** theory was applied to the model to obtain the dispersion relation between the energy and momentum (Figure 4.32a, green lines). The parameters used in the calculation are collected in Table 4.1. Calculations made using this scheme have successfully reproduced experimental results previously [195] [196] [197]. The results of the calculation are shown in Figure 4.32. The theoretical results (green lines) reproduce very well the experimental peak at -0.17 eV, but fail to reproduce the peaks at -0.25 eV and -0.14 eV.

In fact, even changing the shape of the potential well to other values, the sequence of experimental peaks cannot be reproduced by the theory, indicating that not all the peaks seen correspond to a sequence of QWS in the potential well of Figure 4.32.

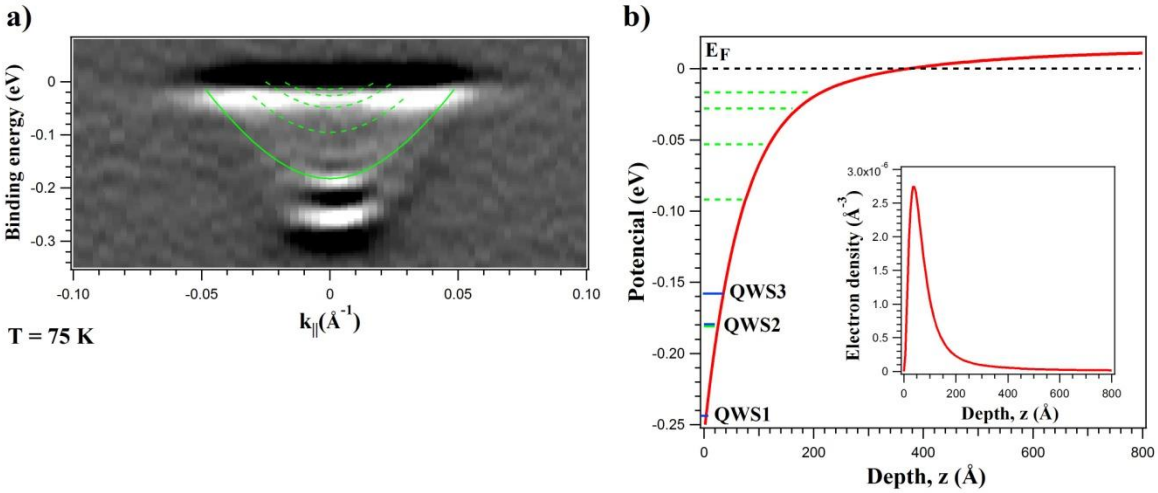

Figure 4.32 *a) Quantized conduction band near the Fermi level for InAs(001)(4x2)-c(8x2) along $\overline{\Gamma J}$ direction at hv = 10 eV and T = 75 K in grey scale (brightness means high intensity), with calculated subbands dispersion shown as green lines (deepest state, continuous line; additional states, dashed lines). b) Calculated downward band bending of the conduction band as a function of depth, showing the theoretical QWS peaks (green) and the three experimental peaks directly observed in Figure 4.31. Note that both in panels a) and b) the deepest lying experimental peak (at -0.25 eV) and the third peak (at -0.14 eV) are not reproduced by the theoretical calculation. Inset: free carrier density as a function of depth.*

In view of these results, and taking into account the previous observation concerning the intensity of the deepest lying peak vs. the second deepest peak, we interpret the deepest peak as being due to an energy loss of the second peak. If we assume that each QWS peak is accompanied by a loss peak, we can now make a deconvolution of the line shape seen in Figure 4.33. The BEs of the QWS peaks are taken from the theoretical calculation, and are allowed to change only within a narrow energy window. All other binding energies and relative intensities were fitted.

The fit identifies five independent components in the line shape, each being accompanied by a loss peak, what gives ten components: QWS1, QWS2, QWS3, QWS4, QWS5, QWS6, QWS7, QWS8, QWS9, QWS10). Their binding energies are shown in Table 4.2. As expected, QWS2, QWS5, and QWS8 have a higher intensity than QWS1, QWS3, and QWS4, respectively. QWS9 and QWS10 also follow this trend, but their position and relative intensity are more difficult to determine, as these peaks lie in the Fermi energy cutoff. In view

of this features, and following previous arguments, we assign QWS_1, QWS_3, QWS_4, QWS_6, and QWS_7, to loss peaks from each of the adjacent main peaks. The energetic distance between each main peak and the corresponding loss peak is in average 0.063 ± 0.05 eV.

Peak	**Experimental BE (eV)**	**Width (eV)**	**Intensity (arb. units)**	**Theoretical BE (eV)**
E_{QWS1}	0.244 ± 0.020	0.056	16 350	-
E_{QWS2}	0.181 ± 0.030	0.068	42 769	0.181
E_{QWS3}	0.158 ± 0.030	0.061	15 088	-
E_{QWS4}	0.122 ± 0.030	0.062	24 773	-
E_{QWS5}	0.095 ± 0.010	0.076	17 562	0.092
E_{QWS6}	0.093 ± 0.030	0.070	14 706	-
E_{QWS7}	0.078 ± 0.010	0.045	12 785	-
E_{QWS8}	0.057 ± 0.030	0.081	20 236	0.053
E_{QWS9}	0.030 ± 0.030	0.047	10 942	0.029
E_{QWS10}	0.015 ± 0.030	0.042	9 380	0.017

Table 4.2 *Experimental and calculated QWS binding energies at $\bar{\Gamma}$ point.*

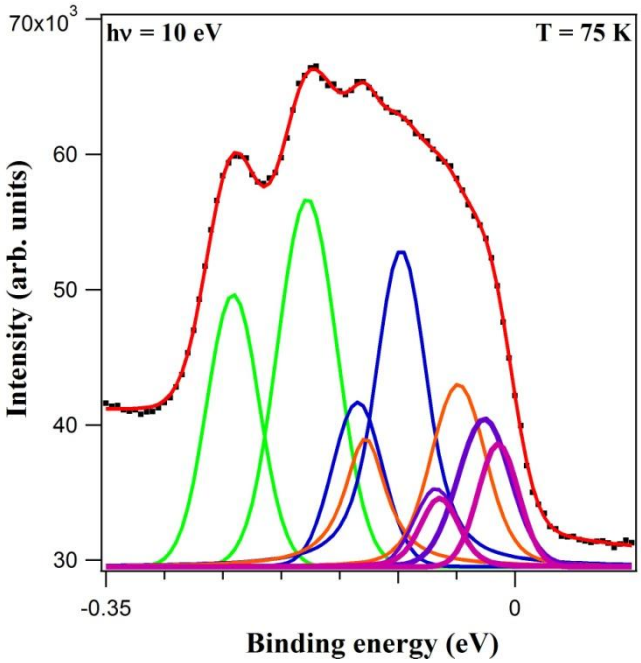

Figure 4.33 *EDC profile at normal emission, hν = 10 eV, T = 75 K (black dots) and fitted line shape (red line). The different peaks used for the fit are shown underneath. Each main peak and its corresponding loss peak are drawn in the same colour: QWS1 and QWS2 (green), QWS3 and QWS5 (blue), QWS4 and QWS8 (orange), QWS6 and QWS9 (violet), QWS7 and QWS10 (purple).*

4.2.11 Discussion

The electronic structure of InAs(001) has been analysed before, both theoretically [167] [197] [198] and experimentally [163] [177] [198] [199]. Energy vs. momentum dispersion relationships were calculated in Refs. [156] [167] [197]. However, there is no detailed experimental information on the electronic structure of the c(8x2) phase using ARPES. In this work several filled surface states have been identified for the c(8x2) reconstruction. The states found and their number are the same as for InSb(001)c(8x2), mainly S1', S2', and S3' are seen. Some of the states found (S1' and S3') were reported before [177]. These states present a resonance for photon energies of 31 and 61 eV and are detected near the X and Γ points. Both states exhibit dispersion along both $\overline{\Gamma J}$ and $\overline{\Gamma J'}$ directions, but their period is very difficult to determine, due to mixing with other states (the same is true for InSb). The more visible periodicity is seen for S1, same as for InSb. This state is observed mainly near $\bar{\Gamma}_{c(8x2)}$ points and it presents a fourfold periodicity along $\overline{\Gamma J'}$ and onefold along $\overline{\Gamma J}$,

but not the full c(8x2) periodicity of the ζ-model. As S1 state is due to filled last-layer bonds, any structural effect related to second layer atoms must be small, and the symmetry of the relevant periodic potential is only (4x1). A comparison with STM images taken at voltages below -0.7 V (Figure 4.2b) allows us to assign S1 to filled In4-As7 and In5-As8 bonds. These two families of bonds (In4-As7 and In5-As8) are not identical, due to the distribution of subsurface dimers. The appearance of two surface bands of close dispersion is expected as in the case of InSb, but ARPES experiments do not show the splitting of S1 away from $\bar{\Gamma}_{c(8x2)}$.

The valence band maximum is located 0.46 eV below the Fermi energy at 300 K, and 0.52 eV at 75 K. Taking into account the band gap of InAs (0.36 eV at 300K and 0.42 eV at 75 K), and the position of the Fermi level in the bulk (0.42 eV above the VBM), there is a downward band bending of 0.12 eV. Due to the downwards band bending, the CBM is below the Fermi level at the surface, giving rise to the formation of a surface accumulation layer of large charge density (see below). The small temperature induced shift observed is attributed to the freezing of a small number of electron-hole pairs excited at RT. The surface electron density may present strong correlation effects [165], as experimentally confirmed for InAs(111) [190].

We observe the appearance of a surface accumulation layer with a c(8x2) periodicity, due to the electron confinement in the potential well of the bent bands. The accumulation layer forms a 2D electron gas in 1D potential well, giving rise to confinement in the direction perpendicular to the surface plane. The charge in the accumulation layer can be determined from the Luttinger theorem by adding the contribution of the individual QWS, which provides a value $6.6x10^{12}$ cm^{-2}. Five quantum well states are identified: QWS2, QWS5, QWS8, QWS9, QWS10. These states exhibit quasi parabolic dispersion with parallel momentum, in agreement with the expected behaviour for a 2D electron gas. Similar effects have been observed InP [193], CdO [195] and doped InAs(111) [195]. However, the data obtained for InAs(001) revel that there are five extra states (QWS1, QWS3, QWS4, QWS6, QWS7). Each of these peaks is located at the same energetic distance within experimental accuracy (60 meV) from one of the five QWS2, QWS5, QWS8, QWS9, QWS10 peaks. This feature suggests that QWS1, QWS3, QWS4, QWS6, QWS7 are loss peaks. We hypothesize that the losses are related to the excitation of surface plasmons by the outgoing photoelectron in the 2D electron gas. Plasmons have been detected in the surface of InAs by RHEED [165] [188] [200], and their experimental BE is in good agreement with the loss energy found. The value of the plasmon loss depends of the termination of the reconstruction [165]. Thus,

the surface plasmon energy is only 0.005 eV for the In terminated InAs(100). The value of the plasmon loss energy depends also on the density of electrons in the accumulation layer. In turn, this density depends on the bulk doping and especially on the surface termination. As a surface feature, it can be affected by processes like exposure to gasses [188]. The nature of the 2D plasmon is interesting, as it seems to be strongly coupled to phonons at the InAs(001) surface. The charge density is not homogenous, and the thickness of the layer is comparable to the probing depth of the incoming electron. Each QWS corresponds to a different electron density, and is expected to contribute with a plasmon of slightly different energy. The same is true for each of the layers where the QWS are localized. As the charge in each sublayer is depth dependent, the local plasmon in each sublayer will be at different energy, due to electron density differences [188].

Finally, we comment on the value of the band bending. The experimental position of the VBM is 0.52 eV from the Fermi energy (Figure 4.26). Taking into account the value of the band gap, this locates the CBM at 0.11 eV below the Fermi energy. This value if much smaller that the BE of the deeper QWS peaks, as seen in Figure 4.32, and in fact the theoretical calculation was made using a distance of 0.25 eV. The difference between the two values is 0.14 eV. This difference is not specific of InAs(001), as it has been found for several different semiconductors [197]. In fact, it has been proposed that these discrepancies can be understood by considering many-body interactions within the semiconductor electron accumulation layer [197]. We refer the reader to this reference for a complete account on these effects.

4.2.12 Conclusions

InAs(001)(4x2)-c(8x2) present a rich surface electronic structure, including several surface states, whose properties has been described. The behaviour of S1 surface states in reciprocal space with a 4x2 periodicity) is in agreement with the predictions of the ζ-structure model.

The LEED pattern of InAs(001)4x2-c(8x2) reveals the formation of a new phase at low temperature (extra periodicity along [110] direction), which is evidenced by a doubling of periodicity of several features in the electronic structure. Bulk and surface states show an insignificant shift in binding energy upon cooling, indicating that there is no SPV in this surface. This is due to the formation of a charge accumulation layer of metallic nature, which pins the Fermi level at the surface and prevent the formation of SPV.

Due to the formation of a charge accumulation layer, new electronic states are detected near the Fermi level, related to the quantization of the conduction band. These effects are reported for the first time for InAs(001)(4x2)-c(8x2). At low temperature, several QW can be discerned. We interpret the line shape taking into account theoretical calculations predicting theory number and energy position. High-resolution data permit to observe plasmon energy losses in the QWS.

4.3 Conclusions for both semiconductors

The behaviour of both surface states is qualitatively understood from theoretical predictions based on the ζ-structure model.

The LEED pattern of InAs(001)(4x2)-c(8x2) reveals the formation of a new phase at low temperature (extra periodicity along [110] direction). The extra periodicity is also observed in STM images and in ARPES spectra. There are some hints of an extra periodicity in InSb, but it could not be detected using ARPES.

The electronic structure of both InSb(001)-c(8x2) and InAs(001)(4x2)-c(8x2) clarifies the relationship between the structure and the dangling bond distribution.

InSb(001)-c(8x2 is semiconducting and presents strong SPV effects. InAs(001)(4x2)-c(8x2) is metallic, and the Fermi level is pinned by the CBM. Close to the Fermi level, new electronic states appear, due to the quantization of the CB.

General conclusions

The research presented in this thesis covers investigations on the crystalline and electronic structure of several low dimensional systems, including a gold surface, beryllium vicinal crystals, and the surfaces of III-V semiconductors. The physical phenomena investigated range from the observation of spin-orbit splitting of the L point surface state, to the appearance of one-dimensional QWS or the observation of quantization of electronic states in an accumulation layer and the analysis of their properties. The crystalline structure was obtained simultaneously using LEED and STM techniques. These techniques provide a characterization of the reconstruction on the surfaces and also are sensitive to surface phase transitions. The electronic structure of the ordered superstructures was measured by angle resolved photoemission spectroscopy (ARPES).

Surface electronic structure of Au(110)-(1x2)

A full characterization of the electronic structure of Au(110)-(1x2) by ARPES has re-examined the electronic properties of this surface. EDCs obtained for a broad range of photon energies allowed us to characterize in detail the bulk electronic structure along ΓXK direction. Most peaks observed are attributed to sp and d bands, but some indirect transitions have been identified as well

The surface electronic structure has been characterized both along and perpendicular to the missing rows for several photon energies. In the direction perpendicular to the atomic rows, a surface resonance is seen at $\overline{\Gamma}'$ points along $\overline{\Gamma'Y'}$ direction. It has a maximum binding energy of ~0.2 eV. We explain it as a surface resonance related to the L-gap Shockley surface state. After extensive analysis of the EDCs, we report the observation of a weak spin-orbit splitting for this electronic state, with a momentum shift of ~0.2 $Å^{-1}$. Theoretical predictions support the existence of the Rashba splitting for the $\overline{Y}$ point surface state of Au(110)-(1x1).

In the direction parallel to the atomic rows, a surface resonance S1 is observed near $\overline{X}'$ point. This electronic state exhibits a split band (labelled S2) and also mirror reflections with respect to $\overline{X}'$ (bands S1', S2'). The splitting is strong and it depends on the long range ordering of (1x2) domains. An analysis of the dispersion (at constant binding energy) along $\overline{X'S}$ direction shows an almost straight behaviour of the surface state, and that the splitting disappears at $\overline{S}'$ point and then appears again. We interpret this behaviour taking into account

the surface symmetry and the additional symmetry induced by the reconstruction, and explain the splitting observed based on the properties of both.

A Au(110)-(1x1) (unreconstructed) surface was obtained in two different ways. The first method was heating the Au(110) crystal above the order-disorder phase transition. ARPES results show that the surface resonance is seen only at $\bar{Y}$ point in the unreconstructed surface, with a smaller binding energy. Under some circumstances, the surface resonance is still seen at $\bar{\Gamma}$ point, indicating that there are local (1x2) areas of sufficient size to produce the surface folding. The splitting of the S1 state at $\bar{X}'$ point is not observed in the unreconstructed surface, (no evidence of the S2 state). We conclude that the splitting is related to the (1x2) folding. The second method to obtain the unreconstructed surface is the evaporation of Au on the (1x2) reconstructed surface. After a controlled evaporation, local disorder is produced and a (1x1) LEED pattern is observed. In addition, in this case the surface resonance appears only at $\bar{Y}$ point and the surface state S1 of $\bar{X}'$ point is observed, but without any splitting.

There is still some discrepancy in theoretical calculations concerning the existence of a gap at $\bar{\Gamma}'$ in the occupied part of the band structure and for the reconstructed surface. While some calculations predict that the gap is above the Fermi energy, other calculations find that the gap reaches also the occupied part of the band structure. ARPES measurements conclude that the surface resonance state at $\bar{\Gamma}'$ exists for the (1x2) reconstructed surface, even with a weak spin-orbit splitting.

Surface states on vicinal Beryllium surfaces: two-dimensional quantum well states.

Single-crystalline surfaces of beryllium vicinal to the $(10\bar{1}0)$ direction have been analysed using ARPES. The different miscut angles available allowed us to analyse the electronic behaviour in a range of terrace sizes. Due to the specific properties of the hcp lattice, there are two different types of steps in the $(10\bar{1}0)$ surface, so that each terrace contains two different subterraces.

The available samples were cut with 2.95º, 4.48º, 6.06º, and 9º angles along (0001) direction, although actual values (determined from Laue diffraction) varied slightly from the nominal values.

The cleaning process (a difficult issue for these crystals) and the ordering of the vicinal $(10\bar{1}0)$ crystals was studied using STM, LEED and XPS techniques. STM was

used to check cleanliness and ordering. A rectangular LEED pattern with extra spots along (0001) direction is observed, in agreement with the expected behaviour for a vicinal $(10\bar{1}0)$ surface. Split spots are observed predominantly along $\overline{\Gamma A}$ direction, indicating an overall good and regular step superlattice. However, weaker spots along $\overline{\Gamma M}$ direction indicate a minor contribution of facets and/or imperfections. For most miscuts, LEED patterns present not only the nominal periodicity, but also additional, minor contributions from other periodicities. In the case of the two smaller miscuts (2.95º and 4.48º) the quality of the LEED patterns was worse than for the larger miscuts, suggesting that the formation of well-ordered large terraces is more difficult, at least for these particular orientations.

The electronic structure was analysed using ARPES. The most intense state is a surface resonance state SR at $\bar{\Gamma}$ point. The binding energy of this state is close to the recent experimental and theoretical results for the $(10\bar{1}0)$ surface. This state was observed for all miscuts and its dispersion was followed along two high symmetry directions, parallel and perpendicular to steps. Two other surface states S1 and S2 were found at $\bar{A}$ point. Their binding energy changes with the miscut angle, so that the values in the flat surface are deeper than in the vicinal, as expected for the confinement by a step superlattice. The position of the minimum of the surface state S1 in parallel momentum (structure plot) confirms that the electron wave function is referred to the terrace direction.

New extra peaks were observed between the surface resonance state SR and the Fermi level edge. These new states correspond to the quantization of the SR band. Measurements along and perpendicular to steps for several photon energies allowed us to obtain a complete characterization of the new states. The surface bands are not dispersing in the range of ±0.2 $Å^{-1}$ for all photon energies along the $\overline{\Gamma A}$ direction (perpendicular to the steps). In turn, the surface bands) are dispersing with free electron like behaviour along $\overline{\Gamma M}$ direction (parallel to the steps). This behaviour is in complete agreement with the formation of two-dimensional quantum well states. The QWS binding energies were explained using an infinite wall model. The terrace width required is consistent with the LEED values for the samples with smaller terraces (6.06º and 9º). In the case of the samples with larger terraces, the sample quality in terms of long range order and homogeneity was not sufficient to use this simple model.

Surface electronic structure of A_{III}–B_V semiconductors and temperature dependence

InSb(001) and InAs(001) with a c(8x2) reconstruction have been studied using LEED, STM and ARPES from room temperature to 5 K. A temperature induced phase transition is observed for InAs(001)(4x2)-c(8x2) at ~120 K, related to a doubling of the periodicity along [110] direction in LEED patterns. The extra periodicity is also observed in STM images. In the case of InSb(001)-c(8x2), no temperature induced changes are detected in the LEED pattern. However, STM investigations have found also a doubling of periodicity at low temperature. The phase transition is related to freezing of mobile vacants and adatoms at low temperature.

We have characterized the bulk and surface electronic structure using ARPES for both semiconductors. The bulk bands dispersion along ΓX direction has been determined with great accuracy and results compared to theoretical predictions. The location of Γ_6, Γ_7, Γ_8 bands has been determined. Γ_7 (B7) represents the spin-orbit split off band. Γ_8 exhibits the know splitting in heavy and light hole bands away from the Γ bulk point. These bulk bands disperse along $\overline{\Gamma J'}$ and $\overline{\Gamma J}$ directions. Next to identified bulk states, there are additional electronic states that do not disperse with photon energies. These electronic states are identified in most cases with surface states, grouped as: S1 group (S1, S1'), S2 group (S2, S2'), and S3 group (S3, S3'). The binding energies are different for InSb and InAs. STS measurements confirm the existence of these surface states. S1, which is close to the Fermi energy, presents a fourfold periodicity along $\overline{\Gamma J'}$ and onefold along $\overline{\Gamma J}$ for the both crystals. We have identified it as a last layer filled bond state, specific to the ζ-structure model, and related to In4-As7 and In5-As8 bonds, which are not identical. This origin explains also the observed splitting for the InSb(001)-c(8x2). In agreement with this model, the InSb(001)-c(8x2) surface is found to be semiconducting. Other groups of surface states (S2, S3) are shifted to larger values of binding energy for both III-V semiconductors. These states are mixed with bulk bands, and do not exhibit a clear periodicity along $\overline{\Gamma J'}$ and $\overline{\Gamma J}$ directions.

In the case of InSb(001)-c(8x2), ARPES detects no changes in the electronic structure upon decreasing the temperature, with the exception of a uniform shift related to the observed stabilization of a surface photovoltage. The electronic structure of InAs(001)(4x2)-c(8x2) shows a negligible shift in binding energy during the cooling of the crystal. This is due to the occupation of the CB and the formation of a surface accumulation layer in this crystal. New states appear close to the Fermi level, due to the effect of the charge accumulation on the surface. The accumulation layer forms a 2D electron gas in a 1D potential well, generating

an electron confining barrier in the direction perpendicular to the surface plane. The accumulation layer has stronger intensity at low photon energies (10-17 eV), which correspond to probing the valence band and conduction band edges. The accumulation layer is observed near $\bar{\Gamma}_{c(8x2)}$ point due to this fact, but it repeats with the surface periodicity, which corresponds to the c(8x2) reconstruction.

The new electronic states resulting from the confinement are identified and characterized. Three of the peaks are fairly intense, and their dispersion can be followed in reciprocal space. On the basis of theoretical calculations and an analysis of the line shape, ten QWS peaks are identified, although some are very weak. Half of them correspond to loss peaks, related to a strong coupling with surface plasmons.

Bibliography

[1] N. Taniguchi, "On the basic concept of 'nano-technology'", *Proceedings of the International Conference of Production EngineeringSociety of Precision Engineering*, 1974.

[2] J. J. Ramsden and J. Freeman, "The nanoscale", *Nanotechnol. Perceptions*, vol. 5, pp. 3–26, 2009.

[3] J. Ramsden, *Applied Nanotechnology*, Cranfield University, UK: Elsevier Ltd, 2009.

[4] H. Hertz, "Über einen Einfluss des ultravioletten Lichtes auf die electrische Entladung", *Ann. der Phys. und Chemie*, vol. 267, no. 8, pp. 983–1000, 1887.

[5] A. Einstein, "Über einen die Erzeugung und Verwandlung des Lichtes betreffenden heuristischen Gesichtspunkt," *Ann. Phys.*, vol. 322, no. 6, pp. 132–148, 1905.

[6] J. R. Smith, S. K. Lyo, R. Gomer, L. D. Schmidt, D. Menzel, E. W. Plummer, E. Bauer, and M. Boudart, *Interactions on Metal Surfaces (Topics in Applied Physics)*, Springer, 1975, p. 310.

[7] M. P. Seah and W. A. Dench, "Quantitative electron spectroscopy of surfaces: A standard data base for electron inelastic mean free paths in solids", *Surf. Interface Anal.*, vol. 1, no. 1, pp. 2–11, 1979.

[8] F. J. Himpsel, "Angle-resolved measurements of the photoemission of electrons in the study of solids", *Adv. Phys.*, vol. 32, no. 1, pp. 1–51, 1983.

[9] I. Tamm, "On the possible bound states of electrons on a crystal surface", *Phys. Z. Sov. Union.*, vol. 1, no. 733, 1932.

[10] W. Shockley, "On the Surface States Associated with a Periodic Potential", *Phys. Rev.*, vol. 56, no. 4, pp. 317–323, 1939.

[11] H. Lüth, *Solid Surfaces, Interfaces and Thin Films*, Berlin, Heidelberg: Springer Berlin Heidelberg, 2010.

[12] F. Reinert and S. Hüfner, "Photoemission spectroscopy—from early days to recent applications", *New J. Phys.*, vol. 7, no. 1, p. 97, 2005.

[13] E. W. Plummer and W. Eberhardt, "Angle-Resolved Photoemission as a Tool for the Study of Surfaces", *Advances in Chemical Physics*, John Wiley & Sons, Inc., 2007, pp. 533–656.

[14] S. Hüfner, *Photoelectron Spectroscopy: Principles and Applications*, Springer-Verlag, 1995.

[15] J. Martinez-Blanco, "macro ESPECTROSCOPIA", Madrid, Spain, 2006.

[16] V. Joco, “Scientific code FLAN”, Madrid, Spain, 2008.

[17] P. Thiry, “La photoemission angulaire dans les solides structure elecronique de volume et de surface du cuivre”, Université de Paris-Sud, Paris.

[18] J. Martinez-Blanco, “Mecanismos electrónicos de estabilización de superestructuras metálicas y moleculares en superficies de cobre”, Universidad Autónoma de Madrid, Madrid, Spain, 2007.

[19] E. O. Kane, “Implications of Crystal Momentum Conservation in Photoelectric Emission for Band-Structure Measurements”, *Phys. Rev. Lett.*, vol. 12, no. 4, pp. 97–98, 1964.

[20] T. Balasubramanian’s, “Measurements of the hole lifetimes and the electron phonon coupling parameter λ at the surface of the Be(0001) by Angle Resolved Photoemission”, Brandeis University, 1997.

[21] J. J. Kolodziej, B. Such, M. Goryl, F. Krok, P. Piatkowski, and M. Szymonski, “Surface structure investigations using noncontact atomic force microscopy”, *Appl. Surf. Sci.*, vol. 252, no. 21, pp. 7614–7623, 2006.

[22] Prevac, “The 5 Axes LN2 Manipulator with X, Y, Z, R1, R2 Axes Motorised”, Rogow, Poland, 2005.

[23] Prevac, “Heating Power Supply HEAT2-PS”, Rogow, Poland, 2005.

[24] VGScienta, “Electron Spectrometer Scienta R4000”, Uppsala, Sweden, 2011.

[25] VGScienta, “Electron Spectrometer SCIENTA DA30”, Uppsala, Sweden, 2013.

[26] “CELLS - ALBA Synchtrontron Facility, Cerdanyola de Valles, Spain”, [Online], Available: http://www.cells.es/.

[27] “Beamline APE, ELETTRA Synchtrontron Facility, Barssoviza, Italy”, [Online], Available: http://www.elettra.trieste.it/experiments/beamlines/ape/index.html.

[28] “Beamline I4, MaxIV, Lund, Sweden”, [Online], Available: http://www.maxlab.lu.se/beamline/max-iii/i4/i4.html. [Online] .

[29] “Beamline Cassioppe, Soleil Synchrotron Facility, Saint Aubin, France”, [Online], Available: http://www.synchrotron-soleil.fr/Recherche/LignesLumiere/CASSIOPEE.

[30] G. Binnig, H. Rohrer, C. Gerber, and E. Weibel, “Surface Studies by Scanning Tunneling Microscopy”, *Phys. Rev. Lett.*, vol. 49, no. 1, pp. 57–61, 1982.

[31] I. Horcas, R. Fernández, J. M. Gómez-Rodríguez, J. Colchero, J. Gómez-Herrero, and A. M. Baro, “WSxM: A software for scanning probe microscopy and a tool for nanotechnology”, *Rev. Sci. Instrum.*, vol. 78, no. 1, 2007.

[32] J. Tersoff and D. R. Hamann, “Theory of the scanning tunneling microscope”, *Phys. Rev. B*, vol. 31, no. 2, pp. 805–813, 1985.

[33] J. Tersoff and D. R. Hamann, “Theory and Application for the Scanning Tunneling Microscope”, *Phys. Rev. Lett.*, vol. 50, no. 25, pp. 1998–2001, 1983.

[34] D. Wolf, H. Jagodzinski, and W. Moritz, “Diffuse LEED intensities of disordered crystal surfaces : III. LEED investigation of the disordered (110) surface of gold”, *Surf. Sci.*, vol. 77, pp. 265–282, 1978.

[35] W. Moritz and D. Wolf, “Structure determination of the reconstructed Au(110) surface”, *Surf. Sci.*, vol. 88, no. 2–3, pp. L29–L34, Oct. 1979.

[36] P. Fenter and T. Gustafsson, “Structural analysis of the Pt(110)-(1x2) surface using medium-energy ion scattering”, *Phys. Rev. B*, vol. 38, no. 15, pp. 10197–10204, 1988.

[37] M. A. Krzyzowski, P. Zeppenfeld, C. Romainczyk, R. David, G. Comsa, K. E. Kuhnke, and K. Kern, “Thermal disordering of the Pt(110)-(1x2) surface”, *Phys. Rev. B*, vol. 50, no. 24, pp. 18505–18516, 1994.

[38] C.-M. Chan, M. A. van Hove, W. H. Weinberg, and E. D. Williams, “Structural study of the reconstructed Ir(110)-(1 x 2) surface by low-energy electron diffraction”, *Solid State Commun.*, vol. 30, no. 1, pp. 47–49, Apr. 1979.

[39] E. C. Sowa, M. A. Van Hove, and D. L. Adams, “The missing-row model for the reconstructed Pt(110)−(1×2) surface: A leed intensity analysis showing multilayer distortions”, *Surf. Sci.*, vol. 199, no. 1–2, pp. 174–182, 1988.

[40] P. Fery, W. Moritz, and D. Wolf, “Structure determination of the (1x2) and (1x3) reconstructions of Pt(110) by low-energy electron diffraction”, *Phys. Rev. B*, vol. 38, no. 11, pp. 7275–7286, 1988.

[41] M. Shi, H. Bu, and J. W. Rabalais, “Analysis of the reconstructed Ir(110) surface from time-of-flight scattering and recoiling spectrometry”, *Phys. Rev. B*, vol. 42, no. 5, pp. 2852–2863, 1990.

[42] Y. Kuk, L. C. Feldman, and I. K. Robinson, “Atomic displacements in the Au(110)-(1×2) surface”, *Surf. Sci.*, vol. 138, no. 2–3, pp. L168–L174, Mar. 1984.

[43] H. P. Bonzel and S. Ferrer, “A new model for the reconstructed (110)-1x2 surface of Ir, Pt and Au”, *Surf. Sci. Lett.*, vol. 118, pp. 263–268, 1982.

[44] M. Landmann, E. Rauls, and W. G. Schmidt, “First-principles calculations of clean Au(110) surfaces and chemisorption of atomic oxygen”, *Phys. Rev. B*, vol. 79, no. 4, p. 45412, 2009.

[45] A. Nuber, M. Higashiguchi, F. Forster, P. Blaha, K. Shimada, and F. Reinert, “Influence of reconstruction on the surface state of Au(110)”, *Phys. Rev. B*, vol. 78, no. 19, p. 195412, Nov. 2008.

[46] I. K. Robinson, “Direct Determination of the Au(110) Reconstructed Surface by X-Ray Diffraction”, *Phys. Rev. Lett.*, vol. 50, no. 15, pp. 1145–1148, 1983.

[47] W. Moritz and D. Wolf, “Multilayer distortion in the reconstructed (110) surface of Au”, *Surf. Sci. Lett.*, vol. 163, no. 1, pp. L655–L665, Nov. 1985.

[48] E. Vlieg, I. K. Robinson, and K. Kern, “Relaxations in the missing-row structure of the (1×2) reconstructed surfaces of Au(110) and Pt(110)”, *Surf. Sci.*, vol. 233, no. 3, pp. 248–254, Jul. 1990.

[49] T. Gritsch, D. Coulman, T. J. Behm, and G. Ertl, “A scanning tunneling microscopy investigation of the structure of the Pt(110) and Au(110) surface”, *Surf. Sci.*, vol. 257, pp. 297–306, 1991.

[50] G. Binnig, H. Rohrer, C. Gerber, and E. Weibel, “Surface Studies by Scanning Tunneling Microscopy”, *Phys. Rev. Lett.*, vol. 49, no. 1, pp. 57–61, 1982.

[51] R. A. Bartynski and T. Gustafsson, “Experimental study of surface states on the (110) faces of the noble metals”, *Phys. Rev. B*, vol. 33, no. 10, pp. 6588–6598, 1986.

[52] C. H. Xu, K. M. Ho, and K. P. Bohnen, “Self-consistent calculation of the surface electronic structure of the (1x2) reconstructed Au(110) surface”, *Phys. Rev. B*, vol. 39, no. 9, pp. 5599–5604, Mar. 1989.

[53] K.-M. Ho and K. P. Bohnen, “Determination of the Geometry of the Reconstructed Au (110) Surface with First Principles Total-Energy Calculations”, *Europhys. Lett.*, vol. 4, no. 3, pp. 345–349, 1987.

[54] M. Sastry, K. C. Prince, D. Cvetko, A. Morgante, and F. Tommasini, “Photoemission investigation of the reconstructed Au(110) surface”, *Surf. Sci.*, vol. 271, no. 1–2, pp. 179–183, Jan. 1992.

[55] V. Theileis and H. Bross, “Relativistic modified augmented plane wave method and its application to the electronic structure of gold and platinum”, *Phys. Rev. B*, vol. 62, no. 20, pp. 13338–13346, Nov. 2000.

[56] P. Heimann, J. Hermanson, H. Miosga, and H. Neddermeyer, “Photoemission observation of a new surface state band on Cu(110)”, *Surf. Sci.*, vol. 85, no. 2, pp. 263–268, Jul. 1979.

[57] A. Gerlach, G. Meister, R. Matzdorf, and A. Goldmann, “High-resolution photoemission study of the $\bar{Y}$ surface state on Ag(110)”, *Surf. Sci.*, vol. 443, no. 3, pp. 221–226, Dec. 1999.

[58] F. Reinert, G. Nicolay, S. Schmidt, D. Ehm, and S. Hüfner, “Direct measurements of the L-gap surface states on the (111) face of noble metals by photoelectron spectroscopy”, *Phys. Rev. B*, vol. 63, no. 11, p. 115415, Mar. 2001.

[59] S. LaShell, B. A. McDougall, and E. Jensen, “Spin Splitting of an Au(111) Surface State Band Observed with Angle Resolved Photoelectron Spectroscopy”, *Phys. Rev. Lett.*, vol. 77, no. 16, pp. 3419–3422, 1996.

[60] E. V. Chulkov, “Bulk band calculations of the Au(110)”, San Sebastian, Spain, 2006.

[61] P. Heimann, H. Miosga, and H. Neddermeyer, “Occupied Surface-State Bands in sp Gaps of Au(112), Au(110), and Au(100) Faces”, *Phys. Rev. Lett.*, vol. 42, no. 12, pp. 801–804, Mar. 1979.

[62] R. Courths, S. Hüfner, P. Kemkes, and G. Wiesen, “Electronic structure investigation of Cu(110), Ag(110) and Ni(110) surfaces covered with chemisorbed oxygen up to half a monolayer”, *Surf. Sci.*, vol. 376, no. 1–3, pp. 43–59, Apr. 1997.

[63] S. H. Liu, C. Hinnen, C. Nguyen Van Huong, N. R. de Tacconi, and K.-M. Ho, “Surface state effects on the electroreflectance spectroscopy of Au single crystal surfaces”, *J. Electroanal. Chem. Interfacial Electrochem.*, vol. 176, no. 1–2, pp. 325–338, Sep. 1984.

[64] S. LaShell, B. A. McDougall, and E. Jensen, “Spin Splitting of an Au(111) Surface State Band Observed with Angle Resolved Photoelectron Spectroscopy”, *Phys. Rev. Lett.*, vol. 77, no. 16, pp. 3419–3422, Oct. 1996.

[65] L. Petersen and P. Hedegård, “A simple tight-binding model of spin-orbit splitting of sp-derived surface states”, *Surf. Sci.*, vol. 459, no. 1–2, pp. 49–56, Jul. 2000.

[66] G. Nicolay, F. Reinert, S. Hüfner, and P. Blaha, “Spin-orbit splitting of the L-gap surface state on Au(111) and Ag(111)”, *Phys. Rev. B*, vol. 65, no. 3, p. 33407, 2001.

[67] J. Henk, A. Ernst, and P. Bruno, “Spin polarization of the L-gap surface states on Au(111): a first-principles investigation”, *Surf. Sci.*, vol. 566–568, pp. 482–485, Sep. 2004.

[68] M. Nagano, A. Kodama, T. Shishidou, and T. Oguchi, “A first-principles study on the Rashba effect in surface systems”, *J. Phys. Condens. Matter*, vol. 21, no. 6, p. 064239, Feb. 2009.

[69] E. Simon, a. Szilva, B. Ujfalussy, B. Lazarovits, G. Zarand, and L. Szunyogh, “Anisotropic Rashba splitting of surface states from the admixture of bulk states: Relativistic ab initio calculations and k·p perturbation theory”, *Phys. Rev. B*, vol. 81, no. 23, p. 235438, Jun. 2010.

[70] R. Courths, H. Wern, U. Hau, B. Cord, V. Bachelier, and S. Hufner, “Band structure of Cu, Ag and Au: location of direct transitions on the Λ line using angle-resolved photoelectron spectroscopy (ARUPS)”, *J. Phys. F Met. Phys.*, vol. 14, no. 6, pp. 1559–1572, Jun. 1984.

[71] J. C. Campuzano, G. Jennings, and R. F. Willis, “The critical exponents of the Au(110) (1×2) ↔ (1×1) phase transition”, *Surf. Sci.*, vol. 162, no. 1–3, pp. 484–494, Oct. 1985.

[72] J. C. Campuzano, M. S. Foster, G. Jennings, R. F. Willis, and W. Unertl, “Au(110) (1x2)-to-(1x1) Phase Transition: A Physical Realization of the Two-Dimensional Ising Model”, *Phys. Rev. Lett.*, vol. 54, no. 25, pp. 2684–2687, 1985.

[73] J. Villain and I. Vilfan, “Surface deconstruction of Au(110)”, *Surf. Sci.*, vol. 199, no. 1–2, pp. 165–173, Jan. 1988.

[74] S. H. Overbury, W. Heiland, D. M. Zehner, S. Datz, and R. S. Thoe, “Investigation of the structure of Au(110) using angle resolved low energy K+ ion backscattering”, *Surf. Sci.*, vol. 109, no. 1, pp. 239–262, Aug. 1981.

[75] H. Derks, H. Hemme, W. Heiland, and S. H. Overbury, “Low energy ion scattering from the Au(110) surface - structural results”, *Nucl. Instruments Methods Phys. Res. Sect. B Beam Interact. with Mater. Atoms*, vol. 23, no. 3, pp. 374–378, May 1987.

[76] H. Derks, J. Möller, and W. Heiland, “The Temperature Dependence of the Near Order Structure of Au(110) Studied by Ion Scattering Spectrometry (ISS)”, *The Structure of Surfaces II SE - 81*, vol. 11, J. Veen and M. Hove, Eds. Springer Berlin Heidelberg, 1988, pp. 496–501.

[77] E. van de Riet, H. Derks, and W. Heiland, “Observation of pre-phase transitional phenomena on an Au(110) surface”, *Surf. Sci.*, vol. 234, no. 1–2, pp. 53–62, Aug. 1990.

[78] G. Mazzeo, G. Jug, A. C. Levi, and E. Tosatti, “Monte Carlo study of phase transitions and scattering intensities in a model of Au(110)”, *Surf. Sci.*, vol. 273, no. 1–2, pp. 237–251, Jun. 1992.

[79] D. T. Keane, P. A. Bancel, J. L. Jordan-Sweet, G. A. Held, A. Mak, and R. J. Birgeneau, “Evidence for two-step disordering of the Au(110)−1×2 reconstructed surface”, *Surf. Sci.*, vol. 250, no. 1–3, pp. 8–16, Jul. 1991.

[80] H. Göbel and P. von Blanckenhagen, “A study of surface diffusion on gold with an atomic force microscope”, *Surf. Sci.*, vol. 331–333, pp. 885–890, Jul. 1995.

[81] P. Kleban, R. Hentschke, and J. C. Campuzano, “Conformal field theory and the Au(110) (1x2)-to-(1x1) phase transition”, *Phys. Rev. B*, vol. 37, no. 10, pp. 5738–5743, 1988.

[82] M. Sturmat, R. Koch, and K. Rieder, “Real Space Investigation of the Roughening and Deconstruction Transitions of Au(110)”, *Phys. Rev. Lett.*, vol. 77, no. 25, pp. 5071–5074, Dec. 1996.

[83] R. Koch and M. Sturmat, “Real space investigation of the Ising transition of Pt(110)”, *Surf. Sci.*, vol. 385, no. 2–3, pp. L997–L1001, Aug. 1997.

[84] R. Koch and M. Sturmat, “High-temperature STM of the phase transitions of Au(110) and Pt(110)”, *Surf. Sci.*, vol. 402–404, pp. 861–865, May 1998.

[85] R. Koch, M. Sturmat, and J. J. Schulz, “High-temperature STM investigation of Au(110), Pt(110) and Ag(110)”, *Surf. Sci.*, vol. 454–456, pp. 543–551, May 2000.

[86] M. J. Rost, S. B. van Albada, and J. W. M. Frenken, “Domain boundary formation on Au(110)”, *Europhys. Lett.*, vol. 59, no. 4, pp. 559–565, Aug. 2002.

[87] M. J. Rost, S. B. van Albada, and J. W. M. Frenken, “Thermally activated domain boundary formation on a missing row reconstructed surface: Au(110)”, *Surf. Sci.*, vol. 547, no. 1–2, pp. 71–84, Dec. 2003.

[88] P. Heimann, J. F. van der Veen, and D. E. Eastman, “Structure-dependent surface core level shifts for the Au(111), (100), and (110) surfaces”, *Solid State Commun.*, vol. 38, no. 7, pp. 595–598, May 1981.

[89] K.-M. Ho and K. P. Bohnen, “Stability of the Missing-Row Reconstructtion on the fcc (110) Transition-Metal Surface”, *Phys. Rev. Lett.*, vol. 59, no. 16, pp. 1833–1836, 1987.

[90] P. Thiry, D. Chandesris, J. Lecante, C. Guillot, R. Pinchaux, and Y. Pétroff, “E vs k and Inverse Lifetime of Cu(110)”, *Phys. Rev. Lett.*, vol. 43, no. 1, pp. 82–85, 1979.

[91] V. Joco, “Scientific code ELAN”, Madrid, Spain, 2008.

[92] M. Lindroos and A. Bansil, “A Novel Direct Method of Fermi Surface Determination Using Constant Initial Energy Angle-Scanned Photoemission Spectroscopy”, *Phys. Rev. Lett.*, vol. 77, no. 14, pp. 2985–2988, 1996.

[93] J. Martinez-Blanco, “UPS macro for IGOR software”, Madrid, Spain, 2006.

[94] E. Simon, B. Ujfalussy, A. Szilva, and L. Szunyogh, “Anisotropy of exchange interactions between impurities on Cu(110) surface”, *J. Phys. Conf. Ser.*, vol. 200, no. 3, p. 032067, Jan. 2010.

[95] D. Wolf, H. Jagodzinski, and W. Moritz, “Diffuse LEED intensities of disordered crystal surfaces”, *Surf. Sci.*, vol. 77, no. 2, pp. 283–300, Oct. 1978.

[96] J. E. Ortega, S. Speller, A. R. Bachmann, A. Mascaraque, E. G. Michel, A. Närmann, A. Mugarza, A. Rubio, and F. J. Himpsel, “Electron Wave Function at a Vicinal Surface: Switch from Terrace to Step Modulation”, *Phys. Rev. Lett.*, vol. 84, no. 26, pp. 6110–6113, 2000.

[97] J. Lobo, E. G. Michel, A. R. Bachmann, S. Speller, J. Kuntze, and J. E. Ortega, “Tuning the Surface State Dimensionality of Cu Nanostripes”, *Phys. Rev. Lett.*, vol. 93, no. 13, p. 137602, 2004.

[98] J. Lobo and A. Mascaraque, “Observation of the noble-metal L-gap surface state in Cu(311)”, *J. Phys. Condens. Matter*, vol. 18, no. 31, pp. L395–L400, Aug. 2006.

[99] S.-C. Wang, M. B. Yilmaz, K. R. Knox, N. Zaki, J. I. Dadap, T. Valla, P. D. Johnson, and R. M. Osgood, “Electronic structure of a Co-decorated vicinal Cu(775) surface:

High-resolution photoemission spectroscopy", *Phys. Rev. B*, vol. 77, no. 11, p. 115448, Mar. 2008.

[100] A. Mugarza, A. Mascaraque, V. Pérez-Dieste, V. Repain, S. Rousset, F. J. de Abajo, and J. E. Ortega, "Electron Confinement in Surface States on a Stepped Gold Surface Revealed by Angle-Resolved Photoemission", *Phys. Rev. Lett.*, vol. 87, no. 10, p. 107601, 2001.

[101] T. Zambelli, J. Wintterlin, J. Trost, and G. Ertl, "Identification of the 'Active Sites' of a Surface-Catalyzed Reaction", *Science (80)*, vol. 273, no. 5282, pp. 1688–1690, Sep. 1996.

[102] C. E. Tripa and J. T. Yates, "Surface-aligned reaction of photogenerated oxygen atoms with carbon monoxide targets", *Nature*, vol. 398, 1999.

[103] F. J. Himpsel, J. E. Ortega, G. J. Mankey, and R. F. Willis, "Magnetic nanostructures", *Adv. Phys.*, vol. 47, no. 4, pp. 511–597, 1998.

[104] J. E. Ortega, A. Mugarza, A. Närmann, A. Rubio, S. Speller, A. R. Bachmann, J. Lobo, E. G. Michel, and F. J. Himpsel, "Transition from terrace to step modulation in the surface state wave function at vicinal Cu(111)", *Surf. Sci.*, vol. 482–485, pp. 764–769, Jun. 2001.

[105] R. A. Bartynski, E. Jensen, T. Gustafsson, and E. W. Plummer, "Angle-resolved photoemission investigation of the electronic structure of Be: Surface states", *Phys. Rev. B*, vol. 32, no. 4, pp. 1921–1926, 1985.

[106] T. Balasubramanian, L. I. Johansson, P.-A. Glans, C. Virojanadara, V. M. Silkin, E. V. Chulkov, and P. M. Echenique, "Surface electronic band structure and Ā surface state lifetimes at the Be(10$\bar{1}$0) surface: Experiment and theory", *Phys. Rev. B*, vol. 64, no. 20, p. 205401, Oct. 2001.

[107] V. M. Silkin, T. Balasubramanian, E. V. Chulkov, A. Rubio, and P. M. Echenique, "Surface-state hole decay mechanisms: The Be(0001) surface", *Phys. Rev. B*, vol. 64, no. 8, p. 085334, 2001.

[108] T. Balasubramanian, P.-A. Glans, and L. I. Johansson, "Electron-phonon mass-enhancement parameter and the Fermi-line eccentricity at the Be(10$\bar{1}$0) surface from angle-resolved photoemission", *Phys. Rev. B*, vol. 61, no. 19, pp. 12709–12712, 2000.

[109] P. Hofmann, K. Pohl, R. Stumpf, and E. W. Plummer, "Geometric structure of Be(10$\bar{1}$0)", *Phys. Rev. B*, vol. 53, no. 20, pp. 13715–13719, 1996.

[110] S.-J. Tang, P. Sprunger, and E. Plummer, "Electron-phonon coupling and temperature-dependent shift of surface states on Be(10$\bar{1}$0)", *Phys. Rev. B*, vol. 65, no. 23, p. 235428, Jun. 2002.

[111] S.-J. Tang, J. Shi, B. Wu, P. T. Sprunger, W. L. Yang, V. Brouet, X. J. Zhou, Z. Hussain, Z.-X. Shen, Z. Zhang, and E. W. Plummer, "A spectroscopic view

of electron–phonon coupling at metal surfaces", *Phys. Status Solidi*, vol. 241, no. 10, pp. 2345–2352, Aug. 2004.

[112] E. W. Plummer, J. Shi, S.-J. Tang, E. Rotenberg, and S. D. Kevan, "Enhanced electron–phonon coupling at metal surfaces", *Prog. Surf. Sci.*, vol. 74, no. 1–8, pp. 251–268, Dec. 2003.

[113] M. Hengsberger, D. Purdie, P. Segovia, M. Garnier, and Y. Baer, "Photoemission Study of a Strongly Coupled Electron-Phonon System", *Phys. Rev. Lett.*, vol. 83, no. 3, pp. 592–595, 1999.

[114] I. Vobornik, J. Fujii, M. Mulazzi, G. Panaccione, M. Hochstrasser, and G. Rossi, "Surface electron bands and Fermi surface of Be(0001)", *Phys. Rev. B*, vol. 72, no. 16, p. 165424, 2005.

[115] P. T. Sprunger, "Giant Friedel Oscillations on the Beryllium (0001) Surface," *Science (80-.).*, vol. 275, no. 5307, pp. 1764–1767, Mar. 1997.

[116] T. Balasubramanian, E. Jensen, X. L. Wu, and S. L. Hulbert, "Large value of the electron-phonon coupling parameter ($\lambda = 1.15$) and the possibility of surface superconductivity at the Be(0001) surface", *Phys. Rev. B*, vol. 57, no. 12, pp. R6866–R6869, Mar. 1998.

[117] E. V. Chulkov, V. M. Silkin, and E. N. Shirykalov, "Surface electronic structure of Be(0001) and Mg(0001)", *Surf. Sci.*, vol. 188, no. 1–2, pp. 287–300, Sep. 1987.

[118] P. J. Feibelman and R. Stumpf, "Physics of the Be(0001) surface core-level spectrum", *Phys. Rev. B*, vol. 50, no. 23, pp. 17480–17486, 1994.

[119] L. I. Johansson, H. I. P. Johansson, J. N. Andersen, E. Lundgren, and R. Nyholm, "Three surface-shifted core levels on Be(0001)", *Phys. Rev. Lett.*, vol. 71, no. 15, pp. 2453–2456, 1993.

[120] P. Hofmann, R. Stumpf, V. M. Silkin, E. V. Chulkov, and E. W. Plummer, "The electronic structure of Be($10\bar{1}0$)", *Surf. Sci.*, vol. 355, no. 1–3, pp. L278–L282, Jun. 1996.

[121] I. Y. Sklyadneva, R. Heid, P. M. Echenique, K.-P. Bohnen, and E. V Chulkov, "Electron-phonon coupling in surface electronic states on Be($10\bar{1}0$)", *Phys. Rev. B*, vol. 83, no. 19, p. 195437, 2011.

[122] V. M. Silkin and E. V. Chulkov, "Electronic structure of the Be($10\bar{1}0$) surface", *Phys. Solid State*, vol. 37, no. 9, pp. pp.1540–1546, 1995.

[123] M. Milun, P. Pervan, and D. P. Woodruff, "Quantum well structures in thin metal films: simple model physics in reality?", *Reports Prog. Phys.*, vol. 65, no. 2, pp. 99–141, Feb. 2002.

[124] J. E. Ortega and F. J. Himpsel, "Quantum well states as mediators of magnetic coupling in superlattices", *Phys. Rev. Lett.*, vol. 69, no. 5, pp. 844–847, 1992.

[125] R. K. Kawakami, E. Rotenberg, E. J. Escorcia-Aparicio, H. J. Choi, J. H. Wolfe, N. V. Smith, and Z. Q. Qiu, "Determination of the Magnetic Coupling in the Co/Cu/Co(100) System with Momentum-Resolved Quantum Well States", *Phys. Rev. Lett.*, vol. 82, no. 20, pp. 4098–4101, 1999.

[126] A. Mugarza and J. E. Ortega, "Electronic states at vicinal surfaces", *J. Phys. Condens. Matter*, vol. 15, no. 47, pp. S3281–S3310, Dec. 2003.

[127] E. Rotenberg, Y. Z. Wu, J. M. An, M. A. Van Hove, A. Canning, L. W. Wang, and Z. Q. Qiu, "Non-free-electron momentum- and thickness-dependent evolution of quantum well states in the Cu/Co/Cu(001) system", *Phys. Rev. B*, vol. 73, no. 7, p. 75426, 2006.

[128] A. Mugarza, A. Mascaraque, V. Repain, S. Rousset, K. N. Altmann, F. J. Himpsel, Y. M. Koroteev, E. V Chulkov, F. J. de Abajo, and J. E. Ortega, "Lateral quantum wells at vicinal Au(111) studied with angle-resolved photoemission", *Phys. Rev. B*, vol. 66, no. 24, p. 245419, 2002.

[129] R. Chau, B. Doyle, S. Datta, J. Kavalieros, and K. Zhang, "Integrated nanoelectronics for the future", *Nat. Mater.*, vol. 6, no. 11, pp. 810–2, Nov. 2007.

[130] R. Chau, S. Datta, M. Doczy, B. Doyle, B. Jin, J. Kavalieros, A. Majumdar, M. Metz, and M. Radosavljevic, "Benchmarking Nanotechnology for Logic Transistor Applications", *IEEE Trans. Nanotechnol.*, vol. 4, no. 2, pp. 153–158, 2005.

[131] T. Li, M. Mastro, and A. Dadgar, *III-V Compound Semiconductors: Integration with Silicon-Based Microelectronics*, CRC Press; 1 edition, 2010, p. 603.

[132] W. Knap, J. Lusakowski, T. Parenty, S. Bollaert, a. Cappy, V. V. Popov, and M. S. Shur, "Terahertz emission by plasma waves in 60 nm gate high electron mobility transistors", *Appl. Phys. Lett.*, vol. 84, no. 13, p. 2331, 2004.

[133] V. Y. Kachorovskii and M. S. Shur, "Field effect transistor as ultrafast detector of modulated terahertz radiation", *Solid. State. Electron.*, vol. 52, no. 2, pp. 182–185, Feb. 2008.

[134] K. Lüdge, P. Vogt, W. Richter, B.-O. Fimland, W. Braun, and N. Esser, "Metallic nanostructures on Co/GaAs(001)(4×2) surfaces", *J. Vac. Sci. Technol. B Microelectron. Nanom. Struct.*, vol. 22, no. 4, p. 2008, Aug. 2004.

[135] K. Nilson, P. Palmgren, J. Åhlund, J. Schiessling, E. Göthelid, N. Mårtensson, C. Puglia, and M. Göthelid, "STM and XPS characterization of zinc phthalocyanine on InSb(001)", *Surf. Sci.*, vol. 602, no. 2, pp. 452–459, Jan. 2008.

[136] S. Godlewski, G. Goryl, A. Gourdon, J. J. Kolodziej, B. Such, and M. Szymonski, "Internal Architecture and Adsorption Sites of Violet Lander Molecules Assembled on Native and KBr-Passivated InSb(001) Surfaces", *ChemPhysChem*, vol. 10, no. 12, pp. 2026–2033, 2009.

[137] J. S. Prauzner-Bechcicki, S. Godlewski, J. Budzioch, G. Goryl, L. Walczak, P. Sehnal, I. G. Stará, I. Starý, F. Ample, C. Joachim, and M. Szymonski, "[11]Anthrahelicene on InSb(001) c(8×2): a low-temperature scanning probe microscopy study", *Chemphyschem*, vol. 11, no. 16, pp. 3522–8, Nov. 2010.

[138] W. G. Schmidt, "III-V compound semiconductor (001) surfaces", *Appl. Phys. A Mater. Sci. Process.*, vol. 75, no. 1, pp. 89–99, Jul. 2002.

[139] A. Ohtake, "Surface reconstructions on GaAs(001)", *Surf. Sci. Rep.*, vol. 63, no. 7, pp. 295–327, Jul. 2008.

[140] J. J. K. Lång, M. P. J. Punkkinen, P. Laukkanen, M. Kuzmin, V. Tuominen, M. Pessa, M. Guina, I. J. Väyrynen, K. Kokko, B. Johansson, and L. Vitos, "Ab initio and scanning tunneling microscopy study of an indium-terminated GaAs(100) surface: An indium-induced surface reconstruction change in the c(8×2) structure", *Phys. Rev. B*, vol. 81, no. 24, p. 245305, Jun. 2010.

[141] B. Brena, P. Palmgren, K. Nilson, S. Yu, F. Hennies, B. Agnarsson, A. Önsten, M. Månsson, and M. Göthelid, "InSb–TiOPc interfaces: Band alignment, ordering and structure dependent HOMO splitting", *Surf. Sci.*, vol. 603, no. 20, pp. 3160–3169, Oct. 2009.

[142] S.-H. Lee, W. Moritz, and M. Scheffler, "GaAs(001) Surface under Conditions of Low As Pressure: Evidence for a Novel Surface Geometry", *Phys. Rev. Lett.*, vol. 85, no. 18, pp. 3890–3893, 2000.

[143] C. Kumpf, L. D. Marks, D. Ellis, D. Smilgies, E. Landemark, M. Nielsen, R. Feidenhans'l, J. Zegenhagen, O. Bunk, J. H. Zeysing, Y. Su, and R. L. Johnson, "Subsurface Dimerization in III-V Semiconductor (001) Surfaces", *Phys. Rev. Lett.*, vol. 86, no. 16, pp. 3586–3589, 2001.

[144] C. Kumpf, D. Smilgies, E. Landemark, M. Nielsen, R. Feidenhans'l, L. Cao, J. Zegenhagen, B. O. Fimland, L. D. Marks, and D. Ellis, "Structure of metal-rich (001) surfaces of III-V compound semiconductors", *Phys. Rev. B*, vol. 64, no. 7, p. 075307, 2001.

[145] T. Mishima, N. Naruse, S. Cho, T. Kadohira, and T. Osaka, "Direct Imaging of the InSb(001)-c(8×2) Surface: Evidence for Large Anisotropy of the Reconstruction", *Phys. Rev. Lett.*, vol. 89, no. 27, p. 276105, Dec. 2002.

[146] J. J. Kolodziej, B. Such, and M. Szymonski, "Atomic Structure of InSb(001) and GaAs(001) Surfaces Imaged with Noncontact Atomic Force Microscopy", *Phys. Rev. Lett.*, vol. 90, no. 22, p. 226101, Jun. 2003.

[147] G. Goryl, D. Toton, N. Tomaszewska, J. S. Prauzner-Bechcicki, L. Walczak, A. Tejeda, A. Taleb-Ibrahimi, L. Kantorovich, E. G. Michel, and J. J. Kolodziej, "Structure of the indium-rich InSb(001) surface", *Phys. Rev. B*, vol. 82, no. 16, p. 165311, 2010.

[148] D. Toton, J. He, G. Goryl, J. J. Kolodziej, S. Godlewski, L. Kantorovich, and M. Szymonski, "Structure of InSb(001) surface", *J. Phys. Condens. Matter*, vol. 22, no. 26, p. 265001, Jul. 2010.

[149] C. Jiang, "Vacancy ordering in Co3AlCx alloys: A first-principles study", *Phys. Rev. B*, vol. 78, no. 6, p. 64206, 2008.

[150] H. Iddir, D. D. Fong, P. Zapol, P. H. Fuoss, L. A. Curtiss, G.-W. Zhou, and J. A. Eastman, "Order-disorder phase transition of the Cu(001) surface under equilibrium oxygen pressure", *Phys. Rev. B*, vol. 76, no. 24, p. 241404, 2007.

[151] T. Nakagawa, O. Ohgami, Y. Saito, H. Okuyama, M. Nishijima, and T. Aruga, "Transition between tetramer and monomer phases driven by vacancy configuration entropy on Bi/Ag(001)", *Phys. Rev. B*, vol. 75, no. 15, p. 155409, 2007.

[152] G. Goryl, O. Boelling, S. Godlewski, J. J. Kolodziej, B. Such, and M. Szymonski, "Low temperature InSb(001) surface structure studied by scanning tunneling microscopy", *Surf. Sci.*, vol. 601, no. 17, pp. 3605–3610, Sep. 2007.

[153] I. T. Ferguson, A. G. de Oliveira, and B. A. Joyce, "RHEED intensity effects during the growth of InAs, InSb and In(As,Sb) by molecular beam epitaxy", *J. Cryst. Growth*, vol. 121, no. 3, pp. 267–277, Jul. 1992.

[154] O. E. Tereshchenko, E. Placidi, D. Paget, P. Chiaradia, and A. Balzarotti, "Well-ordered (100) InAs surfaces using wet chemical treatments", *Surf. Sci.*, vol. 570, no. 3, pp. 237–244, Oct. 2004.

[155] C. Kendrick, G. LeLay, and a Kahn, "Bias-dependent imaging of the In-terminated InAs(001) (4 x 2)/c(8 x 2) surface by STM: Reconstruction and transitional defect", *Phys. Rev. B. Condens. Matter*, vol. 54, no. 24, pp. 17877–17883, Dec. 1996.

[156] W. G. Schmidt, F. Bechstedt, and J. Bernholc, "GaAs(001) surface reconstructions: geometries, chemical bonding and optical properties", *Appl. Surf. Sci.*, vol. 190, no. 1–4, pp. 264–268, May 2002.

[157] J. J. Kolodziej, B. Such, and M. Szymonski, "Imaging of c(8x2)/(4x6) GaAs(001) surface with noncontact atomic force microscopy", *Phys. Rev. B*, vol. 71, no. 16, p. 165419, 2005.

[158] G. Goryl, D. Toton, N. Tomaszewska, J. S. Prauzner-Bechcicki, L. Walczak, A. Tejeda, A. Taleb-Ibrahimi, L. Kantorovich, E. G. Michel, and J. J. Kolodziej, "Structure of the indium-rich InSb(001) surface", *Phys. Rev. B*, vol. 82, no. 16, p. 165311, Oct. 2010.

[159] H. Höchst and I. Hernández-Calderón, "Angular resolved photoemission of InSb(001) and heteroepitaxial films of α-Sn(001)", *Surf. Sci.*, vol. 126, no. 1–3, pp. 25–31, Mar. 1983.

[160] I. Hernández-Calderón and H. Höchst, “New method for the analysis of reflection high-energy electron diffraction: α-Sn(001) and InSb(001) surfaces”, *Phys. Rev. B*, vol. 27, no. 8, pp. 4961–4965, 1983.

[161] H. U. Middelmann, L. Sorba, V. Hinkel, and K. Horn, “Valence-band-structure determination of InSb by angle-resolved photoemission”, *Phys. Rev. B*, vol. 34, no. 2, pp. 957–962, 1986.

[162] L. Ö. Olsson, Y. O. Khazmi, J. Kanski, L. Ilver, P. O. Nilsson, M. C. Håkansson, and U. O. Karlsson, “Surface electronic structure of InSb(100) 4 × 1 studied by angle-resolved photoelectron spectroscopy”, *Surf. Sci.*, vol. 331–333, pp. 1176–1180, Jul. 1995.

[163] M. C. Håkansson, L. S. O. Johansson, C. B. M. Andersson, U. O. Karlsson, L. Ö. Olsson, J. Kanski, L. Ilver, and P. O. Nilsson, “The electronic structure of In- and As-terminated InAs(001) surfaces”, *Surf. Sci.*, vol. 374, no. 1–3, pp. 73–79, Mar. 1997.

[164] P. De Padova, C. Quaresima, P. Perfetti, R. Larciprete, R. Brochier, C. Richter, V. Ilakovac, P. Bencok, C. Teodorescu, V. Y. Aristov, R. L. Johnson, and K. Hricovini, “Electron accumulation layer on clean In-terminated InAs(001)(4×2)-c(8×2) surface”, *Surf. Sci.*, vol. 482–485, pp. 587–592, Jun. 2001.

[165] M. Noguchi, K. Hirakawa, and T. Ikoma, “Intrinsic electron accumulation layers on reconstructed clean InAs(100) surfaces”, *Phys. Rev. Lett.*, vol. 66, no. 17, pp. 2243–2246, 1991.

[166] J. R. Chelikowsky and M. L. Cohen, “Nonlocal pseudopotential calculations for the electronic structure of eleven diamond and zinc-blende semiconductors”, *Phys. Rev. B*, vol. 14, no. 2, pp. 556–582, 1976.

[167] R. H. Miwa, R. Miotto, and A. C. Ferraz, “In-rich (4×2) and (2×4) reconstructions of the InAs(001) surface”, *Surf. Sci.*, vol. 542, no. 1–2, pp. 101–111, Sep. 2003.

[168] J. S. Blakemore, *Semiconductor Statistics*. 2002, p. 381.

[169] P. John, T. Miller, and T.-C. Chiang, “Core-level photoemission studies of the α-Sn/InSb(100) heterostructure system”, *Phys. Rev. B*, vol. 39, no. 5, pp. 3223–3229, 1989.

[170] M. O. Schweitzer, M. Q. Ding, N. V. Richardson, T. S. Jones, and C. F. McConville, “Temperature-dependent plasmons in InSb”, *J. Phys. Condens. Matter*, vol. 3, pp. S271–S276, Nov. 1991.

[171] E. G. Michel, P. Pervan, G. R. Castro, R. Miranda, and K. Wandelt, “Structural and electronic properties of K/Si(100)2x1”, *Phys. Rev. B*, vol. 45, no. 20, pp. 11811–11822, 1992.

[172] J. E. Demuth, W. J. Thompson, N. J. Di Nardo, and R. Imbihl, “Photoemission-Based Photovoltage Probe of Semiconductor Surface and Interface Electronic Structure”, *Phys. Rev. Lett.*, vol. 56, no. 13, pp. 1408–1411, Mar. 1986.

[173] M. Alonso, R. Cimino, and K. Horn, “Surface photovoltage effects in photoemission from metal-GaP(110) interfaces: Importance for band bending evaluation”, *Phys. Rev. Lett.*, vol. 64, no. 16, pp. 1947–1950, 1990.

[174] M. H. Hecht, “Role of photocurrent in low-temperature photoemission studies of Schottky-barrier formation”, *Phys. Rev. B*, vol. 41, no. 11, pp. 7918–7921, 1990.

[175] A. Bauer, M. Prietsch, S. Molodtsov, C. Laubschat, and G. Kaindl, “Systematic study of the surface photovoltaic effect in photoemission”, *Phys. Rev. B*, vol. 44, no. 8, pp. 4002–4005, 1991.

[176] R. Cortés, A. Tejeda, J. Lobo, C. Didiot, B. Kierren, D. Malterre, E. G. Michel, and A. Mascaraque, “Observation of a Mott Insulating Ground State for Sn/Ge(111) at Low Temperature”, *Phys. Rev. Lett.*, vol. 96, no. 12, p. 126103, Mar. 2006.

[177] P. De Padova, P. Perfetti, C. Quaresima, C. Richter, O. Heckmann, M. Zerrouki, R. L. Johnson, and K. Hricovini, “New electronic surface states on In-terminated InAs(001)4×2-c(8×2) clean surface”, *Surf. Sci.*, vol. 532–535, pp. 837–842, Jun. 2003.

[178] P. De Padova, P. Perfetti, C. Quaresima, C. Richter, M. Zerrouki, O. Heckmann, V. Ilakovac, and K. Hricovini, “Surface states resonance on In-terminated InAs(001)4×2-c(8×2) clean surface”, *Appl. Surf. Sci.*, vol. 212–213, pp. 10–16, May 2003.

[179] L. Walczak, G. Goryl, M. A. Valbuena, I. Vobornik, A. Tejeda, A. Taleb-Ibrahimi, J. J. Kolodziej, P. Segovia, and E. G. Michel, “Surface electronic structure of InSb(001)-c(8×2)”, *Surf. Sci.*, vol. 608, pp. 22–30, Feb. 2013.

[180] J. Tersoff, “Schottky barriers and semiconductor band structures”, *Phys. Rev. B*, vol. 32, no. 10, pp. 6968–6971, 1985.

[181] F. Flores, R. Perez, R. Rincon, and R. Saiz-Pardo, “Electron States at Semiconductor Interfaces: The Intrinsic and Extrinsic Charge Neutrality Levels”, *Philos. Trans. R. Soc. A Math. Phys. Eng. Sci.*, vol. 344, no. 1673, pp. 567–577, Sep. 1993.

[182] W. Mönch, “Empirical tight-binding calculation of the branch-point energy of the continuum of interface-induced gap states”, *J. Appl. Phys.*, vol. 80, no. 9, p. 5076, Nov. 1996.

[183] J. Tersoff and W. Harrison, “Transition-Metal Impurities in Semiconductors—Their Connection with Band Lineups and Schottky Barriers”, *Phys. Rev. Lett.*, vol. 58, no. 22, pp. 2367–2370, Jun. 1987.

[184] K. Smit, “Adsorption of chlorine and oxygen on cleaved InAs(110) surfaces: Raman spectroscopy, photoemission spectroscopy, and Kelvin probe measurements”, *J. Vac. Sci. Technol. B Microelectron. Nanom. Struct.*, vol. 7, no. 4, p. 888, Jul. 1989.

[185] L. F. J. Piper, T. D. Veal, M. J. Lowe, and C. F. McConville, "Electron depletion at InAs free surfaces: Doping-induced acceptorlike gap states", *Phys. Rev. B*, vol. 73, no. 19, p. 195321, 2006.

[186] "New Semiconductor Material: Characteristic and Properties", *IOFFE, Physico-Technical Institute*, [Online]. Available: http://www.ioffe.ru/SVA/NSM/Semicond/InAs/bandstr.html#Basic.

[187] D. C. Tsui, "Observation of Surface Bound State and Two-Dimensional Energy Band by Electron Tunneling", *Phys. Rev. Lett.*, vol. 24, no. 7, pp. 303–306, 1970.

[188] Y. Chen, J. C. Hermanson, and G. J. Lapeyre, "Coupled plasmon and phonon in the accumulation layer of InAs(110) cleaved surfaces", *Phys. Rev. B*, vol. 39, no. 17, pp. 12682–12687, 1989.

[189] S. Kawaji and H. C. Gatos, "Electric field effect on the magnetoresistance of indium arsenide surfaces in high magnetic fields", *Surf. Sci.*, vol. 7, no. 2, pp. 215–228, Jun. 1967.

[190] L. Ö. Olsson, C. B. M. Andersson, M. C. Håkansson, J. Kanski, L. Ilver, and U. O. Karlsson, "Charge Accumulation at InAs Surfaces", *Phys. Rev. Lett.*, vol. 76, no. 19, pp. 3626–3629, 1996.

[191] H. A. Washburn, J. R. Sites, and H. H. Wieder, "Electronic profile of n-InAs on semi-insulating GaAs", *J. Appl. Phys.*, vol. 50, no. 7, p. 4872, Jul. 1979.

[192] M. G. Betti, V. Corradini, V. De Renzi, C. Mariani, P. Casarini, and A. Abramo, "Density of states of a two-dimensional electron gas measured by high-resolution photoelectron spectroscopy", *Solid State Commun.*, vol. 110, no. 12, pp. 661–666, May 1999.

[193] L. Colakerol, T. D. Veal, H.-K. Jeong, L. Plucinski, A. DeMasi, T. Learmonth, P. A. Glans, S. Wang, Y. Zhang, L. F. J. Piper, P. H. Jefferson, A. Fedorov, T C. Chen, T. D. Moustakas, C. F. McConville, and K. E. Smith, "Quantized Electron Accumulation States in Indium Nitride Studied by Angle-Resolved Photoemission Spectroscopy", *Phys. Rev. Lett.*, vol. 97, no. 23, p. 237601, 2006.

[194] L. F. J. Piper, L. Colakerol, P. D. C. King, A. Schleife, J. Zúñiga-Pérez, P.-A. Glans, T. Learmonth, A. Federov, T. D. Veal, F. Fuchs, V. Muñoz-Sanjosé, F. Bechstedt, C. F. McConville, and K. E. Smith, "Observation of quantized subband states and evidence for surface electron accumulation in CdO from angle-resolved photoemission spectroscopy", *Phys. Rev. B*, vol. 78, no. 16, p. 165127, 2008.

[195] P. D. C. King, T. D. Veal, C. F. McConville, J. Zúñiga-Pérez, V. Muñoz-Sanjosé, M. Hopkinson, E. D. L. Rienks, M. F. Jensen, and P. Hofmann, "Surface Band-Gap Narrowing in Quantized Electron Accumulation Layers", *Phys. Rev. Lett.*, vol. 104, no. 25, p. 256803, 2010.

[196] J. Lis, "The Poisson-Schrodinger equations for quatized accumulation layers - what has been missed", *Prep.*, 2014.

[197] P. E. S. Persson, Ph.D. Thesis, Linköping University, S-581 83 Linköping, Sweden, 1986.

[198] M. C. Håkansson, L. S. O. Johansson, C. B. M. Andersson, U. O. Karlsson, L. Ö. Olsson, J. Kanski, L. Ilver, and P. O. Nilsson, "The electronic structure of In- and As-terminated InAs(001) surfaces", *Surf. Sci.*, vol. 374, no. 1–3, pp. 73–79, Mar. 1997.

[199] I. Aureli, V. Corradini, C. Mariani, E. Placidi, F. Arciprete, and A. Balzarotti, "Valence band and In-4d core level photoemission study of de-capped and ion-bombarded-annealed InAs(001) epitaxial surfaces", *Surf. Sci.*, vol. 576, no. 1–3, pp. 123–130, Feb. 2005.

[200] G. R. Bell, T. . S. Jones, and C. F. McConville, "Accumulation layer profiles at InAs polar surfaces", *Appl. Phys. Lett.*, vol. 71, no. 25, 1997.

Publications

1. **L. Walczak**, G. Goryl, M.A. Valbuena, I. Vobornik, A. Tejeda, A. Taleb-Ibrahimi, J.J. Kolodziej, P. Segovia, E.G. Michel, *Surface electronic structure of InSb(001)-c(8×2)*, Surf. Sci. 608 (2013) 22–30.
2. P. Steiner, E. Gnecco, F. Krok, J. Budzioch, **L. Walczak**, J. Konior, M. Szymonski, and E. Meyer, *Atomic-Scale Friction on Stepped Surfaces of Ionic Crystals*, Phys. Rev. Lett. 106, 186104 (2011).
3. J. S. Prauzner-Bechcicki, S. Godlewski, J. Budzioch, G. Goryl, **L. Walczak**, P. Sehnal, I. G. Stará, I. Starý, F. Ample, Ch. Joachim, and M. Szymonski, *[11]Anthrahelicene on InSb(001)-c(8×2): a low temperature scanning probe microscopy study*, ChemPhysChem 2010, 11, 3522 – 3528.
4. G. Goryl, D. Toton, N. Tomaszewska, J. S. Prauzner-Bechcicki, **L. Walczak**, A. Tejeda, A. Taleb-Ibrahimi, L. Kantorovich, E. G. Michel, and J. J. Kolodziej, *Structure of the indium-rich InSb(001) surface*, Phys. Rev. B 82 (165311) 2010,
5. M.A. Valbuena, **L. Walczak**, J. Martinez-Blanco, I. Vobornik, P. Segovia, and E.G. Michel, *Lateral Confinement Effects of M-point Tamm State in Vicinal Cu (100) Surfaces*, Surface Science 630, 144 (2014).
6. N. Tomaszewska, **L. Walczak**, J. Lis, J.J. Kolodziej, *Surface states and charge accumulation states on reconstructed InAs(001) surface*, Surface Science (accepted).
7. **L. Walczak**, V. Joco, J. Martinez-Blanco, I. Vobornik, S.V. Eremeev, E.V. Chulkov and E.G. Michel, *Surface electronic structure of Au(110)-(1x2)*, in preparation.
8. **L. Walczak**, V. Joco, G. Goryl, M. A. Valbuena, T. Balasubramanian, P. Segovia, M. Szymonski and E. G. Michel, *Electronic structure and crystalline structure of vicinal Beryllium surfaces*, in preparation.
9. J.Martínez Blanco, V. Joco, **L. Walczak**, D. Sayago, M. Ruiz-Osés, I. Vobornik, P. Segovia, E.G. Michel, *Adsorption of planar aromatic hydrocarbons on Cu(110) and Ag(110): self assembling and electronic structure*, in preparation.
10. P. Starowicz, R. Kurleto, **Ł. Walczak**, B. Penc, J. Adell, J. Goraus, M. Szlawska, D. Kaczorowski, A. Szytuła, *Electronic structure of Kondo lattice systems; nonmagnetic Ce_2CoSi_3 and antiferromagnetic Ce_2RhSi_3*, Acta Physica Polonica (submitted).

Acknowledgments

„What's more beautiful than the sky, that still embraces everything beautiful (Cóż piękniejszego nad niebo, które przecież ogarnia wszystko co piękne)" Nicolai Copernicus said. While improving my scientific experience, I have discovered a beautiful country with lovely people.

I would like to thank the Ministry of Education, Spanish Government for the fellowship of my thesis and the University Autónoma de Madrid for providing me with facilities for the realization of the fellowship project.

I would like to thank my supervisor, prof. Enrique Garcia Michel, who has spent a lot of his time sharing his knowledge and enthusiasm to help me produce all of the work written here.

I would like to thank Pilar Segovia, Victor Joco, Jesus Martinez Blanco, and Miguel Angel Valbuena for their support and knowledge during the experiments and for many fruitful discussions. I thank also other people from our team (Manuel Plaza, Iulian Preda, Alejandro Oliva Calzado, Silvina Bengio and David Sayago) for their support during the experiments.

A large part of my experiments was realized in three different synchrotron facilities in Europe. I thank these facilities for great condition during the experiments, helpful, and their staff for discussions and advice. I would like to thank my colleagues from the beamlines: Thiagarajan Balasubramanian and Johan Adell (I4, Maxlab, Lund University, Lund, Sweden), Ivana Vobornik and Jun Fuji (APE, ELETTRA, Bassovizza, Italy), Amina Taleb-Ibrahimi and Antonio Tejeda (Cassiopee, Soleil, Saint Aubin, France).

I would like to thank also my colleagues from the Department of Physics of Nanostructures and Nanotechnology and Synchrotron Radiation, Jagiellonian University, Krakow, Poland, where I performed a research stay, for STM, AFM and theoretical support. Especially, I thank Marek Szymoński, Piotr Piatkowski, Jacek Kołodziej, Franciszek Krok, Jakub S. Prauzner-Bechcicki, Jakub Lis, Grzegorz Goryl, Szymon Godlewski, Maria Goryl, Natalia Tomaszewska and Janusz Budzioch.

I extend my gratitude to all people from the Departamento de Física de la Materia Condesada, professors, doctors and students. In particular, I thank Rodolfo Miranda, Amadeo López Vazquez de Parga, Julio Gómez, Jose María Gómez Rodríguez, Daniel Farías, Juan José de Miguel, Miguel Ángel Ramos, Juan José Sáenz, José Vicente Álvarez, Juanjo Hinarejos (who sadly left us too early), Fabian Calleja, Erika Jimenez, Pablo Nieto, Bogdana Borca, Cristina Navio, David Ecija, Ewelina Andrzejewska, Cristian Urban, Katrina Fladisher, Roberto Otero, Marta Trelka, Johnatan Rodríguez, Manuela Garnica, Cecilia Rodrigo, and Josefa Maria Rodriguez.

I thank Elsa Sanchez-Fuentes for her help with administration issues.

I thank also Jose Rodriguez, Rosa Maria Díez Correa, Santiago Marquez, Jose Luis Romera and all technicians of the Department for great technical support.

My Polish and Spanish friends, who supported me during my stay in Madrid: Marek and Zosia Słotarscy with family, Andrzej, Bogusława Woźniak, Mirosław Baran SVD, Krzysztof Mazurek SVD, Marian Sulik SVD, Alberto Delgado-Quijones, Miguel Angel Valbuena, Basia Milc, Piotr Piątkowski.

I want to thank my Parents (Stanisława and Józef) and Parents in Law (Joanna and Marek) and all my family (Iza, Sebastian, Zuza, Patryk, Aleksandra, Arek, Alicja, Krzysiek, Iza, Zosia, Stefan, Tomek and Inez) for permanent support.

I especially thank my wonderful wife (Gosia) and my lovely kids (Marysia and Hania).